

EXPERIMENTAL STUDIES OF PARTICLE  
ACCELERATION AND HEATING DURING  
MAGNETIC RECONNECTION

JONGSOO YOO

A DISSERTATION PRESENTED TO THE FACULTY  
OF PRINCETON UNIVERSITY  
IN CANDIDACY FOR THE DEGREE  
OF DOCTOR OF PHILOSOPHY

RECOMMENDED FOR ACCEPTANCE  
BY THE PROGRAM IN PLASMA PHYSICS  
OF THE DEPARTMENT OF  
ASTROPHYSICAL SCIENCES  
ADVISERS: MASAACKI YAMADA AND HANTAO JI

JUNE 2013

© Copyright by Jongsoo Yoo, 2013.

All rights reserved.

## Abstract

Energy conversion from magnetic energy to particle energy during magnetic reconnection is studied in the collisionless plasma of the Magnetic Reconnection Experiment (MRX). The plasma is in the two-fluid regime, where the ion motion is decoupled from that of the electron within the so-called ion diffusion region.

For ion heating and acceleration, the role of the in-plane (Hall) electric field is emphasized. The in-plane potential responsible for the Hall electric field is established by electrons that are accelerated near the small electron diffusion region. The in-plane electrostatic potential profile shows a well structure along the direction normal to the reconnection current sheet that becomes deeper and wider downstream as its boundary expands along the separatrices where the in-plane electric field is strongest. Since the Hall electric field is 3–4 times larger than the reconnection electric field, unmagnetized ions obtain energy mostly from the in-plane electric field, especially near the separatrices. The Hall electric field ballistically accelerates ions near the separatrices toward the outflow direction. After ions are accelerated, they are heated as they travel into the high pressure downstream region. This downstream ion heating cannot be explained by classical, unmagnetized transport theory, which suggests that the magnetic field should be important due to an effect called re-magnetization.

Electrons are also significantly heated during reconnection. The electron temperature sharply increases across the separatrices and peaks just outside of the electron diffusion region. Unlike ions, electrons acquire energy mostly from the reconnection electric field and the energy gain is localized near the X-point. However, the electron bulk flow energy increase remains negligible. These observations support the assertion that efficient electron heating mechanisms exist around the electron diffusion region and that the generated heat is quickly transported along the magnetic field due to the high parallel thermal conductivity of electrons. Classical Ohmic dissipation based on the perpendicular Spitzer resistivity is too small to compensate the heat flux, indicating the presence of anomalous electron heating.

Finally, a total energy inventory is calculated based on analysis of the Poynting, enthalpy, flow energy, and heat flux in the measured diffusion layer. More than half of the incoming magnetic energy is converted to particle energy during collisionless reconnection. Unlike in the Sweet-Parker model, the outgoing Poynting flux is not negligible, which is due to considerable Hall fields, i.e., the quadrupole out-of-plane magnetic field and the in-plane electric field. The total ion energy gain during reconnection is larger than that of electrons, since the energy gain occurs over a broader region. The total ion thermal energy gain is larger than the increase of the ion flow energy. Finally, the electron thermal energy gain is comparable to the ion thermal energy gain, while the electron flow energy remains insignificant.

## Acknowledgements

In the process of organizing the hundreds of papers that I had printed out over the course of my thesis, I laughed loudly when I stumbled upon my thesis proposal and realized how little I knew about magnetic reconnection at that time. It was primitive and abstract, not saying much on any issues. At the same time, I was proud of myself to realize I will be one of few graduate students who actually addressed most of the originally-proposed objectives of their thesis (putting aside the fact that the whole process took 9 months longer than I initially planned). I was also happy to be able to laugh at my old academic writing, which shows I have learned and improved.

There are many people I need to thank for helping me overcome many challenges and hardships along the way to become a junior scientist. First, thank you to my advisors, Masaaki Yamada and Hantao Ji. Masaaki, I could never thank you enough for your incredible support and patience over the course of my thesis project. I have the utmost respect for your insight and your ability to see the big picture. I will never forget the day when we had an argument about the ion temperature profile and you finally said “you don’t understand!” It turns out that you were right and I was wrong; I was clinging too much to details that were not even right. Hantao, I thank you for your support and encouragement. You have given me good guidance whenever I was stuck on a problem. I admire your ability to read critically and understand the details.

Second, many thanks to the current and former MRX students and post-docs. Clayton Myers, thank you for all your corrections and suggestions on my English writing. Without you, I would still be agonizing over my Korean-style English in this dissertation. Jonathan Jara-Almonte, thank you for providing simulation data. You have the qualities to be one of the best students from PPPL. Seth Dorfman, I always think of you when I need to move a magnetic probe from one place to another. Thanks to you, I managed to break only one magnetic probe (the 90 channel probe does not count since I successfully repaired it). To the two former post-docs, Eric Lawrence and Tim Tharp, you guys showed me how to get

the job done and to move on. In particular, Eric, thank you for building a nice vacuum control system. Tim, thanks for designing a nice screen cage. Although it does not shield the high-frequency noise, it saves a lot of time when I change cable configurations.

Special thanks to technicians from whom I received enormous help. Bob Cutler, I have bugged you hundred times but you are always extremely supportive. When I was struggling with Langmuir probes for more than one and a half years, you were the one who showed me the way to clean the probes properly via sand-blasting. I also admire your talent in finding the most efficient way to build a structure. Peter Sloboda, thank you for making jigs for my probes. Dave Cylinder, thank you for teaching me how to make various probes. With both of your help, I set on MRX record for the number of probes produced by a student, which must be more than 30. I don't think anyone is ever going to try to break that record.

Sincere thanks to my classmates, Erik Granstedt, Eisung Yoon, Jessica Baumgaertel, Luc Peterson, and Craig Jacobson. Erik, you are the one of the nicest people I have ever met. I really hope we work on the same project someday in the future and wish you good luck at Tri-alpha. Eisung, congratulations on beating me to become a father. Jess, I will always remember you as a kind, pretty woman. Luc and Craig, I wish I could have spent more time with you guys. I blame English because I could not follow your jokes!

I also thank all other people in PPPL who have encouraged me throughout this journey. Jongkyu Park, who always cheered me up by saying plasma physics would do better in near future, I still believe you although the situation gets worse and worse. William Tang, my faculty advisor, I very much appreciated your compliment when you said I am a very-talented young man. Phil Efthimion, thank you for shrewd comments and support. You are the one who found me money for the stolen camera. Robert Kaita, my first-year project advisor, you are the best mentor I have ever met. Barbara Sarfaty, you were always nice to me even when I made mistakes. Stefan Gerhardt, one of my thesis readers, thank you for 7 pages of comments that contributed to the quality of my thesis. Amitava Bhattacharjee, the other reader, thank you for your nice comments. I am looking forward to the questions

that you said that you saved for my thesis defense.

My deepest love and gratitude to my parents who must proudly look down at me from heaven. I know that you support my current career path. I remember that you had no problem with me being a scientist. I also appreciate all the support from other members of my family—my three sisters and parents-in-law in Korea, and my sister-in-law in California.

Finally, Hyunmin, my lovely wife, thank you for believing in me even on our toughest days. I already owe you a lot. I will try harder to be a good husband.

To my parents in heaven and lovely wife Hyunmin

# Contents

Abstract . . . . .	iii
Acknowledgements . . . . .	v
List of Tables . . . . .	xii
List of Figures . . . . .	xiii
<b>1 Introduction</b>	<b>1</b>
1.1 Examples of Magnetic Reconnection in Nature . . . . .	3
1.2 Fast Reconnection Problem . . . . .	14
1.3 Previous Research on Particle Heating and Acceleration During Reconnection	20
1.4 Dissertation Objectives . . . . .	30
1.5 Summary and Outline . . . . .	30
<b>2 Energy Transport Equations</b>	<b>35</b>
2.1 Resistive MHD Energy Transport Equations . . . . .	36
2.2 Energy Conversion in the Sweet-Parker Model . . . . .	38
2.3 Two-fluid Energy Transport Equations . . . . .	41
<b>3 Experimental Setup and Plasma Conditions</b>	<b>45</b>
3.1 Magnetic Reconnection Experiment . . . . .	46
3.2 Diagnostics . . . . .	49
3.3 Plasma Parameters and Experimental Regime . . . . .	66

<b>4</b>	<b>Ion Acceleration and Heating by In-plane Potential</b>	<b>73</b>
4.1	In-plane Electrostatic Potential . . . . .	74
4.2	Ion Acceleration by the In-plane Electric Field . . . . .	81
4.3	Downstream Ion Heating . . . . .	87
<b>5</b>	<b>Electron Heating</b>	<b>97</b>
5.1	2-D Electron Temperature Profile . . . . .	98
5.2	Electron Energy Transport near the Diffusion Region . . . . .	102
<b>6</b>	<b>Energy Inventory During Collisionless Reconnection in MRX</b>	<b>113</b>
6.1	Description of Method . . . . .	115
6.2	Energy Inventory During Collisionless Reconnection in MRX . . . . .	120
<b>7</b>	<b>Conclusions and Future Work</b>	<b>125</b>
7.1	Conclusions . . . . .	125
7.2	Possible Impact on Reconnection Research . . . . .	129
7.3	Suggested Future Work . . . . .	130
<b>A</b>	<b>Evaluation of Spacecraft Data Analysis Techniques via Plasma Jogging Experiments</b>	<b>133</b>
A.1	Introduction . . . . .	134
A.2	Experimental Setup . . . . .	137
A.3	Minimum Variance Analysis on Magnetic Field (MVAB) . . . . .	140
A.4	Boundary-Crossing Time Analysis (BCTA) . . . . .	151
A.5	Synthesis of Results . . . . .	159
A.6	Summary and Discussion . . . . .	161
<b>B</b>	<b>Radial Density Asymmetry in MRX</b>	<b>165</b>
<b>C</b>	<b>Glossary of Symbols for Physical Quantities Related to Energy Transport</b>	<b>171</b>



# List of Tables

3.1	Plasma parameters during the quasi-steady period of He discharges with the 4.5 mT fill pressure . . . . .	68
6.1	Energy inventory during collisionless reconnection in MRX . . . . .	120
A.1	MVAB results for data from the same sample measurement points used for BCTA in Fig. A.8 . . . . .	158

# List of Figures

1.1	Schematic view of magnetic reconnection . . . . .	2
1.2	Multi-wavelength (211, 193, and 171 Å) UV snapshot of the Sun in the middle of a large CME event . . . . .	5
1.3	Various UV snapshots (teal–131; blue–335; gold–171 Å) of an X1.4 class flare erupting from an active region . . . . .	6
1.4	Cartoon of a solar-flare loop which shows the magnetic reconnection site to be above the soft X-ray (SXR) loop . . . . .	6
1.5	Cross section of the Earth’s magnetosphere with the Sun to the left . . . . .	8
1.6	Beautiful aurorae created by a geomagnetic substorm . . . . .	9
1.7	Sawtooth oscillation measured in a hot fusion plasma . . . . .	11
1.8	Magnetic field geometry for the Sweet-Parker model . . . . .	14
1.9	Magnetic field geometry for Petschek’s fast reconnection model . . . . .	16
1.10	Schematic picture of two-fluid effects in magnetic reconnection . . . . .	18
1.11	In plane potential profile measured in space and numerical simulations . . . . .	25
1.12	Ion heating associated with a reconnection event in MST . . . . .	26
3.1	Photo of the Magnetic Reconnection Experiment . . . . .	46
3.2	Toroidal cross section of the MRX vacuum chamber . . . . .	47
3.3	Current waveforms in the TF and PF coils . . . . .	48
3.4	2-D magnetic probe array . . . . .	50
3.5	MRX triple Langmuir probe . . . . .	54

3.6	Mach probe diagnostic . . . . .	57
3.7	Photo of an Ion Dynamics Spectroscopy Probe (IDSP) . . . . .	59
3.8	Calibration signals from a neon spectral lamp . . . . .	60
3.9	Example of the measured He spectral lines . . . . .	62
3.10	Sketch of the 22-tip floating potential probe . . . . .	63
3.11	Setup of the MRX interferometer system . . . . .	65
3.12	Line-integrated density measured by the MRX interferometer . . . . .	66
3.13	Histogram of the radial position of the X-point at $t = 330 \mu s$ . . . . .	67
3.14	Radial profile of the out-of-plane electric field at $Z = 0$ in the middle of the quasi-steady period ( $t = 332 \mu s$ ) . . . . .	69
3.15	2-D profile of the out-of-plane quadrupole magnetic field at $t = 330 \mu s$ along with the contours of the poloidal flux $\Psi$ . . . . .	70
3.16	Radial profile of the reconnection magnetic field at $Z = 0$ . . . . .	71
4.1	2-D floating potential profile at $t = 330 \mu s$ along with contours of the poloidal flux $\Psi$ . . . . .	74
4.2	2-D plasma potential profile along with contours of the poloidal flux $\Psi$ . . .	77
4.3	Dependence of the plasma potential well magnitude on the electron density and temperature at $Z = 0$ . . . . .	80
4.4	In-plane ion flow vectors along with contours of $\Phi_p$ and $\Psi$ . . . . .	82
4.5	2-D density profile at $t = 330 \mu s$ measured by a triple Langmuir probe . . .	83
4.6	In-plane flow vectors of ions and electrons along with the poloidal flux $\Phi$ .	84
4.7	Work done by the electric field on ions per unit time and unit volume . . . .	87
4.8	Measured ion temperature profiles . . . . .	88
4.9	2-D ion temperature profiles from simulations with the global boundary conditions relevant to the MRX geometry . . . . .	92
4.10	Profiles of each component of the ion temperature from the simulation with collisions . . . . .	93

4.11	Anticipated ion pressure and temperature profiles from the pressure balance	94
4.12	2-D profiles of the helium neutral temperature . . . . .	95
5.1	2-D electron temperature profile along with the contours of the poloidal flux $\Psi$ . . . . .	99
5.2	Fast camera image of the discharge 131596 at $t = 328 \mu\text{s}$ . . . . .	100
5.3	Neutral emission coefficient as function of electron density and temperature	101
5.4	Work done by the electric field on electrons per unit time and unit volume .	102
5.5	2-D profiles of energy in high-frequency fluctuations along with the contours of the poloidal flux $\Psi$ . . . . .	111
6.1	Schematic of energy fluxes in the collisionless reconnection layer . . . . .	115
6.2	Boundary of the surface where the energy inventory analysis is conducted .	117
A.1	Cross section of the MRX vacuum chamber for plasma jogging experiments	137
A.2	Radial profile of $B_Z$ during the quasi-steady period of a discharge with a jogging current sheet . . . . .	138
A.3	Current sheet motion as a function of the firing voltage for the SF coils. . .	139
A.4	Data from 2-D magnetic probe arrays during the quasi-steady period of the MRX jog experiment discharge 114338 . . . . .	143
A.5	MVAB analysis for data from the discharge 114338 . . . . .	145
A.6	MVAB error analysis . . . . .	148
A.7	Minimum variance analysis for data from a discharge with a time-varying geometry . . . . .	150
A.8	Boundary-crossing time analysis for data from the discharge 114338 . . . .	153
A.9	Boundary-crossing time analysis for a discharge with a flux rope structure .	156
A.10	Idealized X-line geometry . . . . .	158
B.1	2-D profiles of the floating potential and the ion in-plane flow velocity . . .	166

B.2	2-D electron density profiles at $t = 310 \mu s$ and $350 \mu s$ . . . . .	167
B.3	Selective shielding of the inductive electric field by the plasma . . . . .	168

# Chapter 1

## Introduction - Magnetic Reconnection

The Sun is home to two of the most explosive phenomena in the solar system: solar flares and coronal mass ejections (CMEs). These powerful events that trigger geomagnetic substorms can have a huge impact on our lives by damaging satellites, disrupting short-wave radio communications, and causing wide-area electrical blackouts. What gives rise to the observed sudden releases of energy from the Sun? The study of magnetic reconnection has begun to answer this question.

The concept of magnetic reconnection was first suggested by Giovanelli, 1946 as a mechanism for particle acceleration in solar flares. Since then, magnetic reconnection has been recognized as one of the fundamental processes in magnetized plasmas, whether in the laboratory, the solar system, or distant objects in the universe. For example, reconnection is responsible for sawtooth relaxations in a tokamak, a toroidal device used in thermonuclear fusion experiments [Yamada *et al.*, 1994]. It is also widely believed that reconnection plays a key role not only in dynamic phenomena in the solar system such as solar flares, CMEs, and magnetospheric substorms, but also those in astrophysical plasmas such as stellar flares and outbursts generated in accretion disks [Priest and Forbes, 2000; Zweibel and Yamada, 2009; Yamada, Kulsrud, and Ji, 2010].

The basic concept of magnetic reconnection must be introduced in order to under-

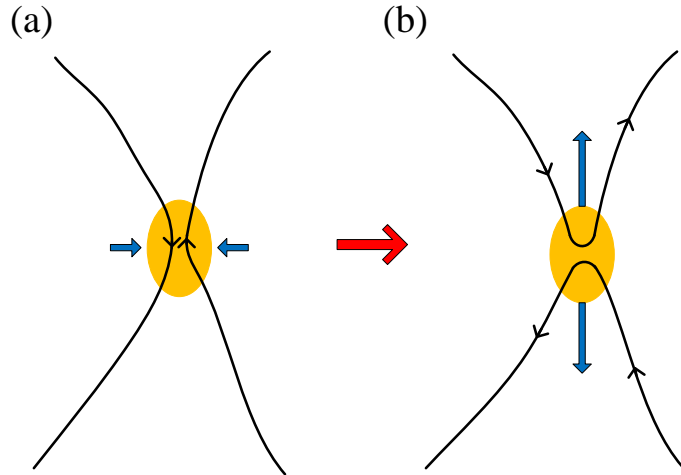


Figure 1.1: Schematic view of magnetic reconnection. (a) Before reconnection, two different field lines approach each other so that non-ideal MHD effects become important locally within the diffusion region (marked in orange). (b) After reconnection, newly reconnected field lines have high tension and therefore quickly pull away from the diffusion region. During this fast tension release, conversion of magnetic energy to particle energy occurs as fluid elements attached to the field lines are accelerated.

stand why it is regarded as a major mechanism for many impulsive events observed in magnetized plasma. Fundamentally, magnetic reconnection is a topological rearrangement of magnetic field lines, during which the fast conversion from magnetic energy to particle energy occurs. Here, “topological rearrangement” means a process of breaking and reconnecting magnetic field lines as shown in Fig. 1.1. In the framework of ideal magnetohydrodynamics (MHD), which is an excellent model for describing global dynamics of highly electrically conductive plasmas, magnetic field lines are frozen-in to the plasma and remain intact. In other words, field lines always move with the corresponding plasma and cannot be broken. However, when a pair of field lines approach each other, non-ideal effects become locally important. Then, plasma fluid elements attached to each field line can be mixed together in the small area, called the diffusion region (marked in orange in Fig. 1.1), where the field lines break and reconnect. The newly connected field lines have large magnetic tension (i.e., they are highly bent as shown in Fig. 1.1-(b)). As the new field lines

move out of the diffusion region, the magnetic tension is relieved rapidly and fluid elements are accelerated to gain energy. Because magnetic reconnection facilitates the fast conversion of magnetic energy to particle energy, it is a strong candidate as the major mechanism responsible for the range of explosive phenomena observed in magnetized plasmas.

Magnetic reconnection involves a global process where magnetic energy is released into a large-scale volume of plasma. At the same time, reconnection includes a local process that changes the local connectivity of field lines. Therefore, the dynamics of reconnection depend on both the local plasma parameters and the global boundary conditions. Moreover, it seems that there is a complex coupling between the local and global scales, which makes magnetic reconnection even more challenging. This is why, in spite of the progress made in the past few decades, significant work remains in order to understand this intriguing phenomenon.

In this dissertation, energy conversion processes during magnetic reconnection are discussed. Because the importance of reconnection comes from its effectiveness in converting magnetic energy to particle energy, identifying major mechanisms for energy conversion is one of the most important problems in magnetic reconnection.

This introductory chapter is organized as follows: First, some examples of reconnection in nature are introduced. Then, a brief review on the fast reconnection problem, which is why the observed reconnection rate is much faster than that predicted by resistive MHD theory, is presented. Next, previous research on particle heating and acceleration during reconnection is summarized. Then, the objectives of this dissertation are described. Finally, the summary and outline of this dissertation are presented.

## **1.1 Examples of Magnetic Reconnection in Nature**

In this section, examples of magnetic reconnection in various magnetized plasmas are examined. This section will cover only a few key examples. More extensive reviews on re-

connection in nature can be found elsewhere [e.g. Priest and Forbes, 2000; Birn and Priest, 2007; Yamada, Kulsrud, and Ji, 2010].

### **1.1.1 Solar Flares on the Sun**

The Sun is full of dynamic activity as shown in Fig. 1.2, which is a composite image taken during a solar storm on August 1, 2010. This photo is a multi-wavelength (211, 193, and 171 Å) extreme ultraviolet (EUV) snapshot from NASA's Solar Dynamics Observatory (SDO). The eruption in this image covers almost the entire northern hemisphere of the Sun. This large-scale eruption is believed to require a rapid, global change of the magnetic topology, which implies the presence of magnetic reconnection.

Solar flares are one of the most explosive phenomena among this dynamic solar activity. They are characterized by a sudden brightening in the solar atmosphere. It is now widely believed that solar flares result from a rapid release of magnetic energy stored in the solar coronal magnetic field through reconnection. Fig. 1.3 shows UV snapshots taken during an X1.4 class flare that erupted from a large active region on July 12, 2012. Magnetic reconnection is believed to occur slightly above the bright loop (soft X-ray loop or SXR loop) and to generate jets and energetic particles as shown in Fig. 1.4. When the energetic particles travel along the magnetic field and collide with the dense chromosphere plasma, they generate bursts of light including hard X-rays (HXR). As the chromosphere plasma is heated by energy dissipation from energetic particles, it evaporates into the loops, which creates the SXR loop. This reconnection-based explanation of solar flares has been supported by observations of a typical soft X-ray cusp-like structure [Tsuneta, 1996].

Many open questions still remain regarding solar flares due to their dynamic complexities and a lack of detailed measurements. First, it is not clear how the solar flare is triggered (i.e., the trigger problem). Before the onset of a solar flare, there must be energy transferred from the lower layers of the Sun to the solar corona, so that enough energy is stored in the coronal magnetic field to drive the flare. Then, there should be a moment that the global

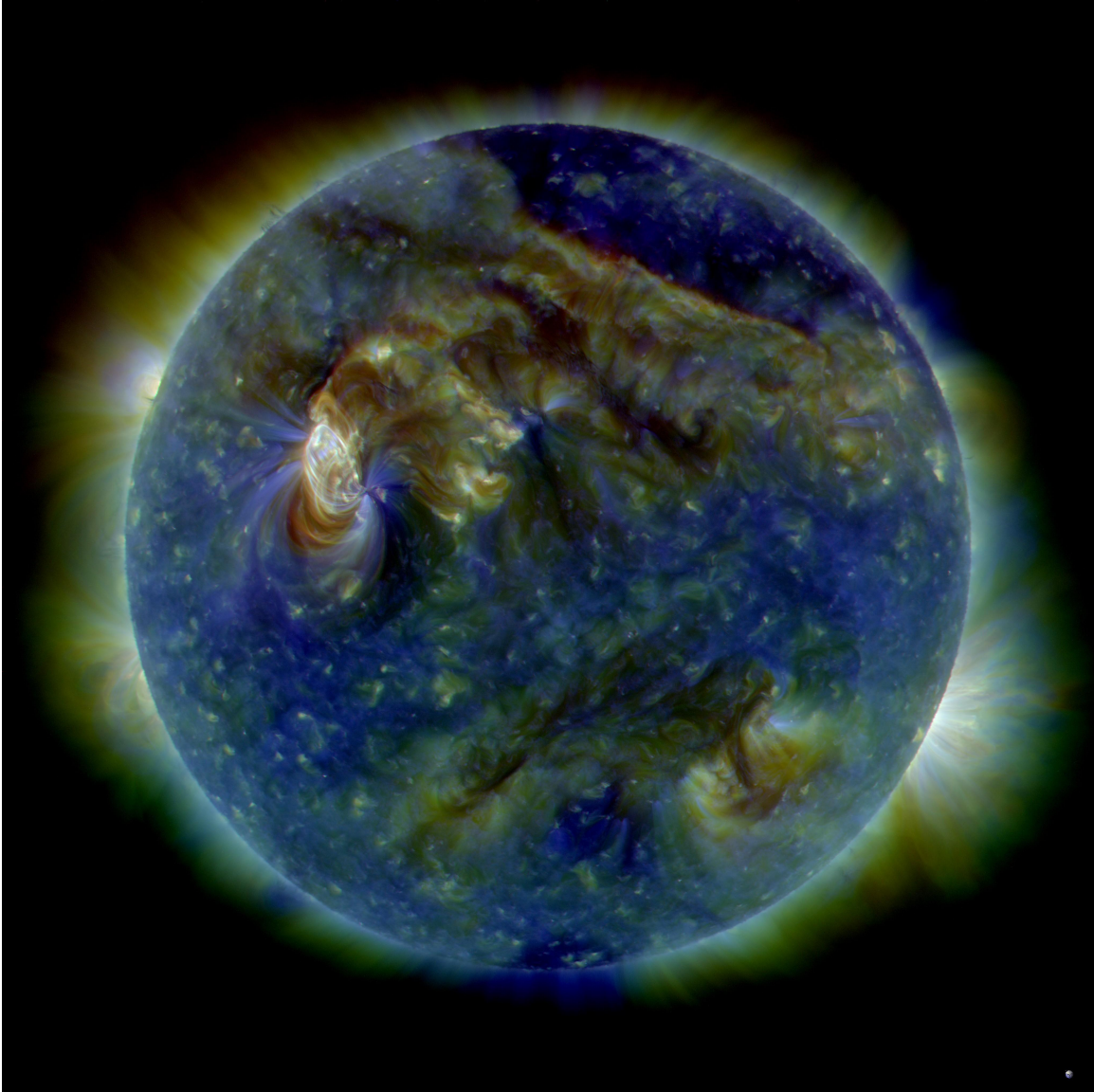


Figure 1.2: Multi-wavelength (211, 193, and 171 Å) UV snapshot of the Sun in the middle of a large CME event. Multiple filaments on the solar surface erupted on August 1, 2010, creating CMEs, a C3 class solar flare (white area on upper left), and a solar tsunami (wave-like structure, upper right).

Figure Credit: NASA/SDO/AIA ([www.nasa.gov](http://www.nasa.gov))

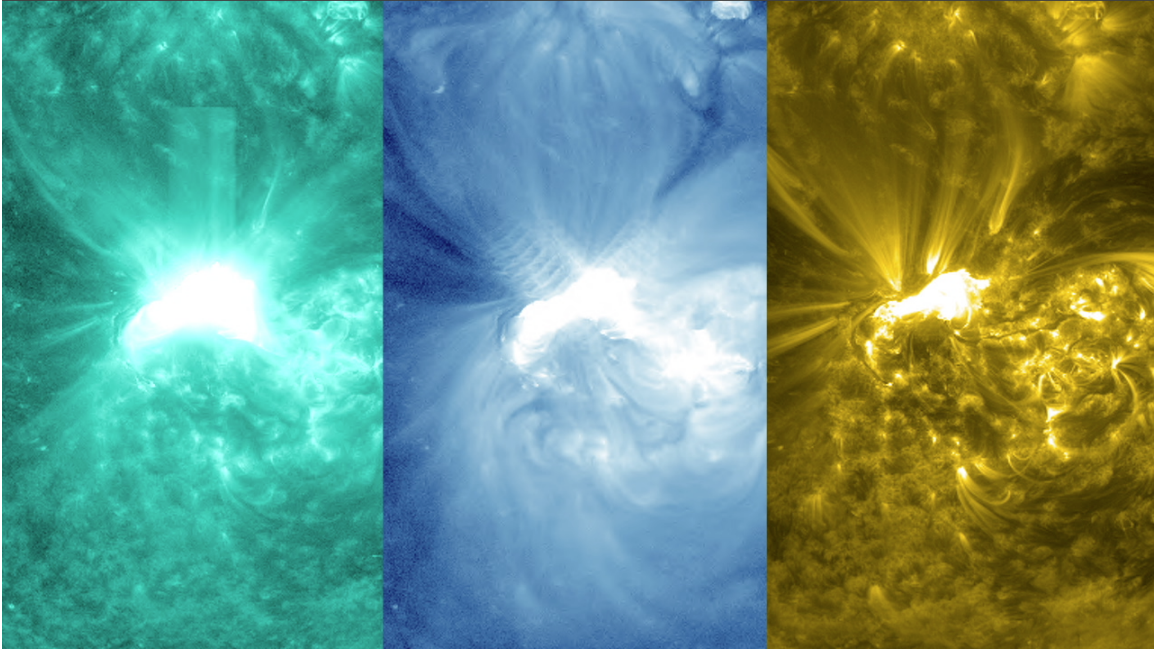


Figure 1.3: Various UV snapshots (teal–131; blue–335; gold–171 Å) of an X1.4 class flare erupted from a sunspot on July 12, 2012.

Figure Credit: NASA/SDO/AIA (svs.gsfc.nasa.gov)

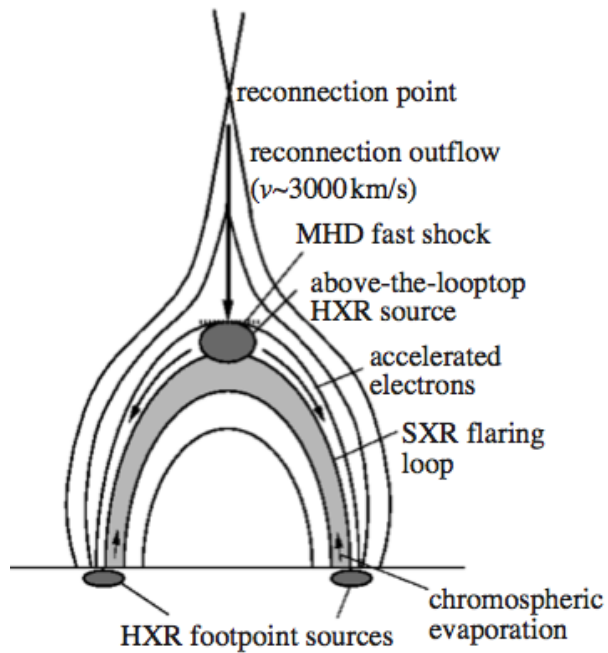


Figure 1.4: Cartoon of a solar-flare loop which shows magnetic reconnection site to be above the soft X-ray (SXR) loop. This figure is adapted from Harra, 2002.

magnetic geometry can no longer contain the stored energy and magnetic reconnection is triggered by, for example, ideal MHD instabilities. Although this trigger problem is important for space weather forecasting, it is still one of the most difficult problems in solar physics since the evolution of the global solar magnetic field geometry is extremely difficult to measure. As part of an effort to understand trigger mechanisms, researchers have tried to identify any structures that can be a precursor of eruptive events. A sigmoid, which is a forward-S or inverse-S shaped loop, is widely considered to be one of the such precursors [Canfield, Hudson, and McKenzie, 1999].

Second, further research is required to understand why a large number of particles become energetic in impulsive flares (i.e., the numbers problem). Observations of solar flares suggest that a significant fraction of the stored magnetic energy can be released in the form of energetic particles [Lin and Hudson, 1976; Lin *et al.*, 2003; Emslie *et al.*, 2005; Krucker *et al.*, 2010]. These observations are remarkable since the population of energetic particles is usually so small that their energy is negligible compared to bulk thermal energy. The key issue related to this problem is whether a single reconnection point as shown in Fig. 1.4 can produce such a large number of energetic particles. By noticing that a single X-line model may not be efficient for energetic particle generation, Drake *et al.*, 2006 suggest a mechanism based on Fermi acceleration from contracting, volume-filling islands that accommodate multiple reconnection points. However, there are still other possibilities and the debate on this issue is ongoing. Thus, more observations and theoretical modeling are needed for further understanding. Subsection 1.3.1 contains a more detailed review on this issue.

Another open question is how important the observed three-dimensional (3-D) structures are for solar flares (i.e., the 3-D problem). The standard model illustrated in Fig. 1.4 is two-dimensional (2-D). However, observations of solar flares reveal the dynamic evolution of complex, 3-D magnetic geometries. Although various 3-D reconnection processes have been studied, there is no strong or consistent agreement on the importance of 3-D

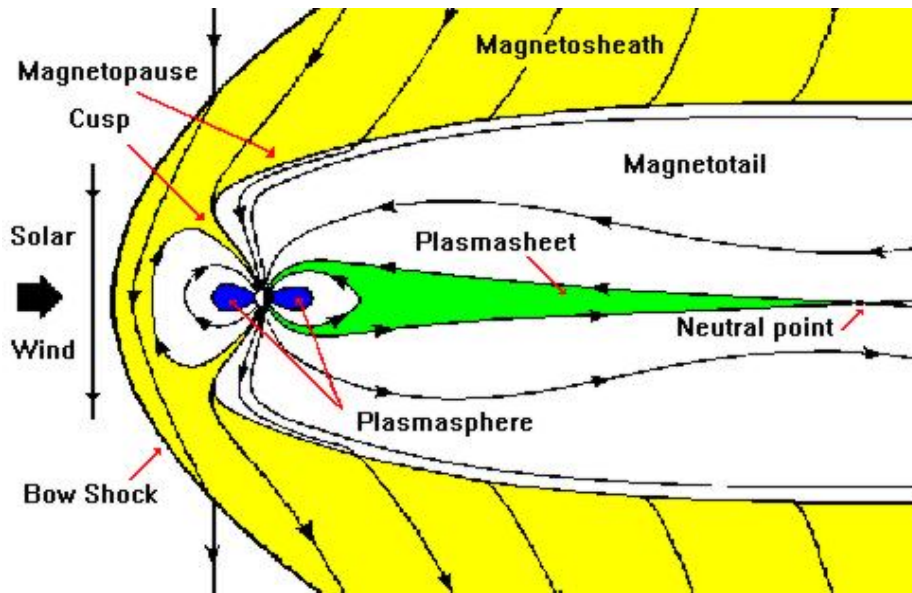


Figure 1.5: Cross section of the Earth's magnetosphere with the Sun to the left. The shape of the magnetosphere is determined by the direct interaction between the solar wind and the Earth's dipole field. Magnetic reconnection occurs at the dayside magnetopause and in the magnetotail. Figure from <http://helios.gsfc.nasa.gov>.

reconnection.

Solar flares are a good example of reconnection in a complex geometry. Considerable progress has been made toward understanding solar flares through detailed observation of solar activity from modern satellites such as Yohkoh (Sunbeam in Japanese), SOHO (Solar and Heliospheric Observatory), TRACE (Transition Region And Coronal Explorer), RHESSI (Ramaty High Energy Solar Spectroscopic Imager), Hinode (Sunrise in Japanese), and STEREO (Solar TERrestrial RELations Observatory). However, key questions on this explosive phenomenon remain unsolved and they will not be answered without improvements in the general understanding of magnetic reconnection.

### 1.1.2 Geomagnetic Substorms in the Earth's Magnetosphere

The magnetosphere of the Earth is the cavity created by the Earth's geomagnetic field that is shaped by the interplanetary magnetic field and plasma from the Sun known as the solar



Figure 1.6: Beautiful aurorae created by a geomagnetic substorm on September 3, 2012 as a result of a CME on August 31, 2012.

Figure Credit: NASA/Goddard Space Flight Center, Photo taken by David Cartier, Sr. ([www.nasa.gov](http://www.nasa.gov))

wind. The interaction with the solar wind deforms the geomagnetic dipole field; it compresses the field lines of the day side and stretches the lines out to form a long tail (the magnetotail) on the night side as shown in Fig. 1.5. Magnetic reconnection plays an important role in this dynamic interaction between the geomagnetic field and the solar wind. It is believed that magnetic reconnection occurs at two sites in the magnetosphere [Dungey, 1961]. The first site is the frontside (dayside) magnetopause where reconnection results in the transfer of magnetic flux and plasma from the solar wind to the magnetotail. The second reconnection site is in the magnetotail where reconnection releases the incoming magnetic flux and mass into the inner magnetosphere. This intermittent release of energy causes geomagnetic substorms that initiate beautiful aurorae in the high latitude regions of the sky as shown in Fig. 1.6.

Dungey's original picture of reconnection in the Earth's magnetosphere has been supported by many *in situ* satellite observations. At the dayside magnetopause, the first direct and incontrovertible evidence of reconnection was provided by Paschmann *et al.*, 1979.

They observed high-speed flows associated with the reversal of the reconnecting magnetic field component ( $B_z$  in the Geocentric Solar Ecliptic (GSE) coordinate system, which is perpendicular to the ecliptic), which was interpreted as the outflow resulting from reconnection. Many similar observations of plasma jets associated with magnetic reconnection have been reported [e.g. Sonnerup *et al.*, 1981; Gosling *et al.*, 1982; Phan *et al.*, 2000; Mozer, Bale, and Phan, 2002; Phan *et al.*, 2004; Vaivads *et al.*, 2004].

Evidence of magnetic reconnection has been also found in the magnetotail. For example, Øieroset *et al.*, 2001 reported a rare encounter of an active diffusion region of collisionless magnetic reconnection. They emphasized measurements of the Hall effect, which is caused by separation of ions and electrons due to the fundamental length scale difference between them [Sonnerup, 1979]. A reconnection X-line structure extending more than 390 Earth radii has been observed in the magnetotail [Phan *et al.*, 2006], which reveals that magnetotail reconnection is a large-scale process and can be in quasi-steady state. Another important observation of reconnection was reported by Angelopoulos *et al.*, 2008. By utilizing multiple satellites, they argue that reconnection occurred before the associated geomagnetic substorm and thereby suggest that substorms are initiated by tail reconnection.

Over the past few decades, *in situ* measurements of various satellites have revealed the presence of magnetic reconnection throughout the Earth's magnetosphere. There have been numerous observations of the typical consequences of magnetic reconnection such as jets of plasma, but only a small number of encounters of the active diffusion region have occurred [e.g. Øieroset *et al.*, 2001; Mozer, Bale, and Phan, 2002; Phan *et al.*, 2004; Vaivads *et al.*, 2004; Borg *et al.*, 2005]. Thus, there are still many questions concerning the microphysics related to the electron diffusion region, which is believed to be embedded in the much larger ion diffusion region (see Fig. 1.10). A new NASA mission called the Magnetospheric Multi-scale (MMS) mission will be launched in 2014 to explore 3-D structures of the diffusion region on scales down to the electron inertial length ( $\delta_e \equiv c/\omega_{pe}$ , where  $c$  is

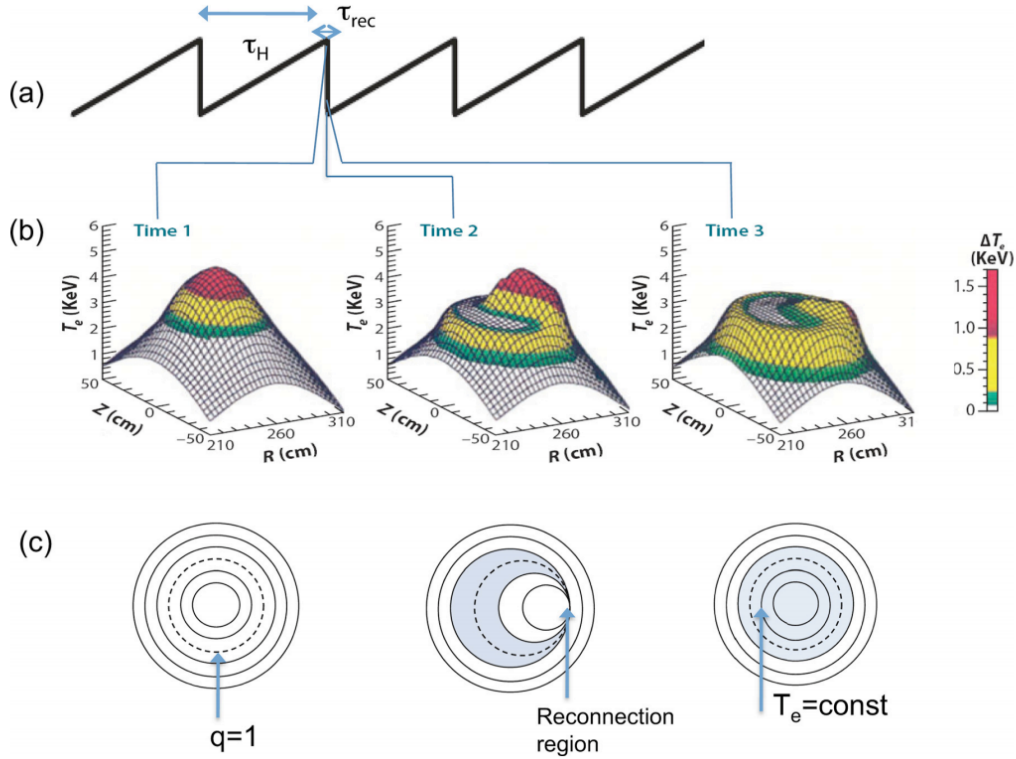


Figure 1.7: Sawtooth oscillation measured in a hot fusion plasma. (a) Typical time evolution of X-ray emission signals. A longer build-up phase ( $\tau_H \sim 100$  ms) is followed by a short crash phase ( $\tau_{rec} \sim 100\text{--}150$   $\mu\text{s}$ ). (b) Two-dimensional electron temperature profile during the crash phase. Initially, the profile is peaked at the center but it becomes flat during the crash due to magnetic reconnection. (c) Schematic picture of magnetic reconnection during sawtooth oscillation. Reconnection occurs at the resonant  $q = 1$  surface. Figure from Yamada, 2011.

the speed of light and  $\omega_{pe}$  is the electron plasma oscillation frequency). The MMS mission is expected to expand our knowledge on the mechanisms that actually break the magnetic field lines in the electron diffusion region.

### 1.1.3 Sawtooth Oscillation in a Tokamak

Sawtooth oscillations are characterized by a periodic collapse or crash of the central plasma pressure. The word sawtooth originates from the shape of a typical time evolution of X-ray emission signals from the core plasma as shown in Fig. 1.7-(a) [von Goeler, Stodiek, and

Sauthoff, 1974]. One cycle of a sawtooth oscillation consists of a long build-up phase and a short crash phase during which reconnection takes place. During the former phase, the poloidal flux slowly builds up as the core current density increases. At the same time, the core electron temperature rises due to good confinement such that the electron temperature profile becomes peaked in the core as shown in the first panel of Fig. 1.7-(b). During the crash, the peaked profile suddenly flattens, as shown in Fig. 1.7-(b).

A classic theory of sawtooth oscillation was developed by Kadomtsev, 1975. According to his theory, the build-up phase continues until the safety factor  $q \equiv rB_\phi/R_0B_\theta$  drops below unity, where  $R_0$  and  $r$  are major and minor radii and  $B_\phi$  and  $B_\theta$  are toroidal and poloidal magnetic fields, respectively. Then, the plasma becomes unstable to an internal MHD kink mode. This instability drives magnetic reconnection at the  $q = 1$  resonant surface, raising  $q$  above unity and flattening the previously peaked temperature profile flat as shown in Fig. 1.7-(c). Kadomtsev, 1975 predicts that reconnection continues until  $q$  exceeds above unity everywhere in the core region. Then, the internal kink mode is stabilized and reconnection ceases.

Although the classical theory of Kadomtsev agrees with the general features of sawtooth oscillations, there are discrepancies between the theory and observations in modern tokamaks. First, the crash time is much shorter than Kadomtsev's prediction [Edwards *et al.*, 1986; Yamada *et al.*, 1994], which is based on a resistive MHD model, the so called Sweet-Parker model [Sweet, 1958; Parker, 1957]. Moreover, the safety factor  $q$  does not usually recover above unity after a crash, which indicates that reconnection is not "complete," even though the temperature gradient of the core plasma completely disappears. Many models have tried to explain this fast, incomplete reconnection during sawtooth oscillations, but this important problem remains unsolved.

The complexity of the sawtooth crash comes from a coupling between the local and global scales. The evolution of the equilibrium and the development of an instability near the  $q = 1$  surface during the build-up phase are global phenomena that require an

MHD description. However, resistive MHD models cannot explain the fast reconnection observed during the crash, indicating that a kinetic treatment is needed locally at the reconnection site. Moreover, it seems that the problem of incomplete reconnection requires an understanding of both the local reconnection process and the evolution of the global configuration.

Sawtooth oscillations are a good example of reconnection during magnetic self-organization in a magnetized plasma. If there are energy sources either external or internal, the global magnetic configuration will gradually evolve to a new equilibrium and the plasma parameters will slowly adjust to it. When a new equilibrium is susceptible to some instabilities, the plasma reorganizes itself rapidly to a new stable equilibrium. Magnetic reconnection plays a key role in this self-organization process, providing a mechanism to change the magnetic topology and convert magnetic energy to particle energy while conserving magnetic helicity [Taylor, 1986]. This process is called plasma relaxation since the new equilibrium is in a lower magnetic energy state. To emphasize this aspect of the sawtooth crash, it is also called a “sawtooth relaxation.”

Sawtooth relaxation demonstrates an important feature of reconnection during magnetic self-organization: local reconnection is coupled with the global evolution of a magnetized plasma. It is the unstable *global* equilibrium that drives *local* magnetic reconnection. As reconnection proceeds, the system undergoes rapid topological changes and relaxes into a lower energy state, which means that *local* magnetic reconnection changes the *global* configuration. Then, the change in the *global* plasma condition alters aspects of *local* reconnection and eventually stops the process. In this sense, sawtooth relaxation is a fast reconnection problem with a complex boundary condition. This is why collaboration between experts on fast reconnection and fusion scientists specializing in MHD instabilities are essential to solve this long-standing problem in fusion science.

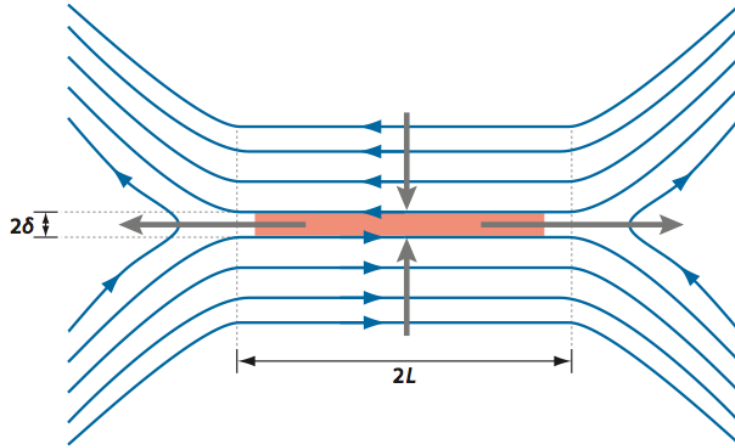


Figure 1.8: Magnetic field geometry for the Sweet-Parker model. Oppositely directed field lines are brought together and reconnect in a diffusion layer (red color). The field line diffuses over the half width of the diffusion layer  $\delta$ , which is much smaller than the system size, thereby reducing the required diffusion (reconnection) time. Figure from Zweibel and Yamada, 2009.

## 1.2 Fast Reconnection Problem

The fast reconnection problem has been a focal point of research since the classical Sweet-Parker reconnection rate [Sweet, 1958; Parker, 1957], which is based on resistive MHD and the Spitzer resistivity [Spitzer, 1962], was determined to be too small to explain the observed fast dynamic evolution in astrophysical plasmas. Although the work in this dissertation does not directly address fast reconnection mechanisms, it is worthwhile to review previous research on this problem and to discuss outstanding issues since it has for many years been the most prevalent topic in the reconnection community. Thus, in this section, a brief review on the history of the fast reconnection problem will be made without detailed theoretical descriptions. More extensive reviews on this problem can be found in other reconnection literature [e.g. Biskamp, 2000; Birn and Priest, 2007; Zweibel and Yamada, 2009].

The frozen-in law of ideal MHD states that magnetic field lines cannot be broken. However, if a finite resistivity exists, field lines can “slip” through a plasma by diffusion. This

diffusion time scale  $\tau_D = L^2\mu_0/\eta$  in a typical astrophysical plasma is too enormous to explain explosive phenomena such as solar flares. Here,  $L$  is a characteristic length scale of the system,  $\mu_0$  is the permeability of free space, and  $\eta$  is plasma resistivity. For a typical solar flare,  $\tau_D$  is about  $10^{14}$  s, while the observed duration of a solar flare is less than  $10^3$  s [Biskamp, 2000].

The Sweet-Parker model narrowed the huge gap between theory and observation. As shown in Fig. 1.8, they introduced the concept of a current sheet of much smaller width  $\delta$  than the system size  $L$ . Then, the field line need to diffuse only over  $\delta$ , so that the required diffusion time scale reduces significantly. The Sweet-Parker reconnection time  $\tau_{SP}$  is given by the geometric mean of the diffusion time and the Alfvén time  $\tau_A$ , such that  $\tau_{SP} = (\tau_D\tau_A)^{1/2}$ , where  $\tau_A$  is  $L/V_A$  and  $V_A$  is the Alfvén velocity. It may be rewritten as  $\tau_{SP} = \sqrt{S}\tau_A$ , where  $S \equiv \mu_0V_AL/\eta$  is the Lundquist number. However, it was soon realized that the Sweet-Parker reconnection model is still not adequate for astrophysical phenomena since  $S$  is usually large for astrophysical plasmas. For example,  $S$  is on the order of  $10^{14}$  in a typical solar flare, which gives the Sweet-Parker time of about  $10^7$  s, which is still far too slow.

This discrepancy seemed to be resolved when Petschek, 1964 presented a reconnection model that allowed much faster energy release. He circumvented the narrow outflow channel of the Sweet-Parker model by introducing slow-mode shocks into the outflow region as shown in Fig. 1.9. The reconnection diffusion region becomes X-shaped rather than double Y-shaped as in the Sweet-Parker model. In this case, the maximum reconnection time scales as  $(\ln S)\tau_A$ , which can be a few percent of the Alfvén time, fast enough to account for astrophysical phenomena. The model was soon generally accepted and widely cited over the following two decades.

In the 1980s, however, researchers started to realize that the Petschek model is not a self-consistent resistive MHD model. Numerical simulations with spatially uniform resistivity fail to reproduce Petschek’s configuration [Biskamp, 1986]. Moreover, if the configu-

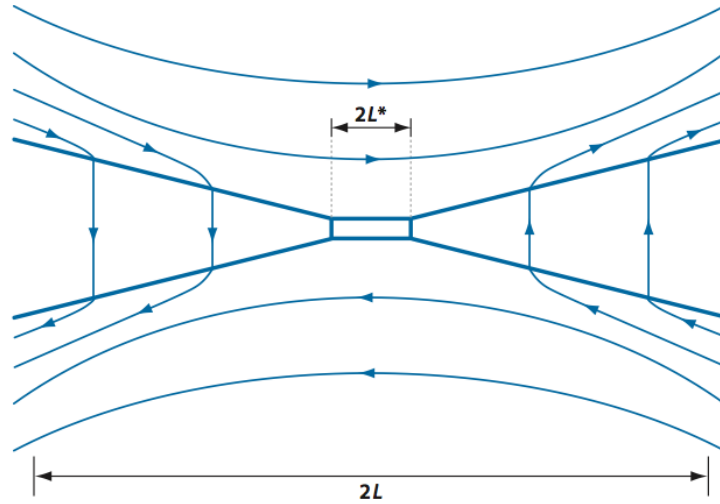


Figure 1.9: Magnetic field geometry for Petschek's fast reconnection model. The diffusion layer is short, and most of the fluid does not must pass through the layer. Two pairs of slow-mode shocks turn the fluid toward the outflow direction. Figure from Zweibel and Yamada, 2009.

ration is imposed, it relaxes to the Sweet-Parker geometry in a few Alfvén times [Uzdensky and Kulsrud, 2000]. Uzdensky and Kulsrud, 2000 also show that the Petschek-type diffusion region can be maintained if anomalous (high) resistivity is enforced locally at the diffusion region. This means that Petschek's model is just a possible resistive MHD configuration if there is an effective fast reconnection mechanism at the X-point (the center of the X-type diffusion region).

In addition to the fact that Petschek's theory was not supported by MHD simulations, more observations in magnetospheric and hot fusion plasmas supported the assertion that the reconnection rate is still fast even in collisionless plasmas. These observations suggest that the physics of fast reconnection are something beyond resistive MHD. Thus, researchers started to look for mechanisms to explain collisionless reconnection. Since then, two main different candidates for collisionless reconnection have been studied: (1) anomalous resistivity at the diffusion region; (2) two-fluid effects in the diffusion region due to the fundamental length scale difference between ions and electrons.

Anomalous resistivity has long been considered as a fast reconnection mechanism. The basic idea is that electrostatic or electromagnetic fluctuations enhance the resistivity at the diffusion layer, thereby facilitating fast reconnection. Because physical quantities such as the magnetic field and the pressure have gradients across the diffusion layer, it is possible that instabilities arise there. Several different instability mechanisms have been considered. Among them, lower hybrid drift instabilities (LHDI) are the most promising and most studied class of instabilities. LHDI are driven by cross-field currents and density gradients [Davidson and Gladd, 1975]. Both electrostatic and electromagnetic branches of LHDI have been observed in or around the diffusion region in both laboratory plasmas [Carter *et al.*, 2001; Ji *et al.*, 2004] and in space [Pickett *et al.*, 2001; Bale, Mozer, and Phan, 2002; Zhou *et al.*, 2009]. However, there is no clear evidence so far that shows these fluctuations lead to fast reconnection. Recently, Mozer, Wilber, and Drake, 2011 show that anomalous drag due to fluctuations is unlikely to be a major cause of fast reconnection at the sub-solar magnetopause by analyzing data from 100 sub-solar, low-amplitude crossings of the THEMIS (Time History of Events and Macro-scale Interactions during Substorms) satellites. Furthermore, recent 3-D simulations suggest that the electromagnetic branches of LHDI observed near the X-point in MRX are not primarily responsible for the fast reconnection in MRX [Roytershteyn *et al.*, 2013].

The importance of two-fluid effects in the diffusion region was first recognized by Sonnerup, 1979. As shown in Fig. 1.10, ions become unmagnetized first and form an ion diffusion region of the length scale on the ion skin depth  $\delta_i \equiv c/\omega_{pi} = V_A/\omega_{ci}$ , where  $\omega_{pi}$  is the ion plasma oscillation frequency and  $\omega_{ci}$  is the ion cyclotron frequency. Electrons, on the other hand, are tied to the magnetic field until they reach an electron diffusion region of the much smaller length scale on the electron skin depth  $\delta_e \equiv c/\omega_{pe}$ . Since electrons are still magnetized in the ion diffusion region, they flow in along the reconnecting field lines in the inflow region and out along the reconnected lines in the outflow regions. This difference in behavior between electrons and ions leads to a strong Hall effect from the

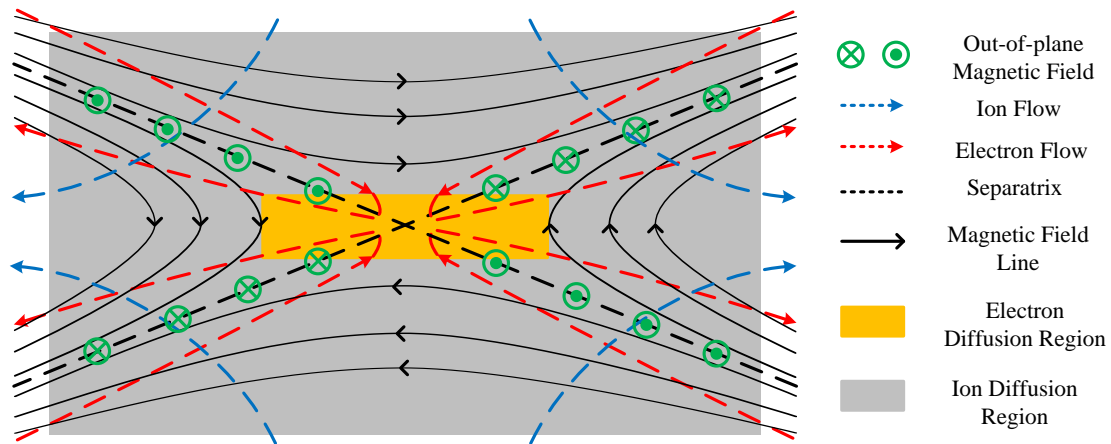


Figure 1.10: Schematic picture of two-fluid effects in magnetic reconnection. Ions decouple from electrons in the ion diffusion region whose width is on the order of the ion skin depth  $\delta_i$ . Electrons are frozen in the magnetic lines until they reach to the electron diffusion region of the width on the order of the electron skin depth  $\delta_e$ . The electron flow pattern creates the quadrupole out-of-plane magnetic field, a signature of the Hall effect.

$\mathbf{J} \times \mathbf{B}$  force inside the ion diffusion region. The electron flow pattern generates in-plane currents that produce a quadrupole out-of-plane magnetic field, which was first predicted by Sonnerup, 1979 and has been considered a signature of the Hall effect ever since. The basic reason for fast reconnection in this regime is that the Hall effect allows for a broader ion outflow channel than the Sweet-Parker model. The wide outflow channel is similar to that of the Petschek model but it originates from different physical mechanism: two-fluid effects versus MHD shocks.

Fast reconnection due to two-fluid effects has been verified by the combined efforts of numerical simulations, space observations, and laboratory experiments [Yamada, Kulsrud, and Ji, 2010]. After many pioneering works [e.g. Drake and Burkhart, 1992; Mandt, Denton, and Drake, 1994; Biskamp, Schwarz, and Drake, 1995; Shay *et al.*, 1998; Hesse *et al.*, 1999], the computational study of two-fluid effects on fast reconnection culminated with the Geospace Environmental Modeling (GEM) magnetic reconnection challenge, which concluded in 2001. The challenge program proved that a quasi-Alfvénic reconnection rate

( $V_{in} \sim 0.1V_A$ ,  $V_{in}$  is the inflow velocity) can be achieved if the Hall effect is included in simulations [Birn *et al.*, 2001]. Another important conclusion is that the reconnection rate is controlled by the ion physics rather than the electron physics that directly governs the mechanisms responsible for breaking the magnetic field lines. This insensitivity of the reconnection rate to electron dynamics is believed to result from the quadratic dispersion character of whistler waves brought by the Hall effect [Mandt, Denton, and Drake, 1994; Shay and Drake, 1998; Drake, Shay, and Swisdak, 2008]. The existence of the Hall effect is supported by various space observations [e.g. Deng and Matsumoto, 2001; Øieroset *et al.*, 2001; Mozer, Bale, and Phan, 2002] and laboratory experiments [Ren *et al.*, 2005; Brown, Cothran, and Fung, 2006].

It is now widely accepted that two-fluid effects facilitate fast reconnection in collisionless plasmas. There are, however, still many open questions related to this problem. The first problem is how fast reconnection is triggered. Many reconnection phenomena in nature are impulsive; the release of magnetic energy happens quickly compared to the slow build-up period. There is no general theory on this sudden release of magnetic energy. The transition from collisional to collisionless reconnection is a candidate for impulsive reconnection [Ma and Bhattacharjee, 1996; Cassak, Shay, and Drake, 2005; Yamada *et al.*, 2006], but not every plasma in nature is initially collisional before the onset of fast reconnection. The impulsive nature could come from the coupling between local and global scales as demonstrated with sawtooth relaxation events [Yamada, 2011].

Another problem is related to secondary island formation in the current sheet. A secondary island is often associated with a region of high plasma density and a high out-of-plane magnetic field; thus it is referred to as a plasmoid. It is now known that a system with a large Lundquist number  $S > 10^4$  has a current sheet unstable to the formation of plasmoids [Bhattacharjee *et al.*, 2009; Daughton *et al.*, 2009b; Samtaney *et al.*, 2009]. The formation and ejection of plasmoids lead to a spike in the reconnection rate. It requires more study to understand how secondary island formation affects the reconnection pro-

cess, especially the energy conversion process.

Finally, more understanding is needed on magnetic reconnection in 3-D geometry. A recent simulation by Daughton *et al.*, 2011 shows a dramatic difference between the dynamic evolution of the diffusion region in 3-D compared to 2-D, even though a simple periodic boundary is imposed along the out-of-plane direction. It is unclear how to expand our knowledge of 2-D reconnection to 3-D reconnection. Moreover, 3-D reconnection may be intrinsically different from 2-D reconnection [Boozer, 2012]. This problem is also important for understanding reconnection phenomena with a complex 3-D geometry such as solar flares.

In summary, although the long-standing question on fast reconnection in collisionless plasma seems to be solved in the context of two-fluid dynamics, there is still significant remaining work for the complete understanding of magnetic reconnection in nature.

## **1.3 Previous Research on Particle Heating and Acceleration During Reconnection**

In this section, previous research on particle energization during reconnection is reviewed. In the first subsection, energetic particle generation is discussed. The next subsection contains a brief review on studies of ion heating and bulk acceleration. Finally, a short review on electron thermal heating during reconnection is presented.

### **1.3.1 Energetic Particle Generation**

The history of observations of energetic particles in solar flares starts with Forbush, 1946. Since then, numerous observations and analyses have supported the assertion that energetic particle generation in solar flares is related to the release of the energy stored in coronal magnetic fields through magnetic reconnection [see e.g. Lin, 2011]. Hard x-ray measurements reveal the generation of energetic electrons up to the MeV range, and  $\gamma$ -ray

measurements indicate the existence of ions up to the GeV range. As briefly introduced in Subsection 1.1.1, a significant fraction (up to 50%) of the released magnetic energy is deposited in energetic particles in some solar flares [Lin and Hudson, 1976; Lin *et al.*, 2003; Emslie *et al.*, 2005; Krucker *et al.*, 2010]. It still remains unsolved how such a large number of particles become non-thermal in solar flares, although there have been many suggested mechanisms [for a more extensive review see Zharkova *et al.*, 2011]. Among them, only models directly related to reconnection will be reviewed in this subsection.

One candidate mechanism for energetic particle generation is direct acceleration by the out-of-plane reconnection electric field. This effect was studied via test particle simulations using a reconnection geometry obtained from MHD simulations [e.g. Sato, Matsumoto, and Nagai, 1982]. Although high-energy particles can be generated by the meandering/Speiser motion in the vicinity of the X-point [Speiser, 1965], this direct acceleration mechanism does not produce a large amount of energetic particles because not many particles travel all of the way in to the X-point. Another acceleration mechanism exists in the downstream region of the X-line geometry where particles obtain energy while drifting along the current sheet due to gradients in the magnetic field [e.g. Scholer and Jamitzky, 1987; Hoshino *et al.*, 2001]. Furthermore, Hoshino, 2005 points out that energetic electrons can also be generated due to a strong in-plane electric field. (This in-plane electric field results from two-fluid effects and is sometimes called the Hall electric field.) The large in-plane electric field around the separatrices (boundaries between the upstream and downstream plasmas) can trap electrons until they gain considerable energy from the reconnection electric field. To emphasize the trapping effect, this mechanism is called “surfing” acceleration. More recently, large-scale electron acceleration by parallel electric fields has been proposed by Egedal, Daughton, and Le, 2012. This mechanism, which is based on trapped-particle dynamics was developed to explain anisotropic ( $T_{\parallel} > T_{\perp}$ ) electron distribution functions measured by the Wind satellite when it encountered an ion diffusion region in the magnetotail [Egedal *et al.*, 2008]. The existence of parallel electric fields near the separatrices has

also been observed in other numerical simulations [Pritchett, 2010].

In addition to the above mechanisms that are active in a single X-line geometry, there are also models based on a multiple X-line geometry with secondary magnetic islands inside the current sheet. Drake *et al.*, 2006 show that electrons gain energy while reflecting back and forth from the ends of contracting magnetic islands. The physical basis for this model is similar to that of the first-order Fermi acceleration mechanism. Another process for energetic particle production is magnetic island coalescence [Pritchett, 2008; Oka *et al.*, 2010]. Here, electrons are energized as small magnetic islands merge into large islands. The energization mechanism is different depending on the existence of a relatively uniform out-of-plane magnetic field or a guide field. With a guide field, the process is dominated by the formation of density cavities along one pair of separatrices, which is a mechanism first suggested by Drake *et al.*, 2003. Without a guide field, the acceleration comes mostly from the particle drift along the inductive electric field [Pritchett, 2008]. The role of direct acceleration by the local inductive field from the coalescence can be also important [Oka *et al.*, 2010].

So far, it is not clear which mechanism is dominant in solar flares. It is possible that energetic particles are generated via a combination of some, if not all, of the mechanisms. The process may have multiple steps since some mechanisms such as the acceleration through contracting islands and the “island surfing” mechanism are more effective when there is a pre-acceleration stage. It is also possible that the large population of energetic electrons observed in solar flares is produced by a large-scale inductive electric field associated with topological changes caused by reconnection.

The correlation between energetic electrons and ions should be also explained. The mechanisms that generated energetic ions have thus far received less attention and the mechanisms described above are less effective when acting on ions. However, there is a positive correlation between  $> 300$  keV electrons and  $> 30$  MeV protons [Shih, Lin, and Smith, 2009], which indicates that there are common acceleration mechanisms. Drake

*et al.*, 2009 suggested that ions are first accelerated in the reconnection exhaust and then undergo a first-order Fermi acceleration process in contracting islands, which requires a multiple X-line geometry.

Due to the limited resolution of remote-sensing diagnostics, it is difficult to measure the reconnection geometry in solar flares. In the magnetosphere, on the other hand, *in situ* measurements make it possible to see whether there is positive correlation between reconnection and energetic particle generation and whether the reconnection site has a single or multiple X-line geometry. In the Earth's magnetotail, energetic electrons (up to  $\sim 300$  keV) in an active reconnection region have been measured [Øieroset *et al.*, 2002]. Observations of energetic electrons in downstream regions were also reported [Imada, Hoshino, and Mukai, 2005; Imada *et al.*, 2007]. More recently, measurements by the Cluster spacecraft showed the presence of energetic electrons within magnetic islands [Chen *et al.*, 2008; Retinò *et al.*, 2008], which supports mechanisms based on a multiple X-line geometry. On the other hand, the direct connection between energetic ions and reconnection has not been fully confirmed, although there have been direct measurements of energetic ions [e.g. Meng *et al.*, 1981; Sarafopoulos *et al.*, 2001].

Energetic particles associated with magnetic reconnection have been also observed in laboratory plasmas. Stenzel *et al.*, 1983 reported runaway-type fast electrons inside a current sheet with a large guide field. Non-thermal electrons have been also observed during sawtooth crashes and disruptions in hot tokamak plasmas [see Savrukhin, 2006, and references therein]. A high-energy tail in the ion energy distribution function has been measured in the Mega-Ampere Spherical Tokamak (MAST) related to internal reconnection events [Helander *et al.*, 2002]. Similar fast ions are also observed in the Madison Symmetric Torus (MST) reversed field pinch during tearing mode magnetic reconnection [Magee *et al.*, 2011]. Brown *et al.*, 2002 reported the detection of energetic ions during magnetic reconnection in the Swarthmore Spheromak Experiment (SSX).

Observations and numerical simulations support the assertion that reconnection plays a

key role in the production of energetic particles, but it is still not well understood how they are produced in the reconnection region. Many mechanisms have been suggested, but more research is required to reach a consensus on this issue.

### 1.3.2 Ion Heating and Bulk Acceleration

In Earth's magnetosphere, Alfvénic ion jets have been attributed to reconnection outflows [e.g. Paschmann *et al.*, 1979; Gosling *et al.*, 1986; Phan *et al.*, 2000; Øieroset *et al.*, 2001]. The in-plane (Hall) electric field has been identified as the cause of the ion bulk acceleration close to the upstream Alfvén velocity  $V_A$  [Shay *et al.*, 1999]. The Hall electric field is electrostatic and mostly perpendicular to the local magnetic field. It is strongest near the separatrices and negligible upstream. The component of the Hall electric field normal to the current sheet is bipolar; it points toward the current sheet. Thus, the in-plane potential profile shows a well structure along the direction normal to the current sheet. The in-plane electric field is considered to be another signature of two-fluid effects along with the quadrupole out-of-plane magnetic field. As shown in Fig. 1.11, the potential well structure has been observed in the magnetosphere [Mozer, Bale, and Phan, 2002; Wygant *et al.*, 2005] and in many numerical simulations [e.g. Shay *et al.*, 1998; Pritchett, 2001; Karimabadi, Daughton, and Scudder, 2007; Drake, Shay, and Swisdak, 2008; Pritchett, 2010].

Direct ion acceleration by the Hall electric field has not yet been observed in laboratory plasmas. The in-plane electric field during reconnection was indirectly measured by Gekelman, Stenzel, and Wild, 1982 at UCLA. They inferred the electric field by measuring  $\mathbf{J} \times \mathbf{B}$  and  $\nabla p$ . The measured in-plane ion flow pattern is qualitatively similar to that observed in numerical simulations [e.g. Shay *et al.*, 1998; Pritchett, 2001]. However, no significant ion acceleration was observed and it was claimed that anomalous scattering by waves was responsible for this result. Ion flow close to  $V_A$  was observed during spheromak merging experiments [Brown *et al.*, 2008; Ono *et al.*, 2011], but they did not clarify the specific ion

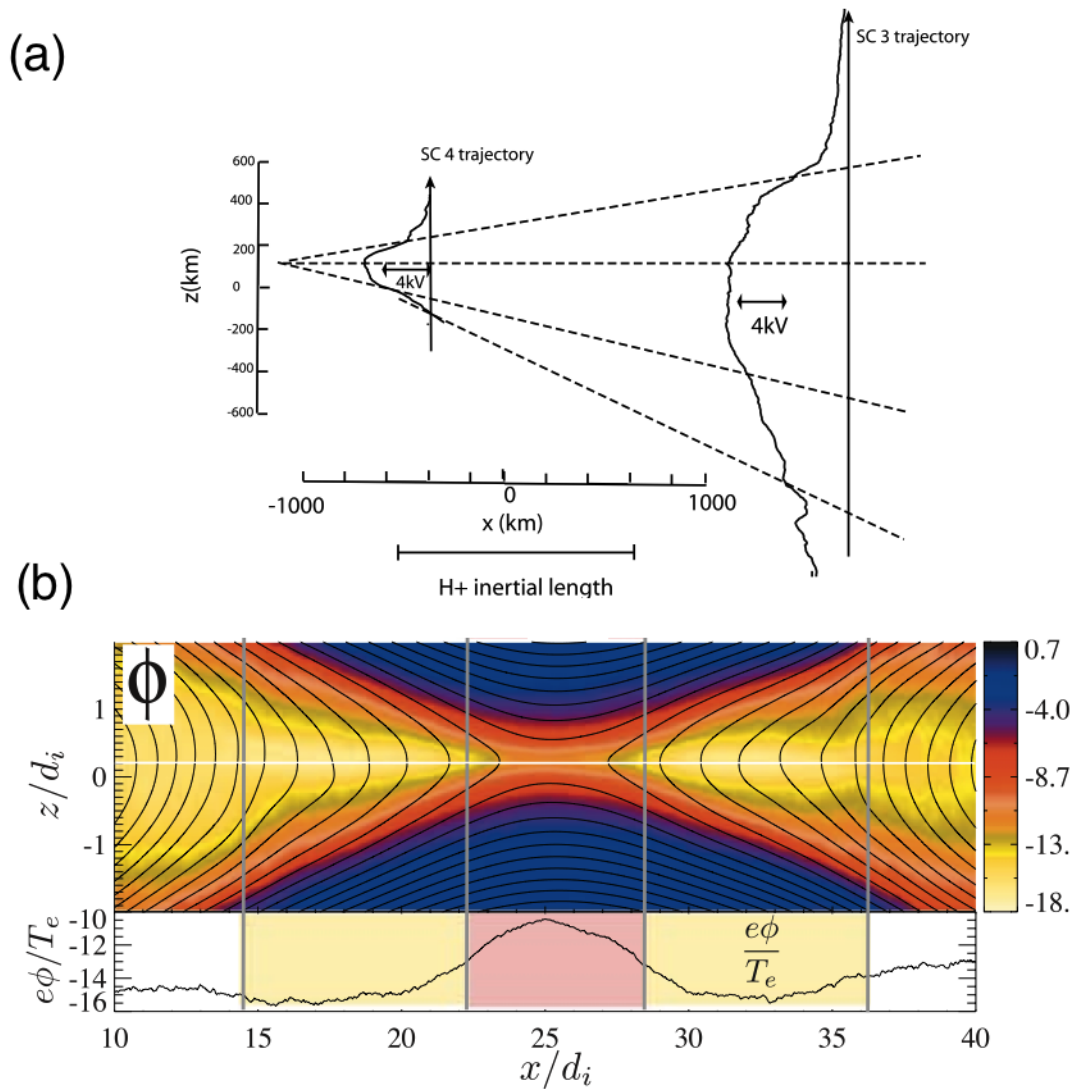


Figure 1.11: In plane potential profile measured in space and numerical simulations. (a) Structure of the potential well along the normal direction ( $z$  in the figure) measured in the magnetotail. The potential well measured by Cluster Spacecraft 3 (SC 3) is deeper and broader than that of Cluster Spacecraft 4 (SC 4), since SC 3 passed further downstream. Figure from Wygant *et al.*, 2005. (b) 2-D in-plane potential profile in a numerical simulation. The potential well becomes deeper and broader downstream, which agrees with the spacecraft measurement. Figure from Karimabadi, Daughton, and Scudder, 2007.

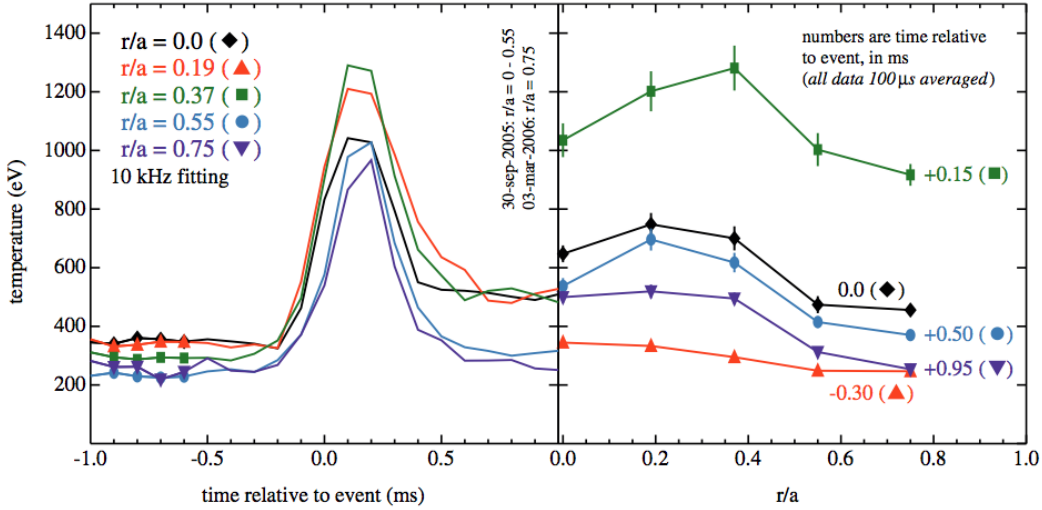


Figure 1.12: Ion heating associated with a reconnection event in MST. Left: Carbon impurity temperature profile relative to the timing of the reconnection event. Impurity ions are significantly heated during a global reconnection event. Right: Radial profiles of the carbon impurity temperature associated with a global reconnection event. Ion heating occurs at each radial location.

Figure from Gangadhara *et al.*, 2007.

acceleration mechanisms. In this dissertation, the first simultaneous measurement of both the Hall electric field and ion acceleration toward the outflow direction are presented.

Ion heating associated with reconnection has been observed in laboratory plasmas [Fujisawa *et al.*, 1991; Scime *et al.*, 1992; Ono *et al.*, 1996; Hsu *et al.*, 2000; Stark *et al.*, 2005; Gangadhara *et al.*, 2007; Fiksel *et al.*, 2009; Magee *et al.*, 2011; Ono *et al.*, 2011] and numerical simulations [e.g. Hoshino *et al.*, 1998; Pei, Horiuchi, and Sato, 2001; Drake *et al.*, 2009]. In the magnetosphere, highly structured ion distribution functions far from Maxwellian have been observed [Hoshino *et al.*, 1998; Wygant *et al.*, 2005]. Specifically, counter-streaming ion beams generated by the Hall electric field are believed to be responsible for the ion pressure increase at the center of the current sheet [Wygant *et al.*, 2005]. However, no clear ion thermal energy increase in the reconnection layer has yet been reported.

Despite many observations of ion heating in laboratory plasmas during reconnection,

the mechanisms behind the observed ion heating remain unresolved. In the TS-3 device at the University of Tokyo, the observed global ion heating was attributed to thermalization of sheared Alfvénic flows generated by the so-called “slingshot” effect [Ono *et al.*, 1996]. More recently, ion heating downstream of the X-point was explained in terms of fast shock or viscous damping of the reconnection outflow [Ono *et al.*, 2011]. However, MHD analysis was not valid in the plasma and no quantitative analysis was made to verify the suggested mechanisms. Moreover, other possibilities such as compressional heating and/or conversion of the translational energy of the merging spheromaks exist since ion heating was observed during the fast merging of two spheromaks with or without a guide field. In the low  $\beta$  plasmas of the Versatile Toroidal Facility (VTF) device at the Massachusetts Institute of Technology, ions are heated from 0.3 to about 2 eV by interactions with the in-plane electric field [Stark *et al.*, 2005]. However, the observed ion heating is small, compared to the electron temperature (20 eV). Moreover, the measured in-plane electric field profiles are different from those seen in numerical simulations, indicating that effects unique in the VTF device such as boundary conditions may play a role. In previous measurements done in MRX, ion heating in the reconnection layer was attributed to uncertain non-classical mechanisms [Hsu *et al.*, 2000]. In the Madison Symmetric Torus (MST), a Reversed Field Pinch (RFP) device, Gangadhara *et al.*, 2007 identified ion heating related to a drop in stored magnetic energy as shown in Fig. 1.12, but specific heating mechanisms were not identified. Fiksel *et al.*, 2009 observed mass-dependent ion heating, and stochastic heating was postulated to account for the heating. Magee *et al.*, 2011 reported anisotropic ion heating and super thermal tail generation during development of non-linear tearing modes, but still the energization processes remained unknown.

A sharp ion temperature increase across the separatrices has been observed in many simulations [e.g. Hoshino *et al.*, 1998; Drake *et al.*, 2009]. It is believed that the direct interactions of ions with the in-plane electric field are responsible for the observed ion temperature increase. First, the strong Hall electric field generates various non-Maxwellian ion

distributions in the reconnection layer, which can significantly increase the local ion pressure. Hoshino *et al.*, 1998 identified four different types of ion distribution functions in kinetic simulations and successfully compared these results to observations from the Geotail satellite. Another possible mechanism for ion heating has been identified by Drake *et al.*, 2009. When cold, unmagnetized ions come across the boundary, they are suddenly accelerated by the strong in-plane electric field. As ions are re-magnetized inside the boundary, they gain not only the Alfvénic flow velocity but also an equal thermal velocity, which is similar to the classical pick-up process [Mobius *et al.*, 1985]. Thus, this mechanism is called the ion pick-up model. Comparison with solar wind data from the ACE and Wind spacecraft shows that the temperature increment is proportional to ion mass, which agrees with the pick-up model. On the other hand, actual temperature increments are consistently lower than predicted by the model.

So far, many observations have suggested that a significant fraction of the energy released during reconnection is converted to ion thermal energy, especially in laboratory plasmas. Many possible mechanisms have been suggested such as the damping of Alfvénic fluctuations, viscous damping of flows, stochastic heating, and the pick-up process. To verify ion thermalization processes during reconnection, more quantitative analysis based on measured data in the reconnection layer is required and this dissertation provides some of the much-needed analysis.

### **1.3.3 Electron Heating**

In the classical Sweet-Parker model, electrons are expected to be heated via Ohmic dissipation. However, electron heating mechanisms during collisionless magnetic reconnection are not straightforward and have not been studied in as much detail. In this dissertation, the bulk flow energy of electrons will not be extensively discussed since it is negligible compared to other forms of energy, although the electrons are accelerated near the electron diffusion region.

Electron heating related to magnetic reconnection was observed in early reconnection experiments with a large guide field at UCLA [Stenzel, Gekelman, and Wild, 1982]. They found that magnetic energy was mostly converted to electron thermal energy and that anomalous resistivity (resistivity larger than the classical Spitzer value) existed in the current sheet. More recently, Ji *et al.*, 2004 reported non-classical electron heating in the collisionless reconnection layer of MRX. Classical Ohmic heating was estimated to account for only about 20% of the heat flux required to sustain the observed electron temperature profile that peaks at the center of the reconnection layer. Strong electromagnetic fluctuations were observed at the same time, such that the observed heating could result from wave-particle interactions; this assertion was not proven quantitatively. Electron heating at the reconnection layer was also reported by Ono *et al.*, 2011. They postulated that electrons were heated Ohmically, but no quantitative analysis was provided. In the Earth's magnetotail, a statistical survey on electron thermal temperature as a function of distance from the X-point was conducted by Imada, Hoshino, and Mukai, 2005. Interestingly, electron heating is more likely to occur in downstream regions somewhat away from the X-point.

So far, few mechanisms have been suggested for non-classical electron heating during collisionless reconnection. Possible candidates include anisotropic heating by mirror trapping and the parallel electric field [Egedal *et al.*, 2008] and anomalous resistivity due to high-frequency fluctuations [Stenzel, Gekelman, and Wild, 1982; Ji *et al.*, 2004].

It is important to identify mechanisms for observed non-classical electron heating in laboratory plasmas since it is related to the physics that actually breaks magnetic field lines at the X-point. The existence of non-classical heating indicates the existence of effective thermalization mechanisms there. However, there have been only a handful of studies of bulk electron heating in reconnection because energetic electron generation has attracted the most attention. In some solar flares, the bulk electron heating may not be important because most of the electrons become non-thermal. In the magnetotail and laboratory experiments, on the other hand, electron thermal energy is more important because the

population of energetic electrons remains small. Thus, more research directed toward understanding electron heating is required and this dissertation addresses key issues related to non-classical electron heating during collisionless reconnection.

## **1.4 Dissertation Objectives**

There is as of yet no consensus on how particles gain energy in the collisionless diffusion layer. To fill this gap, in this dissertation, energy conversion mechanisms for both ions and electrons during collisionless magnetic reconnection are discussed, based on measurements in the Magnetic Reconnection Experiment (MRX). Due to diagnostics limitations, energetic particle generation during collisionless reconnection will not be discussed in this dissertation. The main objectives of this dissertation are:

- (1) To provide a description of the in-plane (Hall) electric field, measured in the ion diffusion layer in MRX, including what determines its shape and magnitude;
- (2) To present where and how ions are accelerated and heated during collisionless reconnection and to assess the role of the Hall electric field in ion acceleration and heating;
- (3) To discuss possible mechanisms for the observed ion heating downstream;
- (4) To identify where electrons are heated and to find mechanisms for the observed non-classical electron heating;
- (5) To estimate how much of the incoming magnetic energy is converted to each form of energy in the reconnection region.

## **1.5 Summary and Outline**

This dissertation provides detailed studies of energy conversion from magnetic energy to particle energy during collisionless magnetic reconnection in MRX. By utilizing extensive 2-D scans of many probes such as Langmuir probes, Mach probes, and ion dynamics

spectroscopy probes, 2-D profiles of the essential plasma parameters are obtained. Plasma parameters such as density and temperature are controlled in a manner that the plasma is in the collisionless regime.

This dissertation is composed of seven main chapters and three appendices:

**Chapter 1.** This chapter introduces magnetic reconnection in astrophysical and laboratory plasmas. The importance of reconnection as an effective mechanism for conversion from magnetic to particle energy is emphasized, which motivates this research. Previous research on various energy conversion mechanisms is extensively reviewed. Finally, the objectives and findings of this dissertation are summarized.

**Chapter 2.** This chapter presents transport equations used for this research. Energy transport equations for resistive MHD are derived and used to briefly review energy conservation in the Sweet-Parker model. Finally, transport equations for two-fluid dynamics are derived.

**Chapter 3.** This chapter describes the experimental apparatus of the Magnetic Reconnection Experiment and the experimental regime for this study. Details about various diagnostics used for this research are provided. Key plasma parameters are presented to show that the plasma is in the collisionless regime.

**Chapter 4.** This chapter discusses ion heating and acceleration mechanisms. It is shown that the in-plane (Hall) electric field plays a major role. The Hall electric field is established by electron dynamics near the electron diffusion region. It accelerates ions near the separatrices up to the half of the Alfvén velocity. Ions are heated downstream by the so-called re-magnetization mechanism with the help of collisions. The measured

neutral temperature profile implies that ions lose energy to neutrals.

**Chapter 5.** This chapter describes non-classical electron heating observed in the reconnection layer. The electron energy obtained from the reconnection electric field is effectively converted to heat near the electron diffusion region. It is shown that classical Ohmic dissipation based on the perpendicular Spitzer resistivity cannot explain the large electron heat flux along the magnetic field, which suggests the existence of an anomalous resistivity.

**Chapter 6.** This chapter presents the energy inventory during collisionless reconnection in MRX. More than half of the incoming magnetic energy is dissipated during reconnection. Due to the large Hall electric field, ions gain more energy than electrons. Both the electron and ion energy gains are dominated by thermal energy.

**Chapter 7.** This chapter draws conclusions and presents ideas for future work.

**Appendix A** This appendix describe results from plasma “jogging” experiments. The current sheet is swept over stationary probes to produce data sets similar to those from spacecraft passing through reconnection layers in space. Data from the jogging experiments are utilized to assess the effectiveness of common spacecraft analysis techniques.

**Appendix B** This appendix discusses the density asymmetry found in MRX discharges. The selective shielding of the inductive electric field from the timing-varying currents of internal coils is identified as the main mechanism for the density asymmetry. Details on the MRX discharge evolution are provided.

**Appendix C** This appendix presents a glossary of symbols used in this dissertation for physical quantities related to energy transport.



## Chapter 2

# Energy Transport Equations

Magnetic energy released during reconnection is converted into different forms of particle energy, such as flow and thermal energy. This energy conversion process is generally complex since the continuous transport of various type of energy occurs. For example, flow energy can be converted into thermal energy via viscous damping, plasmas can be heated by compression, and heat can be generated by collisions between different species. There is also heat exchange between electrons and ions.

These energy transport and conversion processes are governed by the transport equations derived from either the Vlasov or Boltzmann equation with the help of Maxwell's equations. The transport equations are useful to identify mechanisms for particle heating and acceleration during reconnection by determining where particles gain energy and where they are thermalized. In addition, the energy inventory during reconnection can be also determined by examining the transport equations for a volume of interest in a plasma.

In the first part of this chapter, the energy transport equations of resistive MHD are derived. In the following section, energy conversion in the Sweet-Parker model is described as a reference for future discussion. Finally, the transport equations for two-fluid dynamics, which are used throughout this dissertation, are presented.

## 2.1 Resistive MHD Energy Transport Equations

The derivation of the (resistive) MHD equations can be readily found in the literature [e.g. Freidberg, 1987]. The model equations are

$$\frac{\partial \rho}{\partial t} + \nabla \cdot (\rho \mathbf{V}) = 0, \quad (2.1)$$

$$\rho \frac{\partial \mathbf{V}}{\partial t} + \rho \mathbf{V} \cdot \nabla \mathbf{V} = -\nabla p + \mathbf{J} \times \mathbf{B}, \quad (2.2)$$

$$\mathbf{E} + \mathbf{V} \times \mathbf{B} = \eta \mathbf{J}, \quad (2.3)$$

$$\left( \frac{\partial}{\partial t} + \mathbf{V} \cdot \nabla \right) \left( \frac{p}{\rho^\gamma} \right) = \frac{\gamma - 1}{\rho^\gamma} \eta J^2, \quad (2.4)$$

$$\nabla \times \mathbf{E} = -\frac{\partial \mathbf{B}}{\partial t}, \quad (2.5)$$

$$\nabla \cdot \mathbf{B} = 0, \quad (2.6)$$

$$\nabla \times \mathbf{B} = \mu_0 \mathbf{J}, \quad (2.7)$$

where  $\rho$  is the single-fluid mass density  $\rho \equiv \sum_s m_s n_s$  ( $m_s$  is the mass of species  $s$ ,  $n_s$  is the number density),  $\mathbf{V}$  is the single-fluid velocity  $\mathbf{V} \equiv \sum_s m_s n_s \mathbf{V}_s / \rho$ ,  $p$  is the single-fluid pressure  $p \equiv \sum_s n_s T_s$  ( $T_s$  is the temperature of species  $s$  in units of energy), and  $\gamma$  is the polytropic index that is usually taken to be  $5/3$ , corresponding to local thermodynamic equilibrium of a gas of particles with three degrees of freedom. The right-hand side in the equation of state (Eqn. 2.4) is required to include the effect of Ohmic dissipation, which increases the internal energy of the fluid. It is sometimes useful to rewrite Eqn. 2.4 with the internal energy  $u = p/(\gamma - 1)$  as the following thermal energy transport equation:

$$\frac{\partial u}{\partial t} + \nabla \cdot (u \mathbf{V}) = -p \nabla \cdot \mathbf{V} + \eta J^2, \quad (2.8)$$

which indicates the change of internal energy by compression and Ohmic dissipation. Poisson's equation is not used in MHD due to the assumption of quasi-neutrality.

Energy transport and the conversion of electromagnetic field energy is governed by

Poynting's theorem, which is the work-energy theorem of electrodynamics. It can be easily derived from Faraday's law (Eqn. 2.5) and Ampère's law (Eqn. 2.7) as

$$\frac{\partial}{\partial t} \left( \frac{B^2}{2\mu_0} \right) + \nabla \cdot \left( \frac{\mathbf{E} \times \mathbf{B}}{\mu_0} \right) = -\mathbf{J} \cdot \mathbf{E}. \quad (2.9)$$

The absence of the electric field energy  $\epsilon_0 E^2/2$  is due to neglect of the displacement current term in Ampère's law, which is a valid approximation for the evolution of macroscopic fields varying much slower than the speed of light. In plasma, which is highly conducting gas, energy stored in the magnetic field is generally dominant over that stored in the electric field due to quasi-neutrality, with the exception of energy contained in high-frequency fluctuations. For example, the typical magnetic field in an MRX discharge is on the order of 100 G and the strongest electric field is about 1000 V/m. Even with the maximum electric field, the associated magnetic field energy is seven orders of magnitude larger than the electric field energy. The second term on the left-hand side of Eqn. 2.9 is the divergence of the Poynting vector  $\mathbf{P} \equiv \mathbf{E} \times \mathbf{B}/\mu_0$ <sup>1</sup>. The term on the right-hand side stands for the total work done by the field per unit time and unit volume. Integrating Eqn. 2.9 over a volume  $\mathcal{V}$  with the use of the divergence theorem yields

$$\frac{d}{dt} \int_{\mathcal{V}} \frac{B^2}{2\mu_0} d^3x = - \oint_S \mathbf{P} \cdot d\mathbf{a} - \int_{\mathcal{V}} \mathbf{J} \cdot \mathbf{E} d^3x. \quad (2.10)$$

The implication of this equation is simple: the magnetic energy change in a volume  $\mathcal{V}$  is equal to the field energy flowing in and out through the surface  $S$ , less the energy converted into particle energy. Thus, in steady state, the total magnetic energy converted in  $\mathcal{V}$  can be determined by examining the Poynting flux through  $S$ .

Since Maxwell's equations are already incorporated into the Poynting theorem, the next step is to combine the other fluid equations with Eqn. 2.9. First, taking the scalar product

---

<sup>1</sup>To avoid confusion with the Lunquist number  $S$ ,  $\mathbf{P}$  is used to denote the Poynting vector instead of the traditional  $\mathbf{S}$ .

of  $\mathbf{V}$  with the momentum equation (Eqn. 2.2) and using the continuity equation (Eqn. 2.1) yield the following flow energy transport equation:

$$\frac{\partial}{\partial t} \left( \frac{\rho}{2} V^2 \right) + \nabla \cdot \left( \frac{\rho}{2} V^2 \mathbf{V} \right) = \mathbf{V} \cdot (\mathbf{J} \times \mathbf{B} - \nabla p). \quad (2.11)$$

Then, combining Eqns. 2.8, 2.9, and 2.11 with the help of the resistive Ohm's Law (Eqn. 2.3) yields the following energy conservation equation, which is valid for both ideal and resistive MHD:

$$\frac{\partial}{\partial t} \left( \frac{B^2}{2\mu_0} + u + \frac{\rho}{2} V^2 \right) + \nabla \cdot \left[ \mathbf{P} + (u + p)\mathbf{V} + \frac{\rho}{2} V^2 \mathbf{V} \right] = 0. \quad (2.12)$$

Other energy fluxes on the right-hand side are defined as the enthalpy flux  $\mathbf{H} \equiv (u + p)\mathbf{V}$  and the bulk flow energy flux  $\mathbf{K} \equiv (\rho V^2/2)\mathbf{V}$ , respectively. This concludes the derivation of energy transport equations of resistive MHD.

## 2.2 Energy Conversion in the Sweet-Parker Model

The basic assumptions of the Sweet-Parker model include steady-state, 2-D geometry, and incompressibility. Under these assumptions, the inflow ( $V_{in}$ ) and outflow ( $V_{out}$ ) velocities are  $V_A/\sqrt{S}$  and  $V_A$ , respectively [see, e.g. Priest and Forbes, 2000, Chapter 4]. Here,  $V_A \equiv \sqrt{B_{rec}^2/\mu_0\rho}$  is the upstream Alfvén velocity, where  $B_{rec}$  is the reconnection magnetic field strength. The plasma density  $\rho$  is constant over the reconnection plane due to the incompressibility assumption of the model. The incoming Poynting ( $P_{in}$ ), flow energy

( $K_{in}$ ), enthalpy ( $H_{in}$ ) fluxes are

$$P_{in} = E_{rec}B_{rec}/\mu_0 = (B_{rec}^2/\mu_0)V_{in}, \quad (2.13)$$

$$K_{in} = \rho V_{in}^3/2 = (1/2S)P_{in}, \quad (2.14)$$

$$H_{in} = (5/2)p_{in}V_{in} = (5/4)\beta P_{in}, \quad (2.15)$$

where  $E_{rec}$  is the reconnection (out-of-plane) electric field,  $p_{in}$  is the upstream pressure, and  $\beta \equiv p_{in}/(B_{rec}^2/2)$  is the upstream plasma beta. By invoking the conservation of magnetic flux, we find that

$$V_{in}B_{rec} = V_A B_{out}, \quad (2.16)$$

where  $B_{out}$  is the outflow magnetic field strength, whose direction is normal to the current sheet. Thus, the outgoing Poynting ( $P_{out}$ ) and flow energy ( $K_{out}$ ) fluxes are

$$P_{out} = E_{rec}B_{out}/\mu_0 = P_{in}/\sqrt{S}, \quad (2.17)$$

$$K_{out} = \rho V_A^3/2 = (\sqrt{S}/2)P_{in}. \quad (2.18)$$

In the Sweet-Parker model, uncertainty in the pressure profile exists such that the outflow velocity depends on the pressure profile [Ji *et al.*, 1999; Priest and Forbes, 2000]. More accurate treatment would require a solution of the full equations throughout the diffusion layer, which is beyond the scope of the discussion in this section. Thus, for simplicity, the outgoing enthalpy flux ( $H_{out}$ ) will be obtained using Eqn. 2.12. With the steady-state assumption and the divergence theorem, the relation between the incoming and outgoing fluxes is

$$(P_{in} + H_{in} + K_{in})L = (P_{out} + H_{out} + K_{out})\delta, \quad (2.19)$$

where  $L$  and  $\delta$  are the length and width of the layer, respectively (see Fig. 1.8). By conservation of mass, the relation between  $L$  and  $\delta$  is  $LV_{in} = \delta V_{out}$ , which yields

$$\delta = L/\sqrt{S}. \quad (2.20)$$

Using Eqns. 2.13 – 2.20,  $H_{out}$  becomes

$$H_{out} = \left( \frac{1}{2} + \frac{5}{4}\beta \right) \sqrt{S}P_{in} - \frac{P_{in}}{2\sqrt{S}}. \quad (2.21)$$

The above equations indicate that most of the incoming electromagnetic energy is dissipated in the rectangular-shaped diffusion region and that the energy is equally split into plasma flow and thermal energy. The change in the magnetic energy ( $\Delta W_M$ ) inside of the diffusion region per unit time and unit length along the out-of-plane direction is given by

$$\Delta W_M = -4(LP_{in} - \delta P_{out}) = -4LP_{in} \left( 1 - \frac{1}{S} \right). \quad (2.22)$$

The outgoing magnetic energy is smaller than the incoming energy by a factor of  $1/S$ . Since  $S \gg 1$  for most astrophysical and large laboratory plasmas, the outgoing magnetic energy is negligible. Similarly, the changes in the flow ( $\Delta W_K$ ) and enthalpy ( $\Delta W_H$ ) energy are

$$\Delta W_K = 4(LK_{out} - \delta K_{out}) = 2LP_{in} \left( 1 - \frac{1}{S} \right) = -\frac{\Delta W_M}{2}, \quad (2.23)$$

$$\Delta W_H = 4(LH_{out} - \delta H_{out}) = 2LP_{in} \left( 1 - \frac{1}{S} \right) = -\frac{\Delta W_M}{2}. \quad (2.24)$$

Thus, there is an equipartition between flow and thermal energy in the Sweet-Parker model.

This equipartition implies that magnetic reconnection creates hot, Alfvénic streams of

plasma. The expected temperature increase can be easily computed to yield

$$\frac{T_{out} - T_{in}}{T_{in}} = \frac{2}{5\beta} \left(1 - \frac{1}{S}\right) \simeq \frac{2}{5\beta}, \quad (2.25)$$

where  $T_{in}$  and  $T_{out}$  are the upstream and downstream temperature, respectively. Thus, the normalized temperature increase is inversely proportional to  $\beta$ , which is not surprising since lower  $\beta$  means more magnetic energy per particle.

In summary, in the Sweet-Parker model of reconnection, most of the incoming magnetic energy is expected to be dissipated in the diffusion region and there is an equipartition between flow and thermal energy.

### 2.3 Two-fluid Energy Transport Equations

The basic two-fluid equations can be derived by taking moments of the kinetic (Vlasov or Boltzmann) equations for each of the plasma species. Details of this procedure can be found in Braginskii, 1965. The two-fluid equations are:

$$\frac{\partial n_s}{\partial t} + \nabla \cdot (n_s \mathbf{V}_s) = 0, \quad (2.26)$$

$$m_s n_s \left( \frac{\partial \mathbf{V}_s}{\partial t} + \mathbf{V}_s \cdot \nabla \mathbf{V}_s \right) = -\nabla p_s - \nabla \cdot \mathbb{\pi}_s + q_s n_s (\mathbf{E} + \mathbf{V} \times \mathbf{B}) + \mathbf{R}_s, \quad (2.27)$$

$$\frac{3}{2} \left( \frac{\partial p_s}{\partial t} + \mathbf{V}_s \cdot \nabla p_s \right) + \frac{5}{2} p_s \nabla \cdot \mathbf{V}_s = -\nabla \cdot \mathbf{q}_s - \mathbb{\pi}_s : \nabla \mathbf{V}_s + Q_s, \quad (2.28)$$

where the subscript  $s$  stands for the species. Here, plasmas with only one ion species are considered, so that  $s$  is either  $e$  or  $i$ . The scalar pressure  $p = nT$  is the average of the diagonal terms of a pressure tensor  $\mathbb{p}$ , i.e.  $p = \sum_{i=1}^3 \mathbb{p}_{ii}/3$ . The stress tensor  $\mathbb{\pi} = \mathbb{p} - p \mathbb{1}$  is the anisotropic part of the pressure tensor, where  $\mathbb{1}$  is the unit tensor. The frictional drag term  $\mathbf{R}$  originates from collisions with other species. Finally,  $\mathbf{q}$  is the microscopic heat flux due to the random motion of particles, and  $Q$  is the heat generated by collisions with

other species. The above equations can be used to describe the transport of  $n$ ,  $\mathbf{V}$ , and  $p$ , if the microscopic transport quantities  $\mathbf{R}$ ,  $\mathbb{T}$ ,  $\mathbf{q}$ , and  $Q$  are specified. Generally, those microscopic quantities are difficult to compute. The results calculated by Braginskii, 1965 are valid if there are enough collisions to make the distribution function of each species close to Maxwellian.

The Poynting theorem (Eqn. 2.9) is still valid in the two-fluid regime since it comes from Maxwell's equations. Other transport equations for a two-fluid plasma can be derived from the above equations using similar techniques to those used for the MHD analysis in Section 2.1. By taking a scalar product of  $\mathbf{V}_s$  with the momentum equation (Eqn. 2.27), the two-fluid flow energy transport equation becomes

$$\frac{\partial}{\partial t} \left( \frac{\rho_s}{2} V_s^2 \right) + \nabla \cdot \left( \frac{\rho_s}{2} V_s^2 \mathbf{V}_s \right) + \mathbf{V}_s \cdot \nabla p_s + \mathbf{V}_s \cdot (\nabla \cdot \mathbb{T}_s) = \mathbf{J}_s \cdot \mathbf{E} + \mathbf{V}_s \cdot \mathbf{R}_s. \quad (2.29)$$

The third and fourth terms on the left-hand side indicate flow energy change due to the divergence of the pressure tensor. The first term on the right hand side is kinetic energy gain from an electric field. The last term is energy loss due to collisions with other species. Rewriting Eqn. 2.28 with the internal energy  $u$  yields the following transport equation:

$$\frac{\partial u_s}{\partial t} + \nabla \cdot (u_s \mathbf{V}_s) + p_s \nabla \cdot \mathbf{V}_s + \mathbb{T}_s : \nabla \mathbf{V}_s + \nabla \cdot \mathbf{q}_s = Q_s. \quad (2.30)$$

The third term on the left hand side stands for heating by compression, and the fourth term is heating by viscous damping of the flow. Combining Eqns. 2.9, 2.29, and 2.30 yields

$$\frac{\partial}{\partial t} \left[ \frac{B^2}{2\mu_0} + \sum_{s=e,i} \left( u_s + \frac{\rho_s}{2} V_s^2 \right) \right] + \nabla \cdot \left[ \mathbf{P} + \sum_{s=e,i} (\mathbf{H}_s + \mathbf{K}_s + \mathbf{q}_s + \mathbb{T}_s \cdot \mathbf{V}_s) \right] = 0, \quad (2.31)$$

where  $\mathbf{H}_s = (u_s + p_s) \mathbf{V}_s$  and  $\mathbf{K}_s = (\rho_s V_s^2 / 2) \mathbf{V}_s$ . Here, relations between  $\mathbf{R}$  and  $Q$ , i.e.  $\mathbf{R}_e = -\mathbf{R}_i$ , and  $Q_e + Q_i = -\mathbf{R}_e \cdot (\mathbf{V}_e - \mathbf{V}_i)$ , are used, which result from the momentum and energy conservation. It is worth noting that the microscopic energy fluxes  $\mathbf{q}$  and  $\mathbb{T} \cdot \mathbf{V}$

are included, which are neglected in the MHD transport equations.

These energy transport equations are applied to the analysis of data obtained in the reconnection layer in MRX. For analysis of microscopic quantities, results in Braginskii, 1965 will be used as reference.



# Chapter 3

## Experimental Setup and Plasma Conditions

The experiments reported in this dissertation were conducted on the Magnetic Reconnection Experiment (MRX) at the Princeton Plasma Physics Laboratory (PPPL) [Yamada *et al.*, 1997]. MRX is a mid-size laboratory device specifically designed for detailed studies of magnetic reconnection. MRX has the unique ability to create discharges with a negligible guide field.<sup>1</sup> In MRX plasmas, the MHD criteria ( $S \gg 1$ ,  $L \gg \rho_i$ ) are satisfied in the bulk of plasma, while two-fluid effects exist near the reconnection site. MRX also has versatility in controlling external experimental conditions such as the system size  $L$  and the magnitude of the guide field.

In this chapter, the MRX experimental apparatus is briefly described. Then, diagnostics used for this dissertation are discussed. Finally, key plasma parameters and details of the experimental regime are presented.

---

<sup>1</sup>A guide field means a relatively uniform out-of-plane magnetic field component.

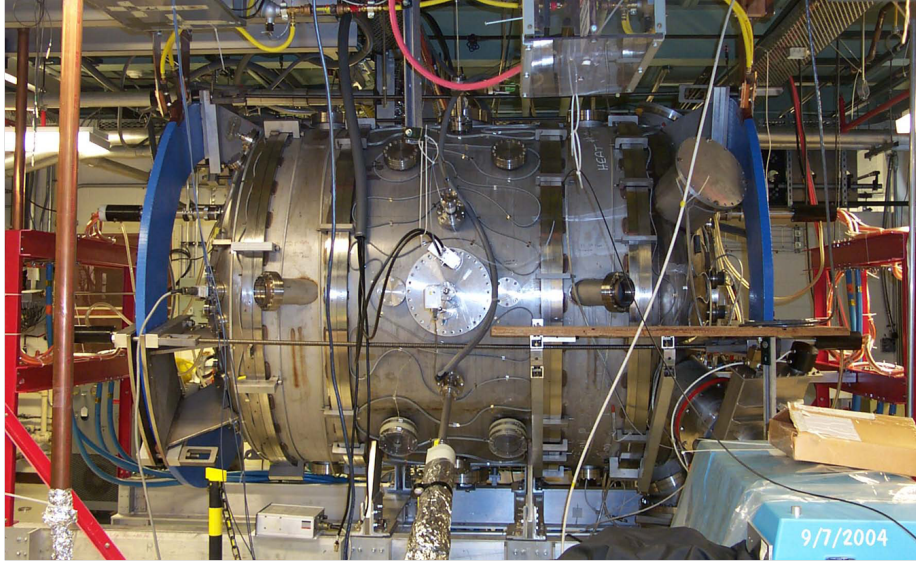


Figure 3.1: Photo of the Magnetic Reconnection Experiment. MRX has a cylindrical vacuum vessel. Various diagnostics are inserted into the machine through the large mid-plane port to measure important physical quantities.

### 3.1 Magnetic Reconnection Experiment

Figure 3.1 shows a photo of the Magnetic Reconnection Experiment. The vacuum vessel is cylindrical and its inner radius is 76.2 cm. The wall is made of made of quarter-inch-thick 304 stainless steel. The axial length of the vacuum chamber is about 1.7 m. Two large blue circular coils on the far left and far right of the vessel are equilibrium field (EF) coils that supply relatively uniform axial magnetic field. The EF coils are used to control the radial position of the current sheet by balancing the radial hoop force.

Figure 3.2-(a) shows a cutaway view of the MRX vacuum chamber. The local coordinate system used throughout this dissertation is also shown:  $R$  is radially outward,  $Y$  is the out-of-plane (symmetric) direction, and  $Z$  is the axial direction. The distance between the two flux cores can be varied externally. For data shown in this dissertation with the exception of Appendix A, the flux cores are separated by 42 cm. Various probes such as a 2-D magnetic probe array are inserted radially to measure important local physics quantities.

The gray circles in Fig. 3.2 indicate the cross sections of the donut-shaped “flux cores”

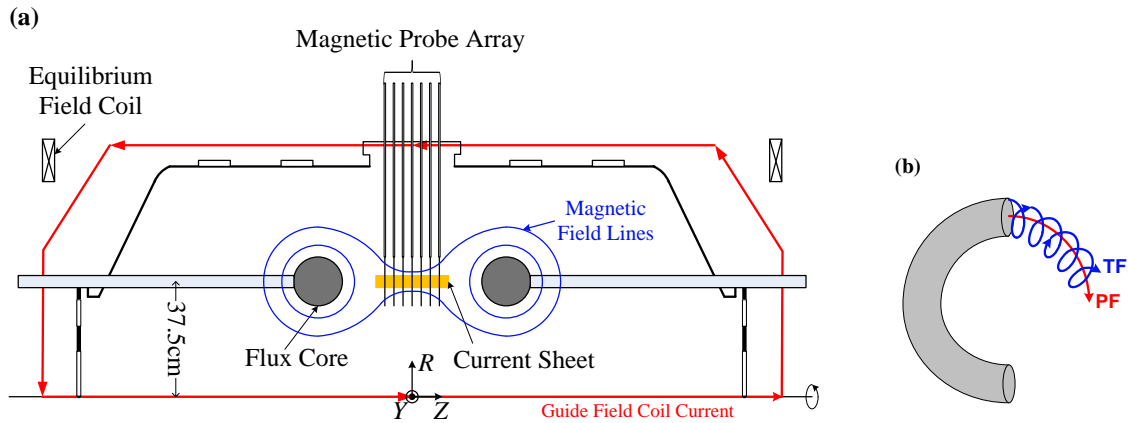


Figure 3.2: (a) Toroidal cross section of the MRX vacuum chamber. The gray circles indicate the location of the two flux cores. The orange color denotes the shape of the current sheet formed during pull reconnection. The blue lines are samples of magnetic field lines. The red lines indicate the path of the guide field coil current. (b) Coil windings of the flux core. The PF coils are wound toroidally, while TF coils are wound poloidally.

inside of which there are two sets of coils: poloidal field (PF) coils and toroidal field (TF) coils, as shown in Fig. 3.2-(b) [Yamada *et al.*, 1981]. The PF coils are wound toroidally to generate the X-line geometry at the middle of the MRX device and to drive magnetic reconnection. The TF coils are wound poloidally to inductively create the plasma around the flux cores. Typical current waveforms for the present experiment are shown in Fig. 3.3. First, the PF coils are energized by firing four  $60 \mu\text{F}$  capacitors charged to 12 kV. Around the time the PF current reaches its maximum, the TF coils are energized by firing additional three  $60 \mu\text{F}$  capacitors charged to 14 kV. The time-varying TF current generates a strong poloidal inductive electric field around flux cores, thereby breaking down the gas which is puffed into the vessel before firing of the PF capacitors.

Right after the plasma is created, there is significant global pressure imbalance since both the magnetic and plasma pressures are high near the flux cores. This pressure imbalance drives plasma inflow from the flux cores to the center, “pushing” the magnetic flux toward the center, although the PF current decreases. This relatively violent stage is called

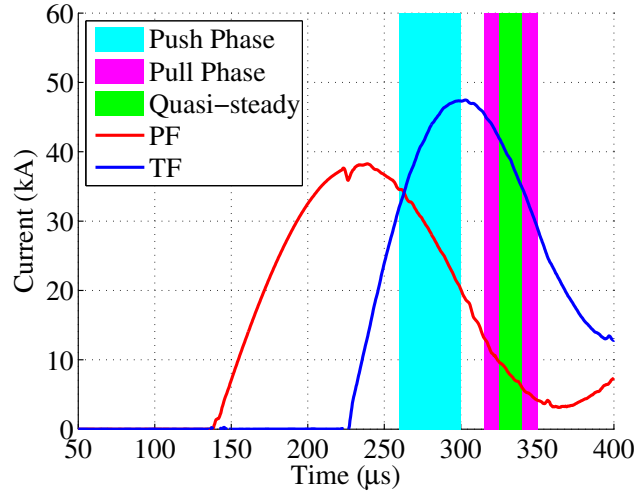


Figure 3.3: Current waveforms in the TF and PF coils. The PF coils are first fired to create the X-line geometry and the TF coils are fired to create plasma. The cyan box indicates the push reconnection phase, while the magenta box denotes the pull reconnection phase. The quasi-steady period is a short (15–20  $\mu\text{s}$ ) period in the middle of pull reconnection.

the push reconnection phase in MRX. The approximate time interval of the push phase is denoted in cyan in Fig. 3.3. It begins right after the plasma formation period and continues for about 30  $\mu\text{s}$ .

After the global pressure imbalance is relieved, effects from the decreasing the PF coil current become dominant. Then, the magnetic flux is pulled towards the flux cores and a current sheet forms that is elongated along the  $Z$  direction (indicated in orange in Fig. 3.2-(a)). In this phase, the initial out-of-plane magnetic field that is produced during the plasma formation phase becomes negligible compared to the reconnecting magnetic field such that anti-parallel reconnection is achieved. This stage of the MRX discharge is called the pull reconnection phase, which is denoted in magenta in Fig. 3.3. In the middle of pull reconnection, the reconnection rate stays relatively constant, even though plasma quantities vary slightly. This period of time is called the quasi-steady period, which lasts for only about 15–20  $\mu\text{s}$ . Data obtained during the quasi-steady, pull reconnection period is presented in this dissertation, with the exception of Appendix B where the broader discharge evolution is briefly discussed.

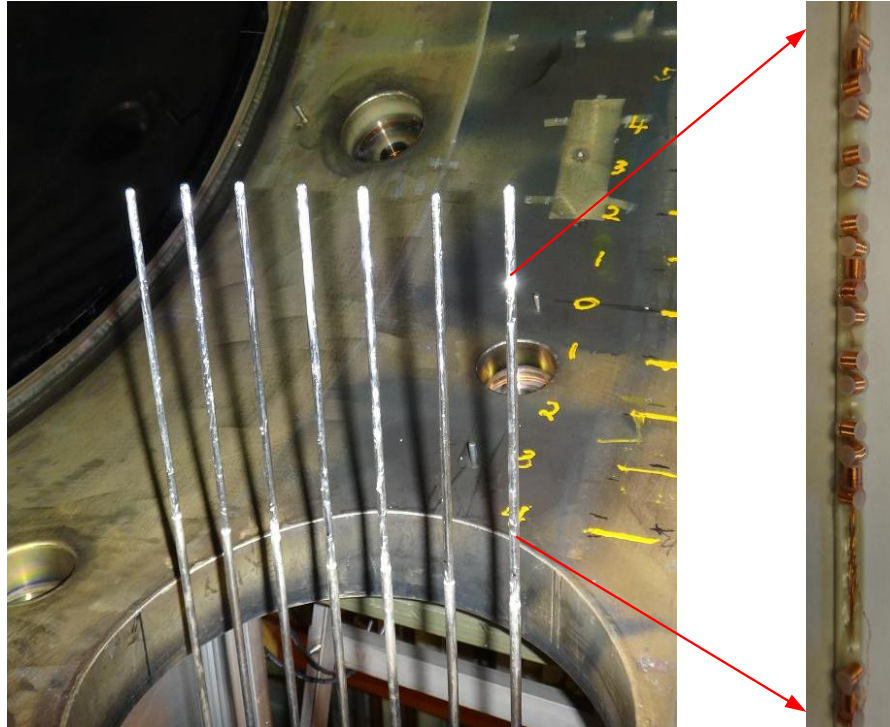
Only a small amount of a positive guide field ( $< 10$  G) is applied to control the  $Z$  position of the X-point by canceling the inherent negative guide field found in MRX discharges. During the plasma formation period, an out-of-plane magnetic field is generated around the flux cores due to the in-plane plasma current that is driven by the poloidal inductive field from the TF coil currents. Since the TF current polarities are set to be opposite to each other, the out-of-plane field on each side is also oppositely directed. Ideally, the strength of this out-of-plane magnetic field is the same, but in reality there is a slight imbalance between the two flux cores. This imbalance shifts the X-point from the strong-field (negative) to the weak-field (positive) side. Applying a small amount of a positive external guide field compensates for the flux core imbalance and shifts the X-point position back to  $Z = 0$ .

The time response of the MRX data acquisition system must be fast enough to record the dynamics during the short quasi-steady period. As such, data from magnetic and electrostatic probes are recorded by GE ICS-645 PCI digitizers at a rate of 2.5 MHz for 1.2 ms. Additional signals that require better time resolution are acquired using high bandwidth oscilloscopes.

## 3.2 Diagnostics

To study energy conversion processes during reconnection in MRX, extensive sets of diagnostics are necessary. Due to the relatively low electron temperature ( $\leq 12$  eV) and short discharge duration ( $< 1$  ms), *in-situ* measurements of plasma quantities are possible in MRX. In this section, the diagnostics used in this dissertation will be briefly described. The key diagnostics include magnetic probes, Langmuir probes, Mach probes, and Ion Dynamics Spectroscopy Probes (IDSPs).

(a)



(b)

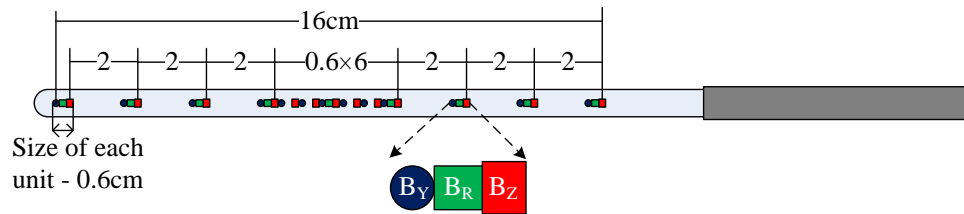


Figure 3.4: 2-D magnetic probe array. (a) Photo of 2-D magnetic probes inside of the MRX chamber. There are a series of miniature pickup coils inside each probe. (b) Alignment of the pickup coils. Each probe has 35 total pickup coils: 9 for  $B_R$  and 13 for both  $B_Y$  and  $B_Z$ .

### 3.2.1 Magnetic Probes

A new set of magnetic probes was constructed for the study of energy conversion processes in MRX. The resolution of the previous work horse 2-D magnetic probe, the 90-channel probe, is too coarse (4 cm) to resolve the electron layer. The new magnetic probes were designed to have a maximum radial resolution of 6 mm while covering the same 16 cm radial extent as the 90-channel probe. Figure 3.4-(a) shows the 2-D array of new magnetic probes. It consists of 7 probes with the separation of 3 cm along  $Z$ . Many miniature magnetic pickup coils, purchased from Syrma Technology, are aligned inside of the magnetic probe. The diameter and height of the coils are 1.75 mm. Figure 3.4-(b) shows the alignment of the pickup coils. The total number of coils per probe is 35, with 13 for  $B_Y$  and  $B_Z$  and 9 for  $B_R$ .

With a 2-D array of the new magnetic probes, the evolution of all three component of the magnetic field can be measured. The magnetic pickup probe is based on Faraday's law. The change in the magnetic flux through the pickup coil induces a voltage across the leads of the coil ( $V_{coil}$ ). The magnitude of the magnetic field component along the axis of the pickup coil can be determined as

$$B = \frac{1}{NA} \int V_{coil} dt, \quad (3.1)$$

where  $NA$  is the effective area of the coil, which is calibrated using a 7 turn Helmholtz coil with approximately 2 cm diameter and coil separation. A typical value of the effective area is  $2.4 \text{ cm}^2$ . Passive electronic integrators are used to integrate  $V_{coil}$  before the signals are digitized in order to reduce the noise and impact from the digitizer offset voltage and bandwidth limitations.

The time response of a magnetic probe is limited by the inductance  $L$  of the coil and the resistance  $R$  seen by the probe. The inductance of the miniature coil is about  $20 \mu\text{H}$  and  $R$  is determined by the input impedance of the integrator, which is  $50 \Omega$ . Thus, the shortest

time scale  $\tau$  which can be resolved by the coil is

$$\tau = \frac{L}{R} \approx 0.4 \mu\text{s}. \quad (3.2)$$

This time response is comparable to the digitization rate and fast enough to resolve changes on the Alfvén transit timescale ( $\sim 3 \mu\text{s}$ ).

2-D magnetic field profiles can be used to compute the current density with the use of Ampère’s law (Eqn. 2.7). Toroidal symmetry needs to be assumed in order to obtain the in-plane current density from the 2-D magnetic field profiles. Although toroidal asymmetry can be locally significant in a certain period time of a discharge, data from the quasi-steady period should not be strongly asymmetric due to the inherent global symmetry of MRX. Moreover, variation of the magnetic field lines along the out-of-plane direction is much smaller than that within the reconnection plane especially during the quasi-steady period. Thus, 2-D magnetic field measurement is sufficient to reconstruct important features of the in-plane current density. Assuming toroidal symmetry, each component of the current density is given by

$$J_R = -\frac{1}{\mu_0} \frac{\partial B_Y}{\partial Z}, \quad (3.3)$$

$$J_Y = \frac{1}{\mu_0} \left( \frac{\partial B_R}{\partial Z} - \frac{\partial B_Z}{\partial R} \right), \quad (3.4)$$

$$J_Z = \frac{1}{\mu_0 R} \frac{\partial}{\partial R} (R B_Y). \quad (3.5)$$

Finally, another physical quantity that can be obtained from the magnetic probes is the out-of-plane reconnection electric field. Again assuming axisymmetry, the poloidal flux function  $\psi$  can be determined as

$$\begin{aligned} \psi(R, Z, t) &= \int_0^R 2\pi R' B_Z(R', Z, t) dR' \\ &= \int_0^R 2\pi R' B_Z(R', Z_0, t) dR' - \int_{Z_0}^Z 2\pi R B_R(R, Z', t) dZ'. \end{aligned} \quad (3.6)$$

The poloidal flux  $\psi$  is set to be zero at the machine axis ( $R = 0$ ). Eqn. 3.6 implies that  $B_Z$  profile from the center of the machine to the measurement region ( $R \sim 37.5$  cm) must be known to compute  $\psi$ . Since new magnetic probes have only a 16 cm radial coverage, a separate magnetic probe that has a larger radial coverage (40 cm) with a coarser resolution ( $\sim 4$  cm) is utilized. The inductive out-of-plane reconnection electric field  $E_Y$  can be calculated as

$$E_Y = -\frac{1}{2\pi R} \frac{\partial \psi}{\partial t}. \quad (3.7)$$

### 3.2.2 Langmuir Probes

A single-tip Langmuir probe that requires a sweep of the bias voltage ( $\Phi_B$ ) is not suitable for MRX since the quasi-steady period of the discharge is short and the plasma potential varies quickly from about  $-150$  V to  $150$  V due to the interaction between the plasma and the in-plane inductive electric field caused by the time-varying TF coil current.<sup>2</sup> Thus, triple Langmuir probes are used to measure electron temperature and density [Chen and Sekiguchi, 1965]. Figure 3.5-(a) shows a photo of a triple Langmuir probe. The tip diameter is 0.8 mm and its length is 1.2 mm. The four tips made of tungsten form a square and the distance between adjacent tips is 2 mm. The tips must be cleaned by sand-blasting before the Langmuir probe is installed; otherwise, data from the triple Langmuir probe is unreliable as it produces artificially high  $T_e$  and low  $n_e$ .

Figure 3.5-(b) shows a schematic of the MRX triple Langmuir probe diagnostic. The two electrodes labeled  $\Phi_+$  and  $\Phi_-$  are biased in a double probe configuration. Two additional unbiased tips provide floating potential measurements. Assuming the Maxwellian distribution function, the current-voltage characteristic of the Langmuir probe is

$$I_p(\Phi) = -I_{sat} + en_e A \sqrt{\frac{T_e}{2\pi m_e}} \exp\left[-\frac{e(\Phi_p - \Phi)}{T_e}\right], \quad (3.8)$$

---

<sup>2</sup>Refer to Appendix B for more discussion.

(a)



(b)

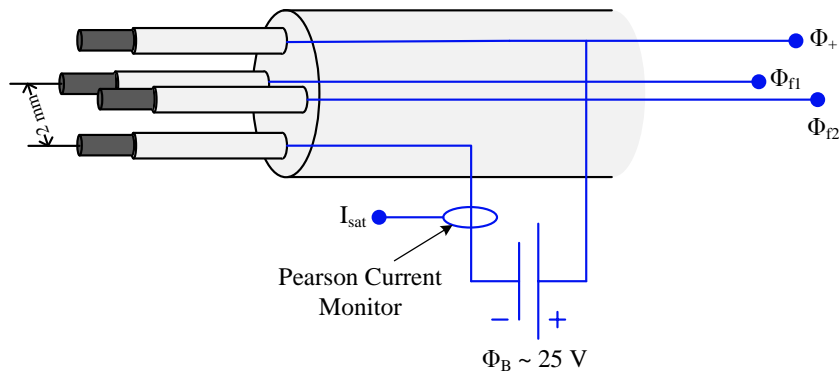


Figure 3.5: MRX triple Langmuir probe. (a) Photo of a MRX triple Langmuir probe. It consists of two tips in a double probe configuration and two additional floating potential tips. (b) Schematic of the Langmuir probe measurement. Two floating potential tips are needed to minimize effects from local electric fields.

where  $I_p(\Phi)$  is the current flowing from the probe to the plasma,  $A$  is the probe area, and  $\Phi_p$  is the plasma potential. The bias voltage  $\Phi_B$  is chosen to be several times larger than  $T_e$  such that the  $\Phi_-$  tip collects the ion saturation current  $I_{sat}$ . Then, the electron temperature can be deduced by measuring  $\Phi_+$  and  $\Phi_f$ . Since the double probe is floating, the  $\Phi_+$  tip draws the same amount of the electron current. With the use of  $I_p(\Phi_+) = -I_p(\Phi_-)$  and  $I_p(\Phi_f) = 0$ , the relation between  $\Phi_+$  and  $\Phi_f$  can be computed as [Hutchinson, 2005]:

$$\frac{I_p(\Phi_+) - I_p(\Phi_f)}{I_p(\Phi_+) - I_p(\Phi_-)} = \frac{1}{2} = \frac{1 - \exp[-(\Phi_+ - \Phi_f)/T_e]}{1 - \exp(-\Phi_B/T_e)}. \quad (3.9)$$

When  $\Phi_B \gg T_e$ , the above equation simplifies to  $\Phi_+ - \Phi_f = (\ln 2)T_e$ , from which the electron temperature can be determined. The major reason for the additional floating potential tip is to minimize the effect from local electric fields. Because the in-plane electric field can be as high as 1000 V/m in MRX discharges, the 2 mm separation between tips can cause an error of about 3 eV in  $T_e$  measurement. By averaging over the two  $\Phi_f$  tips and placing  $\Phi_+$  in the middle of them, this effect can be significantly reduced.

The plasma density can be computed by measuring the ion saturation current, which is given by [Hutchinson, 2005]:

$$I_{sat} = \exp(-0.5)Aen_iC_s, \quad (3.10)$$

where  $C_s$  is the ion sound velocity, which is usually given by  $\sqrt{T_e/m_i}$  when  $T_e \gg T_i$ . Since  $T_i$  is comparable to or slightly larger than  $T_e$  in MRX discharges, this simple expression may not work. However, as long as  $T_i < 2T_e$ , the ion saturation current does not strongly depend on  $T_i$  [see, e.g. Fig. 9 in Hutchinson, 2002]. Therefore,  $C_s \approx \sqrt{T_e/m_i}$  is a valid approximation for MRX discharges. When a new Langmuir probe is installed, its probe area  $A$  is cross-calibrated with a reference Langmuir probe by comparing their signals in a quiet, toroidally symmetric plasma. The probe area of the reference Langmuir probe is calculated by using the actual dimensions of the probe. In this case, it is required

to use an empirical calibration factor of two, which was obtained via an independent measurement using a second-harmonic interferometer system [Bretz, Jobes, and Irby, 1997]. More recently, a CO<sub>2</sub> laser interferometer was installed and confirmed that the Langmuir probe density measurement was about a factor of two low (see Subsection 3.2.5).

The effective ionic charge  $Z_{eff}$  must be calculated to infer the electron density from the measured ion density. In helium discharges of MRX,  $Z_{eff} \leq 1.13$  was previously determined [Trintchouk *et al.*, 2003]. The population of doubly-ionized helium is negligible due to the relatively high second ionization energy (54 eV) compared to the electron temperature of 5–12 eV. Since the MRX base pressure ( $< 2 \times 10^{-6}$  torr) has been improved since then,  $Z_{eff}$  is expected to be closer to unity. Thus, in this dissertation,  $Z_{eff} \approx 1$  is used.

The triple Langmuir probe measurement generally has 10–20% of uncertainty. In this dissertation, error bars on the Langmuir probe data are chosen between 10% of the average value and standard the deviation of the data set at the given location, whichever is larger.

### 3.2.3 Mach Probes

Mach probes are utilized to measure local ion flow speed ( $V_i$ ). Figure 3.6-(a) shows a photo of a Mach probe that can measure  $V_{iZ}$  or  $V_{iY}$ , depending on the orientation of the probe. The Mach probe has 5 tips: one  $\Phi_+$ , two  $\Phi_-$  tips, and two  $\Phi_f$  tips. The area of the  $\Phi_-$  tip is about 2 mm<sup>2</sup>.

Figure 3.6-(b) shows a schematic of the Mach probe diagnostic. Two oppositely-facing  $\Phi_-$  tips collect the ion saturation current  $I_{sat}$ . The difference between  $I_{sat}$  collected by the two electrodes depends on the local ion flow. Since the dimension of the tip is much smaller than the ion gyro-radius, the unmagnetized limit of Mach probe theory can be applied to MRX. The local ion flow speed ( $V_d$ ) along the direction normal to the surface of the  $\Phi_-$  tip

(a)



(b)

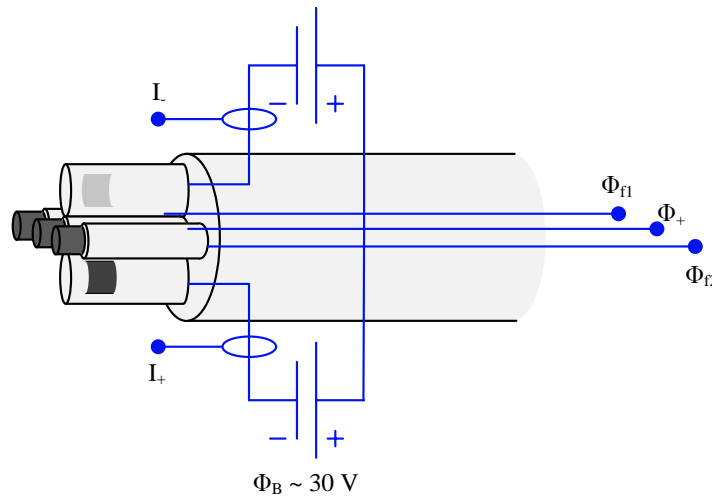


Figure 3.6: Mach probe diagnostic. (a) Photo of a Mach probe used for this dissertation. It consists of 5 tips: one  $\Phi_+$ , two  $\Phi_-$  tips, and two  $\Phi_f$  tips. (b) Schematic of the Mach probe circuit. Two oppositely facing tips collect ion saturation current. Two floating potential tips provide the local electron temperature.

is given by [Hutchinson, 2002]

$$V_d = 1.49 C_s \tanh^{-1} \left( \frac{I_{s+} - I_{s-}}{I_{s+} + I_{s-}} \right), \quad (3.11)$$

where  $I_{s+}$  and  $I_{s-}$  are the ion saturation current collected by the upstream and downstream electrodes, respectively. Although the calibration factor of 1.49 from Hutchinson, 2002 is based on rigorous particle-in-cell simulations, individual probes must be calibrated because the factor can be affected by the geometry of probes. Thus, the ion flow data independently measured by spectroscopy probes (see Subsection 3.2.4) is used to calibrate the MRX Mach probe data. Due to better spatial and temporal resolution and the ability to measure the flow velocity continuously, the ion flow data measured by Mach probes is presented in this dissertation.

The Mach probes used here are also designed to measure the local electron temperature. By making the area of the  $\Phi_+$  tip two times larger than that of a  $\Phi_-$  tip and utilizing the two additional  $\Phi_f$  tips, the local electron temperature, which is necessary to determine  $C_s$ , can be also determined. In this case, however, there are additional errors from the asymmetry between the  $\Phi_+$  tip and  $\Phi_-$  tips. Thus,  $T_e$  measured by a triple Langmuir probe is used to compute  $C_s$  in this dissertation whenever it is available.

### 3.2.4 Ion Dynamics Spectroscopy Probes (IDSPs)

The IDSP is an insertable optical probe that can measure local ion temperature and flow velocities via Doppler spectroscopy [Fiksel, Hartog, and Fontana, 1998]. Figure 3.7 shows a photo of one of the IDSPs used for this dissertation. The IDSP collects photons from the volume between the lens and the view dump, and they are transmitted to a spectrometer<sup>3</sup> through a bundle of 92 (100  $\mu\text{m}$  diameter) optical fibers. The signals are recorded

---

<sup>3</sup>McPherson model 2061 – 1 m focal length,  $f/7$ , 2400 line/mm grating, 0.05  $\text{\AA}$  resolution,  $\pm 0.025$  nm reproducibility, wavelength range of 185–650 nm.

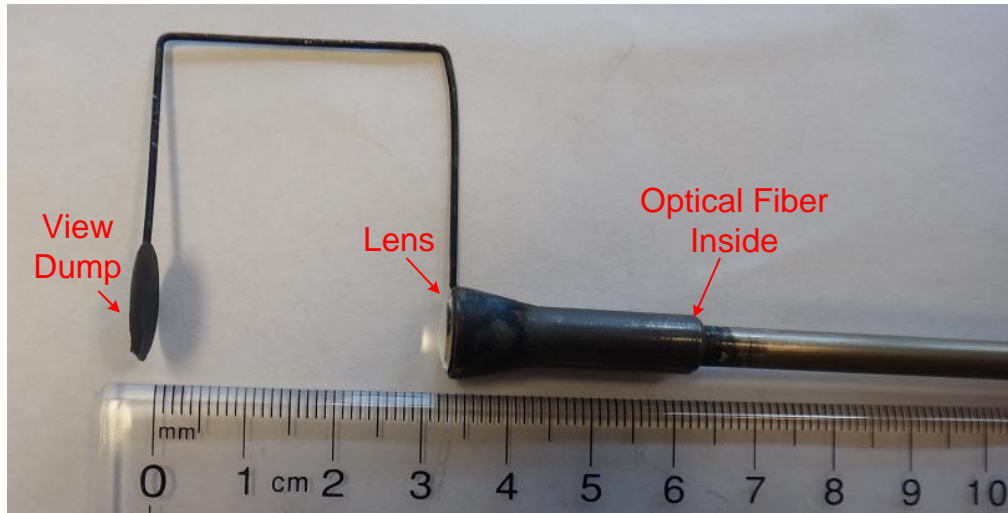


Figure 3.7: Photo of an Ion Dynamics Spectroscopy Probe (IDSP). The IDSP collects photons from the volume between the lens and the view dump so that it can measure local ion temperature and flow velocity. A bundle of optical fibers is inserted and located at the focal point of the lens, transmitting the photons to the spectrometer.

by a gated, intensified charge-coupled device (ICCD) camera.<sup>4</sup> The ICCD camera has the ability to take two images during a single discharge. The spatial resolution of the IDSP is determined by the distance between the lens and the view dump (3–4 cm), while the temporal resolution is given by the gate-open time of the ICCD camera (5.6  $\mu\text{s}$ ).

The spectroscopy system must be calibrated to obtain physical data from the recorded images. Signals from the spectrometer are recorded as  $1024 \times 1024$  pixel images by the ICCD camera. The abscissa of the image represents the wavelength, and the ordinate indicates the vertical position at the entrance to the spectrometer. Because the optical fibers are aligned vertically, the ordinate does not have any physical meaning. The abscissa, on the other hand, need to be converted into the corresponding wavelength. In this dissertation, the spectral line used for the ion temperature measurement is He II 4686 Å. Thus, a neon spectral lamp is employed for calibration since neon has many atomic lines near the relevant He II line.

<sup>4</sup>Princeton Instrument model PI-MAX2-1003 –  $1024 \times 1024$  pixels,  $12.8 \times 12.8 \mu\text{m}$  pixel size,  $13.1 \times 13.1$  mm field of view, HBF Gen III filmless intensifier, 50 % quantum efficiency at  $\lambda = 450\text{--}550$  nm.

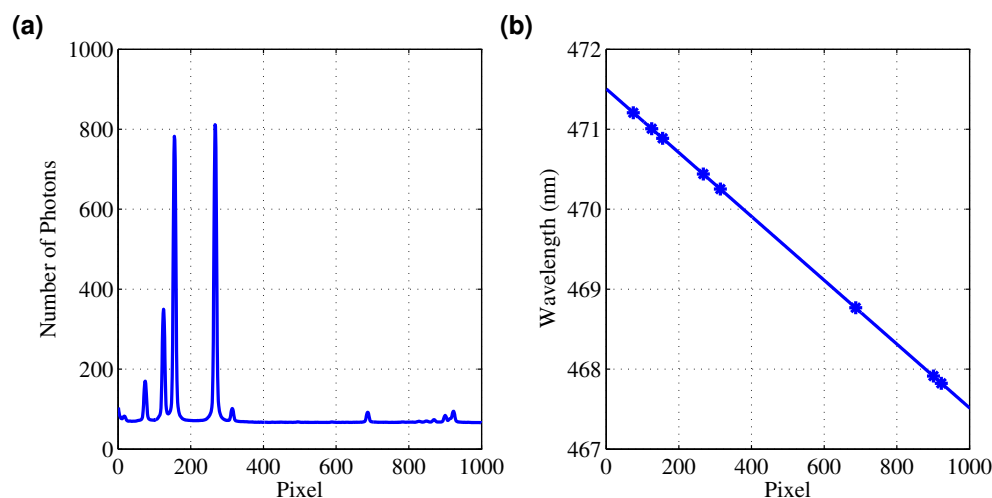


Figure 3.8: Calibration signals from a neon spectral lamp. (a) A total of eight neon spectral lines are individually fit by the Gaussian function to find the corresponding pixel for each spectra. (b) Linear fit of the calibration results. The linear function is used to convert the pixel number into the wavelength.

Figure 3.8-(a) shows signals from the neon spectral lamp. There are eight Ne I spectral lines recorded by the ICCD camera. By fitting each of the lines to a Gaussian function, the pixel number corresponding to each line is identified. Since the wavelengths of the Ne I lines are known,<sup>5</sup> the relation between the pixel number and wavelength can be found by fitting the results to a linear function, as shown in Fig. 3.8-(b). It is determined that the wavelength per pixel is  $0.0398 \text{ \AA}$ .<sup>6</sup> The natural broadening of the spectroscopy system is determined by measuring the broadening of the Ne I lines, since the temperature of the Ne spectral lamp is negligible. The measured broadening is 3.2 pixels and the corresponding temperature is about 2.8 eV for helium gas.

The spectral lines of interest are the He II  $4686 \text{ \AA}$  and He I  $4713 \text{ \AA}$  lines. Both spectral lines have fine structure that must be taken into account. The relative amplitude and separation between the fine structure components are determined, based on recent quantum-

<sup>5</sup>Refer to the NIST atomic spectra database.

<sup>6</sup>The spectroscopy system is extremely sensitive to external conditions such as vibrations and the room temperature. It is recommended that this calibration process be repeated frequently when the ion flow data is needed.

mechanical calculations [Wiese and Fuhr, 2009]. Then, the ion or neutral temperature and velocity can be obtained via the following process. From the non-relativistic Doppler effect, the relation between velocity and the observed wavelength  $\lambda$  is

$$v = \frac{\lambda - \lambda_s}{\lambda_s} c, \quad (3.12)$$

where  $\lambda_s$  is the rest wavelength and  $c$  is the speed of light. In the case of a single Maxwellian fit, by introducing a dimensionless variable  $x = (\lambda - \lambda_s)/\lambda_s$ , the final Gaussian function for the 1-D Maxwellian velocity distribution becomes

$$f(x) = A \exp \left[ -\frac{m_p c^2}{2e} B (x - C)^2 \right] + D, \quad (3.13)$$

where  $A$  is related to intensity,  $B$  is  $\mu/T_{fit}$  where  $\mu = m_i/m_p$  and  $T_{fit}$  is the measured temperature in units of eV,  $C$  is  $V_D/c$  where  $V_D$  is the drift velocity, and  $D$  is added to take the background noise into account. The correct temperature ( $T_{cor}$ ) is determined by subtracting temperature from the instrumental broadening ( $T_{ins}$ ), i.e.  $T_{cor} = T_{fit} - T_{ins}$ . For the multiple Maxwellian fit, Eqn. 3.13 is changed into:

$$f(x) = A \sum_{n=1}^N S_n \exp \left[ -\frac{m_p c^2}{2e} B \left( \frac{\lambda_s}{\lambda_n} x - \frac{\lambda_n - \lambda_s}{\lambda_s} - C \right)^2 \right] + D, \quad (3.14)$$

where  $S_n$  is the normalized relative strength of the  $n$ -th fine structure component whose wavelength is  $\lambda_n$ . In this case,  $\lambda_s$  can be either an average value or a nominal value of the spectral line. It is worth noting that the number of free parameters has not changed. The He II 4686 Å line has 13 fine structure components, while the He I 4713 Å has 4 components.

Figure 3.9-(a) shows an example of the measured He II 4686 spectra and fitting. The red curve is the result of fitting to the sum of 13 Gaussian functions, while the green curve is from fitting to a single Gaussian. The multiple Gaussian case shows a better fit to the measured spectra. Moreover, the single Gaussian fit results in higher ion temperature. In

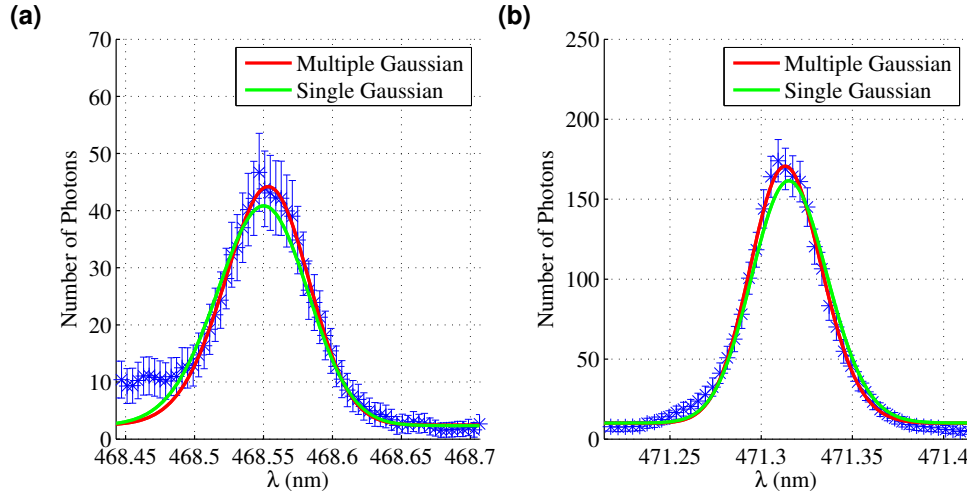


Figure 3.9: Example of the measured He spectral lines at  $(R, Z) = (37.5, 12)$ cm. (a) He II 4686 spectra. The blue asterisks are measured spectra with error bars of the square root of the number of photons. The red curve stands for fitting to the sum of the 13 Gaussian functions, while the green curve is results of fitting to the single Gaussian function. (b) He I 4713 spectra. The red curve is fitting to the sum of the 4 Gaussian functions, which corresponds to the 4 fine structure components.

this example,  $T_i$  from the multiple Gaussian fit is 10.5 eV, while  $T_i$  from the single Gaussian fit is 13.1 eV. In general, the single Gaussian fitting overestimates  $T_i$  by 15–25%. The ion drift velocity is also different: 12.4 km/s (multiple) and 14.3 km/s (single). Thus, multiple Gaussian fitting is necessary to minimize errors in ion temperature and flow measurements.

It should be noted that due to the reproducibility of the spectrometer, the error in the IDSP flow velocity measurement cannot be smaller than 1.6 km/s for helium ions. It should be also mentioned that the bump in the left side of the spectra ( $\lambda < 468.5$  nm) in Fig. 3.9-(a) is caused by an unknown molecular line.<sup>7</sup> Thus, that portion of the spectra is excluded from the fitting process.

The range of the spectroscopy system is large enough to measure the He II 4686 Å and He I 4713 Å lines at the same time. Figure 3.9-(b) shows the He I 4713 Å spectra. The multiple Gaussian fit agrees better with the measured spectra than the single Gaussian

<sup>7</sup>To confirm that the bump is caused by impurities, the measurement was repeated in a hydrogen discharge. The bump remains, while the He II 4686 spectra disappears.

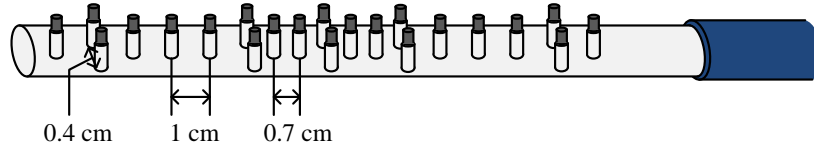


Figure 3.10: Sketch of the 22-tip floating potential probe. It consists of 22 floating potential tips with 17 measurement points. At 5 radial locations, additional information on the local electric field can be gained from examining differences between the two closely located tips.

fit. The neutral temperature is 3.1 eV (multiple) and 3.8 eV (single). The typical neutral temperature in the discharges for this work is 3–4 eV. The measured neutral velocity is negligible (within the measurement error), indicating that neutral-ion coupling via charge exchange collisions is weak.

### 3.2.5 Other diagnostics

#### Floating Potential Probe

The radial floating potential profile is measured by a 22-tip floating potential probe. Figure 3.10 shows the alignment of the probe. It has 17 radial measurement points with the maximum resolution of 0.7 cm. There are five radial locations where two tips exist with a small separation ( $\sim 4$  mm) along the direction perpendicular to the probe shaft. The purpose of the additional five tips is to provide an approximate value of the local electric field ( $E \sim -\Delta\Phi_f/d$ , where  $\Delta\Phi_f$  is the difference between the two measured floating potential and  $d$  is the distance between the tips).

The measured floating potential profile can be converted to the plasma potential profile, if electron temperature is available. The relation between the plasma potential ( $\Phi_p$ ) and the

floating potential ( $\Phi_f$ ) can be obtained from Eqn. 3.8 as

$$\Phi_p = \Phi_f + 0.5 \left[ \ln \left( \frac{m_i}{2\pi m_e} \right) - 1 \right] T_e, \quad (3.15)$$

where  $T_e$  is in units of eV. Here, the approximations  $n_i = n_e/Z_{eff} \approx n_e$  and  $C_s \approx \sqrt{T_e/m_i}$  are used. This plasma potential is used to compute the in-plane electric field.

### Fluctuation Probe

High frequency fluctuations are measured by a fluctuation probe. The probe is designed to measure all three components of magnetic fluctuations and the out-of-plane component of electrostatic fluctuations in the floating potential. The magnetic fluctuations are measured by pickup coils whose effective area is about 1.0 cm<sup>2</sup>. The electrostatic fluctuations are measured by the use of two floating tips separated by 1 mm. Inside of the probe shaft close to the coils and floating potential tip, there is a 4-channel miniature amplifier board, which is used to improve the signal-to-noise ratio by amplifying the signal close to its source and providing impedance matching. Details of the circuit of the amplifier board can be found in Carter, 2001. The time response of the probe-amplifier system is about 20 ns.

Signals from the fluctuation probe are digitized by high bandwidth oscilloscopes. By numerically integrating the magnetic fluctuation signals from the pickup coils and Fourier transforming them after subtracting the average trend, the intensity in the high frequency fluctuations ( $\gtrsim 0.5$  MHz) can be obtained. Electrostatic signals can be directly Fourier-transformed.

### MRX interferometer

The MRX laser interferometer employs a CO<sub>2</sub> laser with continuous output power up to 10 W at a wavelength of 10.6  $\mu\text{m}$ .<sup>8</sup> Figure 3.11 shows the setup of the MRX interferometer.

<sup>8</sup>Access Laser model Merit-S – 2.4 mm beam diameter at the output, 5.5 mrad beam divergence.

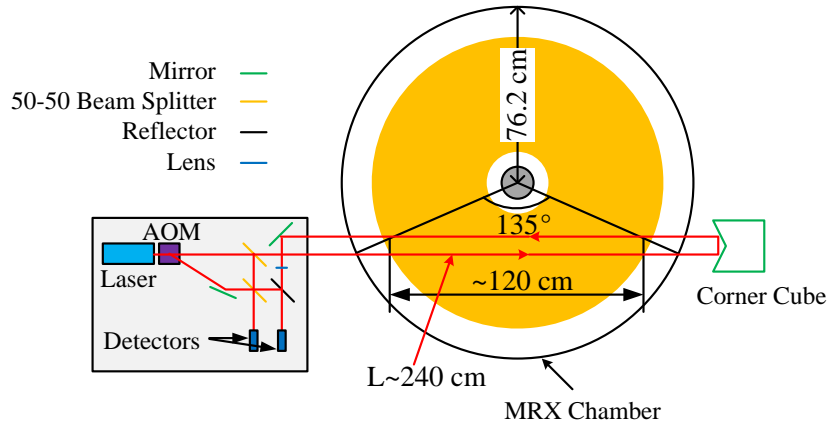


Figure 3.11: Setup of the MRX interferometer system. It utilizes a CO<sub>2</sub> laser and an acousto-optic modulator (AOM). One detector supplies the reference signal, while the other records the plasma signal. The phase difference between two signals contains information on the line-integrated density. The yellow color stands for the bulk plasma. The path length through the plasma  $L$  is about 240 cm.

The laser beam first passes an acousto-optic modulator (AOM),<sup>9</sup> where it is split into two beams with frequencies  $f_p$  and  $f_r$  ( $f_p - f_r = 40$  MHz). By the use of two beam splitters, two beams are split into four beams. Two of the beams of difference frequencies directly arrive at a reference detector.<sup>10</sup> The plasma detector receives the two remaining beams with one of them passing through the plasma. The phase difference ( $\Delta\phi$ ) between the two signals provides the line-integrated density. The relation is given by [Hutchinson, 2005]

$$\frac{\Delta\phi}{2\pi} = -\frac{1}{2\lambda n_c} \int n_e(l) dl = \frac{\langle n_e \rangle L}{2n_e \lambda}, \quad (3.16)$$

where the cutoff density is  $n_c = \omega^2 \epsilon_0 m_e / e^2 = 9.92 \times 10^{18} / \text{cm}^3$  for a wavelength of 10.6  $\mu\text{m}$ .

Figure 3.12 shows the measured line-integrated density in a deuterium plasma. Since the total path length of the beam through the plasma is about 240 cm as shown in Fig. 3.11, the peaked line-averaged density is about  $2.1 \times 10^{14} / \text{cm}^3$ . The averaged density measured

<sup>9</sup>IntraAction Corp. model AGM-406B1 – 77 mrad beam separation, driven by a 40 MHz RF generator.

<sup>10</sup>Vigo System S.A. model PD-10.6-3.

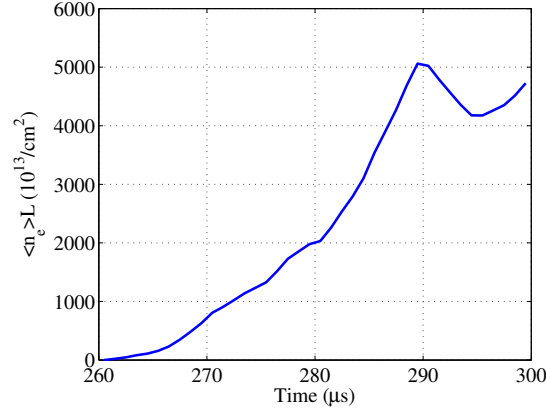


Figure 3.12: Line-integrated density measured by the MRX interferometer. The peak line-averaged density is about  $2.1 \times 10^{14}/\text{cm}^3$  in a deuterium plasma with a fill pressure of 7.3 mT.

by a radial scan of a triple Langmuir probe is only  $1.1 \times 10^{14}/\text{cm}^3$ , thereby confirming the empirical factor of two for the triple Langmuir probe measurement.

### 3.3 Plasma Parameters and Experimental Regime

Using extensive  $R$ - $Z$  scans of the previously described probes, 2-D profiles of various plasma parameters such as  $n_e$ ,  $T_e$ ,  $T_i$ ,  $\mathbf{V}_e$ ,  $\mathbf{V}_i$ , and  $\Phi_f$  are obtained. The number of measurement points along the  $Z$  direction is 6–7 and the distance between the measurement points is typically 3 cm. Along the radial direction, electrostatic probes have 13 measurement points with the 1 cm separation, while IDSPs have 7 points every 2 cm. More than 4200 discharges are scrutinized based on the reproducibility of the data from the 2-D magnetic probe array and a reference Langmuir probe in order to select the final data set. The main criteria are the location of the X-point, the plasma current, and the density and temperature measured by the reference Langmuir probe. For example, the radial location of the X-point ( $R_X$ ) traced by the 2-D magnetic probe array is an important criterion to select shots. For 1 cm radial scans, data from shots with  $37 < R_X < 38$  cm is used. For 2 cm radial scans, shots with  $36.5 < R_X < 38.5$  cm are chosen. As shown in Fig. 3.13,  $R_X$

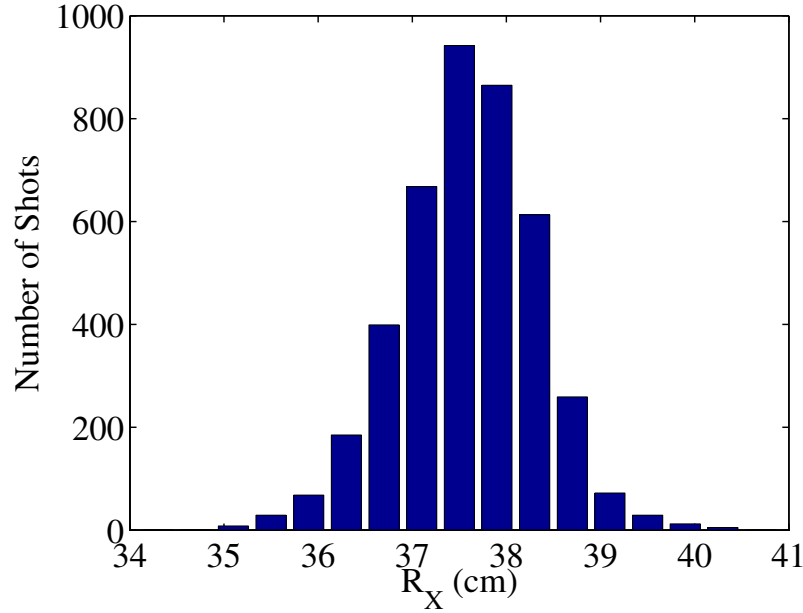


Figure 3.13: Histogram of the radial position of the X-point at  $t = 330 \mu\text{s}$ . The radial location of the X-point ( $R_X$ ) is an important criterion to select shots.

is reasonably reproducible; about 60% of shots satisfy the condition  $37 < R_X < 38$  cm. Overall, about 30% of the 4200 discharges are used for creating the 2-D profiles presented in this dissertation.

Table 3.1 summarizes the important plasma parameters for this work. The plasma parameters are obtained during the quasi-steady period in the pull reconnection phase. Plasma parameters are controlled such that the plasma is in the collisionless regime, which provides the opportunity to identify energy conversion mechanisms during collisionless reconnection under a prototypical magnetic geometry in a laboratory plasma. As shown in Fig. 3.14, the resistivity term ( $\eta_{S\perp} J_Y$ , where  $\eta_{S\perp}$  is perpendicular Spitzer resistivity) accounts for about 10% of the reconnection electric field ( $E_{rec}$ ) at the X point ( $R \approx 37.5$ ), which means that collisionless effects are the dominant mechanisms that break magnetic field lines at the X point. Outside of the current sheet, the electron Lorentz force term ( $\mathbf{V}_e \times \mathbf{B}$  – green curve) balances the reconnection electric field, indicating strong two-fluid effects. It is worth noting that the contribution from the Hall term ( $\mathbf{J} \times \mathbf{B}/en_e$  – red curve) is radially

Table 3.1: Plasma parameters during the quasi-steady period of He discharges with the 4.5 mT fill pressure.

<b>Plasma Parameter</b>	<b>Upstream</b>	<b>Downstream</b>
Density, $n_e$ ( $\times 10^{13}$ /cm <sup>3</sup> )	1–2.5	5–8
Electron temperature, $T_e$ (eV)	5–11	8–12
Ion temperature, $T_i$ (eV)	7–9	7–14
Electron plasma frequency, $f_{pe}$ (GHz)	28–45	63–80
Electron gyro-frequency, $f_{ce}$ (MHz)	250–500	220–420
Electron-ion collision frequency, $\nu_{ei}$ (MHz)	15–33	17–104
Ion plasma frequency, $f_{pi}$ (MHz)	332–525	742–939
Ion gyro-frequency, $f_{ci}$ (kHz)	34–68	30–57
Ion-ion collision frequency, $\nu_{ii}$ (kHz)	99–350	370–670
Electron gyro-radius, $r_{ce}$ (cm)	0.03–0.08	0.04–0.10
Electron mean free path, $\lambda_{mfp,e}$ (cm)	2.0–12.0	1.2–3.8
Electron inertial length, $\delta_e$ (cm)	0.11–0.17	0.06–0.08
Ion gyro-radius, $r_{ci}$ (cm)	3.0–6.8	6.3–7.8
Ion mean free path, $\lambda_{mfp,i}$ (cm)	3.9–13.1	1.9–4.9
Ion inertial length, $\delta_i$ (cm)	9.1–14.4	5.1–6.5
Shoulder reconnecting magnetic field <sup>a</sup> $B_{sh}$ (G)	90–120	
Current sheet width, $\delta_{CS}$ (cm)	1.0–2.5	
Upstream Alfvén velocity, $V_A = B_{sh}/\sqrt{\mu_0\rho}$ (km/s)	21–36	
Reconnection electric field, $E_{rec}$ (V/m)	170–220	
Dreicer runaway field at the X point, $E_{run}$ (V/m)	110–154	
Lunquist number, S	300–400	

<sup>a</sup> Due to the field from the external coils such as the PF and EF coils, the radial profile of the reconnecting magnetic field has a linear component as shown in Fig. 3.16. The shoulder value means the amplitude of the tanh component in Eqn. 3.17.

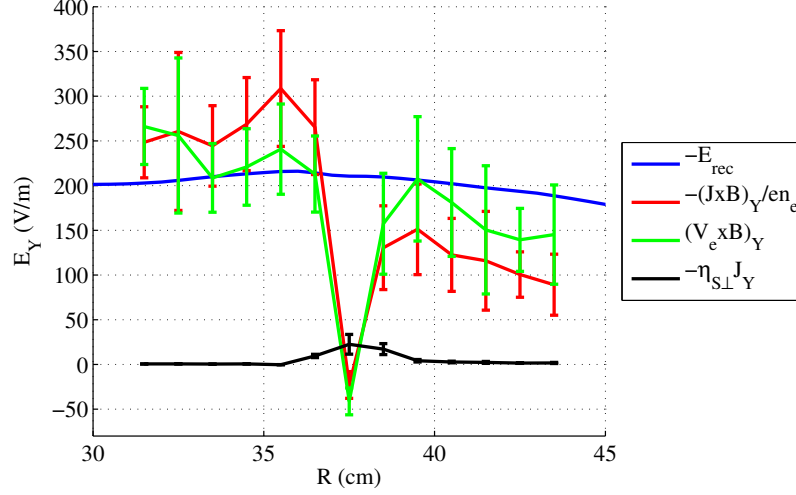


Figure 3.14: Radial profile of the out-of-plane electric field at  $Z = 0$  in the middle of the quasi-steady period ( $t = 332 \mu\text{s}$ ). The resistivity term is about 10% of the total out-of-plane reconnection electric field at the X point ( $R \approx 37.5 \text{ cm}$ ), indicating collisionless reconnection.

asymmetric. This is caused by an upstream density asymmetry due to interaction between the plasma and the in-plane inductive electric field from the time-varying TF currents in the earlier phase of the discharge (refer to Appendix B); the outboard side ( $R > 37.5$ ) has about 2–3 times higher density than the inboard side ( $R < 37.5$ ). The same process is responsible for asymmetric ion inflow such that the profile of the electron Lorentz force term is more symmetric than that of the Hall term.

To facilitate ion temperature measurements, helium discharges with a fill pressure of 4.5 mT are used. With this fill pressure, effects from electron-neutral collisions are limited since the electron-neutral collision frequency ( $\nu_{en}$ ) is less than the electron-ion collision frequency ( $\nu_{ei}$ ). The total momentum-transfer coefficient for electron collisions with helium neutrals is  $\langle \sigma \rangle \approx 6 \times 10^{-8} \text{ cm}^3/\text{s}$  [Itikawa, 1978] assuming  $T_e = 10 \text{ eV}$ . The upper limit of the neutral density with the 4.5 mT fill pressure is  $1.4 \times 10^{14} /\text{cm}^3$ , which is the initial neutral density before the plasma is created. The electron-neutral collision frequency  $\nu_{en}$  is less than 8 MHz. This *upper* bound of  $\nu_{en}$  is less than the *lower* bound of  $\nu_{ei} > 15 \text{ MHz}$  as shown in Table 3.1. Furthermore, the neutral density near the X-point is anti-

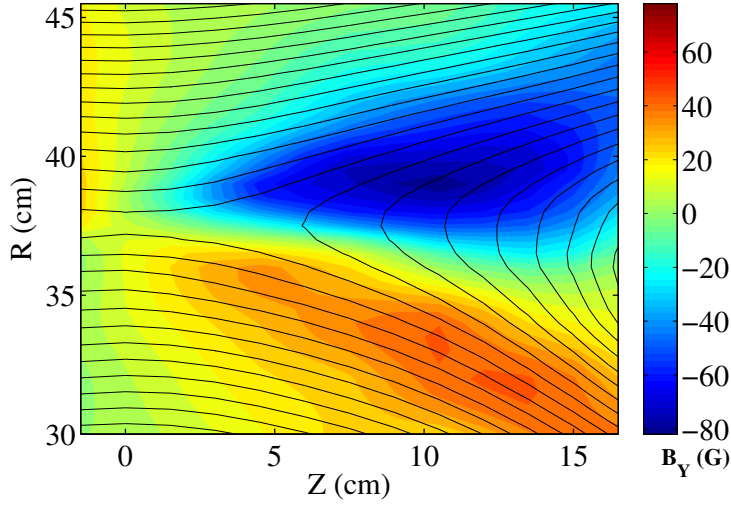


Figure 3.15: 2-D profile of the out-of-plane quadrupole magnetic field at  $t = 330 \mu\text{s}$  along with the contours of the poloidal flux  $\Psi$ . Black lines stand for contours of poloidal magnetic flux  $\psi$ .

pated to be smaller than the initial density due to the high electron temperature and thermal expansion of the neutral gas (neutrals are heated via charge-exchange collisions with ions). Therefore, resistivity due to electron-neutral collisions is estimated to be less than 30% of  $\eta_{S\perp}$  and ignored in this dissertation.

The out-of-plane quadrupole field also supports the existence of strong two-fluid effects in this regime. Fig 3.15 shows the measured 2-D profile of the quadrupole field. The other side ( $Z < 0$ ) of the quadrupole field is not shown due to the limited coverage of the magnetic probes. The maximum magnitude of the quadrupole field reaches 60–70 G, which is about 60–70% of the reconnecting magnetic field. The black lines in Fig. 3.15 are contours of the poloidal magnetic flux  $\psi$ , which represents the in-plane magnetic field geometry. The X point is at  $(R, Z) = (37.5, 0)$  cm.

Information on the current sheet in Table 3.1 is obtained by fitting the measured  $B_Z$  profile to the following Harris-type function:

$$B_Z(R) = B_0 + C(R - R_0) + B_{sh} \tanh\left(\frac{R - R_0}{\delta_{CS}}\right), \quad (3.17)$$

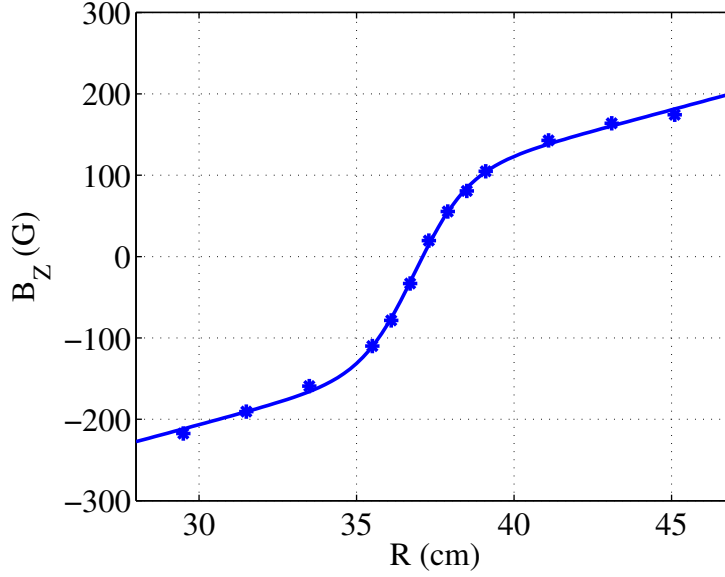


Figure 3.16: Radial profile of the reconnection magnetic field at  $Z = 0$ . The blue asterisks are the measured values and the blue curve shows the fit to a Harris-type function in Eqn. 3.17.

where  $B_{sh}$  is the shoulder value of the reconnecting magnetic field,  $R_0$  is the current sheet location and  $\delta_{CS}$  is the width of the current sheet. The linear part  $B_0 + C(R - R_0)$  is included to take contributions from the external coils (PF and EF coils) into account. Figure 3.16 shows a typical example of the measured  $B_Z$  profile at  $Z = 0$  along with the Harris fitting result. The radial  $B_Z$  profile is well fit by the Harris function given in Eqn. 3.17. As summarized in Table 3.1, the current sheet width determined from the radial  $B_Z$  profile is about 2 cm and the shoulder value of the reconnecting magnetic field is about 100 G.

In summary, we show that the plasma studied in this dissertation is in the collisionless regime. The resistivity term accounts for only 10% of the reconnection electric field at the X-point. The quadrupole field, which is one of the key features of collisionless reconnection, clearly appears. In the following chapters, energy conversion processes in this collisionless plasma are discussed. The measured 2-D profiles are used to identify mechanisms of ion acceleration, heating, and electron heating. The energy inventory during reconnection is also analyzed.



# Chapter 4

## Ion Acceleration and Heating by In-plane Potential

Some of contents in this chapter are reported in Yoo *et al.*, 2013.

Ion acceleration and heating during magnetic reconnection have been widely observed in laboratory plasmas [e.g. Gekelman, Stenzel, and Wild, 1982; Ono *et al.*, 1996; Hsu *et al.*, 2000; Stark *et al.*, 2005; Gangadhara *et al.*, 2007; Fiksel *et al.*, 2009]. Many physical mechanisms have been suggested to explain these phenomena, but none of them have been studied conclusively due to limited diagnostic capabilities.

In this chapter, ion heating and acceleration are addressed using thorough 2-D measurements of key physical quantities such as  $n_i$ ,  $T_i$ ,  $\mathbf{V}_i$ ,  $\mathbf{E}$ , and  $\mathbf{B}$  from within the prototypical magnetic reconnection geometry of MRX. In particular, the first conclusive laboratory measurement of the in-plane electrostatic potential is presented. As seen in numerical simulations [Karimabadi, Daughton, and Scudder, 2007; Drake, Shay, and Swisdak, 2008; Pritchett, 2010] and space observations [Wygant *et al.*, 2005], the potential well along the direction normal to the current sheet becomes deeper and broader downstream, creating a saddle-shaped potential profile in the reconnection plane. This unique in-plane potential

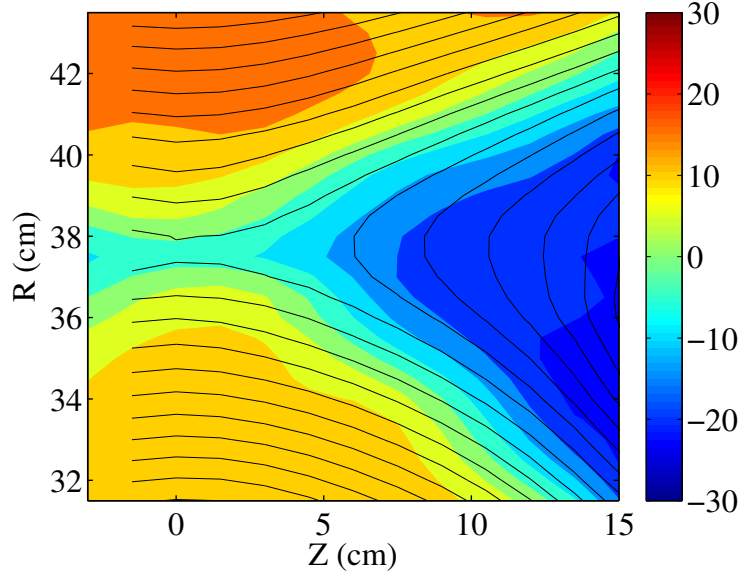


Figure 4.1: 2-D floating potential profile at  $t = 330 \mu\text{s}$  along with contours of the poloidal flux  $\Psi$ . It is measured by the 22-tip floating potential probe at 6 different  $Z$  locations. The profile has a radial floating potential well whose boundaries expand along the separatrices.

profile is established by electron dynamics around the electron diffusion region. A large in-plane electric field ( $|\mathbf{E}_{in}| \sim 500\text{--}800 \text{ V/m}$ ) over a short spatial scale ( $< \delta_i \equiv c/\omega_{pi}$ ) ballistically accelerates ions up to about  $0.5V_A$  near the separatrices. These ions are heated as they travel into the high pressure downstream region. Classical viscous heating in the unmagnetized limit cannot explain the observed peaked ion temperature profile, which suggests that a magnetic field effect referred to here re-magnetization should be important.

## 4.1 In-plane Electrostatic Potential

As introduced in Section 1.3.2, two-fluid effects inside the ion diffusion region lead to the development of the in-plane electrostatic potential that has a well structure along the direction normal to the current sheet. This type of the potential profile is therefore expected to exist in the MRX plasma in the collisionless regime.

Figure 4.1 shows the 2-D profile of  $\Phi_f$  measured by the 22-tip floating potential probe

(Fig. 3.10) at 6 different  $Z$  locations. Similar to observations in space and numerical simulations [e.g. Wygant *et al.*, 2005; Karimabadi, Daughton, and Scudder, 2007; Pritchett, 2010], the floating potential well expands along the separatrices. It is notable that the flux contours in Fig. 4.1 nearly match the  $\Phi_f$  contours, suggesting that  $\Phi_f$  is relatively constant along magnetic field lines.

This floating potential profile reflects the key aspects of the in-plane electrostatic potential profile. However, in order to carry out quantitative analysis,  $\Phi_f$  must be converted to the plasma potential  $\Phi_p$ . As explained in Eqn. 3.15,  $\Phi_p$  depends on the electron temperature, which has strong in-plane variation due to non-classical electron heating around the X-point (see Chapter 5 for more discussion). Thus, the 2-D profile of  $T_e$  measured by the triple probe shown in Fig. 5.1 is used to obtain the  $\Phi_p$  profile.

Within the reconnection layer, the validity of Eqn. 3.15 can be challenged since it is based on the assumption that the distribution function is close to Maxwellian and non-Maxwellian, anisotropic electron distribution functions are commonly found in numerical simulations of collisionless reconnection. Furthermore, in the electron diffusion region of MRX, the generation of runaway electrons is expected because  $E_{rec}$  exceeds the Dreicer runaway field  $E_{run}$  as summarized in Table 3.1.

In order to maximize the validity of Eqn. 3.15, several experimental techniques have been implemented. First, the tips of the Langmuir probes and the floating potential probe are cylindrical so that they can draw electrons from every direction; this minimizes effects from anisotropic electron distribution functions. Second, the floating potential probe is oriented such that the probe shaft shields the tips from direct interaction with the fast streaming of runaway electrons that may be generated. In particular, the runaway electrons are accelerated by the reconnection electric field at the X-point, such that the direction of their velocity is opposite to the reconnection electric field along the out-of-plane direction. Since the probe tips shown in Fig. 3.10 point *along* the electron flow direction, the probe shaft shields the tips from interacting with the fast electrons.

We have also confirmed that the electron distribution function measured by the triple Langmuir probe around the X point does not deviate much from Maxwellian. The  $I-\Phi_B$  curve for the double probe part of the triple probe is obtained by changing the bias voltage. This curve fits to the expected tanh curve within error bars, indicating that the population of fast electrons remains small in MRX discharges. This is likely due to the relatively high electron-ion collision frequency.

Figure 4.2-(a) shows the measured 2-D profile of the plasma potential  $\bar{\Phi}_p$  in the middle of the quasi-steady reconnection period along with contours of the poloidal flux  $\bar{\Psi}$ . The key features of the 2-D floating potential profile from Fig. 4.1 remain, although the  $\bar{\Phi}_p$  profile has more variation along magnetic field lines due to the contribution from  $T_e$ , which has relatively large error bars. The red asterisks in Fig. 4.2-(b) show the radial profile of  $\bar{\Phi}_p$  at  $Z = 0$ . At this location, the magnitude of the potential well is about 10 V. The black dashed line shows the radial  $J_Y$  profile at the same  $Z$  location. It is worth noting that the width of the plasma potential profile is almost the same as that of the current sheet. As shown in Fig. 4.2-(c), the magnitude of the radial potential well becomes deeper downstream, reaching 35 V. It also becomes wider downstream as its boundary expands along the separatrices. These results are consistent with recent numerical simulations [Karimabadi, Daughton, and Scudder, 2007; Drake, Shay, and Swisdak, 2008; Pritchett, 2010].

The in-plane potential profile is governed by electron dynamics around the electron diffusion region (EDR). In particular, the in-plane electric field is the result of the electron force balance, and the Lorentz force from electrons accelerated by  $E_{rec}$  is the fundamental driving force of the Hall electric field. To test this hypothesis, let us write down the electron momentum equation

$$n_e m_e \frac{d\mathbf{V}_e}{dt} = -en_e(\mathbf{E} + \mathbf{V}_e \times \mathbf{B}) - \nabla \cdot \mathbb{p}_e + en_e \mathbf{v} \cdot \mathbf{J}, \quad (4.1)$$

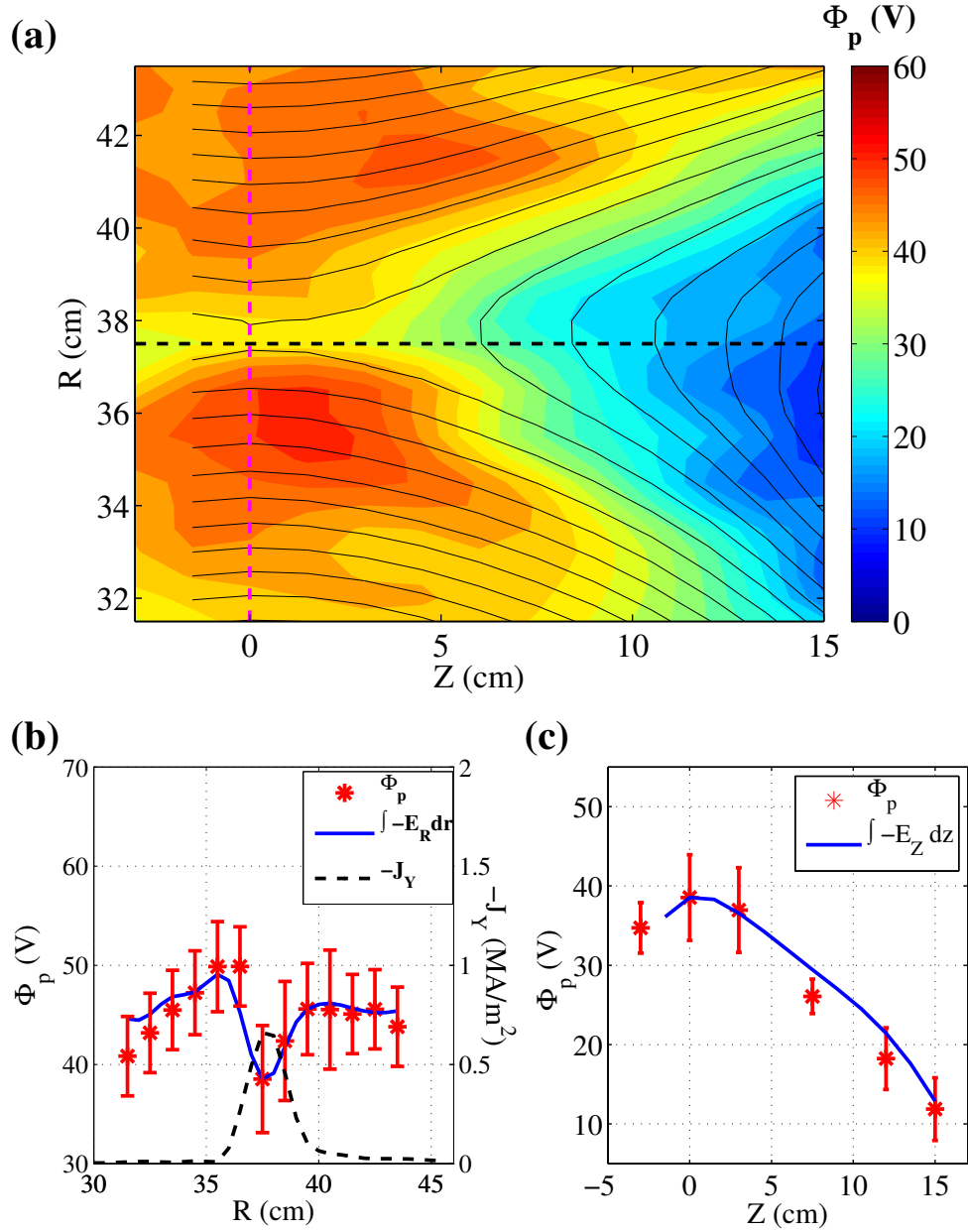


Figure 4.2: (a) 2-D plasma potential profile with contours of the poloidal flux  $\Psi$ . (b) Radial profile of  $\Phi_p$  at  $Z = 0$  (along the magenta dashed line in (a)). The red asterisks are the measured  $\Phi_p$  and the blue line is the radial integration on the right hand side of Eqn. 4.2. The black dashed line shows the radial  $J_Y$  profile at the same  $Z$  location. (c) Axial profile of  $\Phi_p$  at  $R = 37.5$  cm (along the black dashed line in (a)). The red asterisks are the measured  $\Phi_p$  and the blue line comes from the integration on the right-hand side of Eqn. 4.4 along  $Z$ .

where  $\mathbb{p}_e$  is the electron pressure tensor and  $\eta$  is the resistivity tensor. After the negligible electron inertial term and resistivity term are ignored and the pressure tensor is assumed to be isotropic, the  $R$  component of the above equation at  $Z = 0$  leads to

$$E_R \approx -V_{eY}B_Z - \frac{1}{en_e} \frac{\partial p_e}{\partial R}. \quad (4.2)$$

Since both  $B_R$  and  $B_Y$  are small at  $Z = 0$ , the out-of-plane component of the electron diamagnetic drift  $V_{eY}^*$  can be approximated as  $V_{eY}^* \equiv (\nabla p_e \times \mathbf{B})_Y / (en_e B^2) \approx -(1/en_e B_Z) \partial p_e / \partial R$ . Then, Eqn. 4.2 can be rewritten as

$$E_R \approx -(V_{eY} - V_{eY}^*)B_Z. \quad (4.3)$$

In these experiments, the diamagnetic drift term is not negligible due to strong electron heating near the current sheet that cannot be explained by classical Ohmic heating [Ji *et al.*, 2004]. The radial electric field reverses sign at the X point where the sign of  $B_Z$  also reverses. This indicates that the bipolar radial electric field is the result of electron force balance [Li and Horiuchi, 2008]. Since  $V_{eY}$  contains the diamagnetic component, Eqn. 4.3 implies that the electron diamagnetic drift does not contribute to  $E_R$ ; only pure acceleration by  $E_{rec}$  plays a role [Uzdensky and Kulsrud, 2006]. By integrating the right-hand side of Eqn. 4.3 along  $R$ , the radial potential profile can be estimated. The electron flow velocity is obtained by  $\mathbf{V}_e = -\mathbf{J}/en_e + \mathbf{V}_i = -\nabla \times \mathbf{B}/\mu_0 en_e + \mathbf{V}_i$ . As shown in Fig. 4.2-(b), the estimated values from Eqn. 4.3 (the blue line) agree with the measured values (red asterisks).

This analysis can be extended in the outflow direction as well. The electron momentum equation along the outflow direction at  $R = 37.5$  cm yields

$$E_Z \approx V_{eY}B_R - \frac{1}{en_e} \frac{\partial p_e}{\partial Z}. \quad (4.4)$$

As electrons flow out of the EDR with high  $V_{eY}$ , they create a further potential decrease along the outflow direction  $Z$ . The amount of the further potential decrease can be estimated by integrating Eqn. 4.4 along  $Z$ , which agrees with the measured values as shown in Fig. 4.2-(c). Due to the high mobility of electrons, the potential drop around the EDR is conveyed along magnetic field lines, creating a strong  $\mathbf{E}_{in}$  near the separatrices as shown in Fig. 4.2-(a).

In addition to estimating the structure of the potential well, we can also look at how it may vary with key parameters such as the plasma density  $n_e$  and the shoulder value of the reconnecting magnetic field  $B_{sh}$ . The radial potential well magnitude  $\Delta\Phi_p$  at  $Z = 0$  can be obtained by integrating Eqn. 4.2 as

$$\Delta\Phi_p = - \int dR E_R \approx \int dR \frac{1}{en_e} \left( J_Y B_Z - \frac{\partial p_e}{\partial R} \right) \approx \frac{B_{sh}^2}{2\mu_0 e \langle n_e \rangle} + \Delta T_e, \quad (4.5)$$

where  $\langle n_e \rangle$  is the average electron density over the current sheet, and  $\Delta T_e$  is difference in  $T_e$  between just outside of the current sheet and the center. Here, the  $n_e$  profile is assumed to have a weak radial dependence. This equation indicates that larger potential wells are expected in low density plasmas such as those found in the magnetotail [Wygant *et al.*, 2005].

The scaling in Eqn. 4.5 is verified experimentally by measuring the depth of the potential well in a series of discharges with different electron densities. In particular, the electron density at the current sheet center is varied by changing the He fill pressure and the PF waveform is adjusted to maintain the shoulder value of the reconnecting magnetic field at  $B_{sh} = 100$  G. As shown in Fig. 4.3,  $\Delta\Phi_p - \Delta T_e$  decreases as the electron density in the current sheet increases. The red dashed curve illustrates the expected magnitude from Eqn. 4.5.

From this scaling, the in-plane electric field is predicted to be much larger than the out-of-plane reconnection electric field. The maximum magnitude of  $\mathbf{E}_{in}$  can be computed by

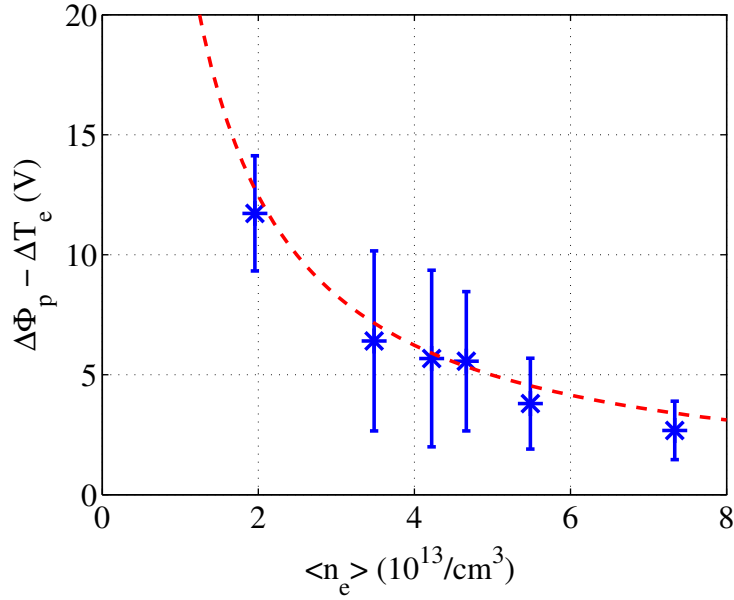


Figure 4.3: Dependence of the plasma potential well magnitude on the electron density and temperature at  $Z = 0$ . The red dashed line is the anticipated value of  $\Delta\Phi_p - \Delta T_e$  by Eqn. 4.5.

using Eqn. 4.5. After ignoring  $\Delta T_e$ , which is the contribution from the diamagnetic drift term, the maximum radial electric field  $E_{max}$  at  $Z = 0$  is given by

$$E_{max} \approx \frac{B_{sh}^2}{2\mu_0\delta_{CS}en_e} \approx 0.05 \frac{B_{sh}^2}{\sqrt{\mu_0 m_e n_e}}, \quad (4.6)$$

where the empirical current sheet width  $\delta_{CS} \approx 10\delta_e$  is used. Because the potential decrease at  $Z = 0$  is propagated along the separatrices due to the high parallel electric conductivity of electrons,  $E_{max}$  can represent the magnitude of  $\mathbf{E}_{in}$  at the separatrices. On the other hand, using the collisionless reconnection scaling  $E_{rec}/B_{rec} \sim 0.1V_A$ , the reconnection electric field can be estimated as

$$E_{rec} \approx 0.1V_A B_{rec} = 0.1 \frac{B_{rec}^2}{\sqrt{\mu_0 m_i n_e}}, \quad (4.7)$$

which indicates  $E_{rec}$  is smaller than  $|\mathbf{E}_{in}|$  by a factor of  $0.5\sqrt{m_i/m_e}$  and both scale as  $B^2/n^{1/2}$ . In space data, the reconnection electric field is indeed much smaller than the in-plane electric field [Mozer and Retinò, 2007].

In MRX discharges, the separation between two electric fields is not as large as in space. The average measured  $|\mathbf{E}_{in}|$  is about 700 V/m, while  $E_{rec}$  is about 200 V/m. First, due to the contributions from the external coil currents, the magnitude of the reconnecting magnetic field  $B_{rec}$  is about factor of two larger than the shoulder value  $B_{sh}$  far upstream where  $E_{rec}/B_{rec} \sim 0.1V_A$  is approximately valid.<sup>1</sup> The reconnection electric field far upstream is also slightly smaller than 200 V/m. Second, the contribution from  $\Delta T_e \approx 3$  eV in Eqn. 4.5 is not negligible in MRX due to the electron heating at the current sheet center. However, the in-plane electric field is still the dominant field around the separatrixes.

In summary, the measured in-plane potential profile has a well structure along the radial direction, which becomes deeper and wider downstream. The potential profile is governed by electron dynamics around the electron diffusion region. The sharp decrease of the potential near the separatrixes creates a large in-plane electric field ( $\sim 700$  V/m) there.

## 4.2 Ion Acceleration by the In-plane Electric Field

In this section, the impact of the in-plane electric field on ions flowing into the ion diffusion region is discussed. The strong Hall electric field ballistically accelerates ions near the separatrixes since the spatial scale of the Hall electric field ( $\sim 2$  cm) is smaller than the ion gyro-radius ( $\sim 5$  cm). Fig. 4.4 shows 2-D in-plane flow vectors measured by Mach probes along with contours of  $\Phi_p$ . Considerable changes in the ion flow occur near the separatrixes where ions are accelerated and turn into the outflow direction. It is worth noting that the radial stagnation point of the ion inflow is shifted to the inboard side ( $R < 37.5$ ), which

---

<sup>1</sup>As shown in Fig. 3.16, the vacuum field (linear) component in  $B_Z$  can be comparable to  $B_{sh}$  outside of the ion diffusion region. Thus, there is a subtlety in defining the reconnection rate and upstream Alfvén velocity in MRX discharges.

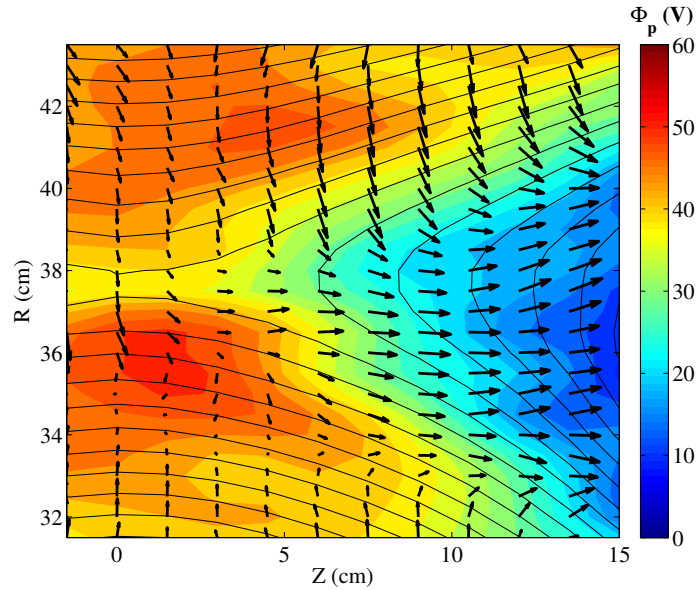


Figure 4.4: In-plane ion flow vectors along with contours of  $\Phi_p$  and  $\Psi$ . The flow vectors are measured every 1 cm along  $R$  and every 3 cm along  $Z$ . The maximum ion velocity is 16 km/s. As ions flow across the separatrices, they are accelerated by  $\mathbf{E}_{in}$  and turned into the outflow direction.

is caused by the upstream density asymmetry [Cassak and Shay, 2007]; the outboard side ( $R > 37.5$ ) has about 2–3 times larger density than the inboard side as shown in Fig. 4.5. The density asymmetry is caused by the in-plane inductive electric field from the time-varying TF currents in the earlier phases of the discharge.<sup>2</sup>

The above flow pattern of ions is significantly different from that of electrons. This difference is responsible for the in-plane current that produces the well-known quadrupole out-of-plane magnetic field profile [Ren *et al.*, 2008b]. Figure 4.6 shows a clear difference between in-plane flow profiles of electrons and ions, demonstrating the presence of two-fluid effects in MRX. The difference is more prominent in the inflow region as ions flow across magnetic field lines, while electrons approach the X point mostly along the magnetic field. Unmagnetized ions are affected directly by the Hall electric field that is mostly perpendicular to the magnetic field. On the other hand, the highly magnetized electrons remain bound to the field and continue inward toward the EDR. The parallel electron velocity

<sup>2</sup>Refer to Appendix B for more discussion

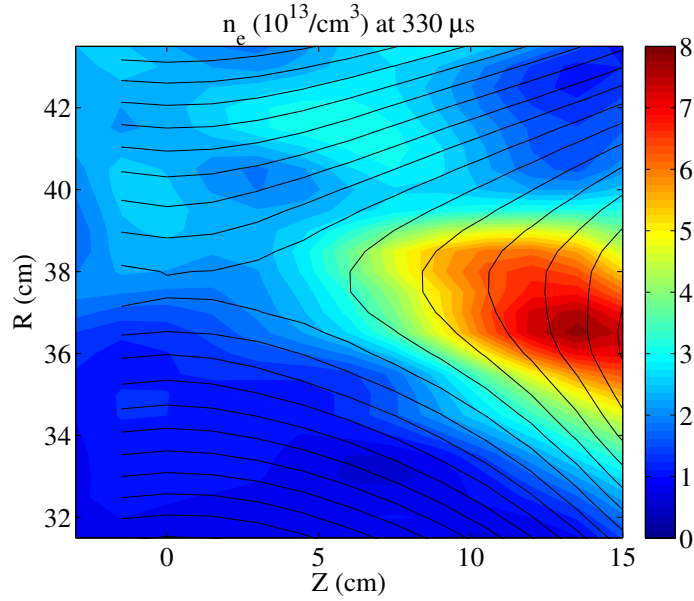


Figure 4.5: 2-D density profile at  $t = 330 \mu\text{s}$  measured by a triple Langmuir probe. A clear density difference between the inboard side and outboard side is shown. The upstream density is  $1\text{--}3 \times 10^{13} / \text{cm}^3$  and the downstream density reaches up to  $8 \times 10^{13} / \text{cm}^3$ .

is believed to be generated by parallel electric fields localized near the separatrices [Uzdensky and Kulsrud, 2006], which are difficult to measure because their magnitude ( $< 10 \text{ V/m}$ ) is expected to be smaller than the error in the electric field measurements.

The electron outflow profile is also different from that of ions. The bottom panel of Fig. 4.6 shows the  $Z$  profile of the outflow of each species. Electrons are quickly accelerated to about  $100 \text{ km/s}$  ( $\gtrsim 3V_A$ ) inside the electron diffusion region ( $Z \lesssim 5 \text{ cm}$ ). The electron outflow velocity  $V_{eZ}$  decreases as they re-attach to the magnetic field lines downstream. Ions, on the other hand, continue to be accelerated by  $\mathbf{E}_{in}$ , such that the outflow reaches about half of the Alfvén velocity. The outflow channel of ions is broader than that of electrons as shown in the right panel of Fig. 4.6. This two-scale outflow channel is one of the most important characteristics of collisionless reconnection, since the broader ion outflow channel facilitates fast reconnection.

The bulk flow energy of ions remains low despite the large potential drop across the separatrices. The maximum ion outflow of  $16 \text{ km/s}$  corresponds to  $5 \text{ eV}$  of energy per

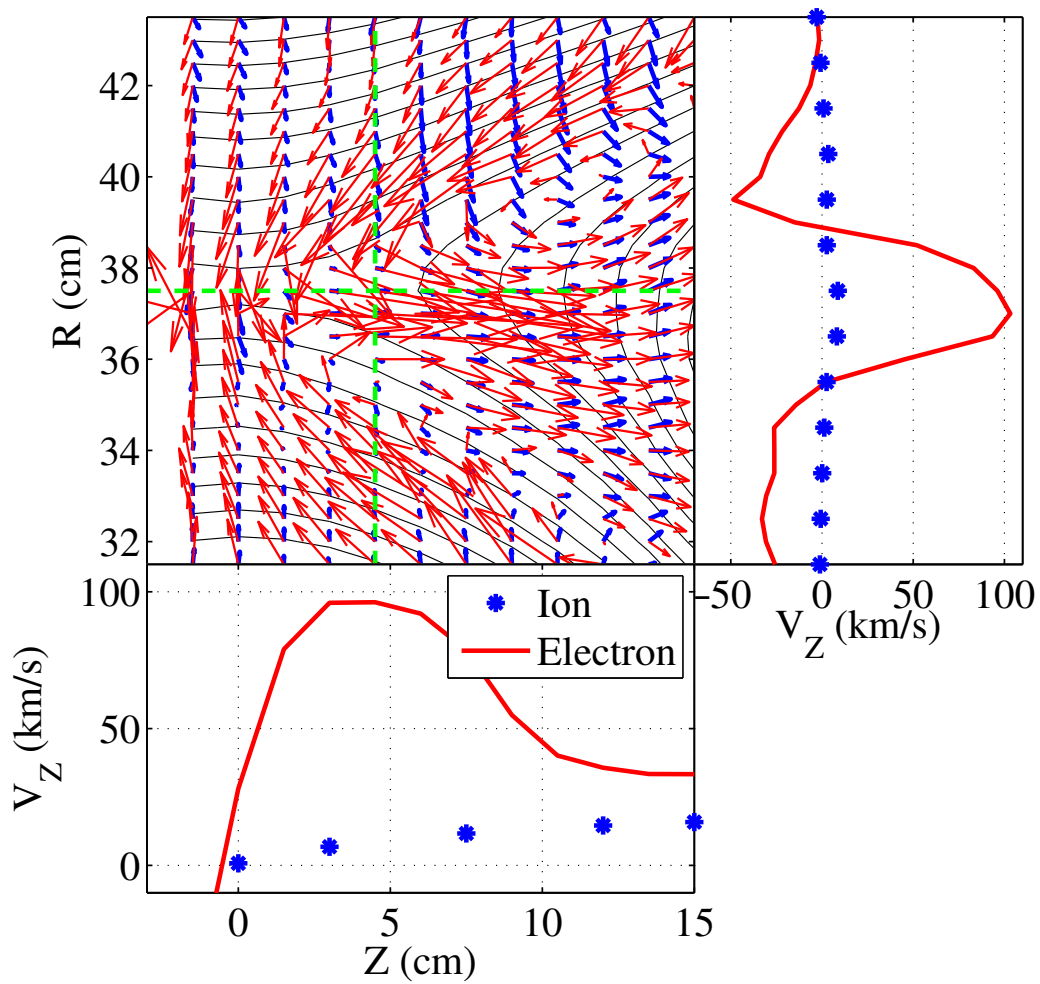


Figure 4.6: In-plane flow vectors of ions and electrons along with the poloidal flux  $\Phi$ . A clear difference between the in-plane flow profiles demonstrates two-fluid effects. The green dashed lines indicate the location of the 1-D profiles shown in the right and bottom panels. The bottom panel shows the  $Z$  profile of outflow velocities at  $R = 37.5$ . The right panel shows the radial profile of  $V_Z$  at  $Z = 4.5$  cm.

helium ion, which is much smaller than the magnitude of the potential decrease across the separatrices ( $\gtrsim 30$  V). The potential drop along the central axis of the outflow region is more than 20 V, which is enough to accelerate ions up to the Alfvén velocity. This indicates ions must lose considerable momentum as they pass through the downstream region.

One possible cause of the observed sub-Alfvénic ion outflow is the high downstream pressure. The measured downstream ion pressure is 2–4 times larger than the upstream pressure because of the high density and ion heating in the downstream region. Thus, ions must do work on the ambient plasma as they exit the reconnection layer, assuming that there are enough collisions. In this case, the amount of energy lost per ion due to the high downstream pressure per ion ranges from 10–20 eV, depending on the path of the ion. This momentum loss is related to the observed ion downstream heating that will be discussed in the following section 4.3.

Another possible cause of the sub-Alfvénic ion outflow is frictional drag by neutrals. The frictional force  $\mathbf{F}_{fric}$  can be expressed as

$$\mathbf{F}_{fric} = m_i \frac{\Delta \mathbf{V}_i}{\Delta t} \approx m_i \nu_{in} (\mathbf{V}_i - \mathbf{V}_n) \approx m_i \sigma_{in} \langle v_i \rangle n_n \mathbf{V}_i, \quad (4.8)$$

where  $\nu_{in}$  is the ion-neutral collision frequency,  $\mathbf{V}_n$  is the neutral velocity,  $\sigma_{in}$  is the cross section for ion-neutral collisions,  $\langle v_i \rangle$  is the average ion velocity, and  $n_n$  is neutral density. The cross section  $\sigma_{in}$  is dominated by the charge-exchange collision cross section, which is about  $2 \times 10^{-15}$  cm<sup>2</sup> for 3–20 eV ions [Janev *et al.*, 1987]. The quantity  $\langle v_i \rangle$  is the ion thermal velocity  $v_{i,th}$ , if  $v_{i,th}$  is larger than the flow velocity. Since  $V_{iZ} \gtrsim v_{i,th}$  after the ion outflow is fully developed,  $\langle v_i \rangle$  is taken as  $V_{iZ}$ . Due to the negligible neutral flow velocity measured by the IDSP,  $\mathbf{V}_n$  is ignored. To estimate the drag by neutrals, the local neutral density must be measured. IDSP measurements of the 477.1 nm He I line combined with a collisional-radiative model [McWhirter, 1965; Stotler, Post, and Reiter, 1993] reveal that the neutral density at  $Z = 0$  matches the initial fill density within  $\pm 50\%$  error bars

[Lawrence *et al.*, 2013]. Thus, the estimated local neutral density based on a 4.5 mT He fill pressure is  $1.4 \times 10^{14} / \text{cm}^3$ . Then, with the maximum ion outflow  $V_{iZ,max}$  of 16 km/s, the frictional force per ion  $F_{fric} \approx m_i \nu_{in} V_{iZ,max}$  is  $4.8 \times 10^{-17}$  N, which corresponds to the force from an electric field of 300 V/m. Note that this is comparable to the Hall electric field, such that the drag by neutrals may be a major reason for the observed sub-Alfvénic ion outflow.

To confirm this neutral effect, however, more precise measurements of the local neutral density in the downstream region are required. The downstream neutral density is expected to be smaller than the initial neutral density since both  $n_e$  and  $T_e$  are high enough to ionize most of the existing neutrals. On the other hand, the presence of the flux cores may increase the population of neutrals via the so-called “recycling” effect, meaning that ions interacting with the wall return to the bulk plasma as neutrals. Since the importance of drag by neutrals depends largely on the local neutral density, more research is needed to obtain a better understanding of the neutral effect.

For the final topic regarding ion acceleration, we can examine which of the electric field components are most responsible for the ion energy gain. As a result of the strong Hall electric field and ion acceleration near separatrices, ions obtain energy mostly from the Hall electric field, which agrees with recent simulation results [Pritchett, 2010; Goldman *et al.*, 2013]. Figure 4.7 shows the profile of the work done by the electric field on the ions per unit time and unit volume,  $\mathbf{J}_i \cdot \mathbf{E}$ . The work done by  $\mathbf{E}_{in}$  is localized downstream and strongest around the separatrices with values of about  $30 \text{ W/cm}^3$ . On the other hand, the work done by  $E_Y$  is fairly uniform over the measurement region, which is inside the ion diffusion region and has a smaller magnitude of about  $5 \text{ W/cm}^3$ . The uniform profile of  $J_{iY} E_Y$  is due to the relatively constant  $V_{iY}$  ( $\sim 7 \text{ km/s}$ ) and  $E_Y$  ( $\sim 200 \text{ V/m}$ ) profiles.

In summary, ions are ballistically accelerated up to about  $0.5V_A$  by the strong in-plane electric field near the separatrices. The sub-Alfvénic outflow is possibly caused by the high downstream ion pressure and frictional drag via ion-neutral collisions. Since the Hall

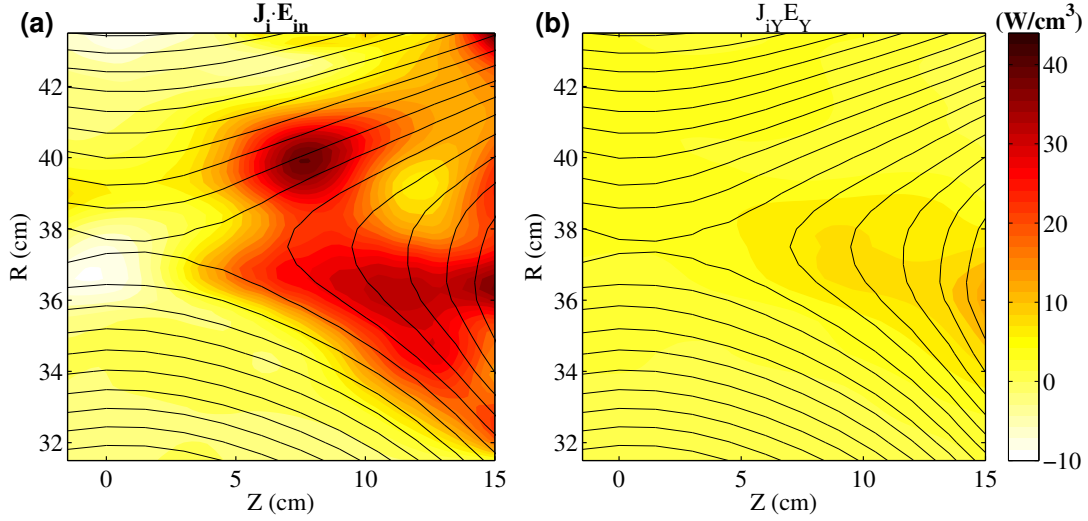


Figure 4.7: (a) Work done by the Hall electric field on ions per unit time unit volume ( $\mathbf{J}_i \cdot \mathbf{E}_{in}$ ). It is localized downstream and strongest around the separatrices. (b) Work done by the reconnection electric field ( $\mathbf{J}_Y \cdot \mathbf{E}_Y$ ) on ions per unit time and unit volume. It is relatively small and uniform over the measurement region.

electric field is larger than the reconnection electric field, ions gain energy mostly from the Hall electric field near the separatrices.

### 4.3 Downstream Ion Heating

Ion temperature is measured by the IDSPs described in Subsection 3.2.4. By varying the direction of the line-of-sight of the IDSP, ion temperatures along the  $R$ ,  $Y$ , and  $Z$  directions are separately measured to examine possible ion temperature anisotropy in the MRX plasma. Ion temperatures along each direction will be referred to as  $T_{iR}$ ,  $T_{iY}$ , and  $T_{iZ}$ , respectively. The average ion temperature  $T_i$  is defined as  $(T_{iR} + T_{iY} + T_{iZ})/3$ . The ability of the ICCD camera to record two images during a discharge is utilized to monitor the change in temperature profile during the quasi-steady pull reconnection phase. The first image is taken just before the quasi-steady period ( $t = 310 \mu\text{s}$ ), and the second image is obtained in the middle of the quasi-steady period ( $t = 330 \mu\text{s}$ ).

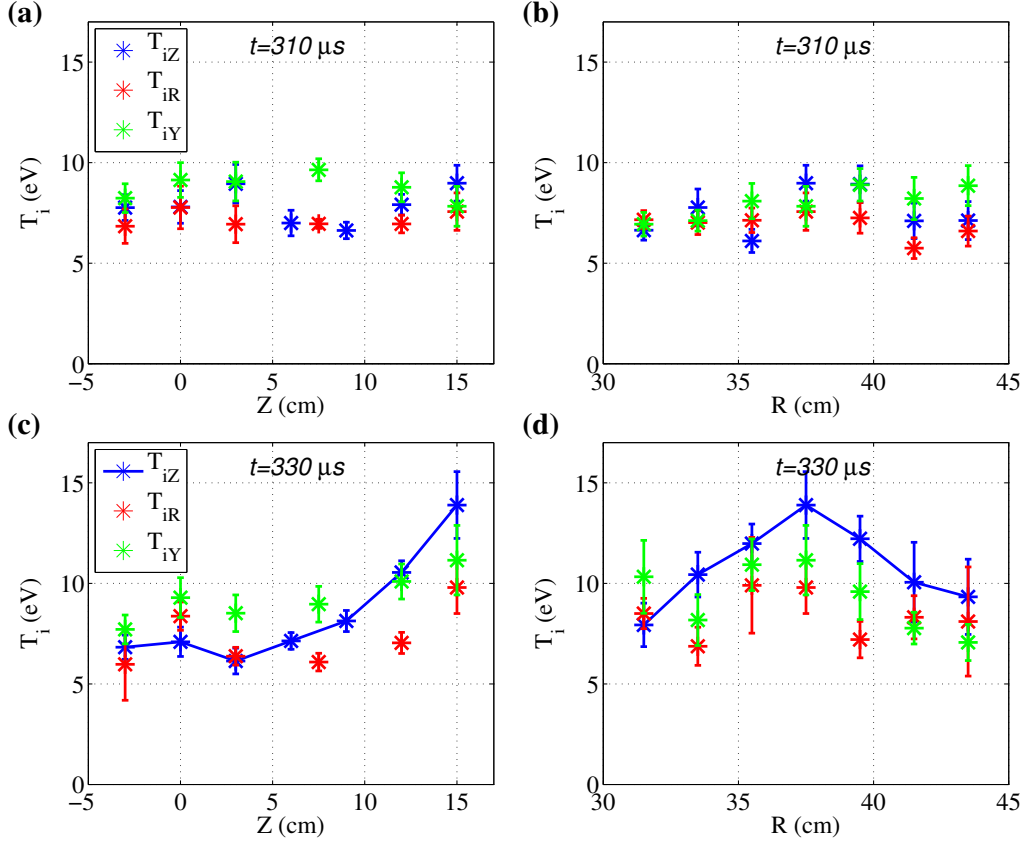


Figure 4.8: Measured ion temperature profiles. (a)/(c) Axial profile of each component of  $T_i$  at  $R = 37.5$  cm at  $t = 310$  and  $330 \mu s$ , respectively. (b)/(d) Radial profile of ion temperature at  $Z = 15$  cm at  $t = 310$  and  $330 \mu s$ , respectively. At  $t = 310 \mu s$ , the  $T_i$  profiles are relatively flat and no significant differences among  $T_{iR}$ ,  $T_{iY}$ , and  $T_{iZ}$  exist. At the later time, ions are heated downstream and  $T_{iZ}$  becomes hottest there.

Before the quasi-steady period, the ion temperature is fairly flat and no significant differences among  $T_{iR}$ ,  $T_{iY}$ , and  $T_{iZ}$  are observed. As shown in Fig. 4.8-(a) and (b), both the  $Z$  profile of the ion temperature at  $R = 37.5$  cm and the radial profile of  $T_i$  at  $Z = 15$  cm are relatively uniform. The value of ion temperature at this time is 7–9 eV over the entire 2-D measurement region ( $31.5 < R < 43.5$  and  $-3 < Z < 15$ ), and this value is considered to be the upstream ion temperature during the quasi-steady period as shown in Table 3.1.<sup>3</sup>

<sup>3</sup>The upstream ion temperature during the quasi-steady period was measured but the results are not reliable because of a low signal-to-noise ratio due to the low upstream electron temperature.

At the later measurement time of  $t = 330 \mu\text{s}$ , on the other hand, ion heating is observed downstream. As shown in Fig. 4.8-(c), the ion temperature starts to rise at  $Z = 9$  cm. The increase is most prominent in  $T_{iZ}$ , which peaks at  $Z = 15$  cm. The radial ion temperature profile at  $Z = 15$  cm in Fig. 4.8-(d) also shows clear downstream ion heating. All three components of the ion temperature peak at the radial center of the outflow region ( $R = 37.5$  cm). Since ion acceleration is weak in the region where ions are heated, these profiles suggest that energy from  $\mathbf{E}_{in}$  is primarily used to heat ions further downstream.

The observed downstream heating cannot be explained by classical viscous damping in the unmagnetized limit. First, the region where ions are heated does not match the area where classical viscous damping is strong. In the absence of a magnetic field, the heat generated by ion viscous damping,  $Q_{vis}^i = -\mathbb{T} : \nabla \mathbf{V}_i$ , is written in Braginskii, 1965 as

$$Q_{vis}^i = 0.96 n_i T_i \tau_i \mathbb{T} : \nabla \mathbf{V}_i, \quad (4.9)$$

where  $\tau_i$  is the ion collision time and  $\mathbb{T}$  is the rate-of-strain tensor. The collision time  $\tau_i$  is given by

$$\tau_i = \frac{3\sqrt{m_i} T_i^{3/2}}{4\sqrt{\pi} \lambda_{ii} e^4 Z_{eff}^4 n_i}, \quad (4.10)$$

where  $\lambda_{ii}$  is the Coulomb logarithm for ion-ion collisions. The strain tensor  $\mathbb{T}$  is

$$\mathbb{T} = \nabla \mathbf{V}_i + (\nabla \mathbf{V}_i)^T - \frac{2}{3} (\nabla \cdot \mathbf{V}_i) \mathbb{I}, \quad (4.11)$$

where  $(\nabla \mathbf{V}_i)^T$  is the transpose of the tensor  $\nabla \mathbf{V}_i$ . This equation implies that the viscous damping is strong where large velocity shear and/or acceleration exist. According to the measured velocity profiles, the viscous damping is actually strongest near the separatrices where ions are significantly accelerated.

Furthermore, ion heat conduction is too large to sustain the observed ion temperature

gradient. Without a magnetic field, the ion heat flux is

$$\mathbf{q}_i = -\chi^i \nabla T_i, \quad (4.12)$$

where  $\chi^i = 3.9n_i T_i \tau_i / m_i$  is the ion thermal conductivity. The average energy loss by the heat conduction term ( $\nabla \cdot \mathbf{q}_i$ ) in Eqn. 2.30 in the vicinity of  $(R, Z) = (37.5, 14)$  is estimated to be  $48 \pm 11 \text{ W/m}^3$ , which is an order of magnitude larger than the viscous heating power of  $3.7 \pm 0.8 \text{ W/m}^3$ . The sum of the compression ( $p_i \nabla \mathbf{V}_i$ ) and convection  $\nabla \cdot (u_i \mathbf{V}_i)$  terms is positive ( $14 \pm 3 \text{ W/m}^3$ ), indicating energy loss. The heat generated by ion-electron collisions,  $Q_i$ , is negligible due to a large ion-electron collision time on the order of  $100 \mu\text{s}$ . The local internal energy change is expected to be insignificant since the plasma is in a quasi-steady state condition. These results suggest that other heating mechanisms are responsible for the observed downstream ion heating.

One possible mechanism that can explain the observed downstream heating is the re-magnetization of the ions in the outflow region. In particular, the influence of the magnetic field increases away from the X point, especially further downstream ( $Z > 12 \text{ cm}$ ) where the magnetic field becomes strong enough to make the local ion gyro-radius smaller than the local inertial length of 5–6 cm. In this case, although the ions are not fully-magnetized since  $\nu_{ii} > f_{ci}$ , the ion gyro-motion can prolong the transit of the ions through the outflow region, significantly increasing the chance that ions are thermalized via collisions and/or scattered by wave-particle interactions.

Another effect of this re-magnetization process is that the frictional drag caused by the high density downstream plasma can be more effective. Since the downstream plasma density ( $5\text{--}8 \times 10^{13} / \text{cm}^3$ ) is higher than the upstream density ( $1\text{--}2.5 \times 10^{13} / \text{cm}^3$ ), the local ion mean free path is reduced from 6–12 to 2–5 cm. Furthermore, due to the magnetic field, ions cannot exit the downstream region along straight-line trajectories. Thus, as the ions travel further downstream, they lose energy to the ambient plasma through collisions—

a process that generates heat. This mechanism differs from the aforementioned classical viscous heating mechanism because this process instead results from a beam-plasma interaction.

To address the possible mechanisms for the observed downstream heating, 2-D fully kinetic simulations are performed using global boundary conditions directly relevant to the MRX geometry.<sup>4</sup> Actual experimental conditions such as the two flux cores and reconnection drive from the decreasing PF coil current are implemented in the particle-in-cell code, VPIC [Bowers *et al.*, 2008]. The coordinate system in the simulations is  $(x, y, z)$ , corresponding  $(R, Y, Z)$  in the MRX coordinate system. A detailed discussion on the boundary conditions can be found in Dorfman *et al.*, 2008. In addition, Coulomb collisions are modeled using the Takizuka-Abe particle-pairing algorithm [Takizuka and Abe, 1977]. More discussion on the collision operator implementation can be found in Daughton *et al.*, 2009a. The initial conditions for the simulations are matched to the experimentally measured parameters of ions. For example, the mass ratio  $m_i/m_e$  is set to 400 in the simulation by adjusting the electron mass.

Figure 4.9 shows 2-D profiles of the ion temperature when simulation reaches steady-state. In both simulations, ions are heated downstream regardless of the existence of collisions. However, the profile of heating in each case is very different, indicating that the heating mechanism is also different in each case.

In the simulation without collisions, the kinetic effects from the characteristic bounce motion of the ions inside the potential well [Drake *et al.*, 2009; Aunai, Belmont, and Smets, 2011b] is dominant. The biggest difference between the two profiles is that the simulation without collisions has a higher ion temperature around the X point. The radial potential well magnitude around the X point is about twice as large in the collisionless simulation due to a density depletion [Dorfman *et al.*, 2008]. The profile of the ion temperature along the normal direction  $T_{ix}$  depends on the magnitude of the potential well that is responsible

---

<sup>4</sup>Simulations are conducted by J. Jara-Almonte.

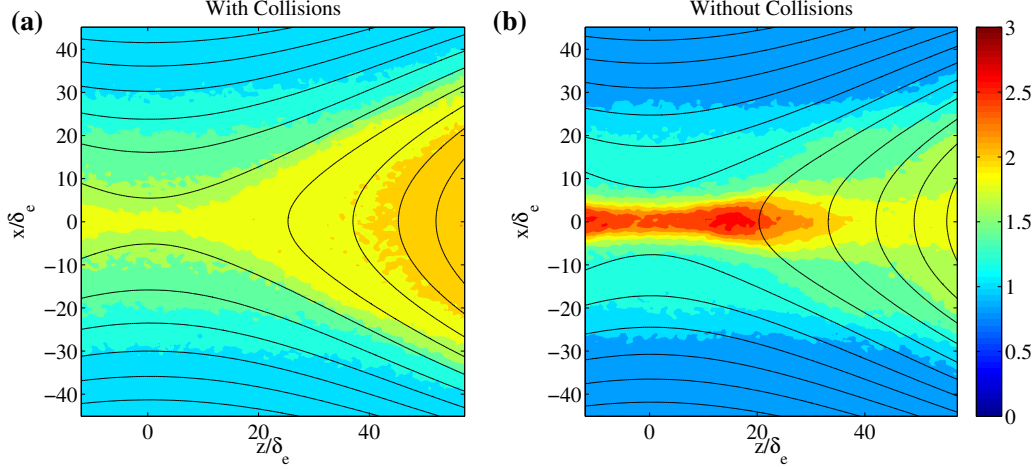


Figure 4.9: 2-D ion temperature profiles from simulations with the global boundary conditions relevant to the MRX geometry. (a) Results from a simulation with ion-ion collisions. Ions are heated downstream similar to the measured data. (b) Results from a simulation without collisions. The ion temperature is highest around the X-point due to the high  $T_{ix}$  originated from the counter-streaming beam structure.

for the counter-streaming ion beam structure [Wygant *et al.*, 2005; Aunai, Belmont, and Smets, 2011b]. With a larger potential well magnitude,  $T_{ix}$  is much higher in the collisionless simulation than in the simulation with collisions because the separation between counter-streaming beams is larger. In addition to this kinetic effect, there is heating by re-magnetization further downstream ( $z > 50\delta_e$ ) where  $T_{iz}$  increases as fast ions in the outflow interact the high magnetic field near the flux cores.

In the simulation with collisions, both re-magnetization and ion thermalization by collisions play an important role. Figure 4.10-(a) shows  $z$  profiles of each component of the ion temperature at  $x = 0$  (corresponding to  $R = 37.5$  cm). Profiles of  $T_{iy}$  and  $T_{iz}$  qualitatively agree with the experimentally measured profile shown in Fig. 4.8-(c).  $T_{iz}$  is lowest at the X-point and highest downstream.  $T_{iy}$  does not change as much as  $T_{iz}$ . The radial profiles at  $z = 57\delta_e$ , which corresponds to  $Z = 15$  cm, are shown in Fig. 4.10-(b). Similar to the experimental measurement, ions are heated inside the separatrices. Compared to the collisionless simulation, temperature anisotropy is significantly diminished further downstream due to collisions.

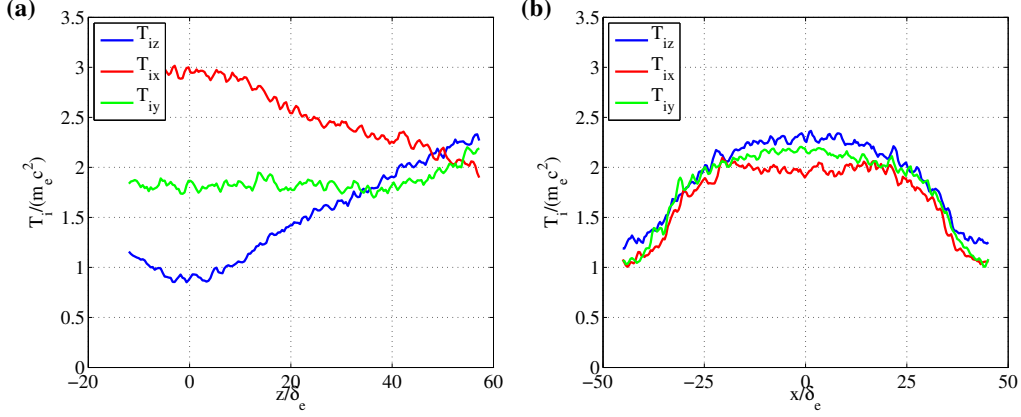


Figure 4.10: Profiles of each component of the ion temperature from the simulation with collisions. (a)  $z$  profile at  $x = 0$ , corresponding to  $R = 37.5$  cm.  $T_{iz}$  is lowest at  $z = 0$  but highest downstream due to the thermalization process. (b)  $x$  profile at  $Z = 57\delta_e$ , corresponding to  $Z = 15$  cm. Ions are heated inside the separatrices.

The high  $T_{ix}$  around the X-point in the simulation with collisions is also caused by the counter-streaming beams created by the bipolar normal electric field. The measured radial ion temperature  $T_{iR}$ , on the other hand, is not peaked at the X-point. In the experiments, the measured He II 4686 Å spectra at the X-point did not clearly show a counter-streaming beam structure. However, pressure balance indicates that the ion temperature along the normal direction  $T_{iR}$  should be peaked at the center. As shown in Fig. 4.11-(a), there is a dip in the sum of the magnetic pressure ( $p_m = B^2/2\mu_0$ ) and electron pressure ( $p_e = n_e T_e$ ). Thus, for pressure balance across the current sheet to be satisfied, the radial component of the ion pressure  $p_{i,RR}$  must be peaked at the center. The red line indicates the required  $p_{i,RR}$  profile when the upstream ion temperature is set to be 7 eV. Figure 4.11-(b) shows the expected  $T_{iR}$  derived profile from the pressure profile. There is about factor of three increase in  $T_{iR}$  at the current sheet center.

The computed radial force balance for ions also indicates the peaked profile of  $p_{i,RR}$ . Under the assumption of steady state, the radial component of the ion momentum equation (Eqn. 2.27) at  $Z = 0$  is

$$E_R + V_{iY} B_Z \approx \left( \frac{1}{en_i} \right) \frac{\partial p_{i,RR}}{\partial R}, \quad (4.13)$$

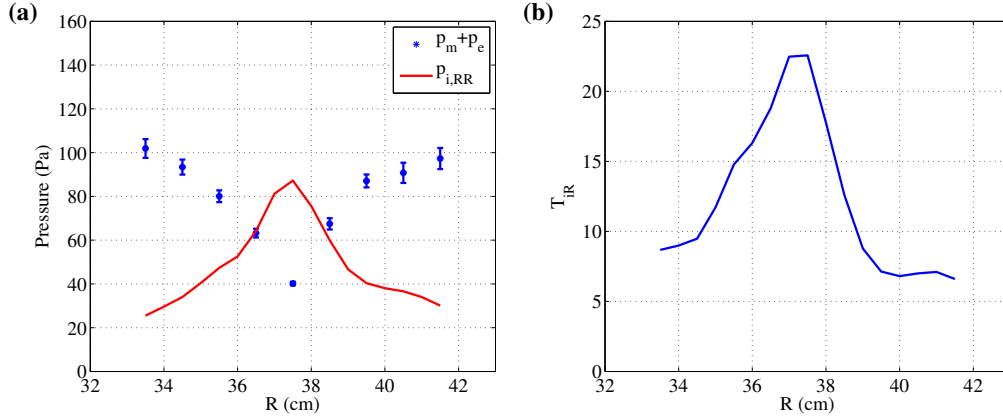


Figure 4.11: Anticipated ion pressure and temperature profiles from the pressure balance. (a) Blue asterisks - measured radial profile of the sum of  $p_m$  and  $p_e$ . It has a dip at the current sheet center. Red line - calculated radial component of the ion pressure  $p_{i,RR}$  when pressure balance across the current sheet is assumed. (b) Anticipated  $T_{iR}$  from the ion pressure profile shown in (a).  $T_{iR}$  sharply increases at the current sheet center, which is similar to simulations.

where second order terms from the toroidal geometry are ignored. Compared to the magnitude of  $E_R$ ,  $V_{iY}B_Z$  is small, especially inside the current sheet. Thus, the pressure gradient term must peak at the center to balance the bipolar electric field.

The discrepancy between the measured and anticipated  $T_{iR}$  profiles possibly results from limitations in the IDSP diagnostics. The spatial and temporal resolution of the IDSP is not enough to resolve the fine-scale ion temperature profile. The width of the peaked  $T_{iZ}$  profile is similar to the width of the current sheet of about 2 cm, but the IDSP resolution is 3 cm. The temporal resolution of the IDSP is  $5.6 \mu s$  (as set by the gate width of the ICCD camera), but the potential profile undergoes quick changes due to the inductive electric field from the time-varying TF current. Thus, improved diagnostics with better resolution such as an ion energy analyzer must be implemented to capture the peaked  $T_{iR}$  profile in the experiment.

Finally, the measured 2-D neutral temperature profiles are presented in Fig. 4.12. Due to excellent signal-to-noise ratio of the He I 4714 Å spectra, the error bars on the neutral temperature measurement are small ( $< 0.5$  eV). The neutral temperature is typically 2.5–4

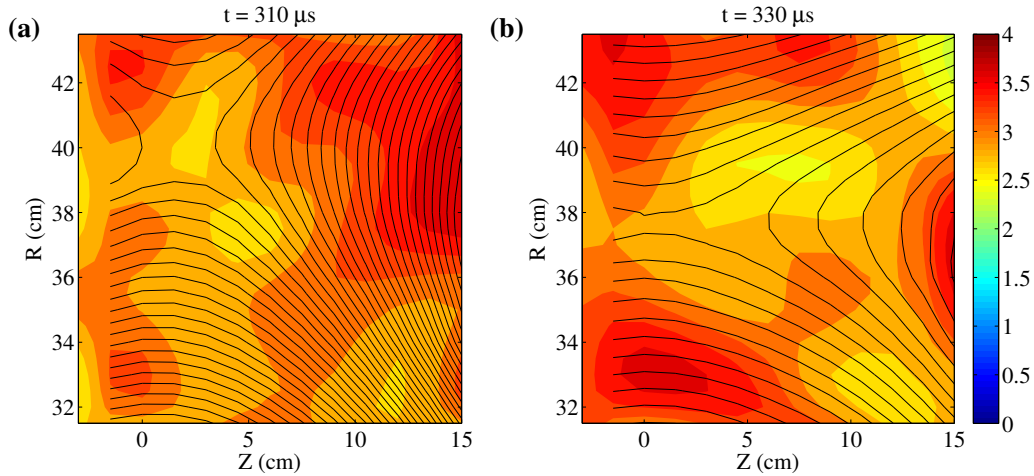


Figure 4.12: (a) 2-D profile of the helium neutral temperature before the quasi-steady period ( $t = 310 \mu s$ ). It is relatively uniform around 3 eV. (b) Same profile during the quasi-steady period ( $t = 330 \mu s$ ). The neutral temperature is low around the separatrices where electrons have higher temperature.

eV during the quasi-steady period. However, no strong neutral heating is observed during the quasi-steady period since the neutral temperature at  $t = 310 \mu s$  is similar. It is worth noting that the neutral temperature is lower near the separatrices at  $t = 330 \mu s$ . This region coincides with the region where strong electron heating is observed as presented in Fig. 5.1 of Chapter 5. A higher electron temperature can lead to the lower neutral density resulting in a weaker coupling between ions and neutrals that may result in a locally depressed neutral temperature.

These profiles indicate that ions may lose energy to neutrals throughout the discharge. However, the importance of neutrals in this regime is uncertain due to the lack of the precise neutral density measurement.

In summary, we observed downstream ion heating that cannot be explained by the classical viscous damping in the unmagnetized limit. A magnetic field effect called re-magnetization is important to explain the observed downstream heating. The magnetic field affects ion orbits, such that ions remain in the downstream region long enough to be

thermalized by collisions. A comparison between the experimental data and 2-D kinetic simulation results supports this picture of ion downstream thermalization.

# Chapter 5

## Electron Heating

Since both electric fields and currents are abundant in the diffusion region and electrons are the primary current carriers, electrons are expected to gain energy during reconnection. In the collisional regime where the resistivity term balances the reconnection electric field at the X-point ( $\eta J_Y \approx E_{rec}$ ), the energy conversion mechanism is simply classical Ohmic heating. However, in the collisionless regime, it is still unclear how electrons are heated and accelerated in the diffusion region.

The electron bulk flow energy gain in MRX is negligible regardless of whether the plasma is in the collisional or collisionless regime. The measured maximum electron outflow velocity during collisionless reconnection is only a few times larger than the Alfvén velocity, which is much slower than the outflow velocities obtained from 2-D numerical simulations [Ren *et al.*, 2008a].

The electron thermal energy gain in MRX, on the other hand, is significant even in the collisionless regime. The radial electron temperature profile at  $Z = 0$  peaks at the center of the current sheet and Ohmic dissipation based on the perpendicular Spitzer resistivity cannot explain the profile due to the large electron heat flux along the magnetic field [Ji *et al.*, 2004]. However, this estimation was based on a 1-D measurement that required assumptions about the upstream electron temperature profile.

In this chapter, the first 2-D measurement of the electron temperature profile in MRX is presented. The electron temperature sharply increases across the separatrices and peaks at the edge of the electron diffusion region. Both the flow and thermal energy transport equations are analyzed near the electron diffusion region where electrons gain the most energy during reconnection. The outgoing energy associated with the parallel electron heat flux is larger than the amount of classical Ohmic dissipation by about a factor of 4.5, and is comparable to the total electron energy gain from the electric field. This suggests that there are mechanisms that efficiently thermalize electrons inside the diffusion region. The low electron flow energy gain and the large outgoing heat flux can only be explained by anomalous resistivity.

## 5.1 2-D Electron Temperature Profile

Electrons are significantly heated during collisionless reconnection in MRX. Figure 5.1 shows the 2-D electron temperature profile measured by a triple Langmuir probe. The upstream electron temperature is 5–7 eV. Inside the separatrices, electrons are heated up to 11–12 eV. The electron temperature is highest just outside of the electron diffusion region ( $Z \approx 6$  cm). This profile suggests that heat is generated near the diffusion region and quickly transported along the magnetic field lines due to the high parallel thermal conductivity of electrons. The blue dashed box shows the region where the energy transport analysis is conducted later in this chapter.

Emission from the plasma captured by a fast camera<sup>1</sup> corresponds to the measured electron temperature profile. As shown in Fig. 5.2, the visible light intensity is enhanced inside the separatrices (downstream) by about a factor of four. The region inside the magenta box corresponds to the entire measurement region shown in Fig. 5.1. The bright downstream

---

<sup>1</sup>Vision Research Phantom V7.3 camera with 1  $\mu$ s exposure time.

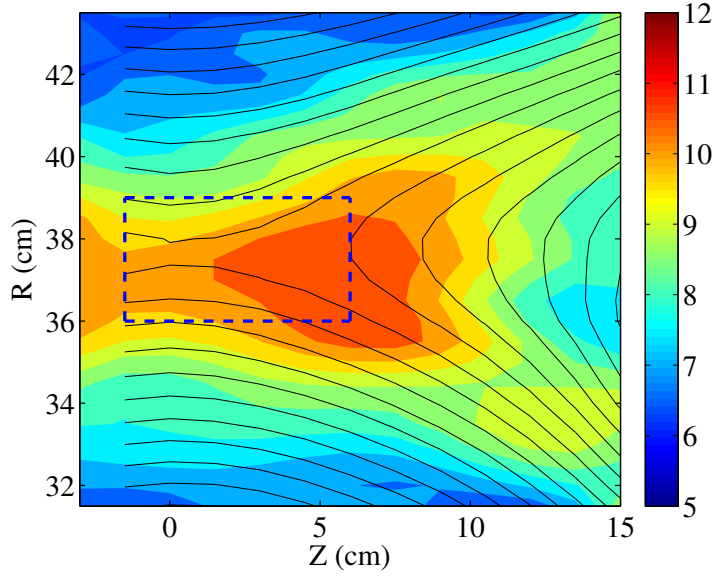


Figure 5.1: 2-D electron temperature profile measured by the triple Langmuir probe along with the contours of the poloidal flux  $\Psi$ . The upstream electron temperature is 5–7 eV, while the electron temperature inside the separatrices reaches up to 11–12 eV. The blue dashed box stands for the region where the energy transport analysis is applied later in this chapter.

region in the fast camera image coincides with the high downstream electron temperature profile measured by a triple Langmuir probe. Because the signal from the fast camera is dominated by helium neutral emission, this fast camera image is a strong indication of the high electron temperature inside the separatrices.

More quantitative analysis is required to confirm this argument. The neutral emission intensity depends on plasma parameters such as  $n_e$ ,  $T_e$ , and  $n_n$ , where  $n_n$  is the neutral density. Based on the collisional-radiative model [McWhirter, 1965; Stotler, Post, and Reiter, 1993], the total emitted power ( $P_{emi}$ ) from a He spectral line can be written as

$$P_{emi} = C_{n,emi}n_n + C_{p,emi}n_i, \quad (5.1)$$

where  $C_{n,emi}$  is the neutral emission coefficient and  $C_{p,emi}$  is the continuum emission coefficient. For MRX plasma parameters, the second term on the right-hand side is

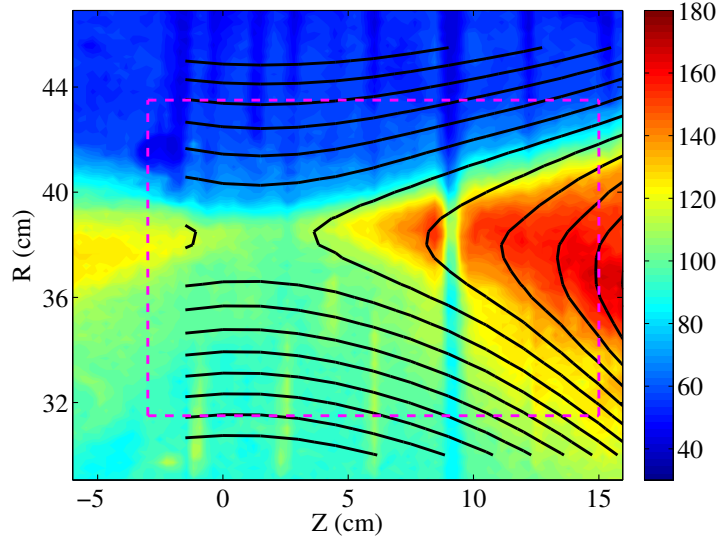


Figure 5.2: Fast camera image of the discharge 131596 at  $t = 328 \mu\text{s}$ . Contours of the measured poloidal magnetic flux  $\Psi$  are also shown. The dashed magenta box corresponds to the measurement region in Fig. 5.1. Shadows from the inserted probes appear in the image. This image indicates that  $T_e$  sharply increases across the separatrices.

negligible such that  $P_{emi} \approx C_{n,emi} n_n$ . The coefficient  $C_{n,emi}$  is a function of  $n_e$  and  $T_e$  and is available in the literature [e.g. Goto, 2003]. As shown in Fig. 5.3-(a),  $C_{n,emi}$  has a weak dependence on the electron density especially when  $n_e > 2 \times 10^{13} /\text{cm}^3$ . Thus, the sharp increase of the neutral emission across the separatrices cannot be explained by the high downstream electron density since the typical electron density in the outboard upstream region exceeds  $2.5 \times 10^{13} /\text{cm}^3$ . The dependence of  $C_{n,emi}$  on  $T_e$ , on the other hand, is strong especially in the electron temperature range of interest (5–15 eV). If the electron temperature increases from 7 to 12 eV and the neutral density profile does not considerably changes across the separatrices, the neutral emission is enhanced by about a factor of about three, which agrees with the fast camera image in Fig. 5.2.

The fast camera image implies that the electron temperature sharply increases across the separatrices. On the other hand, the 2-D  $T_e$  profile measured by the triple Langmuir probe does not show a strong temperature gradient perpendicular to the magnetic field at the separatrices. This is because the  $T_e$  profile is obtained from an extensive  $R$ - $Z$  scan

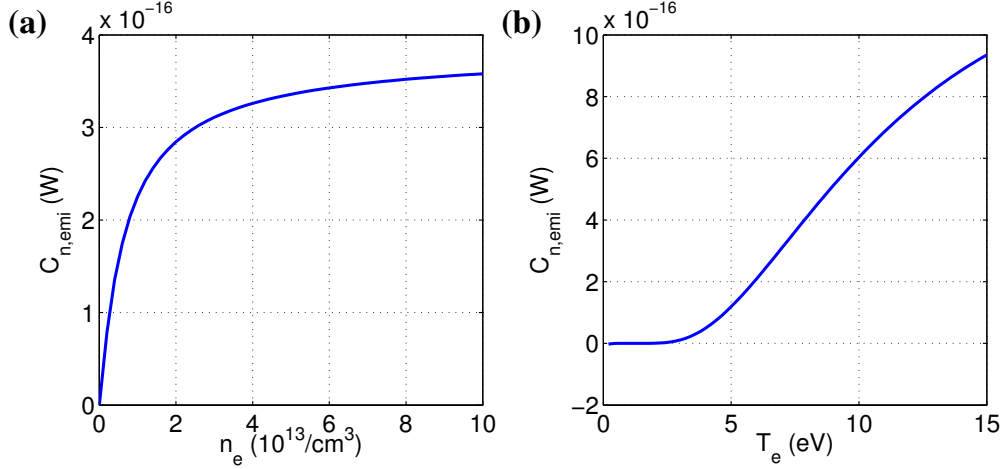


Figure 5.3: Neutral emission coefficient as function of electron density and temperature. (a)  $C_{n,emi}$  as a function of  $n_e$  when  $T_e = 7$  eV. It does not strongly depend on  $n_e$  when  $n_e > 2 \times 10^{13} /\text{cm}^3$ . (b)  $C_{n,emi}$  as a function of  $T_e$  when  $n_e = 3 \times 10^{13} /\text{cm}^3$ . It depends strongly on  $T_e$  when  $T_e > 5$  eV.

acquired over many discharges. Due to shot-to-shot variations and the coarse radial scan (every 1 cm), the sharp boundary is smoothed in the reconstructed 2-D profile, showing a more gradual increase of the electron temperature across the separatrices.

Another feature of the image is that the inboard side is brighter than the outboard side. There are two reasons for this asymmetry. First, the measured electron temperature on the inboard side is actually slightly higher, possibly due to better confinement. This is related to the radial density asymmetry discussed in Section 4.2. Before the quasi-steady period, the inboard side has higher magnetic field and lower electron density than the outboard side. The high magnetic field can contribute to electron confinement. The second reason is due to the toroidal geometry of MRX. The camera takes a 2-D projection of some fraction of the 3-D toroidal plasma. Since the emission from different toroidal planes overlaps on the inboard side, the measured intensity can be enhanced.

Both of the measurements suggest that there are efficient electron heating mechanisms active inside the separatrices. Another piece of evidence for the existence of effective heating mechanisms around the electron diffusion region is the negligible increase in the

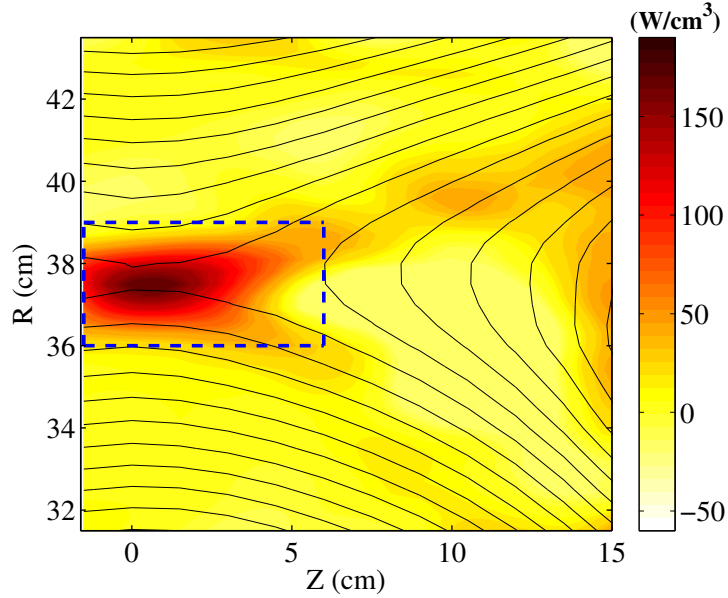


Figure 5.4: Work done by the electric field on electrons per unit time and unit volume ( $\mathbf{J}_e \cdot \mathbf{E}$ ). Unlike ions, electrons gain energy mostly from the reconnection electric field and it is localized near the X-point.

electron flow energy despite the considerable energy gain from the electric field, which is discussed in the following section.

## 5.2 Electron Energy Transport near the Diffusion Region

The symbols used here for quantities related to energy transport are summarized in Appendix C.

The electron energy gain from the electric field is locally high around the X-point. Figure 5.4 represents the 2-D profile of the work done by the electric field on the electrons per unit time and unit volume  $\mathbf{J}_e \cdot \mathbf{E}$  at  $t = 330 \mu\text{s}$ . Unlike ions that gain energy mostly from the Hall electric field over the broad downstream region, electrons obtain energy mostly from the reconnection electric field in a region that is localized near the X-point.

The energy gain inside the small blue dashed box in Fig. 5.4 accounts for about 70% of the total electron energy gain over the entire measurement region. By assuming toroidal symmetry, the electron energy gain from the electric field  $W_{gain}$  per unit time inside the volume of the plasma ( $\mathcal{V}_e$ ) marked by the blue dashed box in Fig. 5.1 and Fig. 5.4 can be calculated as

$$W_{gain} = \int_{\mathcal{V}_e} (\mathbf{J}_e \cdot \mathbf{E}) d^3x = \iint 2\pi R dR dZ (\mathbf{J}_e \cdot \mathbf{E}) = (3.4 \pm 0.3) \times 10^5 \text{ (W)}. \quad (5.2)$$

Compared to this energy gain, the flow energy gain ( $W_k$ ) per unit time inside  $\mathcal{V}_e$ , which can be expressed as

$$W_k = \int_{\mathcal{V}_e} \left[ \frac{\partial}{\partial t} \left( \frac{\rho_e}{2} V_e^2 \right) + \nabla \cdot \left( \frac{\rho_e}{2} V_e^2 \mathbf{V}_e \right) \right] d^3x = (1.8 \pm 0.4) \times 10^3 \text{ (W)}, \quad (5.3)$$

is negligible. The contribution from the first term inside the integrand is small ( $\sim 3\%$ ) as the plasma is in the quasi-steady period. This means that only 0.8% of the total electron energy gain is converted to bulk flow energy, which supports the assertion that there are efficient heating mechanisms around the electron diffusion region.

### Discussion on Minimal Increase in Flow Energy

Before possible electron heating mechanisms are discussed, it is worthwhile to examine possible reasons for the negligible bulk flow energy increase since it is related to micro-physical processes around the electron diffusion region that are responsible for breaking the magnetic field lines. The out-of-plane component of the generalized Ohm's law is written as

$$E_{rec} = -\frac{m_e}{e} \frac{dV_{eY}}{dt} - (\mathbf{V}_e \times \mathbf{B})_Y - \frac{\nabla \cdot \mathbb{p}_e}{en_e} + en_e \eta J_Y, \quad (5.4)$$

where  $\eta$  is the resistivity, which can be either the perpendicular Spitzer resistivity or anomalous resistivity. The negligible electron bulk flow energy gain corresponds to the insignificance of the electron inertia term. The  $\mathbf{V}_e \times \mathbf{B}$  Hall term is non-dissipative and becomes small inside the electron diffusion region. Thus, both the pressure tensor term and the resistivity term are possible candidates for explaining the minimal electron flow energy. The same conclusion is deduced by re-writing the flow energy transport equation for electrons (Eqn. 2.27) as:

$$\frac{\partial}{\partial t} \left( \frac{\rho_e}{2} V_e^2 \right) + \nabla \cdot \left( \frac{\rho_e}{2} V_e^2 \mathbf{V}_e \right) = \mathbf{J}_e \cdot \mathbf{E} + \mathbf{V}_e \cdot \mathbf{R}_e - \mathbf{V}_e \cdot (\nabla \cdot \mathbb{P}_e). \quad (5.5)$$

After integrating over  $\mathcal{V}_e$ , the equation can be written as

$$\int_{\mathcal{V}_e} [\mathbf{J}_e \cdot \mathbf{E} + \mathbf{V}_e \cdot \mathbf{R}_e - \mathbf{V}_e \cdot (\nabla \cdot \mathbb{P}_e)] d^3x \approx 0, \quad (5.6)$$

since the contribution from the left hand side of the Eqn. 5.5 is small. This equation also suggests two possibilities for the low flow energy increase: (1) the collisional drag; and (2) the contribution from the divergence of the electron pressure tensor.

The collisional drag term  $\mathbf{R}_e$  consists of two parts: the fictional force  $\mathbf{R}_u$  from the difference of the drift velocities ( $\mathbf{V}_e - \mathbf{V}_i$ ), and a thermal force  $\mathbf{R}_t$  from the electron temperature gradient [Braginskii, 1965]. Without considering anomalous resistivity, the frictional force is related the resistivity term as follows:

$$\mathbf{R}_u = en_e(\eta_{S\parallel} \mathbf{J}_{\parallel} + \eta_{S\perp} \mathbf{J}_{\perp}), \quad (5.7)$$

where  $\eta_{S\parallel}$  and  $\eta_{S\perp}$  are the parallel and perpendicular Spitzer resistivities, and  $\mathbf{J}_{\parallel}$  and  $\mathbf{J}_{\perp}$  are the parallel and perpendicular current density, respectively. For anti-parallel reconnection in MRX, the current around the X-point is mostly perpendicular to the magnetic field, such that the approximation  $\mathbf{R}_u \approx en_e \eta_{S\perp} \mathbf{J}$  is valid [Kuritsyn *et al.*, 2006]. The thermal force

$\mathbf{R}_t$  is

$$\mathbf{R}_t = -0.71n_e\hat{\mathbf{b}}(\hat{\mathbf{b}} \cdot \nabla T_e) - \frac{3n_e}{2\omega_{ce}\tau_e}(\hat{\mathbf{b}} \times \nabla T_e), \quad (5.8)$$

where  $\hat{\mathbf{b}} = \mathbf{B}/|\mathbf{B}|$  is the unit vector along the magnetic field and  $\tau_e$  is the electron collision time given by

$$\tau_e = \frac{3\sqrt{m_e}T_e^{3/2}}{4\sqrt{2\pi}\lambda_{ei}e^4Z_{eff}^2n_i}. \quad (5.9)$$

Here,  $\lambda_{ei}$  is the Coulomb logarithm for electron-ion collisions.  $\mathbf{R}_t$  is usually neglected in the collisional drag term calculation since the parallel electron temperature gradient is small due to the high electron conductivity and  $\omega_{ce}\tau_e \gg 1$ . For example, at  $(R, Z) = (37.5, 3)$ , the magnetic field is about 20 G and the temperature gradient across the magnetic field is about 0.2 eV/cm. With the density of  $2 \times 10^{13}$  /cm<sup>3</sup> and the current density of  $7.6 \times 10^5$  A/m<sup>2</sup>, the ratio between the  $Y$  component of  $\mathbf{R}_u$  and  $\mathbf{R}_t$  is

$$\frac{(\mathbf{R}_t)_Y}{(\mathbf{R}_u)_Y} \approx \frac{3en_e|\partial T_e/\partial Z|}{2m_e\omega_{ce}J_Y} = 0.063. \quad (5.10)$$

The  $Y$  component of  $\mathbf{R}_t$  is usually less than 10% of the resistivity term around the diffusion region. Thus, the collisional drag term can be approximated as  $\mathbf{R}_e \approx \mathbf{R}_u \approx en_e\eta_{S\perp}\mathbf{J}$ . Then, the work done by the collisional drag force  $\mathbf{V}_e \cdot \mathbf{R}_e$  becomes the well-known Ohmic dissipation term  $-\mathbf{V}_e \cdot \mathbf{R}_e = -\eta_{S\perp}en_e\mathbf{V}_e \cdot \mathbf{J} \approx \eta_{S\perp}J^2$ .

The Ohmic dissipation based on the perpendicular Spitzer resistivity cannot be the main reason for the low electron flow energy gain. As discussed in Section 3.3, the resistivity term accounts for only about 10% of the reconnection electric field at the X-point. The total energy of Ohmic dissipation inside the volume  $\mathcal{V}_e$  is

$$W_{Spitzer} = \int_{\mathcal{V}_e} \eta_{S\perp}J^2 d^3x = (5.9 \pm 1.2) \times 10^4 \text{ (W)}, \quad (5.11)$$

which is about 17% of  $W_{gain}$ . The reason why  $W_{Spitzer}$  is higher than the expected value of 10% of  $W_{gain}$  is that  $W_{gain}$  includes the electron energy loss to the Hall electric field

(mainly  $E_Z J_Z$ ), which becomes comparable to  $E_Y J_Y$  as the electron outflow velocity develops. This estimation shows that the collisional drag term cannot balance the total energy gain unless the so-called anomalous resistivity exists around the X-point due to high-frequency fluctuations.

The work done by the divergence of the electron pressure tensor  $\mathbf{V}_e \cdot (\nabla \cdot \mathbb{P}_e)$  is the other candidate for the low electron flow energy increase around the electron diffusion region. In many collisionless simulations, the electron pressure tensor term balances the reconnection electric field in the electron diffusion region ( $-(1/en_e)\nabla \cdot \mathbb{P}_e \approx E_{rec}$ ) [e.g. Hesse *et al.*, 1999; Li and Horiuchi, 2008]. In this case,  $\mathbf{V}_e \cdot (\nabla \cdot \mathbb{P}_e)$  can be comparable to  $\mathbf{J}_e \cdot \mathbf{E}$ .

It is extremely difficult to explore the role of the pressure tensor term directly through experimental measurements since it requires precise measurements of the electron distribution function. Instead, its contribution can be estimated by a model based on the second moment of the linearized Vlasov equation [Kuznetsova, Hesse, and Winske, 1998]. The contributions from the nongyrotropic (off-diagonal) pressure tensor terms to the reconnection electric field,  $E_Y^{NG}$  is

$$E_Y^{NG} \approx \frac{\sqrt{2m_e T_e}}{e} \frac{\partial V_{eZ}}{\partial Z}. \quad (5.12)$$

The same result can be derived by assuming that the width of the electron diffusion region is the same as the scale of the meandering electron orbits [Dorfman *et al.*, 2008]. With the measured  $T_e \sim 10$  eV and  $\partial V_{eZ}/\partial Z \sim 3 \times 10^6$  V/m,  $E_Y^{NG}$  is about 32 V/m, which is about the same as the contribution from the resistivity term ( $\sim 20$  V/m) and not enough to balance the reconnection electric field at the X-point ( $\sim 200$  V/m). The total work done by the pressure tensor term over the same volume of plasma is expected to be similar or less than the Ohmic dissipation term since this term is localized within the small electron diffusion region unlike Ohmic heating.

The contribution from the divergence of the electron pressure tensor is estimated to be much smaller in experiments than in the 2-D simulations. Dorfman *et al.*, 2008 pointed out that this discrepancy comes from the fact that the measured width of the electron

diffusion region is larger than the meandering orbit scale. However, there is as of yet no satisfactory physical explanations for this phenomenon. Even after including realistic Coulomb collisions, the width of the layer remains narrower than the measured value [Roytershteyn *et al.*, 2010]. The observed electromagnetic fluctuations propagating at the electron drift velocity near the X-point [Ji *et al.*, 2004] are also unlikely to resolve this issue, even though similar types of fluctuations are found in 3-D simulations [Roytershteyn *et al.*, 2013].

Thus, it is still unknown what balances the  $\mathbf{J}_e \cdot \mathbf{E}$  term in Eqn. 5.6. The collisional dissipation term ( $\mathbf{V}_e \cdot \mathbf{R}_e$ ) based on the perpendicular Spitzer resistivity accounts for about 20%. The work done by the pressure tensor term based on 2-D kinetic theory is estimated to be about the same as the collisional dissipation term. There are two possible candidates for this problem: (1) effects from 3-D structures such as flux ropes that are proven to be important under certain discharge conditions [Dorfman *et al.*, 2013]; and (2) anomalous resistivity inside the MRX electron diffusion region. Later in this chapter, there will be more discussion on which mechanism is supported by the measured electron temperature profile.

### Possible Electron Heating Mechanisms

Now, let us discuss possible electron heating mechanisms. The electron thermal energy transport equation (Eqn. 2.30) is given by

$$\frac{\partial u_e}{\partial t} + \nabla \cdot (u_e \mathbf{V}_e) = Q_e - p_e \nabla \cdot \mathbf{V}_e - \mathbb{T}_e : \nabla \mathbf{V}_e - \nabla \cdot \mathbf{q}_e. \quad (5.13)$$

The total internal energy gain per unit time inside  $\mathcal{V}_e$  is

$$W_u = \int_{\mathcal{V}_e} \left[ \frac{\partial u_e}{\partial t} + \nabla \cdot (u_e \mathbf{V}_e) \right] d^3x = (4.9 \pm 1.0) \times 10^4 \text{ (W)}. \quad (5.14)$$

The heat generated by collisions with other species  $Q_e$  can be approximately equal to the Ohmic dissipation ( $\eta J^2$ ) since the electron heat loss to ions is negligible due to the long ion-electron collision time ( $\gtrsim 100 \mu\text{s}$ ). Then, the amount of heat obtained by electrons via collisions with other species per unit time,  $W_{col}$  becomes

$$W_{col} \approx \int_{\mathcal{V}_e} \eta J^2 d^3x, \quad (5.15)$$

where the resistivity  $\eta$  can be either the perpendicular Spitzer value or be anomalous. The second term on the right hand side of Eqn. 5.13 is the compressional heating term. The total amount of compressional electron heating power inside the plasma volume,  $W_{comp}$  is

$$W_{comp} = - \int_{\mathcal{V}_e} p_e \nabla \cdot \mathbf{V}_e d^3x = (3.9 \pm 0.8) \times 10^4 (W). \quad (5.16)$$

The next term is the viscous heating term. Since this term is related to the anisotropic part of the electron pressure tensor  $\mathbb{\pi}$ , direct measurement is very difficult. Thus, in order to analyze this term, results in Braginskii, 1965 are used. Although the required condition of a strong magnetic field ( $\omega_{ce}\tau_e \gg 1$ ) is violated in the vicinity of the X-point where  $|\mathbf{B}| < 10$  G, that region is tiny compared to the region over which the volume integral is conducted. Neglecting terms of order  $(\omega_{ce}\tau_e)^{-2}$ , the heat generated by viscosity per unit time and unit volume is given by

$$Q_{vis} = -\mathbb{\pi}_e : \nabla \mathbf{V}_e \approx 0.24 n_e T_e \tau_e \left[ \nabla \cdot \mathbf{V}_e - \hat{\mathbf{b}} \cdot \nabla (\hat{\mathbf{b}} \cdot \mathbf{V}_e) \right]^2. \quad (5.17)$$

With this approximation, the total electron heating per unit time by viscosity,  $W_{vis}$  is

$$W_{vis} = \int_{\mathcal{V}_e} Q_{vis} d^3x = (4.3 \pm 0.9) \times 10^4 (W). \quad (5.18)$$

The final term on the right hand side of Eqn. 5.13 ( $\nabla \cdot \mathbf{q}_e$ ) stands for energy loss by microscopic heat flux. The electron heat flux  $\mathbf{q}_e$  also requires precise information on the electron distribution function. Thus, the heat flux is estimated using results in Braginskii, 1965. Similar to the collisional drag  $\mathbf{R}_e$ ,  $\mathbf{q}_e$  consists of two parts: (1) heat flux due to the relative velocity between electrons and ions,  $\mathbf{q}_u$ ; and (2) heat flux due to the electron temperature gradient,  $\mathbf{q}_t$ . The quantity  $\mathbf{q}_u$  is given by

$$\mathbf{q}_u = \frac{0.71T_e}{e} \mathbf{J}_{\parallel} + \frac{3}{2} \frac{T_e}{e\omega_{ce}\tau_e} \hat{\mathbf{b}} \times \mathbf{J}. \quad (5.19)$$

The second term on the right hand side can be ignored because  $\omega_{ce}\tau_e \gtrsim 50$  is satisfied at the boundary for the volume integral and only the heat flux at the boundary is required due to the divergence theorem.  $\mathbf{q}_t$  is

$$\mathbf{q}_t = -\chi_{\parallel}^e \hat{\mathbf{b}} (\hat{\mathbf{b}} \cdot \nabla T_e) - 0.79 \frac{\chi_{\parallel}^e}{\omega_{ce}\tau_e} \hat{\mathbf{b}} \times \nabla T_e, \quad (5.20)$$

where  $\chi_{\parallel}^e = 3.16n_e T_e \tau_e / m_e$  is the parallel thermal conductivity. Here, the heat flux due to the perpendicular thermal conductivity ( $\chi_{\perp}^e$ ) is ignored, which is smaller than  $\chi_{\parallel}^e$  by  $\mathcal{O}[(\omega_{ce}\tau_e)^2]$ . The second term on the right hand side can be also neglected for the same reason.

The heat flux is dominated by  $\mathbf{q}_t$  inside the volume of the plasma discussed so far due to the high parallel thermal conductivity. A typical value of the thermal conductivity there is  $\sim 1 \times 10^6$  (W/m·eV). Even with the typical measured value of the electron temperature gradient along the magnetic field of 0.1 eV/cm, the  $R$  and  $Z$  components of  $\mathbf{q}_t$  become much larger than those of  $\mathbf{q}_u$ . The out-of-plane component does not contribute to the heat flux since  $\partial/\partial Y = 0$ . Therefore,  $\mathbf{q}_e$  can be approximated as

$$\mathbf{q}_e \approx \chi_{\parallel}^e \hat{\mathbf{b}} (\hat{\mathbf{b}} \cdot \nabla T_e). \quad (5.21)$$

With this approximation, the total amount of heat loss inside the plasma volume per unit time,  $W_{loss}$  is

$$W_{loss} = \iint 2\pi R dR dZ \nabla \cdot \mathbf{q}_e = (3.0 \pm 1.0) \times 10^5 \text{ (W)}, \quad (5.22)$$

which is larger than other heating terms and comparable to the total energy gain  $W_{gain}$  in Eqn. 5.2. The error bar for the electron heat flux is high because it is sensitive to the electron temperature profile due to the high parallel conductivity and the electron temperature has error bars of about 1 eV. Although the measurement error is high,  $W_{loss}$  is convincingly higher than the integration of any of the other terms in Eqn. 5.13.

Although it is not definite due to large measurement errors, this massive electron heat flux supports the existence of anomalous resistivity around the X-point. Applying the volume integral to Eqn. 5.13 yields

$$W_u = W_{col} + W_{comp} + W_{vis} - W_{loss}. \quad (5.23)$$

If  $W_{col}$  is  $W_{Spitzer} = 5.9 \times 10^4 \text{ (W)}$ , this equation is not satisfied due to the large energy loss by the heat flux  $W_{loss}$ . The value of  $W_{col}$  estimated from the above equation is  $2.7 \times 10^5 \text{ (W)}$ , which is about 4.5 times larger than  $W_{Spitzer}$ .

This value is large enough to balance the flow energy transport equation (Eqn. 5.5). Rewriting Eqn. 5.6 yields

$$W_{gain} \approx W_{res} + W_{pe}, \quad (5.24)$$

where  $W_{res} = - \iint 2\pi R dR dZ (\mathbf{V}_e \cdot \mathbf{R}_e) \approx W_{col}$ , and  $W_{pe} = \iint 2\pi R dR dZ \mathbf{V}_e \cdot (\nabla \cdot \mathbb{p}_e)$ . With  $W_{res} = 2.7 \times 10^5 \text{ (W)}$ ,  $W_{pe}$  is about  $0.7 \times 10^5 \text{ (W)}$ , which agrees with the estimate based on Eqn. 5.12. The most important difference between  $W_{pe}$  and  $W_{res}$  is that  $W_{pe}$  cannot contribute to the electron thermal energy transport. Thus, to balance both Eqn. 5.23 and Eqn. 5.24, the Ohmic dissipation must be larger than the value based on the Spitzer

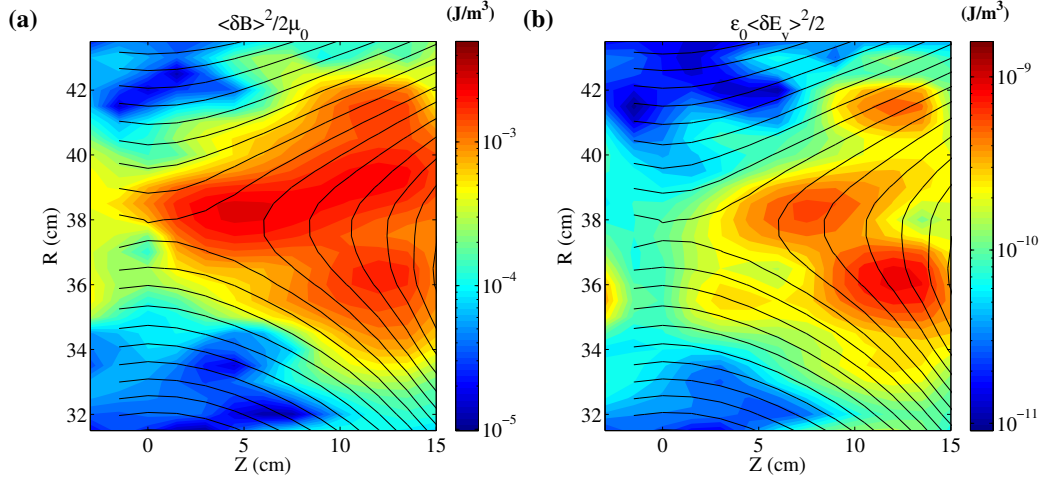


Figure 5.5: 2-D profiles of energy in high-frequency (1–10 MHz) fluctuations along with the contours of the poloidal flux  $\Psi$ . (a) Energy in high-frequency *magnetic* fluctuations. The fluctuation energy peaks at the edge of the electron diffusion region where the current density is highest. (b) Energy in high-frequency *electrostatic* fluctuations along the out-of-plane direction ( $\delta E_Y$ ). Similar to the magnetic fluctuations, fluctuation energy is large downstream.

resistivity, implying the presence of anomalous resistivity.

As a possible candidate for anomalous resistivity, high-frequency magnetic and electrostatic fluctuations are measured by the fluctuation probe described in Subsection 3.2.5. Figure 5.5-(a) shows the 2-D profile of energy in magnetic fluctuations of 1–10 MHz. Although the wave energy is small because the typical fluctuation amplitude is  $\sim 5$  G, the 2-D profile clearly shows that the fluctuation energy is higher inside the separatrices. It does not peak at the X-point but rather at the end of the electron diffusion region where the current density is highest. Similar to magnetic fluctuations, energy in the out-of-plane component of the electrostatic fluctuations increases downstream and does not peak at the X-point. A typical amplitude for the electrostatic fluctuations is  $\sim 100$  V/m. These profiles indicate that high-frequency fluctuations may contribute to the electron thermalization. As electrons move out of the electron diffusion region, they can be effectively thermalized due to these high-frequency fluctuations in the lower hybrid frequency range.

Further research is required to identify non-classical electron heating mechanisms near

the electron diffusion region. More quantitative analyses are required to confirm possible contributions from the observed fluctuations in the lower hybrid frequency range to the electron heating. Non-linear interactions between different waves can also heat electrons near the X-point [Wang, 2008]. There can be other types of fluctuations with higher frequencies, which are not currently measured in MRX but have been observed in space [e.g. Vaivads *et al.*, 2006] and in laboratory [Fox *et al.*, 2010]. High-frequency fluctuations close to  $f_{pe}$  may also explain the discrepancy between experiments and simulations since current simulations with  $f_{pe}/f_{ce} \sim 1$  are not suitable to fluctuations in the plasma with  $f_{pe}/f_{ce} \gg 1$ , which is satisfied in the MRX plasma. The dynamics of fine-scale 3-D structures such as flux ropes can contribute to the non-classical heating through coalescence of the flux ropes.

In summary, non-classical electron heating around the electron diffusion region is observed. The energy loss due to the parallel electron heat flux is larger than the classical Ohmic dissipation by about factor of 4.5. Analyses on the energy inventory around the electron diffusion region supports that anomalous resistivity is responsible for the observed electron heating.

## Chapter 6

# Energy Inventory During Collisionless Reconnection in MRX

Magnetic reconnection is known for the ability to efficiently convert magnetic energy to particle energy. In collisional reconnection, most of the incoming magnetic energy is expected to be converted to particle energy as predicted by the Sweet-Parker model.<sup>1</sup> On the other hand, there is no theory on the energy conversion efficiency of collisionless reconnection. This is one of the most fundamental problems remaining in the reconnection community since the importance of magnetic reconnection results from its ability to quickly dissipate magnetic energy.

For quantitative discussions on the energy conversion rate, information on the energy conversion efficiency is essential since the energy conversion rate depends on both the efficiency and the reconnection rate. (Here, the conversion efficiency means the ratio between the dissipated magnetic energy and the incoming magnetic energy.) In particular, the energy conversion efficiency of collisionless reconnection is expected to be reduced from the collisional case. The reason for the lower conversion efficiency is that the magnetic geometry changes from a Y-shape diffusion region to an X-line magnetic geometry

---

<sup>1</sup>See Section 2.2 for detailed discussions.

as collisionality decreases [Yamada, 2007]. While the X-line geometry facilitates fast reconnection by allowing a wider ion outflow channel, it also implies that the outgoing Poynting flux is significant unlike in a Y-shaped diffusion region, thereby decreasing the energy conversion efficiency. Moreover, there is additional outgoing Poynting flux associated with the Hall fields—the quadrupole magnetic field and the in-plane electric field (they are called the Hall fields to emphasize the fact that they are originated from the two-fluid dynamics). Unless the conversion efficiency decreases significantly, however, the overall conversion rate of collisionless reconnection should still be higher since the reconnection rate of collisionless reconnection is much faster.

Despite the importance of the conversion efficiency, few studies have been conducted on the energy inventory during collisionless reconnection. The energy inventory concerns how much of the incoming magnetic energy is converted to different forms of outgoing energy. The contributions to the energy budget between ion thermal and bulk flow energy in collisionless reconnection have been recently studied by Aunai, Belmont, and Smets, 2011a via hybrid numerical simulations where ions are treated as macro-particles and electrons are considered as a finite mass fluid. They found that there was no equipartition such that the ion thermal energy gain was dominant over ion flow energy. Due to the limitations of the hybrid model, neither electron energy gain nor the efficiency of energy conversion were discussed. Thus, more complete discussions on the energy inventory are necessary.

In this chapter, based on the measured 2-D profiles of various physical quantities, the energy inventory during collisionless reconnection in MRX is discussed. We find that more than half of the incoming magnetic energy is converted into particle energy during reconnection. The Poynting flux associated with the Hall fields accounts for more than half of the total outgoing Poynting flux. The ion thermal energy gain is larger than the ion flow energy increase, and the electron thermal energy gain is comparable to that of the ion thermal energy while the electron flow energy remains negligible. Both the outgoing

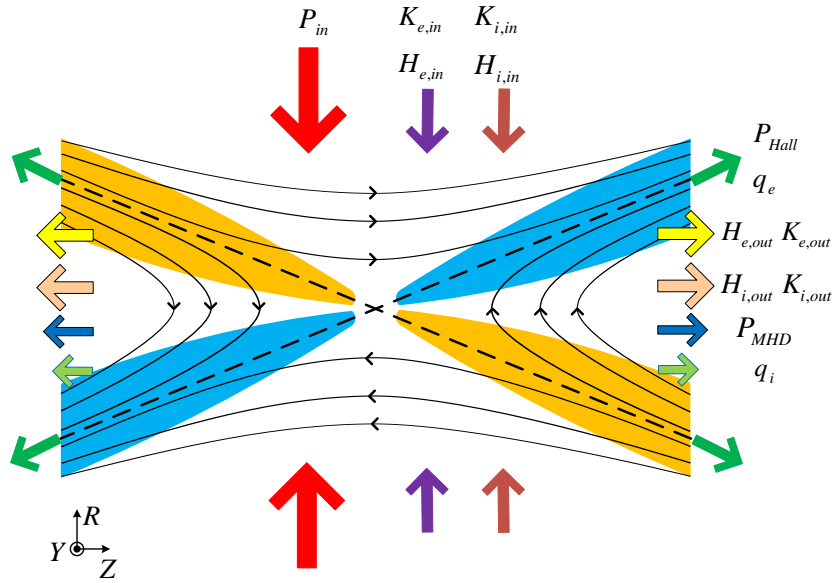


Figure 6.1: Schematic of energy fluxes in the collisionless reconnection layer. The size of arrows is proportional to the amount of the flux. The net change in Poynting flux indicates energy conversion from magnetic energy to particle energy.

ion and electron heat fluxes are estimated to be significant. Analysis of the ion energy inventory indicates significant energy transport from ions to neutrals.

## 6.1 Description of Method

The symbols used here for quantities related to energy transport are summarized in Appendix C.

The change in a certain form of energy inside a volume of plasma can be calculated by analyzing the corresponding energy fluxes through the boundary of that volume. Assuming that the system is in steady state, the energy must be converted to other forms of energy if the outgoing flux is smaller than the incoming flux and vice versa. For example,

the efficiency of magnetic reconnection in the conversion of magnetic energy can be estimated by measuring the Poynting flux at each surface on the boundary of the diffusion region. The energy inventory of the other forms of energy (e.g. flow and thermal) can be also obtained by measuring corresponding fluxes at the boundary surfaces.

Figure 6.1 demonstrates the energy conversion process during collisionless reconnection by showing the relevant energy fluxes. The large incoming Poynting flux ( $\mathbf{P}_{in} = (E_Y B_Z / \mu_0) \hat{e}_R$ , where  $\hat{e}_R$  is the unit vector along the  $R$  direction) is reduced to two smaller outgoing Poynting fluxes:  $\mathbf{P}_{Hall}$  and  $\mathbf{P}_{MHD}$ . The flux  $\mathbf{P}_{Hall}$  is the outgoing Poynting flux associated with the Hall fields that can be written as

$$\mathbf{P}_{Hall} = \frac{1}{\mu_0} (-E_Z B_Y \hat{e}_R + E_R B_Y \hat{e}_Z), \quad (6.1)$$

where  $\hat{e}_Z$  is the unit vector along  $Z$  direction. The MHD part of the outgoing flux is the conventional flux related to the normal magnetic field and reconnection electric field, that is

$$\mathbf{P}_{MHD} = -\frac{E_Y B_R}{\mu_0} \hat{e}_Z. \quad (6.2)$$

Other fluxes such as the incoming flow energy ( $\mathbf{K}_{in}$ ) and enthalpy ( $\mathbf{H}_{in}$ ) fluxes are defined similarly. The incoming fluxes related to particle energy are smaller than the outgoing fluxes,  $\mathbf{K}_{out}$  and  $\mathbf{H}_{out}$ , indicating particle energy gain. There are also net heat fluxes ( $\mathbf{q}_e$  and  $\mathbf{q}_i$ ) due to particle heating in the diffusion region.

The volume of plasma where the energy inventory analysis is conducted is defined in Fig. 6.2 by the magenta dashed lines. Since energy conversion occurs throughout the ion diffusion region, the boundary should cover the whole ion diffusion region. Due to limitations in the measurements, only half of the reconnection plane is selected and symmetry along the  $Z$  direction is assumed. The area is selected such that 2-D profiles of all of the

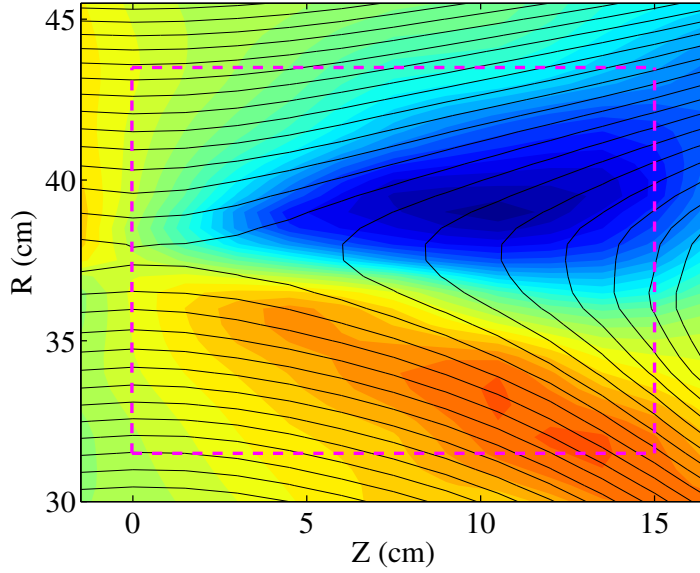


Figure 6.2: Boundary of the surface where the energy inventory analysis is conducted. The magenta dashed lines specify the volume of plasma for the analysis. The 2-D profile shown here is the out-of-plane quadrupole magnetic field along with the contours of the poloidal flux  $\Psi$ .

desired quantities are available.<sup>2</sup> Although this area does not cover the whole reconnection layer, it includes the important regions where strong energy conversion occurs. Toroidal symmetry is assumed along the out-of-plane direction.

With this boundary, the amount of energy flowing into or out of the specified volume ( $\mathcal{V}_b$ ) can be calculated. For example, the total incoming magnetic energy per unit time  $W_{P,in}$  is given by

$$W_{P,in} = - \oint_{S_b} \mathbf{P}_{in} \cdot d\mathbf{a} = \frac{2\pi}{\mu_0} \int_{Z_1}^{Z_2} dZ [R_1 E_Y(R_1, Z) B_Z(R_1, Z) - R_2 E_Y(R_2, Z) B_Z(R_2, Z)], \quad (6.3)$$

<sup>2</sup>The coverage of all probes with which  $R$ - $Z$  scans are performed is different from that of the 2-D magnetic probe array.

where  $(R_1, Z_1) = (31.5, 0)$  and  $(R_2, Z_2) = (43.5, 15)$  correspond to the boundary specified in Fig. 6.2. The outgoing magnetic energy per unit time is again separated into two parts:

$$W_{P,MHD} = \oint_{S_b} \mathbf{P}_{MHD} \cdot d\mathbf{a}, \quad (6.4)$$

$$W_{P,Hall} = \oint_{S_b} \mathbf{P}_{Hall} \cdot d\mathbf{a}. \quad (6.5)$$

Then, the magnetic energy dissipated in  $\mathcal{V}_b$  per unit time is  $-\Delta W_P = W_{P,in} - W_{P,MHD} - W_{P,Hall}$  when the plasma is in steady state. Here, the minus sign is attached to emphasize it is dissipated energy. However, there is a subtlety with respect to the quasi-steady period in MRX. The reconnection rate is nearly steady, but the plasma quantities are slowly changing. For example, due to the decreasing PF current, the vacuum component of the magnetic field is decreasing during the quasi-steady period. Thus, the total magnetic energy in  $\mathcal{V}_b$  is also decreasing, which is not negligible due to the large volume over which the integral is conducted. The total magnetic energy change in  $\mathcal{V}_b$ ,  $W'_P$  is

$$W'_P = \frac{d}{dt} \int_{\mathcal{V}_b} \frac{B^2}{2\mu_0} d^3x. \quad (6.6)$$

After considering this term, the total dissipated magnetic energy in  $\mathcal{V}_b$  per unit time becomes

$$-\Delta W_P = -W'_P + W_{P,in} - W_{P,MHD} - W_{P,Hall} \quad (6.7)$$

Changes in other forms of energy can be obtained similarly. The flow energy change is straightforward. The electron and ion flow energy gains per unit time are

$$\Delta W_{Ke} = \frac{d}{dt} \int_{\mathcal{V}_b} \frac{\rho_e}{2} V_e^2 d^3x + \int_{S_b} \mathbf{K}_e \cdot d\mathbf{a} = W'_{Ke} - W_{Ke,in} + W_{Ke,out}, \quad (6.8)$$

$$\Delta W_{Ki} = \frac{d}{dt} \int_{\mathcal{V}_b} \frac{\rho_i}{2} V_i^2 d^3x + \int_{S_b} \mathbf{K}_i \cdot d\mathbf{a} = W'_{Ki} - W_{Ki,in} + W_{Ki,out}. \quad (6.9)$$

The thermal energy part is more complicated due to the additional  $p\mathbf{V}$  term in the definition of the enthalpy flux. The change in the internal energy  $u = (3/2)p$  should be defined as  $\Delta W_u = \frac{d}{dt} \int_{\mathcal{V}_b} u d^3x + \int_{\mathcal{S}_b} (u\mathbf{V}) \cdot d\mathbf{a}$ . However, it is a convention to consider the enthalpy flux ( $\mathbf{H} = u\mathbf{V} + p\mathbf{V} = (5/2)p\mathbf{V}$ ) as the thermal energy flux. The additional  $p\mathbf{V}$  term originates from the work done by the pressure ( $\nabla p \cdot \mathbf{V}$ ) and the compressional heating power ( $p\nabla \cdot \mathbf{V}$ ). Thus, the electron and ion thermal energy gains per unit time are defined as

$$\Delta W_{He} = \frac{d}{dt} \int_{\mathcal{V}_b} u_e d^3x + \int_{\mathcal{S}_b} \mathbf{H}_e \cdot d\mathbf{a} = W'_{Ue} - W_{He,in} + W_{He,out}, \quad (6.10)$$

$$\Delta W_{Hi} = \frac{d}{dt} \int_{\mathcal{V}_b} u_i d^3x + \int_{\mathcal{S}_b} \mathbf{H}_i \cdot d\mathbf{a} = W'_{Ui} - W_{Hi,in} + W_{Hi,out}. \quad (6.11)$$

The energy losses per unit time due to electron and ion heat fluxes are

$$W_{qe} = \int_{\mathcal{S}_b} \mathbf{q}_e \cdot d\mathbf{a}, \quad (6.12)$$

$$W_{qi} = \int_{\mathcal{S}_b} \mathbf{q}_i \cdot d\mathbf{a}. \quad (6.13)$$

There is an additional flux ( $\mathbb{w}_e \cdot \mathbf{V}_e$ ) related to the anisotropic part of the tensor, as shown in Eqn. 2.31. This flux is ignored since both electron and ion distribution functions are expected to be nearly isotropic at the boundary, which is far away from the X-point.

Another important quantity is the work done by the electric field. The total energy gain of each species in  $\mathcal{V}_b$  per unit time is given by

$$W_e = \int_{\mathcal{V}_b} \mathbf{J}_e \cdot \mathbf{E} d^3x. \quad (6.14)$$

$$W_i = \int_{\mathcal{V}_b} \mathbf{J}_i \cdot \mathbf{E} d^3x. \quad (6.15)$$

From the Eqn. 2.10, the relation among  $\Delta W_P$ ,  $W_e$ , and  $W_i$  is

$$\Delta W_P + W_e + W_i = 0. \quad (6.16)$$

Since the heat exchange between electrons and ions is negligible, the relation between the above quantities can be obtained via energy conservation. By adding Eqn. 2.29 and 2.30, the total energy transport equation for species  $s$  can be written as

$$\frac{\partial}{\partial t} \left( u_s + \frac{\rho_s}{2} V_s^2 \right) + \nabla \cdot (\mathbf{H}_s + \mathbf{K}_s + \mathbf{q}_s + \mathbb{T}_s \cdot \mathbf{V}_s) = \mathbf{J}_s \cdot \mathbf{E}. \quad (6.17)$$

Integrating the above equation over  $\mathcal{V}_b$  yields

$$\Delta W_{Ke} + \Delta W_{He} + W_{qe} = W_e, \quad (6.18)$$

$$\Delta W_{Ki} + \Delta W_{Hi} + W_{qi} = W_i. \quad (6.19)$$

These relations should be satisfied unless there are other sources and sinks of energy such as ion energy loss to neutrals and impurity radiation.

## 6.2 Energy Inventory During Collisionless Reconnection in MRX

Table 6.1: Energy inventory during collisionless reconnection in MRX. All quantities are normalized to the incoming magnetic energy per unit time  $W_{P,in} = 1.9 \pm 0.2$  MW.

Magnetic Energy		Electron Energy		Ion Energy	
$W_{P,in}$	1.00	$W_e$	$0.20 \pm 0.04$	$W_i$	$0.36 \pm 0.07$
$W_{P,MHD}$	$0.23 \pm 0.02$	$\Delta W_{Ke}$	$(1.0 \pm 0.2) \times 10^{-4}$	$\Delta W_{Ki}$	$0.039 \pm 0.008$
$W_{P,Hall}$	$0.27 \pm 0.03$	$\Delta W_{He}$	$0.10 \pm 0.02$	$\Delta W_{Hi}$	$0.12 \pm 0.02$
$W'_P$	$-0.10 \pm 0.01$	$\Delta W_{qe}$	$0.14 \pm 0.07$	$\Delta W_{qi}$	$< (0.11 \pm 0.03)$

Using the measured 2-D profiles of required physical quantities, the contributions to the energy inventory during collisionless reconnection in MRX are estimated. Table 6.1 summarizes the results. Throughout this section, all quantities are normalized to the incoming magnetic energy per unit time  $W_{P,in} = 1.9$  MW. The total magnetic energy dissipated in  $\mathcal{V}_b$  per unit time is  $-\Delta W_P = -W'_P + W_{P,in} - W_{P,MHD} - W_{P,Hall} = 0.60W_{P,in}$ . The total electron energy gain per unit time,  $W_e$ , is 0.20, which is 33% of the dissipated magnetic energy per unit time,  $-\Delta W_P$ . The ion energy gain per unit time,  $W_i$ , is 0.36 and is larger than that of electrons by about a factor of two. The conservation law from the Poynting theorem (Eqn. 6.16) is satisfied within error bars such that  $\Delta W_P + W_e + W_i \approx 0$ .

The outgoing Poynting flux is not negligible in collisionless reconnection in MRX. In particular, the outgoing energy associated with the Hall fields,  $W_{P,Hall}$  exceeds  $W_{P,MHD}$ . Although the Hall fields are localized near the separatrices, the magnitude of  $\mathbf{P}_{Hall}$  is large due to the strong Hall electric field. The large Poynting flux associated with the Hall fields is an important characteristic of collisionless reconnection and is considered a signature of Whistler dynamics that facilitate fast reconnection [Drake, Shay, and Swisdak, 2008].

As summarized in Table 6.1, the ions obtain more energy than the electrons, although the electrons are the primary current carriers. This efficient energy transfer to ions results from the strong Hall electric field. As shown in Fig. 4.7, ion energy gain occurs over the broad downstream region where the strong Hall field exists. On the other hand, electron energy gain is localized around the X-point as shown in Fig. 5.4. Magnetized electrons do not easily obtain energy from the electric field except in the electron diffusion region where they are de-magnetized. This is because if they are magnetized, their motion is mostly determined by the  $\mathbf{E} \times \mathbf{B}$  drift, such that the energy transfer becomes inefficient unless there are parallel electric fields.

Electrons play an important role in ion energy conversion by establishing the Hall electric field. As discussed in Section 4.1, the Hall electric field is a result of the electron momentum balance; the Lorentz force due to electrons accelerated near the electron diffu-

sion region is responsible for the charge separation that creates the electrostatic Hall electric field.

For electrons, the thermal energy increase and the energy loss due to parallel heat conduction are dominant, while their flow energy remains negligible. The terms in Eqn. 6.9 are  $W'_{U_e} = -0.074 \pm 0.015$ ,  $W_{He,in} = 0.25 \pm 0.05$ , and  $W_{He,out} = 0.42 \pm 0.08$ , respectively. The change in the electron thermal energy enclosed in the volume  $\mathcal{V}_b$  is not negligible because the overall plasma density decreases during the quasi-steady period. Both the incoming and outgoing electron flow energy are negligible. The energy loss due to the electron heat conduction is larger than the electron thermal energy gain, but the error bars are large because the electron heat flux is extremely sensitive to the electron temperature gradient along the magnetic field and errors in the Langmuir probe measurement are not negligible (see Section 5.2). Finally, the electron energy conversion in Eqn 6.18 holds within the measurement error such that  $\Delta W_{Ke} + \Delta W_{He} + W_{qe} \approx W_e$ .

The ion thermal energy gain is measured to be about three times larger than the flow energy increase. Unlike with electrons, the ion flow energy increase per unit time is not negligible; it accounts for more than 10% of the total ion energy gain per unit time,  $W_i$ . The terms in Eqn. 6.8 are  $W'_{Ki} = -0.010 \pm 0.002$ ,  $W_{Ki,in} = 0.015 \pm 0.003$ , and  $W_{Ki,out} = 0.064 \pm 0.013$  MW, respectively. The three terms related to  $\Delta W_{Hi}$  are  $W'_{Ui} = -0.084 \pm 0.017$ ,  $W_{Hi,in} = 0.12 \pm 0.02$ , and  $W_{Hi,out} = 0.32 \pm 0.06$ . The ion temperature is assumed to be steady when  $W'_{Ui}$  is computed, since continuous ion temperature measurements are not available. This assumption is valid since the decrease of the internal energy is dominated by a decrease in the plasma density, which is verified by calculating  $W'_{U_e}$  with constant  $T_e$ ; the two results agree to within the measurement error.

The energy loss per unit time due to ion heat conduction is estimated to be significant but not enough to balance the total ion energy inventory, which suggests ions may lose energy to neutrals via charge-exchange collisions. The ion heat flux is calculated by Eqn. 4.12, which does not include effects from the magnetic field. Thus, this is the upper limit of

the ion heat flux because the magnetic field helps with energy confinement. Even though the ion energy loss per unit time by heat flux accounts for about 30% of  $W_i$ , Eqn. 6.19 does not balance as  $\Delta W_{Ki} + \Delta W_{Hi} + W_{qi} = 0.27 < W_i = 0.36$ . The missing part of energy is possibly explained by energy loss to neutrals. Since neutrals are not affected by the magnetic field, they can travel out of the reconnection layer with high energy after charge-exchange collisions. However, for quantitative discussions, more information on the neutral density profile is required.

Finally, the energy loss by impurity radiation is estimated to be insignificant compared to the electron energy gain. Based on the spectroscopy measurements, oxygen has the highest radiation and its radiation is significant only in the downstream region where  $T_e > 10$  eV. The radiation power is given by

$$W_{rad} \approx \int_{V_b} R(T_e) n_e n_o d^3x, \quad (6.20)$$

where  $R(T_e)$  is the specific radiation power coefficient and  $n_o$  is the oxygen impurity density. The coefficient  $R(T_e)$  is a strong function of  $T_e$  around 10 eV. Using the results in Morozov, Baronova, and Senichenkov, 2007 for  $R(T_e)$ , the oxygen radiation power is estimated to be  $\sim (1.0 \times 10^6) \langle n_o/n_e \rangle$ , where  $\langle n_o/n_e \rangle$  is the average oxygen concentration. With 5% of the average concentration, it accounts for about 13% of the total electron energy gain per unit time ( $W_e$ ). The oxygen impurity density calculated from the base pressure ( $< 2 \times 10^{-6}$  Torr) is smaller than  $6 \times 10^{10} / \text{cm}^3$ , which is much less than 1% of the downstream electron density. Although the local impurity density near the flux cores can be higher than this average value, the impurity population is expected to be less than 5%. Therefore, the contribution of impurity radiation to the energy inventory is not significant.

In summary, collisionless reconnection in MRX converts more than half of the incoming magnetic energy to particle energy. The outgoing Poynting flux associated with the Hall fields is comparable to the conventional outgoing Poynting flux. The Hall electric field also

contributes to this fast energy conversion, as ions gain energy mostly from the field. Both the electron and ion energy gains are dominated by thermal energy increase. Energy losses by heat fluxes are significant and the energy inventory for ions indicates a possible energy loss to neutrals.

# Chapter 7

## Conclusions and Future Work

Energy conversion from magnetic to particle energy during collisionless reconnection has been investigated experimentally in the Magnetic Reconnection Experiment. By utilizing various diagnostics including a 2-D magnetic probe array, a multiple-tip floating potential probe, a high-frequency fluctuation probe, Langmuir probes, Mach probes, and ion dynamics spectroscopy probes, 2-D profiles of various physical quantities are obtained. The measured profiles are used to identify energy conversion mechanisms and to estimate the energy inventory during collisionless reconnection. The results of this research are expected to have a broad impact on the reconnection community, since they not only verify recent results from numerical simulations and space observations but they also present many new and interesting challenges.

### 7.1 Conclusions

Experimental studies on energy conversion during collisionless reconnection in MRX lead to the following three central conclusions:

1. The in-plane electrostatic field plays a major role in ion acceleration and heating. It accelerates ions near the separatrices and provides energy for the observed downstream ion heating.
2. Electrons are heated non-classically around the electron diffusion region. Energy from the reconnection electric field is quickly dissipated near the electron diffusion region and classical Ohmic dissipation does not account for the large observed electron heat flux, indicating the presence of anomalous resistivity.
3. Collisionless reconnection in MRX efficiently converts magnetic energy to particle energy. More than half of the incoming magnetic energy is dissipated in the diffusion region.

Each of the above main conclusions is described in detail in the following subsections.

## 7.1.1 Ion Heating and Acceleration

### 1. Electron dynamics determine the in-plane potential profile

The measured in-plane electrostatic profile shows a saddle-shaped structure that becomes wider and deeper along the outflow direction. By examining the electron force balance equation, it is proven that the in-plane electric field balances the Lorentz force from the electron flow accelerated by the reconnection electric field near the electron diffusion region. The potential drop around the electron diffusion region is conveyed along the magnetic field lines, creating a strong in-plane electric field near the separatrices and generating the wider potential well downstream. This saddle-shaped in-plane profile agrees with recent numerical simulations [e.g. Karimabadi, Daughton, and Scudder, 2007; Drake, Shay, and Swisdak, 2008; Pritchett, 2010] and space observations [e.g. Mozer, Bale, and Phan, 2002; Wygant *et al.*, 2005]. The radial potential well magnitude is derived from the electron momentum equation, which scales as  $B_{rec}^2 / \langle n_e \rangle$ . This scaling agrees with measurements from discharges with different average density,  $\langle n_e \rangle$ .

## **2. Ions are accelerated by the strong Hall electric field near the separatrices**

Since the Hall electric field is large ( $\sim 700$  V/m) and has a spatial scale less than the ion gyro-radius, ions are immediately accelerated toward the outflow direction near the separatrices. The maximum outflow speed is about the half of the Alfvén velocity. This outflow velocity is smaller than the anticipated value from the potential drop across the separatrices of about 30 V, which is enough to accelerate ions to the Alfvén velocity.

The sub-Alfvénic ion velocity is possibly caused by two reasons: high downstream pressure and frictional drag by neutrals. Since the measured downstream ion pressure is higher than the upstream pressure by about a factor of three, ions will lose momentum to the ambient plasma if there are enough collisions. This momentum loss is closely related to the observed downstream ion heating. Frictional drag by neutrals via charge-exchange collisions can also result in ion momentum loss. For quantitative discussions, however, precise measurements of the neutral density are required since the importance of this mechanism depends largely on the local neutral density.

## **3. Ions are heated downstream by re-magnetization and collisions**

Downstream ion heating is observed that cannot be explained by classical viscous damping in the unmagnetized limit. The mechanism is identified as the re-magnetization of ions. As ion orbits are affected by the downstream magnetic field, ions stay longer in the diffusion region, which promotes ion thermalization via collisions and possibly scattering by wave-particle interactions. Without considering effects from the magnetic field, the ions undergo only a few collisions before they move out of the diffusion region. Initial results from numerical simulations with global boundary conditions similar to MRX support the assertion that ion thermalization via re-magnetization is an important mechanism.

## 7.1.2 Electron Heating

### 1. Electrons are heated around the electron diffusion region

The 2-D electron temperature profile obtained using triple Langmuir probes shows that electrons are heated around the electron diffusion region. The electron temperature increases sharply across the separatrix and peaks at the edge of the electron diffusion region. This profile suggests that heat is generated around the diffusion region and propagates quickly along the magnetic field lines. Fast camera images support the Langmuir probe measurements by demonstrating a sharp increase of the visible light emission inside the separatrix—an effect which is strongly dependent on the electron temperature.

### 2. Electrons are likely heated by anomalous resistivity

Measurements and analyses suggest that electrons are heated by anomalous resistivity, but the precise mechanisms that generate the anomalous resistivity remain unknown. First, the outgoing electron flow energy from the electron diffusion region remains negligible, although the electron energy gain from the electric field is significant there. Second, classical Ohmic dissipation based on the perpendicular Spitzer resistivity cannot explain the measured 2-D temperature profile. The required heating power exceeds that of classical Ohmic dissipation by a factor of more than four due to the large electron heat flux. To explain the low flow energy gain and high electron heat flux at the same time, the Ohmic dissipation must be larger than the classical value, indicating the presence of anomalous resistivity. Magnetic and electrostatic fluctuations in the lower hybrid frequency range are observed near the X-point and throughout the downstream region. These fluctuations may contribute to the observed non-classical electron heating, but additional measurements on the wave characteristics are required to draw definitive conclusions.

### **7.1.3 Energy Inventory**

#### **1. Collisionless reconnection in MRX efficiently converts magnetic energy to particle energy**

By examining the Poynting fluxes entering and leaving the diffusion region, it is shown that more than half of the incoming magnetic energy is converted to particle energy during reconnection. The outgoing Poynting flux associated with the Hall electric and magnetic fields is larger than the conventional outgoing flux.

#### **2. Ions obtain more energy than electrons and increases in thermal energy dominate the flow energy gain for both ions and electrons.**

The total ion energy gain from the electric field exceeds that of electrons due to the strong Hall electric field. Ions gain energy mostly from the Hall electric field broadly over the downstream region. Unlike ions, electrons gain energy mostly from the inductive reconnection electric field around the small electron diffusion region. The electron thermal energy increase accounts for about half of the total electron energy gain from the electric field. The energy loss by electron heat flux is significant and accounts for the other half. The ion thermal energy increase is larger than that of the flow energy by about a factor of three. The upper limit on the energy loss related to the ion heat flux is estimated to be comparable to the ion thermal energy increase. The ion energy inventory suggests that ions may lose energy to neutrals via charge-exchange collisions.

## **7.2 Possible Impact on Reconnection Research**

The importance of magnetic reconnection comes from its effectiveness in converting magnetic energy to particle energy. The energy inventory in MRX shows that collisionless magnetic reconnection efficiently converts magnetic energy to particle energy, thereby demonstrating that magnetic reconnection can play a key role in explosive phenomena in mag-

netized, collisionless plasmas in nature such as solar flares and sawtooth relaxations in tokamaks.

The work in this dissertation shows that ions can gain more energy than electrons during reconnection and identifies mechanisms to explain the ion energy gain. Ions obtain energy efficiently from the in-plane electric field established by accelerated electrons. The scaling of the in-plane electric field in Eqn. 4.5 can be used to estimate the in-plane electric field and to study ion heating and acceleration in various plasmas. For example, these results can be applied to the long-standing ion heating problem during reconnection in RFP (Reversed Field Pinch) devices.

The results related to electron heating near the X-point provide insight to micro-physics in the the electron diffusion region. The electron energy inventory near the X-point indicates that anomalous resistivity due to wave-particle interactions can be important, although more measurements and analyses are required. The investigation of electron dynamics near the X-point is timely given that NASA's Magnetospheric Multi-Scale (MMS) mission will be launched in 2014 to study the physics of the electron diffusion region. Results in this dissertation can be used to motivate studies of wave characteristics in the electron diffusion region.

## **7.3 Suggested Future Work**

### **7.3.1 Ion Heating**

The ion thermalization process called re-magnetization can be studied in detail via numerical simulations. By tracking the orbits of ion pseudo-particles, the importance of the magnetic field can be assessed. The role of Coulomb collisions in ion thermalization can be also studied by systematically changing the collisionality. Since ions are still heated downstream without imposing Coulomb collisions in simulations, it is also intriguing to study ion thermalization mechanisms in the fully collisionless limit.

Another future topic related to ion heating is the measurement of counter-streaming ion beam structures, which are responsible for the increase in the effective ion temperature in the center of the current sheet. Non-Maxwellian distribution functions are widely observed in both space observations [e.g. Hoshino *et al.*, 1998; Wygant *et al.*, 2005] and numerical simulations [e.g. Shay *et al.*, 1998; Drake *et al.*, 2009; Aunai, Belmont, and Smets, 2011b]. The presence of a radial potential well in MRX directly supports the possibility of counter-streaming ions. In addition, the pressure balance along the radial direction also suggests that the ion temperature sharply increases at the center of the reconnection sheet by kinetic effects from the counter-streaming ion beams. However, data from the IDSP does not show clear signatures of the counter-streaming ion beams. As discussed in 4.2, this discrepancy is possibly caused by the limited resolution of the IDSP. Different diagnostics with better resolution such as an ion energy analyzer are required to address this problem.

### 7.3.2 Electron Heating

The observed non-classical electron heating is related to an important problem, which is the discrepancy in the width of the electron diffusion layer between experiments and simulations. The experimentally measured width is much larger than that in 2-D simulations [Dorfman *et al.*, 2008; Roytershteyn *et al.*, 2010]. Effects from Coulomb collisions contribute to broadening the width but the layer width remains narrow in simulations [Roytershteyn *et al.*, 2010]. Electromagnetic fluctuations traveling along the out-of-plane direction [Ji *et al.*, 2004] are also found in 3-D simulations but they do not resolve the discrepancy [Roytershteyn *et al.*, 2013]. Dorfman *et al.*, 2013 pointed out the possibility of current sheet broadening due to the presence of small, 3-D flux ropes, but this speculation has not been confirmed. The magnetic fluctuations previously reported by Ji *et al.*, 2004 were observed near the X-point. However, the 2-D profiles of the high-frequency fluctuation power show that fluctuations are stronger downstream. These fluctuations may originate from different types of waves propagating along the magnetic fields, which possibly contribute to the de-

velopment of anomalous resistivity near the edge of the electron diffusion region.

To identify the physical mechanisms behind the observed non-classical heating and to verify the presence of anomalous resistivity due to the observed fluctuations, more detailed measurements of wave-characteristics are necessary. In addition, careful comparisons between experiments and simulations are also required.

### **7.3.3 Energetic Particles**

One topic not addressed in this dissertation is energetic particle generation. Runaway electrons are expected to exist near the X-point since the reconnection electric field exceeds the Dreicer runaway field, as summarized in table 3.1. Even though the importance of fast electrons on the energy inventory may be limited due to collisions, it is still valuable to measure if and where the fast electrons are generated. As introduced in Subsection 1.3.1, there are ongoing debates on energetic particle generation between models based on the single X-line geometry and those emphasizing the multiple X-line geometry. Measuring the population of energetic electrons under different magnetic geometries will be beneficial for understanding energetic particle generation.

### **7.3.4 Energy Conversion in Guide-field Reconnection**

Recent results on guide-field reconnection in MRX show that the guide field significantly decreases the reconnection rate [Tharp *et al.*, 2012]. It will be interesting to understand how the guide field affects the reconnection energy conversion process. It is known that the guide field breaks symmetry of the quadrupole field [Huba, 2005]. This symmetry breaking can also alter the profile of the in-plane electrostatic potential, which means that the ion dynamics may be significantly different from the anti-parallel reconnection case. Electron dynamics can be also significantly affected by the presence of the guide field. For example, the guide field may stabilize the fluctuations measured in the downstream region, which may further reduce the reconnection rate.

# **Appendix A**

## **Evaluation of Spacecraft Data Analysis**

### **Techniques via Plasma Jogging**

#### **Experiments**

This appendix is an extended version of a paper published by Yoo and Yamada, 2012.

A laboratory plasma is utilized to assess the effectiveness of several prominent spacecraft data analysis techniques. These include minimum variance analysis on the magnetic field (MVAB) and various boundary-crossing time analyses (BCTA) such as the constant velocity approach (CVA), constant thickness approach (CTA), and minimum thickness variance (MTV). Magnetic field data from measurement points that resemble the formation of multi-spacecraft flying through a reconnecting current sheet is used to check MVAB and BCTA to deduce a proper normal vector. Results from each method are compared to the values measured by 2-D magnetic probe arrays. We examine discharges with a two-dimensional (2-D) X-line structure as well as cases in which a flux rope forms within the layer. All discharges are in a two-fluid regime in which electrons are magnetized but ions are not. We conclude that CVA with four sample measurement points forming a

tetrahedron generates a reasonable unit normal vector  $\hat{\mathbf{n}}$ , relative velocity along the normal vector  $V_n$ , and current sheet thickness  $\delta_{CS}$  for all of the tested cases. Unlike CVA, both CTA and MTV sometimes generate  $V_n$  and  $\delta_{CS}$  that are different from the measured values, which indicates that CTA and MTV are sensitive to changes in the current sheet thickness. CTA is, however, successful at estimating  $\hat{\mathbf{n}}$ . MVAB, on the other hand, often fails to predict a proper normal direction. This is because the reconnecting neutral sheet fundamentally contains 2-D or 3-D structures. MVAB, however, does determine the direction along the reconnecting magnetic field that is close to the real magnetic geometry. Based on these observations, we suggest a hybrid procedure for determining a local coordinate system for data from four spacecraft passing through a reconnecting current sheet.

## A.1 Introduction

For many decades, satellite measurements have been employed to understand the complex nature of the magnetic fields surrounding Earth. These measurements have revealed the presence of magnetic reconnection throughout Earth's magnetosphere [e.g. Paschmann *et al.*, 1979; Phan *et al.*, 2000; Øieroset *et al.*, 2001; Phan *et al.*, 2006; Angelopoulos *et al.*, 2008]. During the past dozen years, the role of magnetic reconnection has been studied in detail through a combined effort that includes numerical simulations, dedicated laboratory plasma experiments, and direct observations from spacecraft [Yamada, Kulsrud, and Ji, 2010]. As a result of this effort, it is now recognized that two-fluid effects resulting from the different behavior of ions and electrons in the reconnection layer play a key role in collisionless reconnection [Yamada, 2007; Zweibel and Yamada, 2009; Mozer, Bale, and Phan, 2002; Vaivads *et al.*, 2004]. In order to further study two-fluid effects in the magnetosphere, the Magnetospheric Multi-Scale (MMS) mission will be launched in 2014 to explore spatial scales down to the electron inertial length ( $c/\omega_{pe}$ ), a measurement regime which is critical to obtain a complete understanding of collisionless reconnection.

One of the foremost challenges of using spacecraft to study reconnection is properly identifying the local magnetic field geometry. Because the number of spacecraft is limited, the spatial profile of the plasma must be inferred from the time series of physical quantities such as the magnetic field and electric field, typically using at most four locations. Several analysis methods have been developed to address this challenging problem. Classical minimum variance analysis on magnetic field data (known as MVAB) [Sonnerup and Cahill, 1967] has been employed for many spacecraft data analyses [e.g. Øieroset *et al.*, 2001]. Alternatively, maximum variance analysis of electric field data (MVAE) [Sonnerup *et al.*, 1987; Paschmann *et al.*, 1990] or the Faraday residue method [Terasawa *et al.*, 1996; Khrabrov and Sonnerup, 1998b] can be employed if electric field measurements are also available. These variance analysis methods (MVAB, MVAE, and the Faraday residue method) are capable of identifying a vector normal to the reconnection current layer using data from a single spacecraft.

If multiple spacecraft are available, more information on the reconnection layer can be obtained via boundary crossing time analysis (BCTA). For example, BCTA was used to estimate the normal component of the relative velocity of a boundary  $V_n$  and current sheet thickness  $\delta_{CS}$  for data from ISEE 1 and ISEE 2 [Berchem and Russell, 1982]. Similar analysis has been carried out on data from 16 crossings of Earth's magnetopause by the spacecraft AMPTE/UKS and IRM [Bauer *et al.*, 2000]. In these studies, which had only two spacecraft, the normal vector  $\hat{n}$  is determined by the single-spacecraft variance analyses such as MVAB. When four spacecraft are available, however,  $\hat{n}$  can be obtained with better accuracy by BCTA without the use of single-spacecraft techniques [Russell *et al.*, 1983]. This is why BCTA has been widely used for data from the four-spacecraft Cluster mission [Vaivads *et al.*, 2004; Eastwood *et al.*, 2005; Khotyaintsev *et al.*, 2006; Eastwood *et al.*, 2007; Retinò *et al.*, 2007, 2008; Rosenqvist *et al.*, 2008].

For a detailed study of reconnection, more information on the magnetic geometry is needed; knowing the direction normal to the current sheet is not enough. In particular,

key physical parameters such as the reconnection rate cannot be estimated without differentiating two tangential directions: the out-of-plane direction and the direction of the reconnecting magnetic field. In some cases, the MVAB or MVAE techniques successfully separate all three principal axes that naturally form a coordinate system, from which the full local magnetic geometry can be inferred. However, when the variances along two principal axes are similar, they cannot reconstruct the magnetic geometry properly. In attempt to address these shortcomings, Mozer and Retinò, 2007 combined MVAB and MVAE to find a rotation matrix transforming the GSE coordinate system into the magnetopause frame. They noticed that MVAB best finds the direction of the reconnecting magnetic field component which is the maximum varying component, while MVAE best locates the maximum varying normal electric field component. In this study, however, the validity of results from the combined procedure could not be checked since the actual magnetic geometry is not known.

For a quantitative test of spacecraft analysis techniques, we need to acquire similar types of data from a known magnetic geometry. A well-controlled, well-diagnosed current sheet in the Magnetic Reconnection Experiment (MRX) provides a unique opportunity to perform such a quantitative test. In particular, the current sheet is swept over the stationary probes via internal pulsed coils. This situation is very similar to the space measurements in which the current sheet moves with respect to spacecraft. This plasma “jogging” experiment is carefully designed and performed so that we can test these methods in the plasma in which we monitor evolution of the profile of the magnetic field measured by multiple magnetic probe arrays.

With the use of data from the plasma jogging experiment, we present a detailed and thorough laboratory test of two of the methods mentioned above, minimum variance analysis of the magnetic field and boundary-crossing time analysis, in a collisionless reconnection layer. First, both methods are tested to produce proper normal vectors. Second, three different versions of BCTA (CVA, CTA, and MTV) are used to estimate  $V_n$  and the

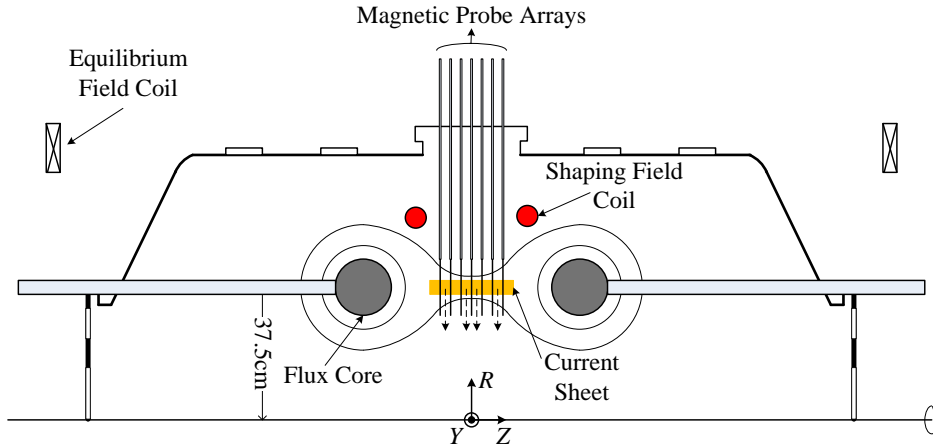


Figure A.1: Cross section of the MRX vacuum chamber for plasma jogging experiments. The red circles show the position of the shaping field (SF) coils which are used to accelerate the motion of the current sheet radially inward.

current sheet thickness  $\delta_{CS}$  and they are compared to measured values in order to evaluate the effectiveness of each method. Third, we compare the results from MVAB and BCTA and present a hybrid procedure for determining a local magnetic geometry based on elements of both MVAB and BCTA which can be used by any four-spacecraft mission such as Cluster and the Magnetospheric Multi-Scale (MMS) mission. It should be noted that we do not perform MVAE or the Faraday residual analysis because we do not currently have sufficient electric field measurement capabilities.

## A.2 Experimental Setup

In addition to PF and TF coils described in section 3.1, another set of coils called the shaping field (SF) coils is utilized to drive the plasma radially inward, as shown in Fig. A.1. This accelerated motion of the current sheet is called “jogging.” The advantage of this jogging experiment is that a simulated “satellite” data set can be obtained when the current sheet region is swept past a stationary probe with a predetermined velocity and

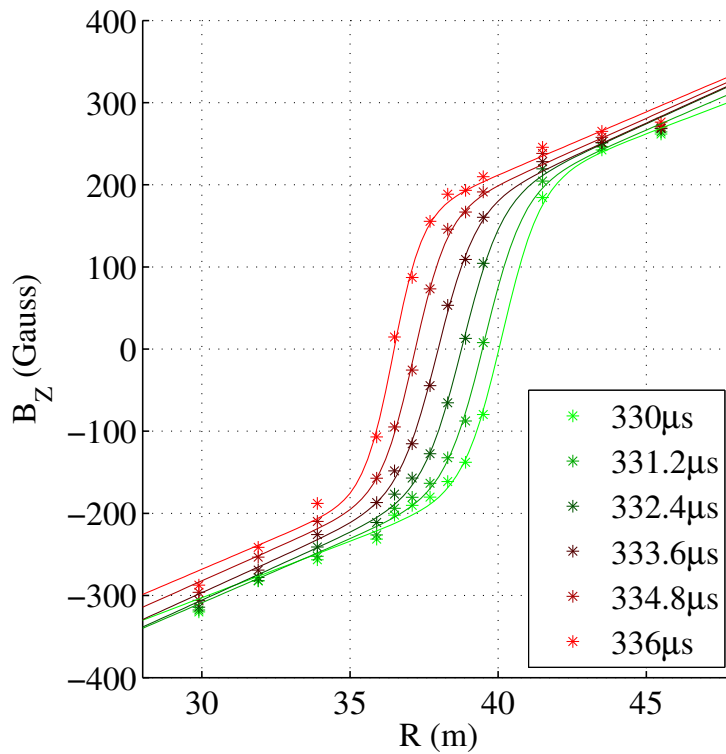


Figure A.2: Radial profiles of  $B_Z$  every  $1.2 \mu s$  during the quasi-steady period of a single discharge, measured by the magnetic probe array at  $Z = 0$ . Asterisks stand for measured data and the solid lines come from fitting the data to a Harris function,  $\sim \tanh((R - R_0)/\delta)$ . The current sheet moves in with a relatively well-maintained structure at about 5.8 km/s.

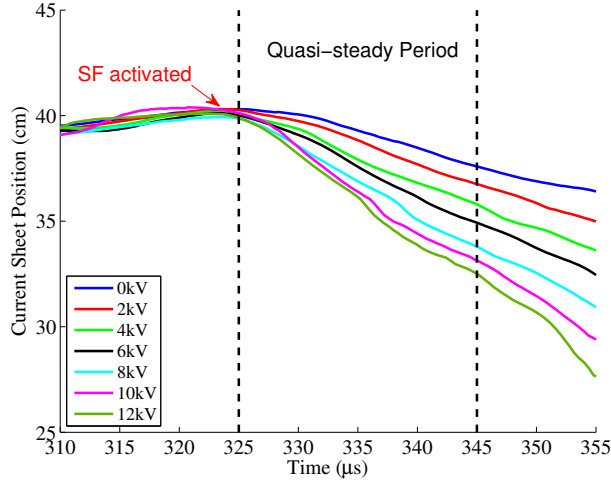


Figure A.3: Current sheet motion as a function of the firing voltage for the SF coils. Shortly after the SF coils are activated, the current sheet starts to move in. The jogging speed of the current sheet is proportional to the firing voltage. Two black dashed lines indicate the quasi-steady period of the MRX plasma.

angle. Figure A.2 illustrates radial profiles of  $B_z$  during the quasi-steady period of a single discharge of the MRX jogging experiment. Asterisks stand for measured data and solid lines are results of fitting the radial profiles into a Harris-sheet type function [Harris, 1962],  $\sim \tanh((R - R_0)/\delta)$  [Ji *et al.*, 1999]. The jogging speed of the current sheet can be controlled by firing the SF coils with various voltages. Figure A.3 shows time profiles of the current sheet location with various SF firing voltages. The SF coils are activated just before the quasi-steady period of the MRX plasma. Shortly after they are fired, the current sheet moves in radially. The location of the current sheet is from the Harris fitting. The jogging speed increases almost linearly with the firing voltage. In the discharge presented in Fig. A.2, the current sheet moves about 3.5 cm over 6  $\mu s$ , yielding a speed of 5.8 km/s, which is about one order of magnitude lower than the Alfvén velocity based on upstream plasma parameters ( $n_e = 2 - 5 \times 10^{13} \text{ cm}^{-3}$  and  $|\mathbf{B}| = 200 - 250 \text{ Gauss}$ ). Every discharge presented in this paper has a similar radial speed (5 – 6 km/s).

## A.3 Minimum Variance Analysis on Magnetic Field (MVAB)

### A.3.1 Description of Method

Following Mozer and Retinò, 2007, the following coordinate system, which is similar to the GSE system for subsolar reconnection, is used throughout this appendix:  $x$  is normal to the current sheet,  $y$  is along the out-of-plane direction, and  $z$  is in the direction of the reconnecting magnetic field. The corresponding local Cartesian coordinates for reconnection during the quasi-steady period in MRX are  $R$ ,  $Y$ , and  $Z$  respectively [Yamada *et al.*, 1997].

The theory behind MVAB can be found in the literature [Sonnerup and Cahill, 1967; Sonnerup and Scheible, 1998]. The fundamental assumption is that the boundary is one-dimensional: physical quantities vary only along the direction normal to the layer. For the magnetic field, this assumption means

$$\nabla \cdot \mathbf{B} = \frac{\partial B_n}{\partial n} = 0, \quad (\text{A.1})$$

and

$$\frac{\partial B_n}{\partial t} = -(\nabla \times \mathbf{E})_n = 0. \quad (\text{A.2})$$

In other words, the magnetic field component normal to the boundary does not vary while spacecraft passes by it. In reality, however, due to 2-D or 3-D structures and temporal variations, the normal component undergoes finite changes. The basic idea of MVAB is that the direction along which the magnetic field component varies least would be a good indicator of the normal vector  $\hat{\mathbf{n}}$ : for a given set of  $M$  magnetic field measurements spanning the

boundary layer crossing time, we need to find  $\hat{\mathbf{n}}$  that minimizes the variance

$$\sigma^2 = \frac{1}{M} \sum_{m=1}^M |(\mathbf{B}^{(m)} - \langle \mathbf{B} \rangle) \cdot \hat{\mathbf{n}}|^2, \quad (\text{A.3})$$

where  $\mathbf{B}^{(m)}$  is the  $m$ -th measured magnetic field record of the data and the average  $\langle \mathbf{B} \rangle$  is just

$$\langle \mathbf{B} \rangle \equiv \frac{1}{M} \sum_{m=1}^M \mathbf{B}^{(m)}. \quad (\text{A.4})$$

Such a unit vector  $\hat{\mathbf{n}}$  can be found by computing eigenvectors of the symmetric matrix  $\mathbf{M}$  defined by

$$M_{\mu\nu} = \langle B_\mu B_\nu \rangle - \langle B_\mu \rangle \langle B_\nu \rangle, \quad (\text{A.5})$$

where  $B_\mu$  and  $B_\nu$  are components of the measured magnetic field based on a Cartesian coordinate system. For MRX data, they are  $B_R$ ,  $B_Y$ , and  $B_Z$ . Since the magnetic variance matrix  $\mathbf{M}$  is symmetric, three eigenvalues  $\lambda_1$ ,  $\lambda_2$ , and  $\lambda_3$  in the order of increasing magnitude are real and corresponding normalized eigenvectors  $\mathbf{u}_1$ ,  $\mathbf{u}_2$ , and  $\mathbf{u}_3$  are orthogonal. Mathematically, each eigenvalue equals the variance along the corresponding eigenvector. Thus, if a spacecraft encounters the current sheet and passes through it, the normalized eigenvector  $\mathbf{u}_1$  that has the minimum variance is a natural choice for the unit normal vector  $\hat{\mathbf{n}}$ , or  $\hat{\mathbf{x}}$ . Because magnetic field component along the direction of the reconnecting magnetic field  $B_z$  varies most across the layer,  $\mathbf{u}_2$  and  $\mathbf{u}_3$  are parallel to  $\mathbf{y}$  and  $\mathbf{z}$  respectively.

The size of the data segment,  $M$ , is chosen by checking that the results of MVAB are stationary. If the basic assumption of MVAB is satisfied, i.e. if the boundary is 1-D, MVAB is independent of the number of data points. This stationary property of MVAB is not guaranteed in real data. If  $M$  is too small or too large, results from MVAB can be different from those with intermediate data segments Sonnerup and Scheible [1998]. Thus, the stationarity of MVAB must be checked to make sure the nested data segment is within the intermediate, or ‘‘plateau’’ region. The smallest data set for MVAB has three points - the

center point which is closest to the boundary and one from each side. The next smallest data segment is constructed by adding one data point to each side. As  $M$  increases, the average magnetic field along the normal vector from MVAB  $\langle \mathbf{B} \rangle \cdot \hat{\mathbf{n}}$  remains nearly unchanged, indicating a plateau region as shown in Fig. A.6-(a). The number of data points  $M$  is chosen such that the data segment is in the plateau region.

To summarize the procedure of determining local coordinates by MVAB, a proper span of magnetic field data centered at the middle of the current sheet must be chosen. Then, the magnetic variance matrix  $\mathbf{M}$  is constructed with the data, and eigenvalues and eigenvectors of  $\mathbf{M}$  are computed. The normalized eigenvector corresponding to the smallest eigenvalue determines the normal direction  $\hat{\mathbf{x}}$ , i.e.,  $\hat{\mathbf{x}} = \pm \mathbf{u}_1$ . The other two eigenvectors  $\mathbf{u}_2$  and  $\mathbf{u}_3$  define  $\hat{\mathbf{y}}$  and  $\hat{\mathbf{z}}$ . Proper signs should be chosen to make sure  $\hat{\mathbf{z}} = \hat{\mathbf{x}} \times \hat{\mathbf{y}}$ . Then, the transformation of values in the original cartesian coordinates  $(R, Y, Z)$  into those in  $(x, y, z)$  is given by

$$\begin{pmatrix} x \\ y \\ z \end{pmatrix} = \begin{pmatrix} \hat{\mathbf{x}} \\ \hat{\mathbf{y}} \\ \hat{\mathbf{z}} \end{pmatrix} \begin{pmatrix} R \\ Y \\ Z \end{pmatrix}. \quad (\text{A.6})$$

### A.3.2 MVAB Results and Analysis

Data from the MRX jogging experiment provides a good opportunity to test MVAB since the full 2-D (or 3-D) magnetic field geometry is independently measured. Whether MVAB generates a proper normal vector can be easily checked by comparing the local magnetic geometry predicted by MVAB with the measured global geometry.

Figure A.4 shows the time evolution of 2-D profiles of the current density  $J_Y$  with contours of the poloidal magnetic flux  $\Psi \equiv \int_0^R 2\pi R' B_Z(Z, R', t) dR'$  and the out-of-plane magnetic field  $B_Y$  measured by the 2-D magnetic probe arrays during the quasi-steady period of a typical MRX jog discharge. The right column shows the quadrupolar  $B_Y$  structure moving in radially with temporal changes mainly due to the TF coil current ringing [Ren

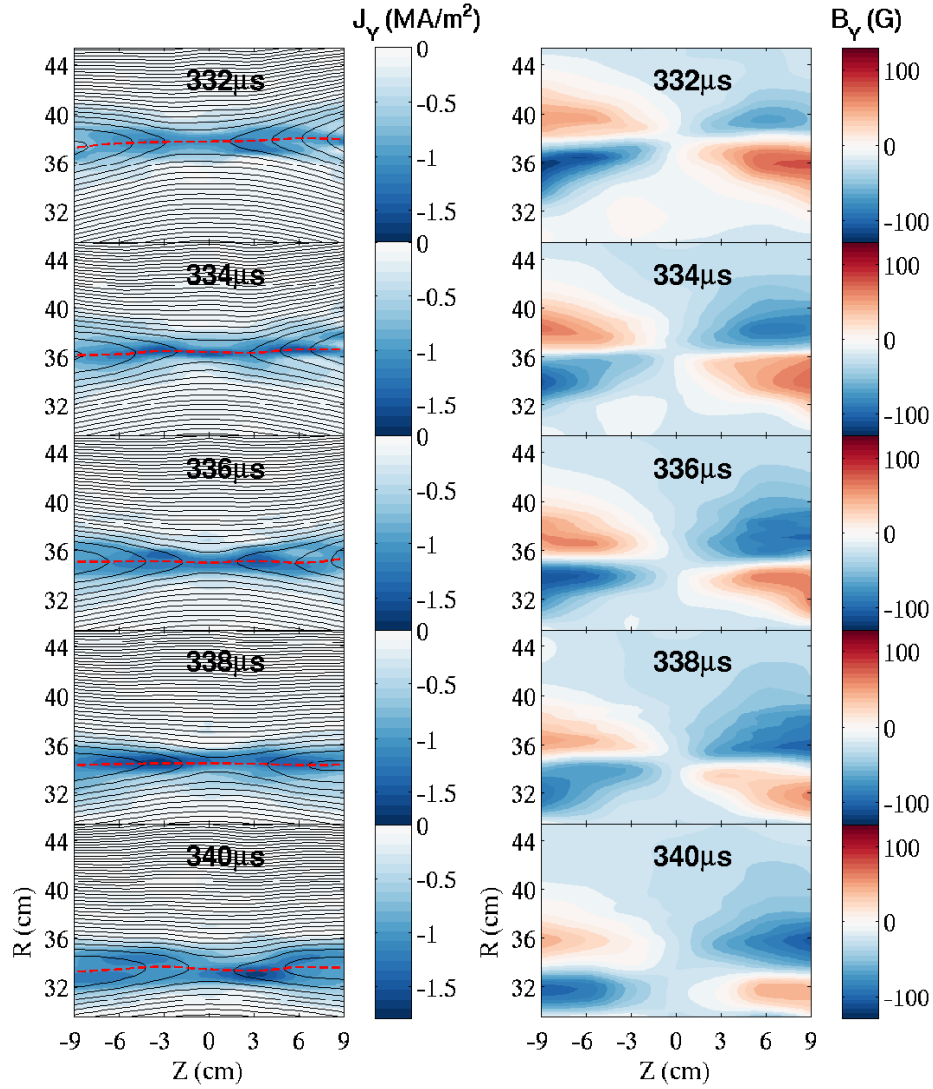


Figure A.4: Data from 2-D magnetic probe arrays during the quasi-steady period of the MRX jog experiment discharge 114338. Colors in left panels demonstrate the profile of the current density  $J_Y$ , while the black lines represent contours of the poloidal flux  $\psi$ . The red dashed lines indicate the location of  $B_Z = 0$  boundary which agrees with the current sheet location from the Harris fitting. Contour plots of the right panels show the time evolution of the out-of-plane magnetic field  $B_Y$  every  $2 \mu s$ . Because of the time-varying TF current, the overall shape of the quadrupole structure undergoes temporal changes. The current sheet moves in radially together with the quadrupolar  $B_Y$  structure with a speed of  $\sim 6$  km/s.

*et al.*, 2008a]. The radial motion of the current sheet is shown in the left column. The current sheet structure is well-maintained and moves in with the quadrupolar  $B_Y$ . The layer clearly has 2-D structures:  $J_Y$  varies along  $Z$  and the  $B_Z = 0$  boundary indicated by red dashed lines is slightly kinked in the  $R - Z$  plane, especially at  $t = 340 \mu s$ . However, the direction normal to the current sheet is generally along  $\hat{e}_R$ , the unit vector for  $R$ , as the curvature of the  $B_Z = 0$  boundary remains small. The angle between the local vector normal to the boundary and  $\hat{e}_R$  is less than 5 degrees. Furthermore, toroidal asymmetry is monitored by an additional magnetic probe at  $Y = -9$  cm and is found to be fairly negligible for this plasma. Therefore, the rotation matrix that transforms from  $(R, Y, Z)$  into  $(x, y, z)$  coordinates for this discharge should have diagonal terms close to unity and off-diagonal terms close to zero. In other words,  $\hat{x} \approx \hat{e}_R$ ,  $\hat{y} \approx \hat{e}_Y$ , and  $\hat{z} \approx \hat{e}_Z$ .

As shown in Fig. A.5, data from four different measurement points ( $Z = 0, 3, 6, 9$  cm;  $R = 36.7, Y = 0$  for all) of the same discharge is used to test MVAB. At  $Z = 0$ , in the right vicinity of the X point, only the reconnecting magnetic field  $B_Z$  varies significantly as shown in Fig. A.5-(c). In this case, variance of  $B_R$  is comparable to that of  $B_Y$  and the normal vector generated by MVAB becomes a mixture of  $\hat{e}_R$  and  $\hat{e}_Y$ . The rotation matrix predicted by MVAB for this example is

$$\begin{pmatrix} x_1 \\ y_1 \\ z_1 \end{pmatrix} = \begin{pmatrix} 0.3576 & 0.9314 & 0.0682 \\ -0.9338 & 0.3560 & 0.0349 \\ 0.0082 & -0.0762 & 0.9971 \end{pmatrix} \begin{pmatrix} R \\ Y \\ Z \end{pmatrix}, \quad (\text{A.7})$$

where the subscript 1 is added to avoid confusion and to emphasize that these are just a ‘suggested’ coordinate system by MVAB at the given location. The normal vector is  $0.3576\hat{e}_R + 0.9314\hat{e}_Y + 0.0682\hat{e}_Z$ , which is closer to  $\hat{e}_Y$  than to the reference normal  $\hat{e}_R$ . Even though three eigenvalues of  $M$  are well-separated as shown in Fig. A.5-(c’), the normal vector does not reflect the real magnetic geometry. The smallest and intermediate eigenvalues are often degenerate ( $\lambda_1 \sim \lambda_2$ ) at  $Z = 0$  in other discharges. However, MVAB

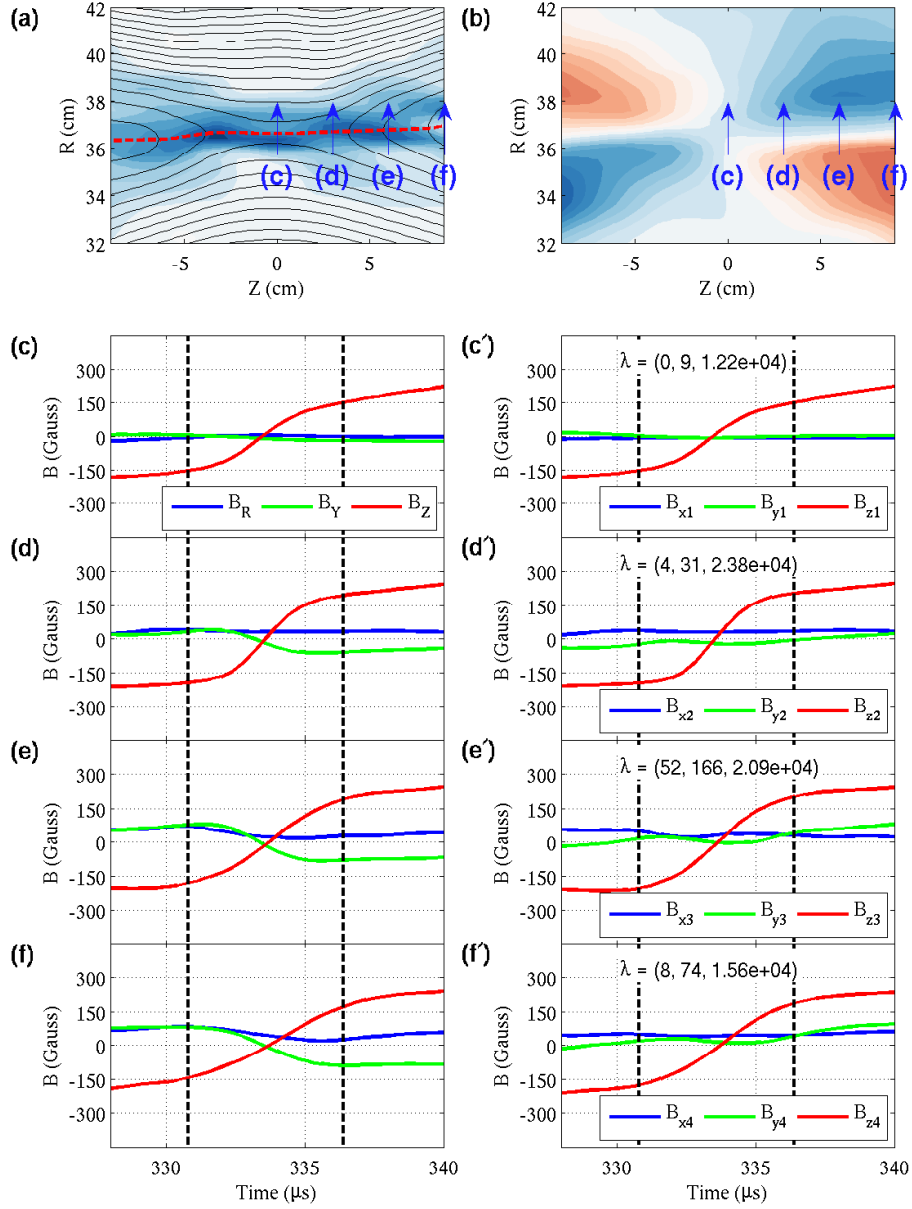


Figure A.5: MVAB analysis for data from the discharge 114338. (a) 2-D profile of  $J_Y$  with contours of  $\Psi$  at the time the current sheet is close to the sample measurement points. (b) 2-D profile of  $B_T$ . Color scales are the same as in Fig. A.4. The arrows indicate the data range used for MVAB. (c)(d)(e)(f) Magnetic field data at  $(R, Z) = (36.7, 0)$ ,  $(36.7, 3)$ ,  $(36.7, 6)$ , and  $(36.7, 9)$  ( $Y = 0$  for all), respectively around the time the current sheet passes. Data between dashed black lines is used for MVAB. (c')(d')(e')(f') Profiles in  $(x, y, z)$  coordinates suggested by MVAB. Three eigenvalues ( $\lambda$ ) of the matrix  $\mathbf{M}$  are shown inside of each panel. The out-of-plane magnetic field ( $B_Y$ ) loses the bipolar shape after the coordinate transform by MVAB.

predicts the direction of the reconnecting field well ( $\hat{z}_1 \simeq \hat{e}_Z$ ).

At  $Z = 3$  cm, the quadrupolar out-of-plane field starts to play a role. While  $B_R$  remains small,  $B_Y$  changes moderately as shown in Fig. A.5-(d). As a result, the three eigenvalues are well-separated and the unit vectors suggested by MVAB reflect the magnetic geometry. The coordinate system determined by MVAB is usually best at  $Z = \pm 3$  cm for MRX jogging experiment data. The transformation matrix predicted by MVAB at this location is

$$\begin{pmatrix} x_2 \\ y_2 \\ z_2 \end{pmatrix} = \begin{pmatrix} 0.9976 & 0.0630 & 0.0297 \\ -0.0687 & 0.9601 & 0.2712 \\ -0.0115 & -0.2726 & 0.9621 \end{pmatrix} \begin{pmatrix} R \\ Y \\ Z \end{pmatrix}. \quad (\text{A.8})$$

Here, the normal vector from MVAB is very close to the reference normal. It is worth noting that  $\hat{z}_2$  has been degraded as it picks up a sizeable  $\hat{e}_Y$  component, which means the Hall field is considered a part of the reconnecting field by MVAB. The predicted out-of-plane direction  $\hat{y}_2$  also has a considerable  $\hat{e}_Z$  component. Thus, as shown in Fig. A.5-(d'), the quadrupolar component of  $B_{y2}$  is weakened after the coordinate transformation. This tendency is enhanced further downstream, so that the transformed out-of-plane magnetic field component  $B_y$  is significantly contaminated by the other two components and frequently loses its bipolar shape (See Fig. A.5-(e') and (f')). This could be one of the reasons why a clear quadrupolar structure has rarely been identified in space [Mozer and Retinò, 2007].

At  $Z = 6$  cm, the variation in  $B_R$  becomes non-negligible because of the 2-D structure of the reconnection geometry. For most cases, this leads to a degenerate condition with  $\lambda_1 \sim \lambda_2$ , making  $\hat{x}_3$  and  $\hat{y}_3$  meaningless. The suggested transformation for this example is

$$\begin{pmatrix} x_3 \\ y_3 \\ z_3 \end{pmatrix} = \begin{pmatrix} 0.7990 & -0.5677 & -0.1984 \\ 0.5927 & 0.6876 & 0.4195 \\ -0.1017 & -0.4528 & 0.8858 \end{pmatrix} \begin{pmatrix} R \\ Y \\ Z \end{pmatrix}. \quad (\text{A.9})$$

$\hat{\mathbf{z}}_3$  is further deviated from  $\hat{\mathbf{e}}_Z$  and both  $\hat{\mathbf{x}}_3$  and  $\hat{\mathbf{y}}_3$  do not reflect the real magnetic geometry. Similar trends continue at  $Z = 9$  cm where MVAB generates the following coordinate transformation:

$$\begin{pmatrix} x_4 \\ y_4 \\ z_4 \end{pmatrix} = \begin{pmatrix} 0.8542 & -0.5036 & -0.1291 \\ 0.4888 & 0.6935 & 0.5293 \\ -0.1770 & -0.5152 & 0.8386 \end{pmatrix} \begin{pmatrix} R \\ Y \\ Z \end{pmatrix}. \quad (\text{A.10})$$

In this example, the suggested normal vector is again closer to  $-\hat{\mathbf{e}}_Y$  than to  $\hat{\mathbf{e}}_R$ , which does not agree with the real magnetic geometry.

To confirm that the above disagreement between the normal vectors from MVAB and the measured magnetic geometry is not due to measurement noise, we perform error estimations following [Khrabrov and Sonnerup, 1998a] where errors associated with random noise in minimum/maximum variance analysis are analytically derived. In the reference, the angular uncertainty is given by

$$|\Delta\phi_{ij}| = |\Delta\phi_{ji}| = \sqrt{\frac{\lambda_1}{(M-1)} \frac{(\lambda_i + \lambda_j - \lambda_1)}{(\lambda_i - \lambda_j)^2}}, \quad i \neq j, \quad (\text{A.11})$$

where  $|\Delta\phi_{ij}|$  is the angular uncertainty of eigenvector  $\mathbf{u}_i$  in the direction of  $\mathbf{u}_j$ . The combined statistical error estimate for  $\langle \mathbf{B} \rangle_n \equiv \langle \mathbf{B} \rangle \cdot \mathbf{u}_1$  is [Sonnerup and Scheible, 1998]

$$|\Delta\langle \mathbf{B} \rangle \cdot \mathbf{u}_1| = \sqrt{\frac{\lambda_1}{M-1} + (\Delta\phi_{12}\langle \mathbf{B} \rangle \cdot \mathbf{u}_2)^2 + (\Delta\phi_{13}\langle \mathbf{B} \rangle \cdot \mathbf{u}_3)^2}, \quad (\text{A.12})$$

where the first term inside of the square root comes from the uncertainty in the average magnetic field associated with the variance  $\lambda_1$ .

Figure A.6 shows the results of the error estimates with  $M = 3 - 41$  for the same data used for MVAB in Fig. A.5. Error bars in this figure are computed by the above equations. The estimated statistical errors in  $\langle \mathbf{B} \rangle$  are generally small as shown in Fig. A.6-(a), which is expected since the signal-to-noise ratio of MRX magnetic data is small. Figure A.6-(b) and

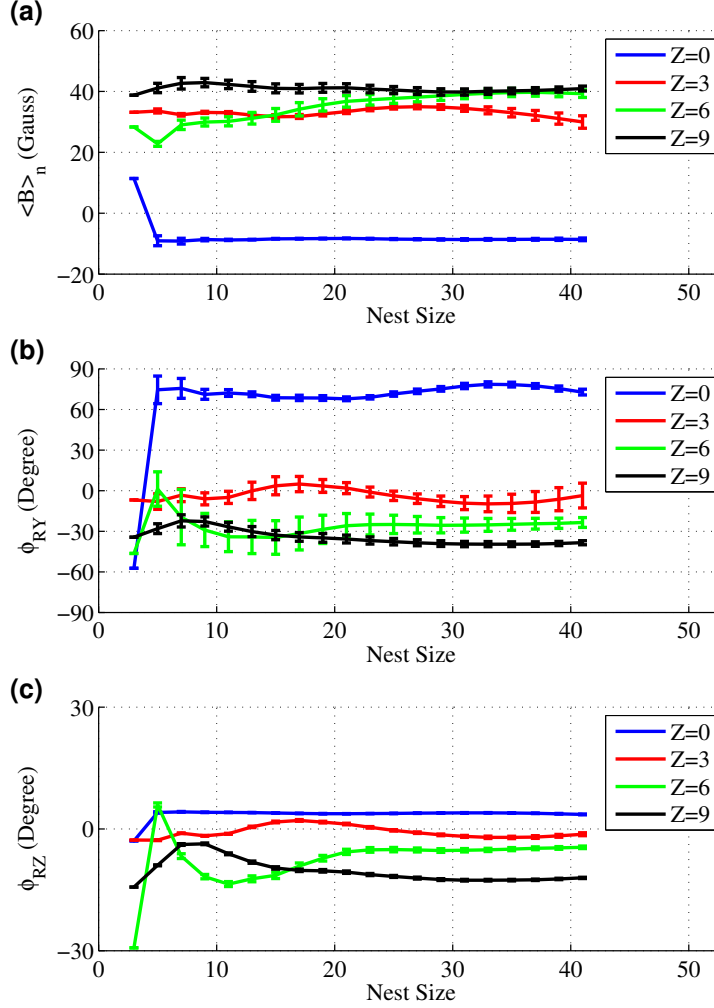


Figure A.6: MVAB error analysis. (a) Average magnetic field component along the suggested normal vector  $\mathbf{u}_1$  from MVAB ( $\langle \mathbf{B} \rangle_n \equiv \langle \mathbf{B} \rangle \cdot \hat{\mathbf{u}}_1$ ) as function of the nest size  $M$ . Error bars are computed by Eqn. A.12. (b) Angle between  $\mathbf{u}_1$  and the reference normal vector  $\hat{\mathbf{e}}_R$  in the R-Y plane ( $\phi_{RY}$ ) as function of  $M$ . Except at  $Z = 3$ , the angle  $\phi_{RY}$  is not close to zero for any value of  $M$ . (c) Angle between  $\mathbf{u}_1$  and the reference normal vector  $\hat{\mathbf{e}}_R$  in the R-Z plane ( $\phi_{RZ}$ ) as function of  $M$ . The angle  $\phi_{RZ}$  is usually smaller than  $\phi_{RY}$  since MVAB well-separates the direction of the reconnecting magnetic field from others.

(c) show the angle between the normal vector from MVAB,  $\mathbf{u}_1$ , and the reference normal vector,  $\hat{\mathbf{e}}_R$ , in the R-Y plane ( $\phi_{RY}$ ), and in the R-Z plane ( $\phi_{RZ}$ ) as a function of the nest size,  $M$ . When the normal vector from MVAB agrees with the measured global magnetic geometry, both  $\phi_{RY}$  and  $\phi_{RZ}$  are close to zero. Except at  $Z = 3$  cm,  $\phi_{RY}$  and  $\phi_{RZ}$  are not close to zero and statistical errors do not account for the difference. Therefore, the disagreement of the results from MVAB with the global magnetic geometry does not come from random noise. A possible explanation of the reason for frequent failures of MVAB based on an idealized 2-D X-line geometry is presented in subsection A.5.

MVAB is also tested in a discharge with a time-varying reconnection geometry. As shown in Fig. A.7-(a), a clear O-point is developed and ejected downstream. This O-point is associated with very high local current density and is believed to have a 3-D structure [Dorfman *et al.*, 2013], so we describe this feature as a “flux rope” to emphasize its 3-D nature even though it is not accompanied with a sizeable guide field. MVAB is conducted for data from the measurement point at  $(R, Z) = (37.6, -6)$  (indicated by green diamond marks in Fig. A.7-(a)) as the flux rope passes by. Due to the O-point structure, there is a bump in  $B_R$  around  $334 \mu\text{s}$  as shown in Fig. A.7-(b).  $B_R$  is supposed to have the minimum variance without the O-point. The transformation matrix produced by MVAB for this case is

$$\begin{pmatrix} x_5 \\ y_5 \\ z_5 \end{pmatrix} = \begin{pmatrix} 0.4401 & 0.8906 & -0.1150 \\ -0.8824 & 0.4052 & -0.2389 \\ -0.1662 & 0.2066 & 0.9642 \end{pmatrix} \begin{pmatrix} R \\ Y \\ Z \end{pmatrix}. \quad (\text{A.13})$$

Again, MVAB fails to predict a proper unit vector normal to the current sheet although the three eigenvalues are well-separated as shown in Fig. A.7-(c). However, it still produces a reasonable tangential vector as  $\hat{\mathbf{z}}_5$  remains close to  $\hat{\mathbf{e}}_Z$ .

These examples show that MVAB generally does not produce a proper normal vector even if the current sheet structure does not undergo significant time variations. However, MVAB is much better for determining the direction of the reconnecting magnetic field,

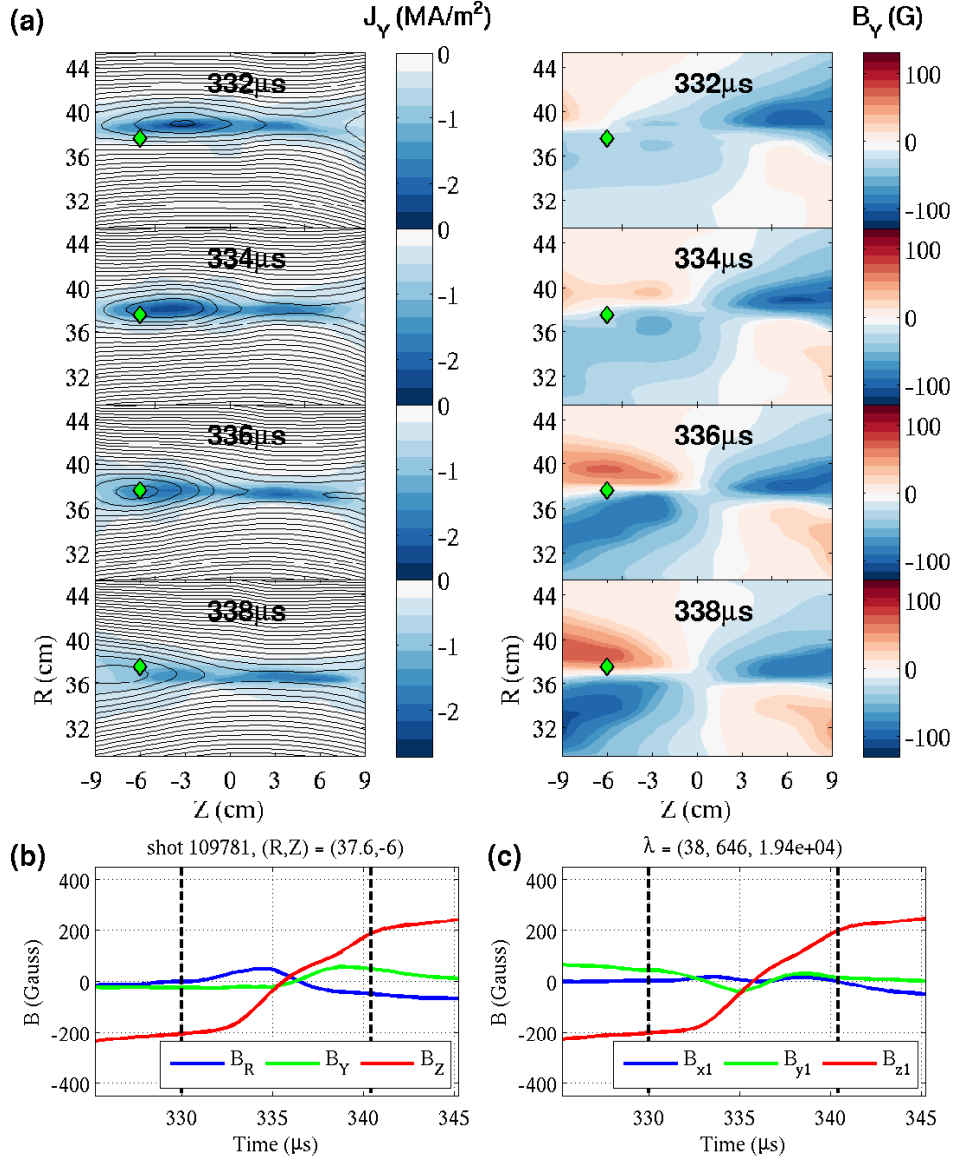


Figure A.7: MVAB for data from a discharge with a time-varying geometry. (a) Left panels: 2-D profiles of  $J_Y$  (color) with contours of  $\psi$  of a discharge containing a flux rope. A clear O-point related to the high local current density is formed and ejected downstream. Right panels: 2-D profiles of  $B_Y$ . Initially, the left side of the quadrupolar structure is destroyed due to the development of the O-point structure ('flux rope'). As the flux rope is ejected downstream, the quadrupolar structure is recovered. The green diamond marks indicate the location of the sample measurement point for data shown in the panel (b). (b) Magnetic field data at a sample measurement point at  $(R, Z) = (37.6, -6)$ . The bump in the normal component  $B_R$  is caused by the passing of the flux rope. (c) The same data after being transformed into the  $(x, y, z)$  coordinate system suggested by MVAB. Three eigenvalues are shown above the panel. Even though three eigenvalues are well-separated for this case, the  $(x, y, z)$  coordinate system constructed by MVAB is far from the real magnetic geometry.

the maximum-varying component, which agrees with [Mozer and Retinò, 2007]. MVAB's prediction for  $\hat{\mathbf{z}}$  is better for measurement points close to the X-point since variations of the other two components are smaller there.

## A.4 Boundary-Crossing Time Analysis (BCTA)

When data from multiple spacecraft is available, the normal vector, speed, and thickness of a boundary based on the boundary-crossing time of each spacecraft. The common assumption of all BCTA techniques is that the boundary is a 1-D plane. The original BCTA by Russell *et al.*, 1983 is called the Constant Velocity Approach (CVA) because it assumes  $V_n$  is a constant during the crossing. Then, the following constraints [Schwartz, 1998] for the boundary normal direction  $\hat{\mathbf{n}}$  and the relative velocity between the layer and the spacecraft  $\mathbf{V}_{rel}$  can be found by assuming  $\mathbf{V}_{rel}$  is a constant during the crossing:

$$(\mathbf{V}_{rel} \cdot \hat{\mathbf{n}})t_{\alpha\beta} = \mathbf{r}_{\alpha\beta} \cdot \hat{\mathbf{n}}, \quad (\text{A.14})$$

where  $\mathbf{r}_{\alpha\beta}$  is the separation vector between any pair of spacecraft and  $t_{\alpha\beta}$  is the difference in time each spacecraft crosses the same boundary. For  $N$  spacecraft, one can find  $N - 1$  independent equations from the above constraint, so that the normal vector and relative velocity along the normal direction  $V_n \equiv \mathbf{V}_{rel} \cdot \hat{\mathbf{n}}$  can be determined if there are four spacecraft and they are not in the same plane.

Since Russell *et al.*, 1983, many different methods based on different assumptions have been developed. By noting that the assumption of a constant velocity may not be proper for current sheets in the magnetopause, Haaland *et al.*, 2004 develop the Constant Thickness Approach (CTA) where the width of the boundary is assumed to be a constant but  $V_n$  a cubic polynomial of time. In another method called the Discontinuity Analyzer (DA) [Dunlop and Woodward, 1998], both the thickness and the velocity can be varied but the normal vector  $\hat{\mathbf{n}}$  must be obtained from single-spacecraft analysis such as MVAB. Finally,

the Minimum Thickness Variation (MTV) method has been developed by combining all of the above three methods [Paschmann *et al.*, 2005]. MTV can be considered as an improved version of DA since it does not require single-spacecraft techniques. Instead, it uses CVA and CTA to find  $\hat{\mathbf{n}}$ , and the velocity is modeled as a cubic polynomial of time rather than a quadratic as in DA.

#### A.4.1 BCTA Results and Analysis: 2D Case

We now apply CVA, CTA, and MTV to data from the MRX jogging experiments to see whether they predict a proper  $\hat{\mathbf{n}}$ ,  $V_n$ , and current sheet thickness  $\delta_{CS}$ . Data from the same discharge shown in Fig. A.4, A.5, and A.6 is used. We choose three test measurement points ( $(R, Z) = (38.5, -3)$ ,  $(38.5, 3)$ , and  $(33.7, 0)$ ;  $Y = 0$  for all) that form a nearly equilateral triangle in the main measurement plane with leg length  $\sim 6$  cm. One more measurement point is provided by an additional probe at  $(R, Y, Z) = (36.5, -9, 0)$ . Figures A.8-(a) and (b) show the location of the four measurement points:  $\mathbf{r}_1$ ,  $\mathbf{r}_2$ ,  $\mathbf{r}_3$ , and  $\mathbf{r}_4$ . The location of  $\mathbf{r}_1$  marked by a red diamond is actually 9 cm below of the plane. Thus, these measurement points form a tetrahedron with the fourth point at  $Y = -9$  cm approximately 10 cm from the others. The upstream density measured by a Langmuir probe for this discharge is about  $4 \times 10^{13} \text{ cm}^{-3}$ , which leads to an ion skin depth of  $\delta_i \equiv c/\omega_{pi} \approx 5.1$  cm for this deuterium plasma. Thus, the separation between measurement points is comparable to  $\delta_i$ .

Figure A.8-(c) shows  $B_Z$  at each measurement point. These time profiles are fitted to the following Harris-type function:

$$B_Z(t) = B_a + B_m \tanh \left[ \frac{t - t_i}{\tau_i} \right] + C_B(t - t_i). \quad (\text{A.15})$$

The third term is required to take the field from external coils such as the PF and equilibrium field coils into account. Following Haaland *et al.*, 2004,  $t_i$  is the crossing time and  $\tau_i$

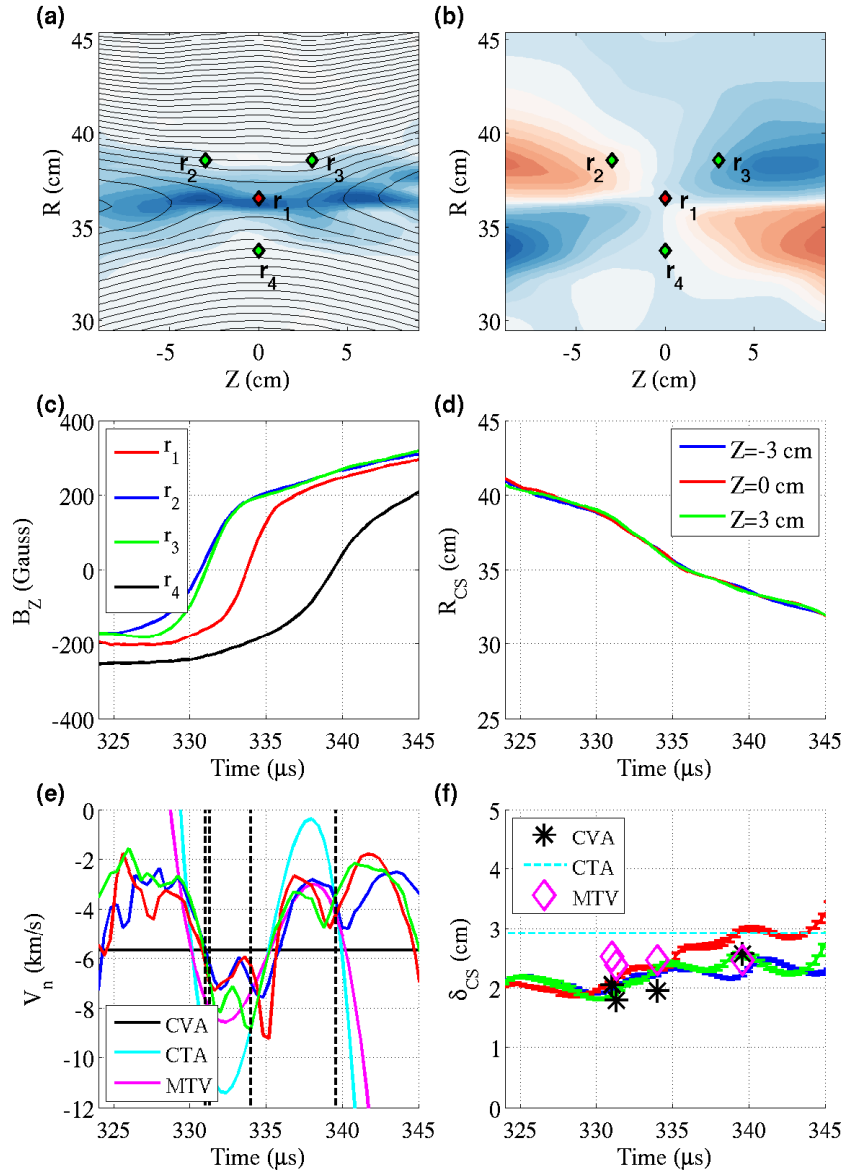


Figure A.8: BCTA for data from the discharge 114338. (a) Profile of  $J_Y$  of the discharge 114338 when the  $B_Z = 0$  boundary is close to  $r_1$ . (b) That of  $B_T$ . Four measurement points ( $r_1$ ,  $r_2$ ,  $r_3$ , and  $r_4$ ) used for BCTA are shown in both panels. Those measurement points form a tetrahedron since  $r_1$ , which is indicated by the red diamond mark, is actually 9 cm below of the main measurement plane. (c) Reconnecting magnetic field  $B_Z$  profiles at 4 sample measurement points for BCTA. (d) Current sheet radial location  $R_{CS}$  measured by magnetic probe arrays at  $Z = -3, 0,$  and  $3$  cm. (e) Normal velocity  $V_n$  from CVA, CTA, and MTV. The red, blue, and green curves are radial velocities of the current sheet ( $dR_{CS}/dt$ ) at  $Z = -3, 0,$  and  $3$  cm, respectively. (f) Current sheet width  $\delta_{CS}$  from CVA, CTA, and MTV. The red, blue, and green curves stand for measured  $\delta_{CS}$  at  $Z = -3, 0,$  and  $3$  cm, respectively.

is half of the crossing duration for  $i$ -th measurement point.

With these crossing times and durations, CVA and CTA are performed to find the normal vector  $\hat{\mathbf{n}}$ . The normal vector from CVA for this example is  $\hat{\mathbf{n}} = 0.9987\hat{\mathbf{e}}_R - 0.0435\hat{\mathbf{e}}_Y - 0.0260\hat{\mathbf{e}}_Z$  and that from CTA is  $\hat{\mathbf{n}} = 0.9923\hat{\mathbf{e}}_R + 0.1147\hat{\mathbf{e}}_Y - 0.0460\hat{\mathbf{e}}_Z$ . Both normal vectors are close to the reference normal  $\hat{\mathbf{e}}_R$ . The normal vector used for MTV is just the renormalized average over the above two normal vectors.

By fitting radial  $B_Z$  profiles from the 2-D magnetic probe arrays into a similar Harris-type function of Eqn. A.15, the radial current sheet location  $R_{CS}$  and width  $\delta_{CS}$  are determined independently. Figure A.8-(d) shows  $R_{CS}$  at  $Z = -3$  cm (the same  $Z$  location of  $\mathbf{r}_2$ ), at  $Z = 0$  cm ( $\mathbf{r}_1$  and  $\mathbf{r}_4$ ), and at  $Z = 3$  cm ( $\mathbf{r}_3$ ), from which the radial velocity of the current sheet can be computed as shown in Fig. A.8-(e) (blue, red, green curves). Black dashed vertical lines indicate four crossing times ( $t_i$ ). These measured values can be compared to estimates from CVA, CTA, and MTV. The black horizontal line in Fig. A.8-(e) indicates the constant  $V_n$  from CVA of  $-5.71$  km/s. Average radial velocities over crossing times measured at  $Z = -3, 0, \text{ and } 3$  cm are  $-5.32, -5.51, \text{ and } -5.80$  km/s, respectively. The cyan curve in the same figure is  $V_n(t)$  from CTA, which is not in quantitative agreement with measured values as the change of velocity is exaggerated. The result from MTV (magenta curve) better describes the actual change of the current sheet velocity during crossings. This is because  $\delta_{CS}$  is also allowed to vary in MTV and  $\delta_{CS}$  is actually changing as shown in Fig. A.8-(f). Again, the red, blue, green curves are results from the Harris fitting and error bars represent uncertainties in the fitting.  $\delta_{CS}$  from CVA (black asterisks) is both qualitatively and quantitatively in agreement with the measured values. On the other hand, the thickness from CTA is 2.92 cm, which is generally higher than the globally measured values. The values from MTV is quantitatively all right, but does not show the tendency of increasing  $\delta_{CS}$  at  $Z = 0$  (red curve) at later times.

The results from CVA are surprisingly close to the measured values even though the radial current sheet velocity varies from  $-8$  to  $-3$  km/s during the crossing as shown in

Fig. A.8-(e). Although the magnitude of the current sheet velocity is changing, its direction remains radial, so that the differences of crossing times by radial separations are still dominant. Furthermore, CVA is not sensitive to changes in the instantaneous velocity. As long as the average velocity over  $t_i$  to  $t_{i+1}$  does not change much, we can expect reasonable results from CVA. However, the change of instantaneous velocity does affect the reliability of results from the Harris fitting by disrupting the time profile of the maximum varying magnetic field component  $B_Z$ . When some of the Harris fittings are poor, we find that normal vectors from CVA can be improved by taking the zero-crossing time of  $B_Z$  as the crossing time  $t_i$ .

The results from CTA are sensitive to the assumption of constant current sheet thickness. In this example,  $\delta_{CS}$  changes over time especially at  $Z = 0$  where both  $\mathbf{r}_1$  and  $\mathbf{r}_4$  exist. The coefficients of the higher order terms of  $V_n(t)$  become considerable due to the small changes in thickness, exaggerating the change in  $V_n$ . CTA is also sensitive to  $\tau_i$  from the Harris fitting; small uncertainties in  $\tau_i$  can significantly alter CTA results. In most of the cases we have tested, the normal vector  $\hat{\mathbf{n}}$  from CTA is reasonable but  $V_n(t)$  and  $\delta_{CS}$  from CTA do not agree well with measured values.

MTV produces better results than CTA especially for  $V_n(t)$ . However,  $\delta_{CS}$  from MTV is sometimes far from measured values. Moreover, MTV is generally unsuccessful in reflecting the actual change in  $\delta_{CS}$ , which is anticipated because MTV minimizes the variance of  $\delta_{CS}$ .

#### A.4.2 BCTA Results and Analysis: 3D case

We have also tested BCTA techniques on data from discharges that undergo significant temporal changes caused by 3-D structures. Figure A.9-(a) shows the time evolution of  $J_Y$  with contours of  $\Psi$  and  $B_Y$ . At  $t = 330 \mu s$ , the position of the main X-point is near  $Z = 0$  based on the quadrupole  $B_Y$  structure. An O-point is formed near  $Z = -3$  cm, generating another X-point probably near  $Z = -11$  cm outside of the measurement window.

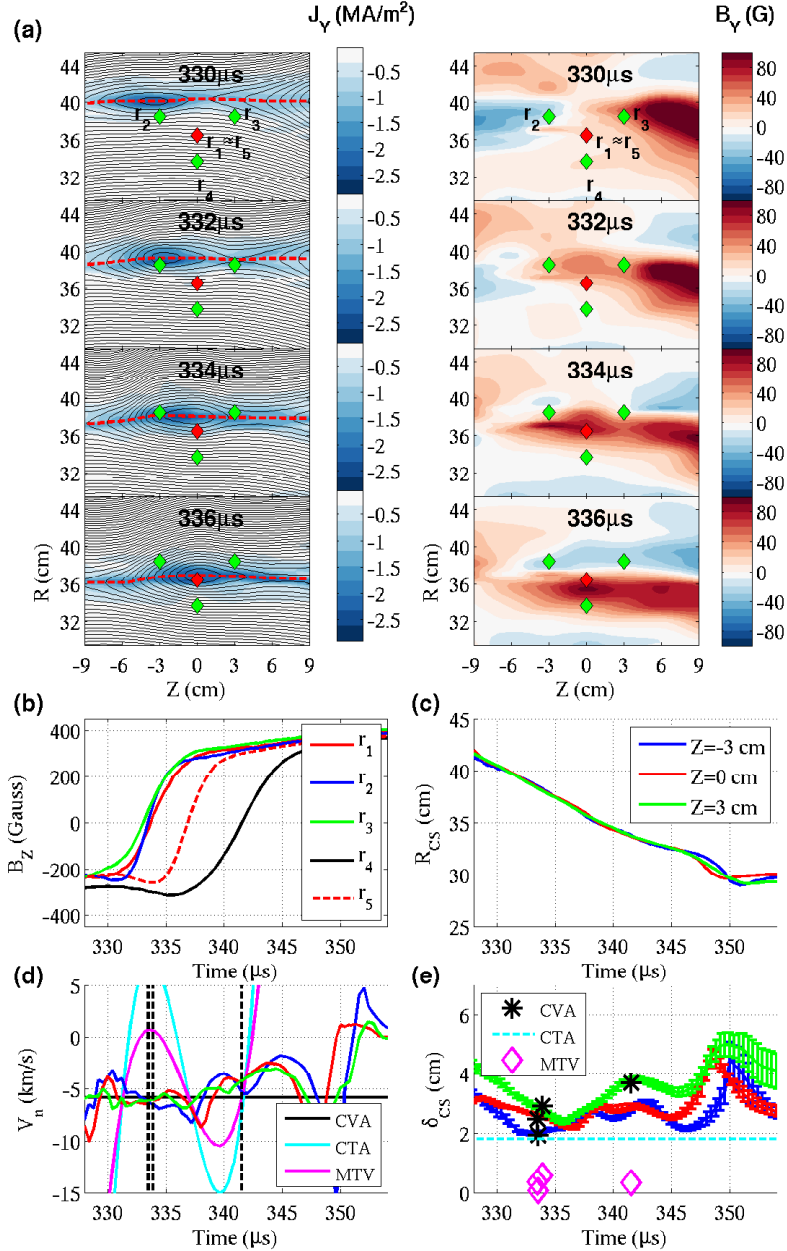


Figure A.9: BCTA for the discharge 114332 which has a ‘flux rope’ structure. (a) Left panels: 2-D profiles of  $J_Y$  (color). Red dashed lines stand for the  $B_Z = 0$  boundary. Right panels: those of  $B_Y$ . A clear O-point is formed and moves to the  $+Z$  direction changing magnetic geometry. The location of the measurement points is indicated by green and red diamonds.  $r_1$  and  $r_5$  has the same  $Z$  location and a similar  $R$  location, but  $r_1$  is located 9 cm below of the main measurement plane. (b) Reconnecting magnetic field  $B_Z$  profiles at sample measurement points. Although  $r_1$  and  $r_5$  have a similar radial position, the  $B_Z = 0$  surface crosses  $r_1$  much earlier, which is a sign of toroidal asymmetry of this discharge. (c) Current sheet radial location  $R_{CS}$  measured by magnetic probe arrays at  $Z = -3, 0,$  and  $3$  cm. (d) Normal velocity  $V_n$  from CVA, CTA, and MTV. (e) Current sheet width  $\delta_{CS}$  from CVA, CTA, and MTV.

As shown in Fig. A.9-(b), the  $B_Z = 0$  boundary passes  $\mathbf{r}_1 = (36.5, -9, 0)$  much earlier than  $\mathbf{r}_5 = (36.4, 0, 0)$ , indicating considerable toroidal asymmetry. This flux rope dynamically evolves, changing the magnetic geometry significantly. As it moves toward the  $+Z$  direction, the original X-point is pushed toward the same direction and the center of the quadrupolar  $B_Y$  structure is shifted to around  $Z = -9$  cm, close to the second X-point, which means the most active X-point is now at  $Z = -9$  cm.

The normal vector from CVA is  $\hat{\mathbf{n}} = 0.9816\hat{\mathbf{e}}_R - 0.1906\hat{\mathbf{e}}_Y + 0.0089\hat{\mathbf{e}}_Z$  and the normal velocity is  $-5.87$  km/s.  $\hat{\mathbf{n}}$  has a sizeable  $\hat{\mathbf{e}}_Y$  component due to the toroidal asymmetry probably caused by kink-type instability along the out-of-plane current direction. As shown in Fig. A.9-(d), the radial velocity of the current sheet (blue, red, and green curves) remains relatively steady and  $V_n$  from CVA agrees with the average radial velocity during crossings which is  $-5.81$  km/s at  $Z = 0$ .  $\delta_{CS}$  from CVA is also in agreement with measured values as shown in Fig. A.9-(e). Since the radial velocity is decreasing,  $\delta_{CS}$  for the last crossing at  $\mathbf{r}_4$  is estimated to be higher than the measured value at  $Z = 0$ .

CTA also produces a reasonable normal vector for this case, which is  $\hat{\mathbf{n}} = 0.9686\hat{\mathbf{e}}_R - 0.2485\hat{\mathbf{e}}_Y + 0.0110\hat{\mathbf{e}}_Z$ . However, the  $V_n(t)$  from CTA is totally deviated from the measured radial velocity profile as shown in Fig. A.9-(d). In this example, the first three crossing times are very close to each other (see the black dashed vertical lines). The durations of the crossings, on the other hand, are diverse since  $\delta_{CS}$  at different axial locations is actually different due to the flux loop formation. To make the current sheet width for each crossing the same,  $V_n(t)$  must change quickly, so that the coefficients of the higher order terms become unrealistically large. In MTV,  $V_n(t)$  is again better than CVA, but the estimated  $\delta_{CS}$  is too small in this case.

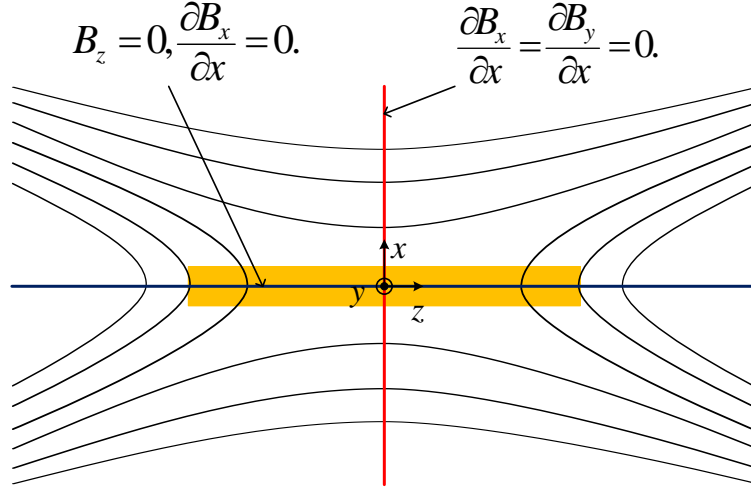


Figure A.10: Idealized X-line geometry. The orange box illustrates the current sheet. The blue line is the boundary of  $B_z = 0$  where  $\partial B_x / \partial x = 0$  is satisfied. The  $\partial B_x / \partial x = 0$  extends along the  $x$  direction only at  $z = 0$  (red line), where  $\partial B_y / \partial x = 0$  is also satisfied.

Location	$\mathbf{u}_1$ (R,Y,Z)	$\mathbf{u}_3$ (R,Y,Z)	Eigenvalues
$\mathbf{r}_1$	(0.8871,0.4612,0.0182)	(-0.0288,0.0159,0.9995)	3, 19, $2.07 \times 10^4$
$\mathbf{r}_2$	(0.9983,-0.0452,-0.0374)	(0.0501,0.3226,0.9452)	1, 47, $1.37 \times 10^4$
$\mathbf{r}_3$	(0.9964,-0.0741,-0.0401)	(0.0149,-0.3134,0.9495)	0.2, 23, $1.80 \times 10^4$
$\mathbf{r}_4$	(0.1002,-0.9942,-0.0388)	(-0.0056,0.0395,0.9992)	0.2, 3, $1.35 \times 10^4$

Table A.1: MVAB results for data from the same sample measurement points used for BCTA in Fig. A.8.  $\mathbf{u}_1$  is the suggested normal vector and  $\mathbf{u}_3$  is the suggested direction of the reconnecting field.

## A.5 Synthesis of Results

### A.5.1 MVAB and BCTA

To compare the results of BCTA with those of MVAB, we perform MVAB for data from the same measurement points as used in subsection A.4.1. Table A.5.1 summarizes MVAB results which have similar trends to those described in section A.3. First, the normal suggested vector  $\mathbf{u}_1$  is close to the reference normal  $\hat{\mathbf{e}}_R$  at  $Z = \pm 3$  ( $\mathbf{r}_2$  and  $\mathbf{r}_3$ ) but it becomes a mixture of  $\hat{\mathbf{e}}_Y$  and  $\hat{\mathbf{e}}_R$  at  $Z = 0$  ( $\mathbf{r}_1$  and  $\mathbf{r}_4$ ). Second, MVAB determines the direction of the reconnecting field component well at  $Z = 0$ , but at  $Z = \pm 3$ ,  $\mathbf{u}_3$  is degraded as the Hall field cannot be distinguished from the reconnecting field.

A fundamental reason that MVAB sometimes fails to determine a proper normal vector is that the X-line magnetic geometry inherently has a 2-D structure. Let us explain this under the idealized 2-D X-line geometry shown in Fig. A.10. The boundary of  $\partial B_x / \partial x = 0$  coincides with the current sheet location at  $x = 0$  and extends along the normal direction ( $\hat{\mathbf{x}}$ ) only at  $z = 0$ . Because MVAB requires a finite number of samples of data around the boundary, at  $z \neq 0$ , it naturally includes data from the region where  $\partial B_x / \partial x = 0$  is not satisfied. Even at  $Z = 0$ , the variance of  $B_x$  is not guaranteed to be minimal since  $\partial B_y / \partial x$  is also zero there. Actually, more than 50 percent of the tested cases for MRX jog experiment data at  $Z = 0$  are degenerate ( $\lambda_1 \sim \lambda_2$ ) since neither  $B_R$  nor  $B_Y$  changes much.

The results in Fig. A.6 support this idea. As shown in Fig. A.6-(a), at  $Z = 0$  in the vicinity of the X point, the length of the error bars becomes smaller with a large nest size  $M$ , which is expected by Eqns. A.11 and A.12. On the other hand, the error bars do not change much at  $Z \neq 0$ . This is because the smallest eigenvalue  $\lambda_1$  becomes larger as  $M$  increases, indicating the source of the variance is not from random noise but from something systematic; the magnetic geometry is not 1-D. With a larger data sample size, more data points lie in the region where  $\partial B_x / \partial x \neq 0$ , increasing the variance  $\lambda_1$ .

CVA, on the other hand, estimates  $\hat{\mathbf{n}}$  based on the moment that the boundary passes

the measurement point. Therefore, as long as the boundary is close to a plane and  $V_n$  is approximately constant over time, it produces a reasonable  $\hat{\mathbf{n}}$  and  $V_n$ . As shown in Fig. A.10, the  $B_z = 0$  boundary that coincides with the location of the current sheet center is a straight line (a plane in 3-D) in spite of the 2-D X-line magnetic geometry. This is why crossing time analysis works even for discharges with flux ropes like Fig. A.9. As shown in Fig. A.9-(a), red dashed lines ( $B_z = 0$  boundaries) remain close to a straight line especially between  $Z = \pm 3$  cm where crossing time analysis is employed.

Another reason for BCTA's better performance is that BCTA utilizes the maximum-varying magnetic field component ( $B_z$ ), while MVAB minimizes the small normal component ( $B_x$ ). Thus, MVAB is more vulnerable to noise and temporal changes than BCTA. The example shown in Fig. A.7 supports that the temporal change in the magnetic geometry can severely affect MVAB results.

## A.5.2 Hybrid Technique for Magnetic Geometry Determination

We have confirmed that the normal vector from BCTA is more reliable than that from MVAB. One disadvantage of BCTA is that it cannot differentiate the two tangential vectors. MVAB, on the other hand, is robust in estimating the direction of the reconnecting magnetic field especially in the vicinity of the X-point where the Hall field is small. Thus, the local magnetic geometry can be precisely determined by appropriately combining two methods.

We suggest the following procedure for the determination of the local magnetic geometry when four spacecraft pass through a current sheet layer. First, employ MVAB for all spacecraft data. Decide which spacecraft is closest to the X-point by either looking at other data such as the ion velocity or comparing  $\lambda_1$  and  $\lambda_2$  for each spacecraft. The one that has the smallest sum of  $\lambda_1$  and  $\lambda_2$  is mostly likely to be closest to the X-point.  $\mathbf{u}_3$  from that spacecraft is a valid indicator for  $\hat{\mathbf{z}}$  and this is a temporary direction for the reconnecting magnetic field,  $\hat{\mathbf{z}}'$ . Find the time evolution of  $B_{z'} = \mathbf{B} \cdot \hat{\mathbf{z}}'$  for each spacecraft. Then,

estimate  $\hat{\mathbf{n}} = \hat{\mathbf{x}}$  and  $V_n$  by crossing time analysis such as CVA. Since  $\hat{\mathbf{n}}$  and  $\hat{\mathbf{z}}'$  may not be orthogonal, decide  $\hat{\mathbf{y}}$  first from  $\hat{\mathbf{y}} = \hat{\mathbf{z}}' \times \hat{\mathbf{x}}$ . Finally,  $\hat{\mathbf{z}}$  is given by  $\hat{\mathbf{z}} = \hat{\mathbf{x}} \times \hat{\mathbf{y}}$ . The transformation matrix obtained by this procedure for data from the discharge 114338 is

$$\begin{pmatrix} x \\ y \\ z \end{pmatrix} = \begin{pmatrix} 0.9987 & -0.0435 & -0.0260 \\ 0.0430 & 0.9969 & -0.0147 \\ 0.0266 & 0.0135 & 0.9975 \end{pmatrix} \begin{pmatrix} R \\ Y \\ Z \end{pmatrix}, \quad (\text{A.16})$$

which is very close to the desired identity matrix.

## A.6 Summary and Discussion

We have tested various techniques for determining the boundary normal direction in space with the use of data from the MRX jog experiment. Multi-spacecraft BCTA techniques are more successful in estimating  $\hat{\mathbf{n}}$  than the single-spacecraft method, MVAB. MVAB deduces the direction of the maximum varying reconnecting magnetic field well. The suggested  $\hat{\mathbf{z}}$  is best in the vicinity of the X-point since the effect from the Hall field is smallest there. Thus, the complete local magnetic geometry can be decided by using BCTA to find the normal vector  $\hat{\mathbf{n}}$  and by employing MVAB to estimate  $\hat{\mathbf{z}}$ . This hybrid procedure is presented in subsection A.5.2.

The better performance of BCTA over MVAB in estimating  $\hat{\mathbf{n}}$  comes from the following reasons. First, the reconnecting current sheet layer fundamentally has 2-D or 3-D structures, which often makes results of MVAB unreliable. Even though the X-line magnetic geometry is 2-D or 3-D, the current sheet itself can be close to a plane as shown in Fig. A.10. BCTA, in this case, can successfully estimate the normal vector. Second, BCTA has more immunity to noise and/or temporal changes since it utilizes the large magnetic field component  $B_z$  while MVAB must rely on the smaller normal component  $B_x$ .

Among BCTA techniques, the performance of CVA is more robust than both CTA and

MTV for MRX jogging data. For CVA, the velocity of the boundary along the normal vector  $V_n$  and the current sheet width  $\delta_{CS}$  are in agreement with the measured values by the 2-D magnetic probe arrays. CTA is more sensitive to the validity of its basic assumption; results of CTA are deviated from the measured values when the current sheet thickness is changing over space and/or time. MTV estimates the instantaneous normal velocity profile  $V_n(t)$  generally better than CTA but it does not reflect the actual variance of  $\delta_{CS}$ . In cases where the constant thickness assumption is quite valid,  $V_n(t)$  can be further improved by applying MTV. One of the major sources of errors of these BCTA techniques is uncertainties in  $t_i$  and  $\tau_i$  from the Harris fitting. CTA and MTV are more sensitive to these errors than CVA.

These results do not necessarily mean CVA is a better method than CTA and MTV. Results from CVA may not be reliable when the current sheet experiences significant acceleration between each crossing. If the spacing between spacecraft is much smaller than the system scale such that the constant thickness assumption is valid, then CTA and MTV should be better choices over CVA. In MRX jogging experiment, because the system size is not much greater than the separation of sample measurement points and the current sheet width changes over space and time,  $V_n(t)$  from CTA and MTV does not reflect the actual normal speed of the boundary.

For BCTA, the distance between measurement points (or spacecraft) is important. If the separation is too small, the normal vector only reflects the local geometry that can be different from the global geometry due to, for example, flux ropes and/or kinked current sheets. If it is too large, the basic assumption of the boundary being a plane may not be satisfied. Moreover,  $V_n$  may not be considered to be a constant. For the MRX jog experiment, separation of  $(1 - 2)\delta_i$  is proper because our system size is about  $10\delta_i$  and the characteristic spatial scale of the kinked current sheet structure along toroidal direction is also expected to be comparable to the ion skin depth.

In the future, we plan to perform a more detailed laboratory test of spacecraft data

analysis techniques by systematically changing the separation of measurement points from the electron skin depth scale (order of mm) like that in the MMS mission to the ion skin depth scale. In addition, change along the out-of-plane direction will be better monitored by placing multiple probes along the symmetric direction.



# Appendix B

## Radial Density Asymmetry in MRX

A radial asymmetry in the plasma density has been consistently observed in the MRX plasma. It has been suggested that this density asymmetry is related to symmetry breaking related to the Hall effect during the counter-helicity merging of two toroidal plasmas [Inomoto *et al.*, 2006]. According to Inomoto *et al.*, 2006, reconnection of the out-of-plane (toroidal) magnetic field generated during plasma formation leads to a current along the radial direction and eventually to a radial shift of the X-point. Depending on the polarity of the toroidal field, the radial shift can be inward or outward. For the case with an inward radial shift, the magnetic field is compressed by the shift, causing a high magnetic pressure on the inboard side. This high magnetic pressure “inhibits” ions from flowing toward the inboard side, such that the plasma density there becomes smaller than on the outboard side. However, in this picture, it is not clear how the high magnetic pressure prevents ions from flowing radially inward since the radial force from  $\mathbf{V}_i \times \mathbf{B}$  is negligible, compared to the force from the pressure gradient.

In this appendix, the mechanism for the radial density asymmetry is discussed. The measured 2-D floating potential profile and ion flow profile reveal that the in-plane inductive field from the time-varying TF currents induces a net ion transport from the inboard to the outboard side. The selective shielding of the inductive field due to the electron inflow

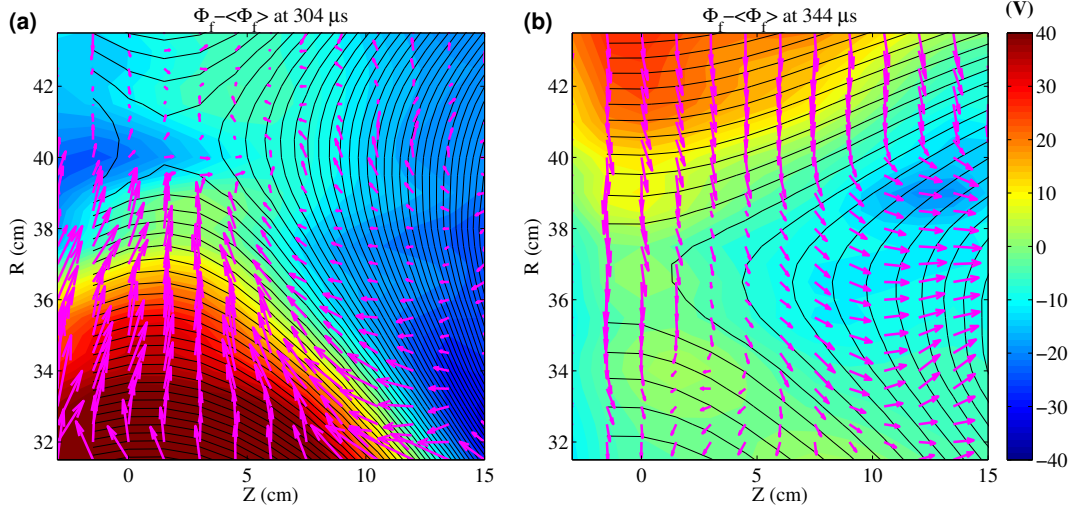


Figure B.1: 2-D profiles of the floating potential and the ion in-plane flow velocity. (a) Profiles at  $t = 304 \mu\text{s}$ . On the inboard side, a large radial electric field ( $> 700 \text{ V/m}$ ) transports ions quickly to the other side. (b) At  $t = 344 \mu\text{s}$ , the outboard side has a large radially inward electric field ( $> 400 \text{ V/m}$ ) that causes a net ion flow to the inboard side.

direction leaves a huge radially electric field on only one side of plasma, which generates a radially asymmetric ion flow pattern.

As shown in Fig. 4.5, the outboard side has 2–3 times larger density than that on the inboard side in the middle of the quasi-steady period. This density profile causes asymmetries in the ion flow (Fig. 4.4), the quadrupole field (Fig. 3.15), and the radial potential profile (Fig. 4.2-(b)). Since MRX has closed magnetic field lines around the center that connect the inboard side to the outboard side, this radial asymmetry requires a net ion transport since ions determine the density profile.

Due to the time-varying TF current, there is a strong in-plane inductive electric field. In the counter-helicity mode where the induced toroidal magnetic field from the two flux cores is equal and opposite, the inductive electric field does not cancel at  $Z = 0$ . With  $dI_{TF}/dt \approx 0.9 \text{ kA}/\mu\text{s}$  where  $I_{TF}$  is the TF coil current, the estimated value of the radial field in vacuum is about  $400 \text{ V/m}$ . However, this strong field may not exist in the presence of the plasma, which is a good conductor. The plasma has a ability to shield most of the

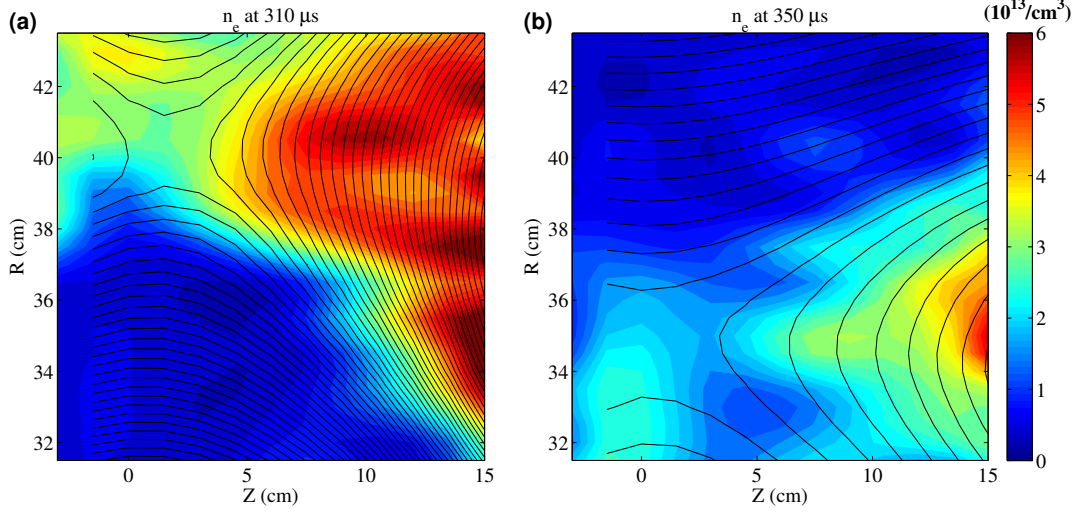


Figure B.2: (a) 2-D density profile at  $t = 310 \mu\text{s}$ . The outboard side has about four times more density. (b) At later time ( $t = 350 \mu\text{s}$ ), the inboard side has a larger density.

inductive field by developing internal currents.

The measured floating potential profile shows that the radial inductive field survives within the plasma, creating an asymmetric ion flow pattern. In particular, it is strong on only one side of the plasma. At  $t = 304 \mu\text{s}$  when the plasma is in the transition from push reconnection to pull reconnection, the inboard side has a huge outwardly directed radial electric field of  $> 700 \text{ V/m}$ , as shown in Fig. B.1-(a). The large electric field induces an ion flow of about  $20 \text{ km/s}$  there, while the outboard side has negligible flow. This suggests that the radial field transports ions from the inboard to the outboard side. At a later time  $t = 344 \mu\text{s}$ , on the other hand, the outboard side has a large inwardly directed radial electric field and there is a net ion flow from the outboard to the inboard side, as shown in Fig. B.2-(b).

The large radial field on one side of plasma and the corresponding net ion transport causes the observed density asymmetry. At the earlier time  $t = 310 \mu\text{s}$  when the quasi-steady period is about to start, the outboard side has about four times larger density than the inboard side, as shown in Fig. B.2-(a). After the quasi-steady period ( $t = 350 \mu\text{s}$ ),

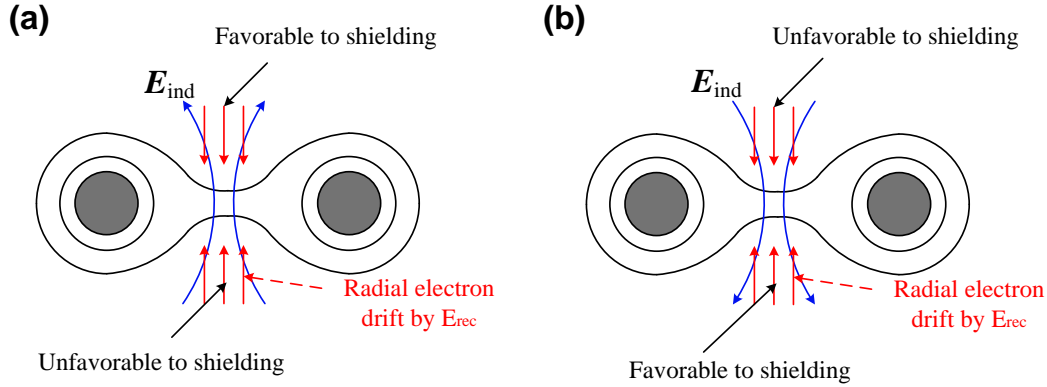


Figure B.3: Selective shielding of the inductive electric field by the plasma. (a) At the earlier time, the electron flow pattern is favorable to shielding of the inductive field on the outboard side. (b) At the later time, it is the opposite.

on the other hand, the inboard side has about twice as much density as the outboard side, as shown in Fig. B.2-(b). This density asymmetry reversal at the later time disproves that the density asymmetry is a result of the counter-helicity merging since the reversal occurs during pull reconnection.

The mechanism for the density asymmetry is the selective shielding of the inductive field by the plasma. As shown in Fig. B.1, the plasma shields the radial inductive field on only one side. The reason for this selective shielding is related to magnetic reconnection geometry. During the transition period that starts around  $t = 290 \mu s$ , the out-of-plane reconnection field is already negative, which is the same as in the pull reconnection period. Thus, the electrons flow radially toward the X-point, as shown by the red arrows in Fig. B.3. At the earlier time, this electron inflow is unfavorable to shielding on the inboard side, since they are forced to move along the direction of the inductive electric field by the reconnection field (B.3-(a)). On the outboard side, the electrons can effectively shield the radial field as they move along the opposite direction of the inductive field. The heavy, weakly magnetized ions can easily lag behind the electrons, thereby inducing a charge separation that cancels the external inductive field. At the later time, as the inductive electric field

direction changes, the situation is reversed, as shown in B.3-(b).

This density asymmetry is expected to be higher in discharges with heavier ions. If the ions are well-magnetized, they would rather execute an  $\mathbf{E} \times \mathbf{B}$  drift than be accelerated by the radial field. This hypothesis needs to be confirmed by experimental measurements.

Although this mechanism for density asymmetry is specific to MRX, it can be used to study reconnection in the magnetopause, where the geometry is also inherently asymmetric [e.g. Phan, Paschmann, and Sonnerup, 1996]. In particular, by using different gases and controlling the TF waveform, the ratio of the upstream density can be varied systematically to address the scaling of the reconnection rate in an asymmetric system [e.g. Cassak and Shay, 2007].



# Appendix C

## Glossary of Symbols for Physical Quantities Related to Energy Transport

Symbol	Definition	Physical Meaning
$\Delta W_M$	Eqn. 2.22	Dissipated magnetic energy per unit time and unit length along the out-of-plane direction in the Sweet-Parker model
$\Delta W_K$	Eqn. 2.23	Increase of flow energy per unit time and unit length along the out-of-plane direction in the Sweet-Parker model
$\Delta W_H$	Eqn. 2.24	Increase of thermal energy per unit time and unit length along the out-of-plane direction in the Sweet-Parker model
$W_{gain}$	$\int_{\mathcal{V}_e} (\mathbf{J}_e \cdot \mathbf{E}) d^3x$	Total electron energy gain from the electric field per unit time inside the volume $\mathcal{V}_e$
$W_k$	Eqn. 5.3	Electron flow energy increase per unit time inside the volume $\mathcal{V}_e$
$W_{Spitzer}$	$\int_{\mathcal{V}_e} \eta_{S\perp} J^2 d^3x$	Ohmic dissipation inside $\mathcal{V}_e$ based on perpendicular Spitzer resistivity inside
$W_u$	Eqn. 5.14	Internal energy increase per unit time inside $\mathcal{V}_e$

Symbol	Definition	Physical Meaning
$W_{col}$	$\int_{\mathcal{V}_e} \eta J^2 d^3x$	Heat obtained by electrons via collisions with other species per unit time inside $\mathcal{V}_e$
$W_{comp}$	$\int_{\mathcal{V}_e} p_e \nabla \cdot \mathbf{V}_e d^3x$	Electron compressional heating power inside $\mathcal{V}_e$
$W_{vis}$	$\int_{\mathcal{V}_e} Q_{vis} d^3x$	Electron heating power by viscosity inside $\mathcal{V}_e$
$W_{loss}$	$\int_{\mathcal{V}_e} \nabla \cdot \mathbf{q}_e d^3x$	Electron heat loss due to the parallel electron conduction per unit time inside $\mathcal{V}_e$
$W_{res}$	$-\int_{\mathcal{V}_e} \mathbf{V}_e \cdot \mathbf{R}_e d^3x$	Heat generated by the collisional drag $\mathbf{R}_e$ per unit time inside $\mathcal{V}_e$
$W_{pe}$	$\int_{\mathcal{V}_e} \mathbf{V}_e \cdot (\nabla \cdot \mathbb{P}_e) d^3x$	Work done by the divergence of the electron pressure tensor per unit time inside $\mathcal{V}_e$
$W_{P,in}$	Eqn. 6.3	Magnetic energy flowing into the volume $\mathcal{V}_b$ per unit time
$W_{P,MHD}$	Eqn. 6.4	Magnetic energy flowing out of $\mathcal{V}_b$ per unit time, associated with $\mathbf{P}_{MHD}$ (see Eqn. 6.2)
$W_{P,Hall}$	Eqn. 6.5	Magnetic energy flowing out of $\mathcal{V}_b$ per unit time, associated with $\mathbf{P}_{Hall}$ (see Eqn. 6.1)
$W'_P$	$\frac{d}{dt} \int_{\mathcal{V}_b} \frac{B^2}{2\mu_0} d^3x.$	Rate of change in magnetic energy enclosed inside $\mathcal{V}_b$
$-\Delta W_P$	Eqn. 6.7	Magnetic energy dissipated inside $\mathcal{V}_b$ per unit time
$W'_{Ke}$	$\frac{d}{dt} \int_{\mathcal{V}_b} 0.5\rho_e V_e^2 d^3x$	Rate of change in electron flow energy enclosed inside $\mathcal{V}_b$
$W_{Ke,in}$	$-\int_{\mathcal{S}_b} \mathbf{K}_{e,in} \cdot d\mathbf{a}$	Electron flow energy flowing into $\mathcal{V}_b$ per unit time ( $\mathbf{K}_{e,in} = 0.5\rho_e V_e^2 V_{eR} \hat{\mathbf{e}}_R$ )
$W_{Ke,out}$	$\int_{\mathcal{S}_b} \mathbf{K}_{e,out} \cdot d\mathbf{a}$	Electron flow energy flowing out of $\mathcal{V}_b$ per unit time ( $\mathbf{K}_{e,out} = 0.5\rho_e V_e^2 V_{eZ} \hat{\mathbf{e}}_Z$ )
$\Delta W_{Ke}$	Eqn. 6.8	Electron flow energy increase inside $\mathcal{V}_b$ per unit time

Symbol	Definition	Physical Meaning
$W'_{Ki}$	$\frac{d}{dt} \int_{\mathcal{V}_b} 0.5\rho_i V_i^2 d^3x$	Rate of change in ion flow energy enclosed inside $\mathcal{V}_b$
$W_{Ki,in}$	$-\int_{S_b} \mathbf{K}_{i,in} \cdot d\mathbf{a}$	Ion flow energy flowing into $\mathcal{V}_b$ per unit time ( $\mathbf{K}_{i,in} = 0.5\rho_i V_i^2 V_{iR} \hat{\mathbf{e}}_R$ )
$W_{Ki,out}$	$\int_{S_b} \mathbf{K}_{i,out} \cdot d\mathbf{a}$	Ion flow energy flowing out of $\mathcal{V}_b$ per unit time ( $\mathbf{K}_{i,out} = 0.5\rho_i V_i^2 V_{iZ} \hat{\mathbf{e}}_Z$ )
$\Delta W_{Ki}$	Eqn. 6.9	Ion flow energy increase inside $\mathcal{V}_b$ per unit time
$W'_{Ue}$	$\frac{d}{dt} \int_{\mathcal{V}_b} 1.5n_e T_e d^3x$	Rate of change in electron internal energy enclosed inside $\mathcal{V}_b$
$W_{He,in}$	$-\int_{S_b} \mathbf{H}_{e,in} \cdot d\mathbf{a}$	Electron enthalpy energy flowing into $\mathcal{V}_b$ per unit time ( $\mathbf{H}_{e,in} = 2.5n_e T_e V_{eR} \hat{\mathbf{e}}_R$ )
$W_{He,out}$	$\int_{S_b} \mathbf{H}_{e,out} \cdot d\mathbf{a}$	Electron enthalpy energy flowing out of $\mathcal{V}_b$ per unit time ( $\mathbf{H}_{e,out} = 2.5n_e T_e V_{eZ} \hat{\mathbf{e}}_Z$ )
$\Delta W_{He}$	Eqn. 6.10	Electron thermal energy increase inside $\mathcal{V}_b$ per unit time
$W'_{Ui}$	$\frac{d}{dt} \int_{\mathcal{V}_b} 1.5n_i T_i d^3x$	Rate of change in ion internal energy enclosed inside $\mathcal{V}_b$
$W_{Hi,in}$	$-\int_{S_b} \mathbf{H}_{i,in} \cdot d\mathbf{a}$	Ion enthalpy energy flowing into $\mathcal{V}_b$ per unit time ( $\mathbf{H}_{i,in} = 2.5n_i T_i V_{iR} \hat{\mathbf{e}}_R$ )
$W_{Hi,out}$	$\int_{S_b} \mathbf{H}_{i,out} \cdot d\mathbf{a}$	Ion enthalpy energy flowing out of $\mathcal{V}_b$ per unit time ( $\mathbf{H}_{i,out} = 2.5n_i T_i V_{iZ} \hat{\mathbf{e}}_Z$ )
$\Delta W_{Hi}$	Eqn. 6.11	Ion thermal energy increase inside $\mathcal{V}_b$ per unit time
$W_{qe}$	$\int_{S_b} \mathbf{q}_e \cdot d\mathbf{a}$	Energy flowing out of $\mathcal{V}_b$ per unit time due to the electron heat flux
$W_{qi}$	$\int_{S_b} \mathbf{q}_i \cdot d\mathbf{a}$	Energy flowing out of $\mathcal{V}_b$ per unit time due to the ion heat flux
$W_e$	$\int_{\mathcal{V}_b} \mathbf{J}_e \cdot \mathbf{E} d^3x$	Electron energy gain inside $\mathcal{V}_b$ per unit time
$W_i$	$\int_{\mathcal{V}_b} \mathbf{J}_i \cdot \mathbf{E} d^3x$	Ion energy gain inside $\mathcal{V}_b$ per unit time



# Bibliography

- Angelopoulos, V., McFadden, J. P., Larson, D., Carlson, C. W., Mende, S. B., Frey, H., Phan, T., Sibeck, D. G., Glassmeier, K.-H., Auster, U., Donovan, E., Mann, I. R., Rae, I. J., Russell, C. T., Runov, A., Zhou, X.-Z., and Kepko, L., *Science* **321**, 931 (2008).
- Aunai, N., Belmont, G., and Smets, R., *Phys. Plasmas* **18**, 122901 (2011a).
- Aunai, N., Belmont, G., and Smets, R., *J. Geophys. Res.* **116**, A09232 (2011b).
- Bale, S. D., Mozer, F. S., and Phan, T., *Geophys. Res. Lett.* **29**, 2180 (2002).
- Bauer, T. M., Dunlop, M. W., Sonnerup, B. U. Ö., Sckopke, N., Fazakerley, A. N., and Khrabrov, A. V., *Geophys. Res. Lett.* **27**, 1835 (2000).
- Berchem, J. and Russell, C. T., *J. Geophys. Res.* **87**, 2108 (1982).
- Bhattacharjee, A., Huang, Y.-M., Yang, H., and Rogers, B., *Phys. Plasmas* **16**, 112102 (2009).
- Birn, J., Drake, J. F., Shay, M. A., Rogers, B. N., Denton, R. E., Hesse, M., Kuznetsova, M., Ma, Z. W., Bhattacharjee, A., Otto, A., and Pritchett, P. L., *J. Geophys. Res.* **106**, 3715 (2001).
- Birn, J. and Priest, E., eds., *Reconnection of magnetic fields* (Cambridge University Press, New York, USA, 2007).
- Biskamp, D., *Phys. Fluids* **29**, 1520 (1986).
- Biskamp, D., *Magnetic reconnection in plasmas* (Cambridge University Press, New York, USA, 2000).
- Biskamp, D., Schwarz, E., and Drake, J. F., *Phys. Rev. Lett.* **75**, 3850 (1995).
- Boozer, A. H., *Phys. Plasmas* **19**, 112901 (2012).
- Borg, A. L., Øieroset, M., Phan, T. D., Mozer, F. S., Pedersen, A., Mouikis, C., McFadden, J. P., Twitty, C., Balogh, A., and Rème, H., *Geophys. Res. Lett.* **32**, L19105 (2005).
- Bowers, K. J., Albright, B. J., Yin, L., Bergen, B., and Kwan, T. J. T., *Physics of Plasmas* **15**, 055703 (2008).

- Braginskii, S. I., in *Reviews of Plasma Physics*, Vol. 1, edited by M. A. Leontovich (Consultants Bureau, New York, 1965) pp. 205–311.
- Bretz, N., Jobes, F., and Irby, J., *Rev. Sci. Instrum.* **68**, 713 (1997).
- Brown, M., Cothran, C., Cohen, D., Horwitz, J., and Chaplin, V., *J. Fusion Energ.* **27**, 16 (2008).
- Brown, M. R., Cothran, C. D., and Fung, J., *Phys. Plasmas* **13**, 056503 (2006).
- Brown, M. R., Cothran, C. D., Landreman, M., Schlossberg, D., Matthaeus, W. H., Qin, G., Lukin, V. S., and Gray, T., *Phys. Plasmas* **9**, 2077 (2002).
- Canfield, R. C., Hudson, H. S., and McKenzie, D. E., *Geophys. Res. Lett.* **26**, 627 (1999).
- Carter, T. A., *Experimental studies of fluctuations in a reconnecting current sheet*, Ph.D. thesis, Princeton University (2001).
- Carter, T. A., Ji, H., Trintchouk, F., Yamada, M., and Kulsrud, R. M., *Phys. Rev. Lett.* **88**, 015001 (2001).
- Cassak, P. A. and Shay, M. A., *Phys. Plasmas* **14**, 102114 (2007).
- Cassak, P. A., Shay, M. A., and Drake, J. F., *Phys. Rev. Lett.* **95**, 235002 (2005).
- Chen, L.-J., Bhattacharjee, A., Puhl-Quinn, P. A., Yang, H., Bessho, N., Imada, S., Muhlbachler, S., Daly, P. W., Lefebvre, B., Khotyaintsev, Y., Vaivads, A., Fazakerley, A., and Georgescu, E., *Nat. Phys.* **4**, 19 (2008).
- Chen, S.-L. and Sekiguchi, T., *J. Appl. Phys.* **36**, 2363 (1965).
- Daughton, W., Roytershteyn, V., Albright, B. J., Karimabadi, H., Yin, L., and Bowers, K. J., *Phys. Plasmas* **16**, 072117 (2009a).
- Daughton, W., Roytershteyn, V., Albright, B. J., Karimabadi, H., Yin, L., and Bowers, K. J., *Phys. Rev. Lett.* **103**, 065004 (2009b).
- Daughton, W., Roytershteyn, V., Karimabadi, H., Yin, L., Albright, B. J., Bergen, B., and Bowers, K. J., *Nat. Phys.* **7**, 539 (2011).
- Davidson, R. C. and Gladd, N. T., *Phys. Fluids* **18**, 1327 (1975).
- Deng, X. H. and Matsumoto, H., *Nature* **410**, 557 (2001).
- Dorfman, S., Daughton, W., Roytershteyn, V., Ji, H., Ren, Y., and Yamada, M., *Phys. Plasmas* **15**, 102107 (2008).
- Dorfman, S., Ji, H., Yamada, M., Yoo, J., Lawrence, E., Myers, C., and Tharp, T. D., *Geophys. Res. Lett.* **40**, 233 (2013).
- Drake, J. F. and Burkhart, G. R., *Geophys. Res. Lett.* **19**, 1077 (1992).

- Drake, J. F., Shay, M. A., and Swisdak, M., *Phys. Plasmas* **15**, 042306 (2008).
- Drake, J. F., Swisdak, M., Cattell, C., Shay, M. A., Rogers, B. N., and Zeiler, A., *Science* **299**, 873 (2003).
- Drake, J. F., Swisdak, M., Che, H., and Shay, M. A., *Nature* **443**, 553 (2006).
- Drake, J. F., Swisdak, M., Phan, T. D., Cassak, P. A., Shay, M. A., Lepri, S. T., Lin, R. P., Quataert, E., and Zurbuchen, T. H., *J. Geophys. Res.* **114**, A05111 (2009).
- Dungey, J. W., *Phys. Rev. Lett.* **6**, 47 (1961).
- Dunlop, M. and Woodward, T. I., in *Analysis Methods for Multi-Spacecraft Data*, edited by G. Paschmann and P. Daly (ISSI SR-001. EAS Publications Divisions, 1998) pp. 271–306.
- Eastwood, J. P., Phan, T.-D., Mozer, F. S., Shay, M. A., Fujimoto, M., Retinò, A., Hesse, M., Balogh, A., Lucek, E. A., and Dandouras, I., *J. Geophys. Res.* **112**, A06235 (2007).
- Eastwood, J. P., Sibeck, D. G., Slavin, J. A., Goldstein, M. L., Lavraud, B., Sitnov, M., Imber, S., Balogh, A., Lucek, E. A., and Dandouras, I., *Geophys. Res. Lett.* **32**, L11105 (2005).
- Edwards, A. W., Campbell, D. J., Engelhardt, W. W., Fahrback, H. U., Gill, R. D., Granetz, R. S., Tsuji, S., Tubbing, B. J. D., Weller, A., Wesson, J., and Zaslache, D., *Phys. Rev. Lett.* **57**, 210 (1986).
- Egedal, J., Daughton, W., and Le, A., *Nat. Phys.* **8**, 321 (2012).
- Egedal, J., Fox, W., Katz, N., Porkolab, M., Ieroset, M., Lin, R. P., Daughton, W., and Drake, J. F., *J. Geophys. Res.* **113**, A12207 (2008).
- Emslie, A. G., Dennis, B. R., Holman, G. D., and Hudson, H. S., *J. Geophys. Res.* **110**, A11103 (2005).
- Fiksel, G., Almagri, A. F., Chapman, B. E., Mirnov, V. V., Ren, Y., Sarff, J. S., and Terry, P. W., *Phys. Rev. Lett.* **103**, 145002 (2009).
- Fiksel, G., Hartog, D. J. D., and Fontana, P. W., *Rev. Sci. Instrum.* **69**, 2024 (1998).
- Forbush, S. E., *Phys. Rev.* **70**, 771 (1946).
- Fox, W., Porkolab, M., Egedal, J., Katz, N., and Le, A., *Physics of Plasmas* **17**, 072303 (2010).
- Freidberg, J. P., *Ideal Magnetohydrodynamics* (Plenum Press, New York, USA, 1987).
- Fujisawa, A., Ji, H., Yamagishi, K., Shinohara, S., Toyama, H., and Miyamoto, K., *Nucl. Fusion* **31**, 1443 (1991).

- Gangadhara, S., Craig, D., Ennis, D. A., Hartog, D. J. D., Fiksel, G., and Prager, S. C., Phys. Rev. Lett. **98**, 075001 (2007).
- Gekelman, W., Stenzel, R. L., and Wild, N., J. Geophys. Res. **87**, 101 (1982).
- Giovanelli, R., Nature **158**, 81 (1946).
- von Goeler, S., Stodiek, W., and Sauthoff, N., Phys. Rev. Lett. **33**, 1201 (1974).
- Goldman, M. V., Newman, D. L., Gosling, J. T., Andersson, L., Eriksson, S., Lapenta, G., and Markidis, S., “Energy transport during magnetic reconnection,” (2013), to be published.
- Gosling, J. T., Asbridge, J. R., Bame, S. J., Feldman, W. C., Paschmann, G., Sckopke, N., and Russell, C. T., J. Geophys. Res. **87**, 2147 (1982).
- Gosling, J. T., Thomsen, M. F., Bame, S. J., and Russell, C. T., J. Geophys. Res. **91**, 3029 (1986).
- Goto, M., J. Quant. Spectrosc. Ra. **76**, 331 (2003).
- Haaland, S. E., Sonnerup, B. U. Ö., Dunlop, M. W., Balogh, A., Georgescu, E., Hasegawa, H., Klecker, B., Paschmann, G., Puhl-Quinn, P., Rème, H., Vaith, H., and Vaivads, A., Ann. Geophys. **22**, 1347 (2004).
- Harra, L. K., Phil. Trans. R. Soc. Lond. A **360**, 2757 (2002).
- Harris, E., Nuovo Cimento **23**, 115 (1962).
- Helander, P., Eriksson, L.-G., Akers, R. J., Byrom, C., Gimblett, C. G., and Tournianski, M. R., Phys. Rev. Lett. **89**, 235002 (2002).
- Hesse, M., Schindler, K., Birn, J., and Kuznetsova, M., Phys. Plasmas **6**, 1781 (1999).
- Hoshino, M., J. Geophys. Res. **110**, A10215 (2005).
- Hoshino, M., Mukai, T., Terasawa, T., and Shinohara, I., J. Geophys. Res. **106**, 25979 (2001).
- Hoshino, M., Mukai, T., Yamamoto, T., and Kokubun, S., J. Geophys. Res. **103**, 4509 (1998).
- Hsu, S. C., Fiksel, G., Carter, T. A., Ji, H., Kulsrud, R. M., and Yamada, M., Phys. Rev. Lett. **84**, 3859 (2000).
- Huba, J. D., Phys. Plasmas **12**, 012322 (2005).
- Hutchinson, I. H., Plasma Phys. Contr. F. **44**, 1953 (2002).
- Hutchinson, I. H., *Principles of plasma diagnostics*, 2nd ed. (Cambridge University Press, Cambridge, UK, 2005).

- Imada, S., Hoshino, M., and Mukai, T., *Geophys. Res. Lett.* **32**, L09101 (2005).
- Imada, S., Nakamura, R., Daly, P. W., Hoshino, M., Baumjohann, W., Mühlbacher, S., Balogh, A., and Rème, H., *J. Geophys. Res.* **112**, A03202 (2007).
- Inomoto, M., Gerhardt, S. P., Yamada, M., Ji, H., Belova, E., Kuritsyn, A., and Ren, Y., *Phys. Rev. Lett.* **97**, 135002 (2006).
- Itikawa, Y., *At. Data and Nucl. Data Tables* **21**, 69 (1978).
- Janev, R. K., Langer, W., Evans, K., and Post, D. E., *Elementary Processes in Hydrogen-Helium Plasmas* (Springer-Verlag, Berlin, Germany, 1987).
- Ji, H., Terry, S., Yamada, M., Kulsrud, R., Kuritsyn, A., and Ren, Y., *Phys. Rev. Lett.* **92**, 115001 (2004).
- Ji, H., Yamada, M., Hsu, S., Kulsrud, R., Carter, T., and Zaharia, S., *Phys. Plasmas* **6**, 1743 (1999).
- Kadomtsev, B. B., *Sov. J. Plasma Phys.* **1**, 389 (1975).
- Karimabadi, H., Daughton, W., and Scudder, J., *Geophys. Res. Lett.* **34**, L13104 (2007).
- Khotyaintsev, Y. V., Vaivads, A., Retinò, A., André, M., Owen, C. J., and Nilsson, H., *Phys. Rev. Lett.* **97**, 205003 (2006).
- Khrabrov, A. V. and Sonnerup, B. U. Ö., *J. Geophys. Res.* **103**, 6641 (1998a).
- Khrabrov, A. V. and Sonnerup, B. U. Ö., *Geophys. Res. Lett.* **25**, 2373 (1998b).
- Krucker, S., Hudson, H. S., Glesener, L., White, S. M., Masuda, S., Wuelser, J.-P., and Lin, R. P., *Astrophys. J.* **714**, 1108 (2010).
- Kuritsyn, A., Yamada, M., Gerhardt, S., Ji, H., Kulsrud, R., and Ren, Y., *Phys. Plasmas* **13**, 055703 (2006).
- Kuznetsova, M. M., Hesse, M., and Winske, D., *J. Geophys. Res.* **103**, 199 (1998).
- Lawrence, E. E., Ji, H., Yamada, M., and Yoo, J., *Phys. Rev. Lett.* **110**, 015001 (2013).
- Li, B. and Horiuchi, R., *Phys. Rev. Lett.* **101**, 215001 (2008).
- Lin, R., *Space Sc. Rev.* **159**, 421 (2011).
- Lin, R. and Hudson, H., *Sol. Phys.* **50**, 153 (1976).
- Lin, R. P., Krucker, S., Hurford, G. J., Smith, D. M., Hudson, H. S., Holman, G. D., Schwartz, R. A., Dennis, B. R., Share, G. H., Murphy, R. J., Emslie, A. G., Johns-Krull, C., and Vilmer, N., *Astrophys. J. Lett.* **595**, L69 (2003).
- Ma, Z. W. and Bhattacharjee, A., *Geophys. Res. Lett.* **23**, 2955 (1996).

- Magee, R. M., Den Hartog, D. J., Kumar, S. T. A., Almagri, A. F., Chapman, B. E., Fiksel, G., Mirnov, V. V., Mezonlin, E. D., and Titus, J. B., *Phys. Rev. Lett.* **107**, 065005 (2011).
- Mandt, M. E., Denton, R. E., and Drake, J. F., *Geophys. Res. Lett.* **21**, 73 (1994).
- McWhirter, R. W. P., in *Spectral Intensities*, edited by R. H. Huddleston and S. L. Leonard (Academic Press, New York, 1965) pp. 201–264.
- Meng, C.-I., Lui, A. T. Y., Krimigis, S. M., Ismail, S., and Williams, D. J., *J. Geophys. Res.* **86**, 5682 (1981).
- Mobius, E., Hovestadt, D., Klecker, B., Scholer, M., Gloeckler, G., and Ipavich, F. M., *Nature* **318**, 426 (1985).
- Morozov, D. K., Baronova, E. O., and Senichenkov, I. Y., *Plasma Phys. Rep.* **33**, 906 (2007).
- Mozer, F. S., Bale, S. D., and Phan, T.-D., *Phys. Rev. Lett.* **89**, 015002 (2002).
- Mozer, F. S. and Retinò, A., *J. Geophys. Res.* **112**, A10206 (2007).
- Mozer, F. S., Wilber, M., and Drake, J. F., *Phys. Plasmas* **18**, 102902 (2011).
- Øieroset, M., Lin, R. P., Phan, T.-D., Larson, D. E., and Bale, S. D., *Phys. Rev. Lett.* **89**, 195001 (2002).
- Øieroset, M., Phan, T.-D., Fujimoto, M., Lin, R. P., and Lepping, R. P., *Nature* **412**, 414 (2001).
- Oka, M., Phan, T.-D., Krucker, S., Fujimoto, M., and Shinohara, I., *Astrophys. J.* **714**, 915 (2010).
- Ono, Y., Tanabe, H., Hayashi, Y., Ii, T., Narushima, Y., Yamada, T., Inomoto, M., and Cheng, C. Z., *Phys. Rev. Lett.* **107**, 185001 (2011).
- Ono, Y., Yamada, M., Akao, T., Tajima, T., and Matsumoto, R., *Phys. Rev. Lett.* **76**, 3328 (1996).
- Parker, E. N., *J. Geophys. Res.* **62**, 509 (1957).
- Paschmann, G., Haaland, S., Sonnerup, B. U. Ö., Hasegawa, H., Georgescu, E., Klecker, B., Phan, T. D., Rème, H., and Vaivads, A., *Ann. Geophys.* **23**, 1481 (2005).
- Paschmann, G., Sonnerup, B. U. Ö., Papamastorakis, I., Baumjohann, W., Schopke, N., and Lühr, H., *Geophys. Res. Lett.* **17**, 1829 (1990).
- Paschmann, G., Sonnerup, B. U. Ö., Papamastorakis, I., Schopke, N., Haerendel, G., Bame, S. J., Asbridge, J. R., Gosling, J. T., Russell, C. T., and Elphic, R. C., *Nature* **282**, 243 (1979).
- Pei, W., Horiuchi, R., and Sato, T., *Phys. Rev. Lett.* **87**, 235003 (2001).

- Petschek, H. E., NASA Spec. Pub. **SP-50**, 425 (1964).
- Phan, T. D., Dunlop, M. W., Paschmann, G., Klecker, B., Bosqued, J. M., Rème, H., Balogh, A., Twitty, C., Mozer, F. S., Carlson, C. W., Mouikis, C., and Kistler, L. M., *Ann. Geophys.* **22**, 2355 (2004).
- Phan, T. D., Gosling, J. T., Davis, M. S., Skoug, R. M., Øieroset, M., Lin, R. P., Lepping, R. P., McComas, D. J., Smith, C. W., Reme, H., and Balogh, A., *Nature* **439**, 175 (2006).
- Phan, T. D., Kistler, L. M., Klecker, B., Haerendel, G., Paschmann, G., Sonnerup, B. U. Ö., Baumjohann, W., Bavassano-Cattaneo, M. B., Carlson, C. W., DiLellis, A. M., Fornacon, K. H., Frank, L. A., Fujimoto, M., Georgescu, E., Kokubun, S., Moebius, E., Mukai, T., Oieroset, M., Paterson, W. R., and Reme, H., *Nature* **404**, 848 (2000).
- Phan, T.-D., Paschmann, G., and Sonnerup, B. U. O., *J. Geophys. Res.* **101**, 7817 (1996).
- Pickett, J. S., Franz, J. R., Scudder, J. D., Menietti, J. D., Gurnett, D. A., Hospodarsky, G. B., Braunger, R. M., Kintner, P. M., and Kürth, W. S., *J. Geophys. Res.* **106**, 19081 (2001).
- Priest, E. and Forbes, T., *Magnetic reconnection - MHD theory and applications* (Cambridge University Press, New York, USA, 2000).
- Pritchett, P. L., *J. Geophys. Res.* **106**, 25961 (2001).
- Pritchett, P. L., *Phys. Plasmas* **15**, 102105 (2008).
- Pritchett, P. L., *J. Geophys. Res.* **115**, A10208 (2010).
- Ren, Y., Yamada, M., Gerhardt, S., Ji, H., Kulsrud, R., and Kuritsyn, A., *Phys. Rev. Lett.* **95**, 055003 (2005).
- Ren, Y., Yamada, M., Ji, H., Dorfman, S., Gerhardt, S. P., and Kulsrud, R., *Phys. Plasmas* **15**, 082113 (2008a).
- Ren, Y., Yamada, M., Ji, H., Gerhardt, S. P., and Kulsrud, R., *Phys. Rev. Lett.* **101**, 085003 (2008b).
- Retinò, A., Nakamura, R., Vaivads, A., Khotyaintsev, Y., Hayakawa, T., Tanaka, K., Kasahara, S., Fujimoto, M., Shinohara, I., Eastwood, J. P., André, M., Baumjohann, W., Daly, P. W., Kronberg, E. A., and Cornilleau-Wehrin, N., *J. Geophys. Res.* **113**, A12215 (2008).
- Retinò, A., Sundkvist, D., Vaivads, A., Mozer, F., André, M., and Owen, C. J., *Nat. Phys.* **3**, 236 (2007).
- Rosenqvist, L., Vaivads, A., Retinò, A., Phan, T., Opgenoorth, H. J., Dandouras, I., and Buchert, S., *Geophys. Res. Lett.* **35**, L08104 (2008).

- Roytershteyn, V., Daughton, W., Dorfman, S., Ren, Y., Ji, H., Yamada, M., Karimabadi, H., Yin, L., Albright, B. J., and Bowers, K. J., *Phys. Plasmas* **17**, 055706 (2010).
- Roytershteyn, V., Dorfman, S., Daughton, W., Ji, H., Yamada, M., and Karimabadi, H., “Electromagnetic instability of thin reconnection layers: Comparison of 3D simulations with MRX observations,” (2013), to be published.
- Russell, C. T., Mellott, M. M., Smith, E. J., and King, J. H., *J. Geophys. Res.* **88**, 4739 (1983).
- Samtaney, R., Loureiro, N. F., Uzdensky, D. A., Schekochihin, A. A., and Cowley, S. C., *Phys. Rev. Lett.* **103**, 105004 (2009).
- Sarafopoulos, D. V., Sidiropoulos, N. F., Sarris, E. T., Lutsenko, V., and Kudela, K., *J. Geophys. Res.* **106**, 13053 (2001).
- Sato, T., Matsumoto, H., and Nagai, K., *J. Geophys. Res.* **87**, 6089 (1982).
- Savrukhin, P. V., *Plasma Phys. Contr. F.* **48**, B201 (2006).
- Scholer, M. and Jamitzky, F., *J. Geophys. Res.* **92**, 12181 (1987).
- Schwartz, S. J., in *Analysis Methods for Multi-Spacecraft Data*, edited by G. Paschmann and P. W. Daly (ISSI SR-001. EAS Publications Divisions, 1998) pp. 249–270.
- Scime, E., Hokin, S., Mattor, N., and Watts, C., *Phys. Rev. Lett.* **68**, 2165 (1992).
- Shay, M. A. and Drake, J. F., *Geophys. Res. Lett.* **25**, 3759 (1998).
- Shay, M. A., Drake, J. F., Denton, R. E., and Biskamp, D., *J. Geophys. Res.* **103**, 9165 (1998).
- Shay, M. A., Drake, J. F., Rogers, B. N., and Denton, R. E., *Geophys. Res. Lett.* **26**, 2163 (1999).
- Shih, A. Y., Lin, R. P., and Smith, D. M., *Astrophys. J. Lett.* **698**, L152 (2009).
- Sonnerup, B. U. Ö., *Magnetic field reconnection*, edited by L. T. Lanzerotti, C. F. Kennel, and E. N. Parker, Vol. 3 (North-Holland Publishing Co., Amsterdam, Netherlands, 1979) pp. 45–108.
- Sonnerup, B. U. Ö. and Cahill, L. J., *J. Geophys. Res.* **72**, 171 (1967).
- Sonnerup, B. U. Ö., Papamastorakis, I., Paschmann, G., and Lühr, H., *J. Geophys. Res.* **92**, 12137 (1987).
- Sonnerup, B. U. Ö., Paschmann, G., Papamastorakis, I., Sckopke, N., Haerendel, G., Bame, S. J., Asbridge, J. R., Gosling, J. T., and Russell, C. T., *J. Geophys. Res.* **86**, 10049 (1981).

- Sonnerup, B. U. Ö. and Scheible, M., in *Analysis Methods for Multi-Spacecraft Data*, edited by G. Paschmann and P. Daly (ISSI SR-001. EAS Publications Divisions, 1998) pp. 185–220.
- Speiser, T. W., *J. Geophys. Res.* **70**, 4219 (1965).
- Spitzer, L., *Physics of fully ionized gases*, 2nd ed. (Interscience Publishers, New York, USA, 1962).
- Stark, A., Fox, W., Egedal, J., Grulke, O., and Klinger, T., *Phys. Rev. Lett.* **95**, 235005 (2005).
- Stenzel, R. L., Gekelman, W., and Wild, N., *J. Geophys. Res.* **87**, 111 (1982).
- Stenzel, R. L., Gekelman, W., Wild, N., Urrutia, J. M., and Whelan, D., *Rev. Sci. Instrum.* **54**, 1302 (1983).
- Stotler, D., Post, D., and Reiter, D., *Bull. Am. Phys. Soc.* **38**, 1919 (1993).
- Sweet, P., *Electromagnetic Phenomena in Cosmical Physics*, edited by B. Lehnert (Cambridge Univ. Press, New York, 1958) p. 123.
- Takizuka, T. and Abe, H., *J. Comput. Phys.* **25**, 205 (1977).
- Taylor, J. B., *Rev. Mod. Phys.* **58**, 741 (1986).
- Terasawa, T., Kawano, H., Shinohara, I., Mukai, T., Saito, Y., Hoshino, M., Nishida, A., Machida, S., Nagai, T., Yamamoto, T., and Kokubuns, S., *J. Geomag. Geoelectr.* **48**, 603 (1996).
- Tharp, T. D., Yamada, M., Ji, H., Lawrence, E., Dorfman, S., Myers, C. E., and Yoo, J., *Phys. Rev. Lett.* **109**, 165002 (2012).
- Trintchouk, F., Yamada, M., Ji, H., Kulsrud, R. M., and Carter, T. A., *Phys. Plasmas* **10**, 319 (2003).
- Tsuneta, S., *Astrophys. J.* **456**, 840 (1996).
- Uzdensky, D. A. and Kulsrud, R. M., *Phys. Plasmas* **7**, 4018 (2000).
- Uzdensky, D. A. and Kulsrud, R. M., *Phys. Plasmas* **13**, 062305 (2006).
- Vaivads, A., Khotyaintsev, Y., André, M., Retinò, A., Buchert, S. C., Rogers, B. N., Décréau, P., Paschmann, G., and Phan, T. D., *Phys. Rev. Lett.* **93**, 105001 (2004).
- Vaivads, A., Khotyaintsev, Y., André, M., and Treumann, R., in *Geospace Electromagnetic Waves and Radiation*, Lecture Notes Physics, Vol. 687, edited by J. W. LaBelle and R. A. Treumann (Springer Berlin Heidelberg, 2006) pp. 251–269.
- Wang, Y., *Nonlinear heating of the reconnection layer by strong lower hybrid instabilities*, Ph.D. thesis, Princeton University (2010).

- Wiese, W. L. and Fuhr, J. R., *J. Phys. Chem. Ref. Data* **38**, 565 (2009).
- Wygant, J. R., Carttell, C. A., Lysak, R., Song, Y., Dombek, J., McFadden, J., Mozer, F. S., Carlson, C. W., Parks, G., Lucek, E. A., Balogh, A., Andre, M., Reme, H., Hesse, M., and Mouikis, C., *J. Geophys. Res.* **110**, A09206 (2005).
- Yamada, M., *Phys. Plasmas* **14**, 058102 (2007).
- Yamada, M., *Phys. Plasmas* **18**, 111212 (2011).
- Yamada, M., Furth, H. P., Hsu, W., Janos, A., Jardin, S., Okabayashi, M., Sinnis, J., Stix, T. H., and Yamazaki, K., *Phys. Rev. Lett.* **46**, 188 (1981).
- Yamada, M., Ji, H., Hsu, S., Carter, T., Kulsrud, R., Bretz, N., Jobes, F., Ono, Y., and Perkins, F., *Phys. Plasmas* **4**, 1936 (1997).
- Yamada, M., Kulsrud, R., and Ji, H., *Rev. Mod. Phys.* **82**, 603 (2010).
- Yamada, M., Levinton, F. M., Pomphrey, N., Budny, R., Manickam, J., and Nagayama, Y., *Phys. Plasmas* **1**, 3269 (1994).
- Yamada, M., Ren, Y., Ji, H., Breslau, J., Gerhardt, S., Kulsrud, R., and Kuritsyn, A., *Phys. Plasmas* **13**, 052119 (2006).
- Yoo, J. and Yamada, M., *J. of Geophys. Res.* **117**, A12202 (2012).
- Yoo, J., Yamada, M., Ji, H., and Myers, C. E., “Observation of ion acceleration and heating during collisionless reconnection in a laboratory plasma,” (2013), to be published in *Phys. Rev. Lett.*
- Zharkova, V., Arzner, K., Benz, A., Browning, P., Dauphin, C., Emslie, A., Fletcher, L., Kontar, E., Mann, G., Onofri, M., Petrosian, V., Turkmani, R., Vilmer, N., and Vlahos, L., *Space Sc. Rev.* **159**, 357 (2011).
- Zhou, M., Deng, X. H., Li, S. Y., Pang, Y., Vaivads, A., Rème, H., Lucek, E., Fu, S., Lin, X., Yuan, Z. G., and Wang, J. F., *J. Geophys. Res.* **114**, A02216 (2009).
- Zweibel, E. G. and Yamada, M., *Annu. Rev. Astron. Astr.* **47**, 291 (2009).